ASPECTS OF TWO-PHASE, GAS-LIQUID, SEPARATION RELATED TO NUCLEAR STEAM SUPPLY SYSTEMS

PROEFSCHRIFT

TER VERKRIJGING VAN DE GRAAD VAN DOCTOR
IN DE TECHNISCHE WETENSCHAPPEN AAN DE
TECHNISCHE HOGESCHOOL DELFT, OP GEZAG
VAN DE RECTOR MAGNIFICUS IR. H. R. VAN
NAUTA LEMKE, HOOGLERAAR IN DE AFDELING
DER ELEKTROTECHNIEK, VOOR EEN COMMISSIE
UIT DE SENAAT TE VERDEDIGEN OP WOENSDAG
29 SEPTEMBER 1971 TE 14.00 UUR

DOOR

CAREL ALBERT PRINS

werktuigkundig ingenieur

geboren te Ginneken en Bavel

Dit proefschrift is goedgekeurd door de promotoren
PROF. IR. D. G. H. LATZKO EN PROF. IR. J. O. HINZE.

"I have often wondered what would have happened if the air we are breathing did contain liquid particles or the water we are drinking, gas bubbles. I suspect that we would all be meeting at this same university to hold a symposium on single-phase flow and to discuss the increased complexity of single-phase flow relative to two-phase flow. I also surmise that we would have developed a comprehensive technology of two-phase flow based upon understanding of liquid gas interface phenomena and that we would be struggling right now trying to extend it to single-phase flow....."

S. LEVY [1]

CONTENTS

LIST OF SYMBOLS

A	Area	m^2
B	Virtual mass coefficient	
C	Coefficient, constant	
D	Diameter	m
d	Bubble diameter	m
F	Force	N
	Function	
f	Function	
G	Mass velocity	kg/m^2s
g	Gravitational constant	m/s^2
H	Height	m
h	Specific enthalpie	J/kg
	Stripwidth, depth of flow	m
I	Radiation intensity	$photons/cm^2s$
K, k	Constant	
L	Length	m
M	Momentum flux	N
n	Coordinate normal to wall	m
O	Channel perifery	m
p	Pressure	N/m^2
Δp	Pressure drop	N/m^2
Q	Heat flow	W
	Radius	m
R	Resistance force per unit volume	N/m^3
	Gas constant	$m^2/s^{2}{}^{\circ}C$
	Radius	m
r	Latent heat of evaporation	J/kg
s	Slip ratio	
	Coordinate along wall	m
T	Absolute temperature	$^{\circ}K$
t	Time	s
	Tubewall thickness	m
u	True phase velocity	m/s
V	Volume	m^3
v	Velocity	m/s
x	Coordinate	m
	Quality	

y	Coordinate	m
z	Coordinate	m

Greek Symbols

α	Gas or solids volume fraction (void fraction)	
β	Volumetric quality	
ε	Strain	
	Turbulence viscosity	Ns/m^2
ζ	Relative humidity of wet air	
η	Dynamic viscosity	Ns/m^2
	Efficiency	
λ	Friction factor	
ρ	Density	kg/m^3
σ	Surface tension	N/m
τ	Shear stress	N/m^2
ϕ	Flow rate	kg/s
ϕ^2	Two-phase friction multiplier	
Ω	Angular momentum flux	

Subscripts

acc	acceleration
b	bubble
c	control volume, measuring cell, compound
CO	carry-over
CU	carry-under
D	drag, downcomer
DB	downcomer region below sparger
E	gas phase exhaust from separator
f	fluid
fr	friction
g	gas phase
G.O.	gas flowing only
gd	dry air
gn	water vapor
H	hydraulic

ℓ	liquid phase
L.O.	liquid flowing only
m	mixture, mass
n	normal to wall
p	particle, plenum
q	quench
R	riser
r	relative, measured, radial
S	sparger
s	system, parallel to wall, superficial
sat	saturation
t	tangential
TP	two-phase
v	vessel, volume
w	wall
z	axial

Superscripts

α	bubble swarm
∞	single bubble
	undisturbed flow

Definitions

$< \; >$	average value	
s	slip ratio: $\frac{u_g}{u_\ell}$	
u	true phase velocity	
	in one dimensional model:	$u_g = < u_g > = \frac{\phi_{vg}}{\alpha A}$
		$u_\ell = < u_\ell > = \frac{\phi_{v\ell}}{(1-\alpha)A}$
v_s	superficial velocity:	$\frac{\phi_v}{A} \rightarrow v_{sg} = \frac{\phi_{vg}}{A}$
		$\rightarrow v_{s\ell} = \frac{\phi_{v\ell}}{A}$

x	Quality:	$\frac{\phi_{mg}}{\phi_{mg} + \phi_{m\ell}}$
β	Volumetric quality:	$\frac{\phi_{vg}}{\phi_{vg} + \phi_{v\ell}}$
Fr	Froude number:	$\frac{u}{\sqrt{gh}}$
Gr	Grashof number:	$\frac{\rho\beta\Delta\theta H^3 g}{\eta^2}$
Nu	Nusselt number:	$\frac{\alpha D}{\lambda}$
Pr	Prandtl number:	$\frac{\eta c}{\lambda}$
Re	Reynolds number:	$\frac{\rho u D}{\eta}$
We	Weber number:	$\frac{\rho u^2 D}{\sigma}$

ABSTRACT

Steam-water separation in nuclear boilers (Boiling Water Reactors and Pressurized Water Reactor steam generators) constitutes a technical and economical problem increasing with unit size, where compaction, a high efficiency and a low pressure loss are determining factors.

Inadequate separation has two aspects, carry-over of water with the steam to the turbine and carry-under of steam with the recirculating water. Of these the carry-under problem was chosen as the subject of this thesis, for which, following the usual division in primary and secondary separation (of mixtures with qualities of 4 to 20% and 80 to 95% respectively), gravity and mechanical separation are investigated as forms of primary separation.

The investigation is divided into an experimental and an analytical part. The test loop, designed for steam-water gravity separation experiments under actual reactor conditions (70 and 50 bar), incorporates a riser (two diameters are used: 0.126 and 0.152 m), an annular downcomer and forced circulation, while the steam is raised outside the loop in a separate boiler. The principal experimental data obtained are quality and void fraction in the downcomer, measured for riser qualities in the range of 4 to 20% at superficial downcomer water velocities up to 0.5 m/s. These results are presented in graphical form for three riser steam flow rates and three different levels above the riser at 50 and 70 bar pressure. A second experiment of exploratory nature concerns axial upcomer separators with a converging-diverging vortex tube and comprises the measurement of separation efficiency and pressure drop. A lucite test loop and the use of air and water permit the additional measurement of the radial distribution of the void fraction at several heights in the vortex tube. The experiment aims at investigating some fundamental aspects of the flow problems related to this particular separator type, which is chosen for its compactness, rather than at results for direct use on an industrial scale.

This is also apparent from the data presented which do not meet the reactor specifications. These measurements are carried out for superficial axial water inlet velocities of 2, 2.5 and 3 m/s with volumetric qualities up to 30% for two cyclone geometries having a 0.1 m vortex tube inlet diameter.

The main purpose of the analytical part of the study is to formulate a two-dimensional mathematical model describing the behaviour of two-phase mixtures in the vortex tube of the separator.

A survey is given of the interaction forces between the phases which determine their relative motion, such as the hydraulic resistance and virtual mass forces as well as the underlying physical phenomena.

The model is generated in two versions. First a one-dimensional model is derived based on the conservation of mass and momentum, for the purpose of quantitative determination of the interaction forces. The auxiliary experiments required are described. Radial void fraction distributions of air-water mixtures flowing through a variable area channel are measured by means of a γ-attenuation technique at 9 locations in the channel, from which the axial distribution of the average values is derived. Comparing this distribution and that of the pressure in the channel with the model predictions the interaction forces are determined by trial and error as a function of the void fraction. The experiments are carried out for superficial water velocities of 1, 2 and 3 m/s and superficial air velocities of 0.5 to 3 m/s and two converging channels: from 0.1 to 0.07 and from 0.1 to 0.05 m.

The two-phase wall friction of air-water mixtures is measured in a circular channel of 0.1 m diameter. A method for direct determination of the wall shear stress is used which measures the shear force exerted on an independently suspended section of the channel. Test loop characteristics restrict these experiments to the range of superficial water and air velocities of respectively 0.8 to 2.2 and 0 to 0.88 m/s. The experimental results are compared with predictions according to the correlations due to Martinelli and Levy.

The second version of the model consists of the conservation laws of mass and momentum applied to the two-dimensional case of rotational symmetric flow, incorporating the empirical relations for the interaction forces determined previously. A method of solution for the set of equations, based on the so called N-strip method is derived. However, this course appears to lead to numerical instability. Possible causes are discussed as well as probable solutions to this deadlock.

For the carry-under problem a simplified model based on the one-dimensional conservation laws is given making use of the experimental results of the gravity separation experiments. A comparison is made between downcomer quality and void fraction predicted by this model with the experimental data. In the range of incipient carry-under the agreement is good; at higher circulation velocities deviations occur, which are connected with the small scale of the experiment.

In conclusion a comparison is given with experimental carry-under results from the Dodewaard boiling water reactor as well as a prediction of the carry-under that would occur in the steam generators of the Stade station, if gravity separation were to be employed.

1. INTRODUCTION

1.1. Statement of the problem.

The separation of steam and water in boilers is a problem as old as the boiler itself. The steam engine or turbine must be fed with steam that is free of the liquid water from which it is raised.
The most effective guarantee against liquid entrainment lies in superheating of the steam, which is found in all modern fossil-fueled boilers, primarily with the objective of increasing the thermodynamic efficiency. Separation in the drum of circulation boilers has the function to maintain the circulation and to protect the superheater against corrosion. Because the space to accomplish this is available, or in other words because drum size is not a decisive factor for the economic feasability of the system, steam-water separation is no longer a problem for conventional circulation boilers.

The introduction of light water reactors as steam supply systems set back the clock, however, for the following reasons. Thermodynamic efficiency no longer rated very high as a means to reduce the kWh-price ★), thereby diminishing the economic incentive for superheat. On the other hand technical problems unknown in fossil-fueled boilers, such as the search for corrosion-resistant high temperature cladding materials and the possible consequences of cladding failures for turbine contamination seriously impeded the progress of nuclear superheat by raising its prospective capital costs. As a result, all commercial light water reactors built or projected to date supply or will supply saturated steam to the turbines. Both the boiling water reactor (BWR) and the pressurized water reactor (PWR) employ circulation systems for steam generation.

Not only is an effective separation system needed to protect the turbine as before, it has to be accomplished in a limited space dictated by economic demands of the nuclear steam supply system (NSSS). Moreover the functions of the separation system are more diverse and the consequences of malfunction more serious than was the case in conventional boilers.

A brief survey of the functions of steam-water separation in a light water NSSS can be made with the aid of the simplified flow diagrams of figure 1-1.

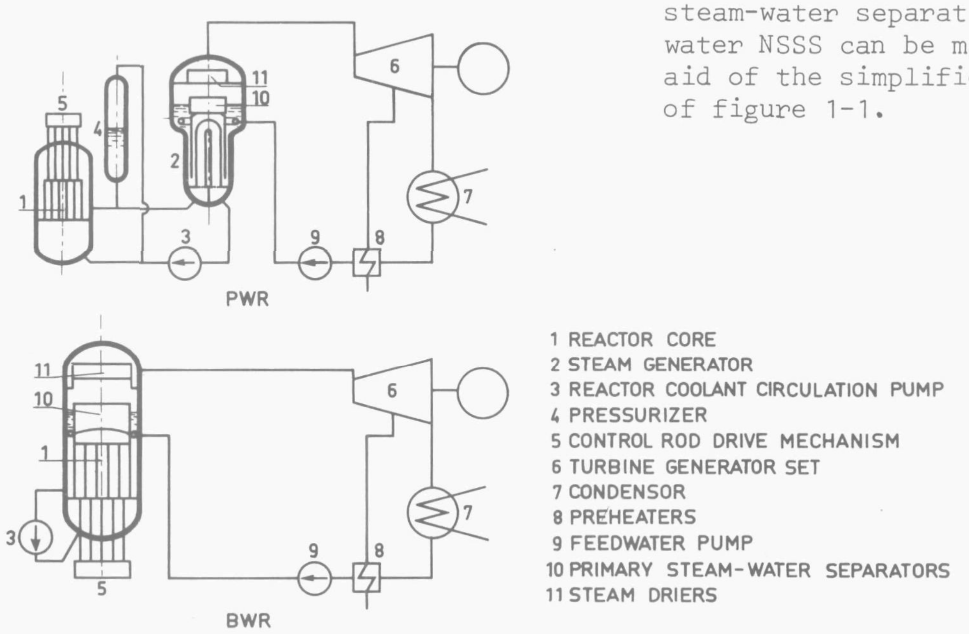

FIGURE 1-1.

Light water nuclear steam supply systems.

★) *The reason is a reversal in the relation fuel costs versus capital costs.*

In the PWR reactor core heat, released by nuclear fission is transferred to the water while flowing through the elements at high pressure (about 155 bar). An intermediate heat exchanger serves as a link between the primary circuit in which the reactor coolant is circulated and the secondary circuit which closely resembles the conventional steam turbine cycle.

The intermediate heat exchanger, or steam generator, is almost exclusively of the vertical U-tube type generating steam by natural circulation on the shell-side. A shroud is placed around the tube bundle to form an annular downcomer between the shell and the shroud.
Feedwater enters at the top of the downcomer. The water between the tubes partly evaporates, thus creating a difference in density between the riser and the essentially steamfree downcomer which provides the driving head for the circulation. The top half of the steam generator, which is usually of larger diameter, is available for the separation of the steam-water mixture that leaves the tube bundle. The steam then passes through the drying equipment and is led to the turbine, while the water returning to the downcomer mixes with the feedwater.
The pressure of the steam is a function of the reactor power, dependent on the reactor power-coolant temperature characteristic employed.
At full power the secondary pressure is about 50 to 60 bar.

The BWR-powerplant is, with a few exceptions, a single loop system, with natural or forced circulation through the core where partial evaporation takes place. The mixture passes through the primary separators whence the water is returned to the downcomer to be recirculated while the steam, after drying, is led to the turbine.
The steam cycle is identical to that in the PWR with the exception of a constant steam pressure at the reactor exit of 70 bar.

It is clear from figure 1-1 that in both cases the turbine has to be protected from liquid entrainment by the separation system.
Figure 1-2 shows, in a simplified way, how the steam is raised in both systems.

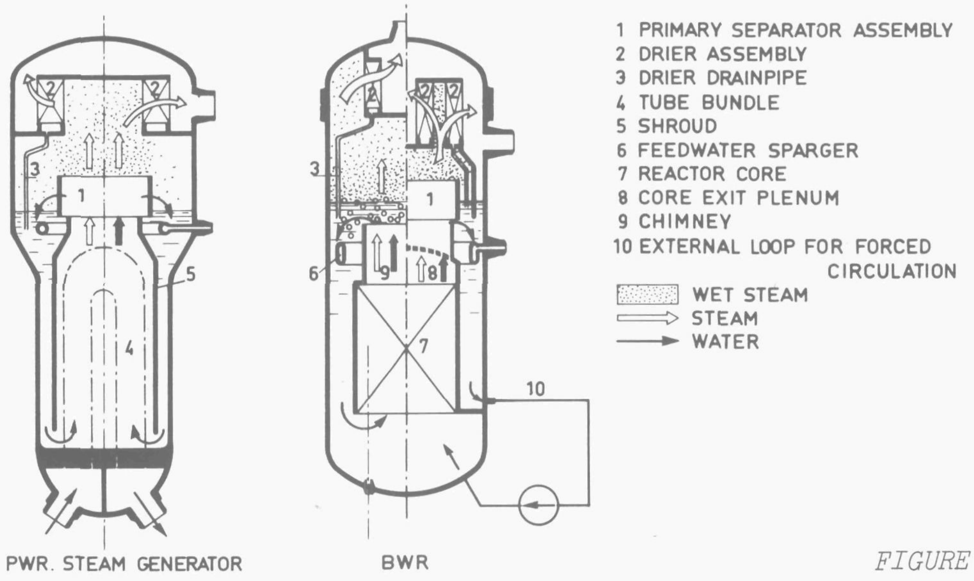

FIGURE 1-2.

Steam-water separation in light water NSSS's.

As follows from the above the separation is usually accomplished in two steps: primary separation of a mixture containing up to 14% steam by weight in BWR's and up to 20% in steam generators and secondary separation or steam drying of wet steam containing 5 to 20% water. The primary separation in its simplest form is gravity separation, where the steam, having a density about 20 to 30 times less than the water, separates under influence of gravitational forces. The steam leaving the free surface as depicted in the left hand side of the BWR-diagram has a tendency to entrain liquid droplets form the surface. For high steam velocities these entrainment forces may overcome the gravitational forces and the separation is incomplete ("carry-over"). Vice versa steam bubbles may be entrained with the water in the downcomer ("carry-under"). When gravity forces no longer suffice, or when compactness of the system is important, a (usually) successful resort is made to centrifugal force in a variety of devices, called mechanical separators. Their gain in space and separating efficiency has to be paid for by higher pressure losses, which could make it necessary for the BWR to change from natural to forced circulation. Because separator compaction will go together with a tendency to increase the core power density higher core pressure losses are also to be expected.
The resulting dangers of hydrodynamic instability and approach of the critical heat flux limits alone would also preclude the use of natural circulation. These problems being virtually absent in the PWR-steam generator it is possible to use mechanical devices for primary separation without the need of a circulation pump.

The second stage in the separating process, where the droplets that have not fallen back by gravity in the space between primary separators and the entrance of the driers are to be removed from the steam, is generally based on principles other than centrifugal force. Wire mesh demisters and chevron driers that have a large internal surface with which the droplets collide are frequently used.
Clinging to the drier surface the droplets coalesce to larger drops that drain by gravity to the drier bottom, without being entrained again by the steam, and thence to the downcomer.

The consequences of insufficient separation for the NSSS can now be reviewed. For primary separation the effects are twofold: steam may be carried under in the downcomer and water may be entrained with the steam. Some carry-under is condensed in the downcomer by the subcooling of the feedwater. The dangers or disadvantages of carry-under are listed in table 1-1. It can be seen that the decrease in circulation for natural circulation systems is much less important for the PWR-steam generator, because the influence of coolant velocity on boiling heat transfer in the tube bundle is small enough to neglect it and hydrodynamic instability is hardly to be expected.

TABLE 1-1

Carry-under of steam

BWR	PWR-steam generator
Reduction of the downcomer density causing a decrease in driving head for natural circulation	
Danger of cavitation of the circulation pump	
Decrease of the subcooling of the water at reactor inlet resulting in: 1. decrease in power due to lower moderator - to - fuel ratio 2. reduced stability margin 3. reduced critical heat flux ratio	
Reduces shielding capability of downcomer	

A high amount of carry-over from the primary separation stage has the indirect effect of increasing the load of the driers. The dangers of carry-over from the driers are given in table 1-2.

TABLE 1-2

Carry-over of liquid

BWR	PWR-steam generator
Damage to turbine blades by erosion	
Thermodynamic efficiency decrease of turbine cycle	
Impurity deposition on turbine blades causing efficiency loss	
Radioactive contamination of turbine and condenser	

From the above the similarities and differences with the conventional boiler should now be clear. The essence of the problem is the same, though insufficient separation involves greater hazards.

Integration of the separation system and the boiler within the same vertical pressure vessel, dictated by economic demands, stresses the need for more compact devices resulting from the much smaller cross-sectional area as compared to the, horizontal, boiler drum.

1.2. Scope and motivation of the study.

The study of carry-under, or rather of the means to prevent it was taken as the subject for this thesis. In the light of the classification of the previous paragraph this means a limitation to one aspect of the primary separation and includes both gravity and mechanical separation. Table 1-1 shows that the emphasis should be on BWR conditions.

From a historical point of view, gravity separation is the logical way to start such an investigation. From the early experiments of the BORAX project in 1953 when it was still necessary to prove the feasibility of the boiling water reactor concept until the building of the Dresden station in 1960, which employs the now abandoned dual cycle incorporating a separate steam drum, gravity separation within the reactor vessel was always used.
The same mode of separation was used in subsequent small to medium sized BWR plants such as Humbolt bay (1963), Kahl (1961) and Dodewaard (1968).
It has become clear however that the power output of such plants is limited to about 60 MWe [48] to 100 MWe [46], [47].
Figure 1-3 shows the relationship between the reactor-vessel diameter, D_v, and the circumscribed core diameter, D_c, for plants of various thermal powers.

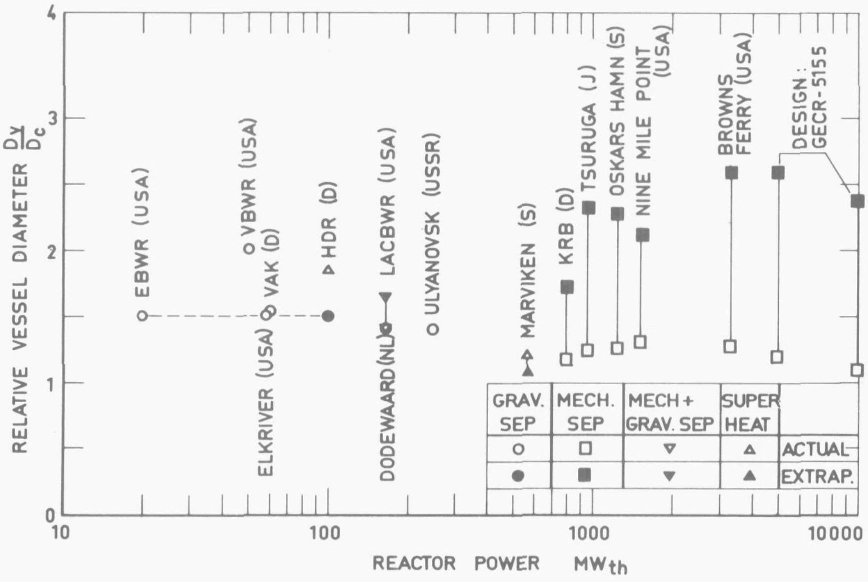

FIGURE 1-3.

Effect of mode of separation on reactor vessel diameter

A comparison of the diameter ratio's for gravity and mechanical separation indicates that the vessel diameter of those employing gravity separation is apparently more determined by separation requirements than by the core. The vessel size of the smaller reactors is economically still acceptable. For reactors with mechanical separation the actual ratio D_v/D_c is plotted as well as an extrapolated value, that would have been needed had gravity separation been employed, based on the same average velocity of the steam leaving the free surface as for the Dodewaard reactor. With this value of the steam velocity (0,33 m/s) the downcomer is large enough to accomodate carry-under limits over a range of readily applicable core exit qualities. Figure 1-3 illustrates the growing discrepancy between the actual vessel diameter and that needed for gravity separation for increasing reactor power. For the Browns Ferry station of 3293 MW_{th} the vessel diameter would have to be 13.35 m instead of the actual 6.38 m.

While gravity separation thus appears to be restricted to small size BWR plants it may still be considered for PWR-steam generators. Realizing that carry-under limits are much less restrictive than for the BWR the vessel diameter is primarily determined by the average steam velocity above the free surface, i.e. by carry-over considerations. This velocity can be regarded as the specific free surface load of the steam dome and can also be expressed in terms of mass velocity. An other important parameter determining the amount of liquid entrained with the steam is the height of the steam dome. If, for a given height, the free surface load is increased beyond a critical value the liquid entrainment has been shown to increase suddenly and gross carry-over occurs [68], [49], [99]. The carry-over at the critical load is a few percent by weight, which can still be removed by driers. As part of a research program [49] the critical load, called permissible steam release rate, was determined experimentally by Allis Chalmers Co. as a function of steam dome height and is partly reproduced in figure 1-4. The working points of various NSSS's plotted in figure 1-4 first of all show that the steam release rate is substancially lower for steam generators than for BWR's. Comparing the required steam dome heights according to the findings of Allis Chalmers with the generally available heights of over 4 m, it also becomes evident gravity separation offers a feasible (and cheaper) alternative to mechanical separators for PWR-steam generator use.

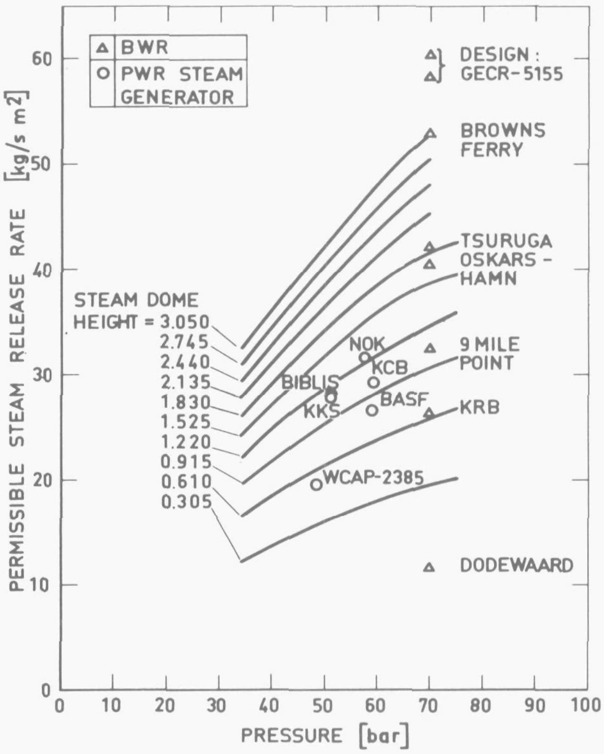

FIGURE 1-4.

Permissible steam release rates for various NSSS's.

It should be emphasized however that the Allis Chalmers curves are only valid for a quiet interface and provisions should be taken to promote an even distribution of the steam over the interface to prevent steam channeling or high local velocities. This condition may prove to be more easily formulated than realized, but does not rule out the possibilities reflected in figure 1-4. Moreover the downcomer velocities ★) in steam generators are much lower than for the BWR's in the figure.

★) *The upper region of the downcomer is taken to be an annulus with the dome and shroud diameter as outside and inside diameter. The amount of water circulated in the system is taken to be 4 times that of the steam generated by weight and the downcomer velocity is the average liquid velocity in the upper downcomer region.*

The investigation of gravity separation, apart from its practical interest (small BWR's and possibly most PWR-steam generators) serves as a starting point for the study of mechanical separators, which is the subject of the second part of this thesis.

Several types of primary separators are in use or planned to be used in BWR's. In general three basic designs are encountered as shown schematically in figure 1-5.

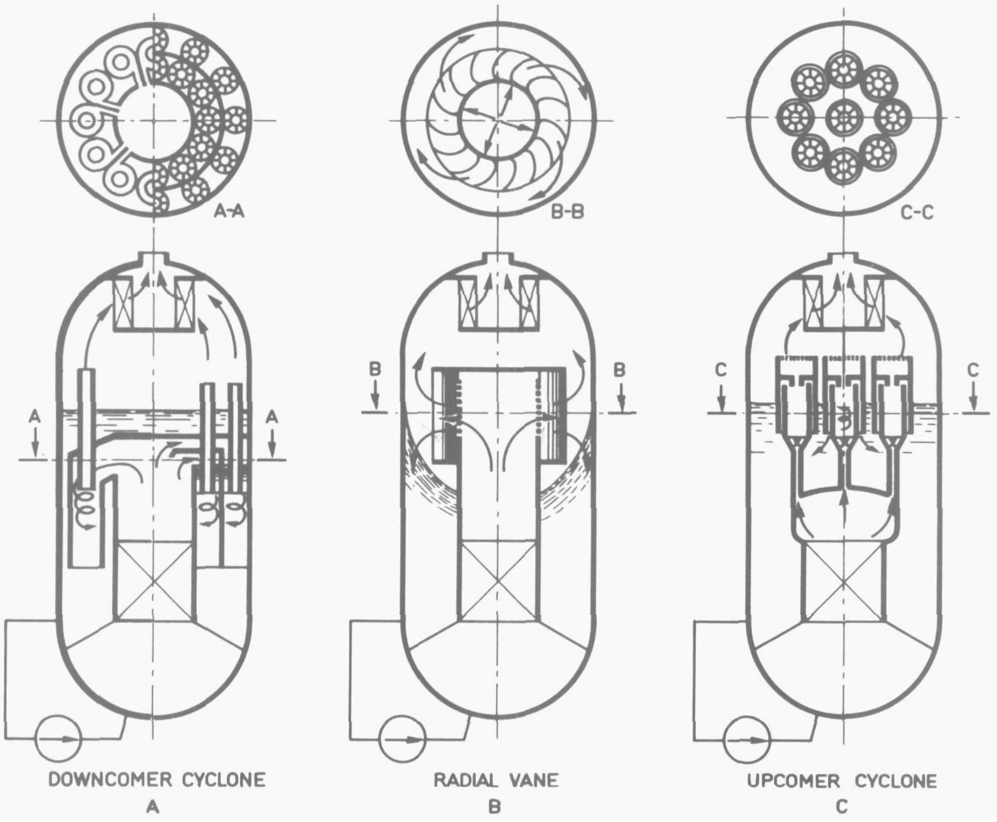

FIGURE 1-5.

Basic types of mechanical separators.

Two of these are true cyclones either placed above the core and called upcomer cyclones or mounted in the downcomer and called downcomer cyclones. The third type, the radial vane separator, is an intermediate form using curved vanes situated in the radial flow region where the mixture rising from the core flows outward towards the riser. Separation is effected by the centrifugal force on the vanes and in the swirl flow near the vessel-wall generated by the tangential component of the flow leaving the vanes. This type is still under development by General Electric Co., but has not yet been proven for a full size unit [51]. The tests performed so far look promising regarding efficiency, cost of fabrication and pressure loss.
A schematic drawing of the radial vane separator is given in figure 1-5.B. Steam and water enter the separators from the mixing plenum above the core. In the case of the downcomer cyclones a 180° turn is made and a swirl is given to the mixture either by tangential inlet or by guide vanes. The lighter steam is forced to the center of the cyclone body or vortex tube while flowing downwards, thus forming a vapor core. The steam again turns

180° to leave the cyclone through an exhaust tube to the steam-dome. The water, *free of steam, flows downwards through the bottom exit. As shown on* the right-hand side in figure 1-5.A the axial type with guide vanes makes it possible to install several rows in the downcomer for better utilization of the downcomer space. The upcomer type depicted in figure 1-5.C also employs guide vanes to generate the swirl. Now the water is turned 180° at the end of the separating section to flow back to the downcomer while the steam passes through the top. The separators are mounted on standpipes that penetrate the plenum cover, so the discharged water can flow back to the downcomer between them.

The advantage of the smaller cyclones over the radial vane separator is the possibility of developing reliable prototypes under full size testing. The downcomer cyclones were first employed by Allis Chalmers Co. and AEG in respectively the Pathfinder and Lingen reactors, while the upcomer type now typical for the General Electric BWR was first used for internal separation in the KRB Gundremmingen reactor.

Lower manufacturing costs as compared to the upcomer cyclone, and the possibility to change fuel elements without having to remove the entire separator assembly are cited as advantages of downcomer over upcomer cyclone [50]. By contrast pressure drop of the downcomer cyclone is *probably* higher due to the flow deflectors, which turn the mixture from plenum to downcomer and distribute it over the successive separator rows. When it comes to compactness the upcomer cyclone (and possibly the radial vane) make a more efficient use of the vessel cross-section, even though the downcomer cyclone may require less vessel height.

In view of these considerations the upcomer cyclone was selected for further study particularly because it appears promising with respect to compactness as wel as having the simplest geometry. The fact that development work performed on the downcomer cyclone as well as on the radial vane was to be found in the open literature also influenced the choice.

The upcomer cyclone, as depicted in figure 1-5.C has a shroud for each separator and is mounted on a standpipe. The shroud and standpipe require more area and height than needed for the separator body itself. Such a separator has been developed by the General Electric Co. and described in patents [52], [53] and by MOEN [47].
Figure 1-6.A gives a more detailed picture of this device, while an alternative design, proposed by the author, is shown in figure 1-6.B.

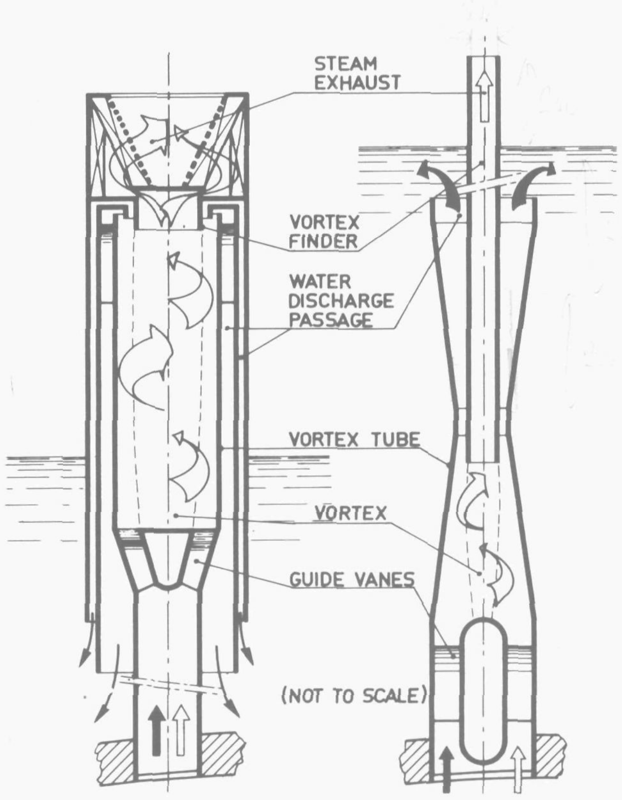

GE UPCOMER SEPARATOR
A

AXIAL FLOW VENTURI SEPARATOR
B

FIGURE 1-6.

Upcomer separators.

This latter proposal differs in two aspects from the former. Firstly the separator is fully submerged, making it possible to omit the shroud and stand pipe. Secondly the vortex tube consists of a converging diverging nozzle for the purpose of increasing the rotation in the converging section. In this way only part of the rotation has to be generated by the guide vanes, which should reduce friction losses. Additional gain is to be expected from the diffuser where part of the kinetic energy is transformed into pressure head.

Without going into matters of separation efficiency and separating length of the vortex tube at this point, a comparison can be made with the G E separator to illustrate the purely geometrical consequences of the venturi separator.

The Browns Ferry station of 1098 MWe is taken as a basis for this comparison. From the mass flow through the core of 12560 kg/s [56] and the capacity of 59.3 kg/s for a GE separator [47] it follows that 212 separators are needed. The separators are placed in a triangular array of 0.343 m pitch [54]. The area required for each separator in the assembly is then 0.1018 m^2, resulting in a circumscribed diameter of the assembly of 5.25 m. A venturi separator with the same vortex tube diameter (0.204 m [53]) as the GE separator and having the same clearance between units would require an area of 0.043 m^2 resulting in a circumscribed diameter for the assembly of 3.41 m. The assembly of venturi separators would look as show in figure 1-7, which gives the GE assembly for comparison on the left hand side. The assembly height is somewhat arbitrary. Both separator types will probably turn out to require about the same height: the gain by omission of the standpipes will be lost by the submergence of the venturi separator needed for water discharge from the separators.

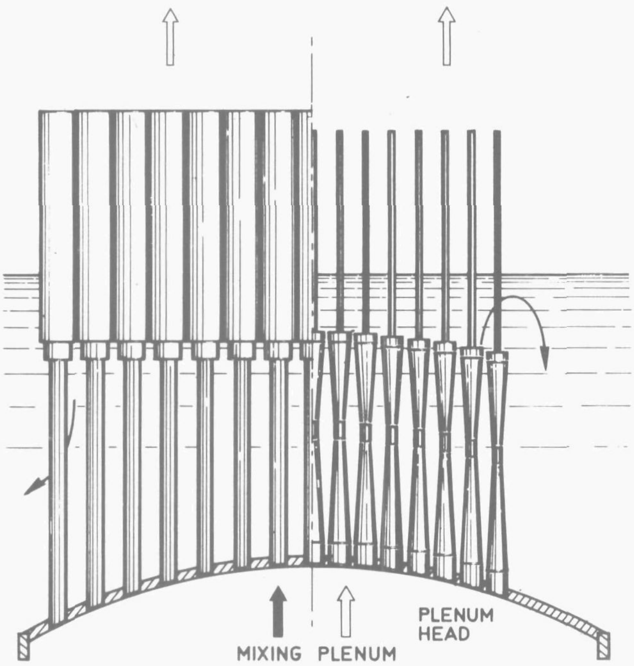

FIGURE 1-7.

Comparison of separator assembly diameter for venturi separators and G.E. separators.

The design of the Browns Ferry reactor is such that 14% by weight of the water entering the core is evaporated. Other reactors have lower percentages. It is interesting to see what the consequences of a lower steam content or mixture quality at inlet would be on separator assembly dimensions. For equal reactor power the amount of water would increase.
For four separator types, the AEG downcomer cyclone, the radial vane separator, the GE upcomer cyclone and the venturi separator their number and assembly diameter are plotted in figure 1-8 (see page 22), for the conditions of the Browns Ferry reactor operated at exit qualities from 6 to 14%. The downcomer cyclone is based on maximum steam-loading [48] which is constant over the quality range considered resulting in a fixed number and a constant in and outside diameter of the

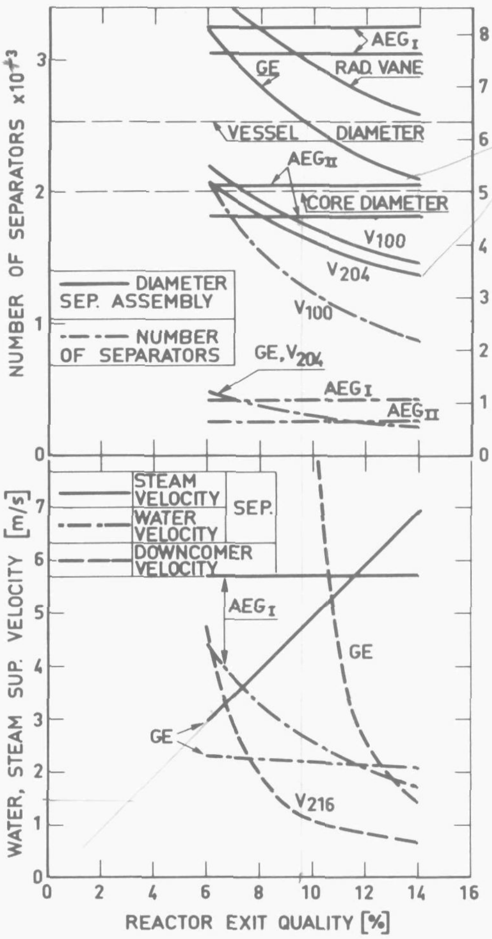

V204 heeft kleiner stuk

FIGURE 1-8.

Separator parameters for four separator types operated at various reactor exit qualities at conditions corresponding to the Browns Ferry station.

triple row arrangement, indicated in the figure by AEG-I. The limiting steam load was increased by 67% as a result of recent development work [55] resulting in smaller assembly diameters marked as AEG-II.

If the reactor were fitted with a radial vane separator the diameter, calculated according to the recommended design procedures of [56], would, as is the case for the AEG-I cyclones, lie beyond the vessel diameter actually employed.

In contrast to the AEG cyclones the GE upcomer separator capacity is limited by total mixture flow rates. With decreasing quality the total flow rate through the reactor increases and an increasing number of separators is needed. This is also shown in figure 1-8, where the curves labeled GE are based on a maximum *flow rate of 59.3 kg/s [47] for the given quality range.* Both the AEG and GE capacity specifications comply with a carry-under of steam of no more than 0.2% in the downcomer. The figure shows that inlet qualities below 9.5% would prohibit the use of the GE separators in the given vessel but at 14% the assembly, as actually designed for the Browns Ferry reactor, has about the same diameter as the core.

The venturi separator is shown in two diameters. For comparison the maximum diameter of the vortex tube is taken to be the same as for the GE separator. Postulating the same capacity it is evident from the curve marked V_{204} that the venturi separator could be used over the entire quality range without restrictions from the reactor-vessel diameter.
However a 0.204 m diameter separator requires a fairly large test facility especially for steam-water testing. The present investigation was initiated therefore with 0.1 m diameter separators. Even though there seem to be no objections from a physical point of view, it is realized that the fabrication costs would probably be prohibitive to the use of such small separators in the reactor because the number of separators in the assembly would become more than four times higher. This is shown by the curves for V_{100}, that are based on the same mass velocity as for V_{204}.

The lower half of figure 1-8 shows some velocities ★) typical for the different designs. The upcomer separator has a nearly constant water velocity and an increasing steam velocity for increasing quality, whereas the AEG-I cyclone shows just the reverse. A further advantage of the venturi separator is the lower downcomer velocity. Although higher than allowed for gravity separation (Dodewaard: 0.38 m/s) some additional beneficial effects could be expected from this.

In view of the foregoing the scope of the present investigation can be summarized as an investigation of the possibilities and limits of gravity separation as a means to prevent carry-under and a preparatory study of the problems inherent to the venturi separator.
For this purpose the work is subdivided into three parts:

- Carry-under experiments in a small scale model at reactor conditions with steam and water.
- Experimental study of the separation process in a venturi separator with air-water mixtures; the separator load, represented in figure 1-8 by the velocities for the upcomer separator, should be regarded as a goal to be attained if full profit is to be drawn from the reduction in assembly size for the venturi concept.
- Analysis of the separation process with the object to formulate a mathematical-physical model to predict separation behaviour.

★) *These, superficial, velocities are calculated as if the total cross section of either the vortex tube or the downcomer at separator discharge level respectively was available for both phases.*

2. EXPERIMENTS

2.1. Gravity separation.

2.1.1. Range of process parameters.

An important factor in the design of laboratory experiments is the possible range of variables. In the case of gravity separation where the experiments are to be performed in a scaled down model the size parameters rate very high in this respect. The riser and downcomer arrangements typical for the systems described in the previous chapter and used in this investigation are shown in figure 2-1. The geometrical variables are the diameter of the riser and the downcomer and the interface height above the riser outlet. The values of these variables for the model are shown in the figure. The other independent variables are the steam and water flow rates and the system pressure.

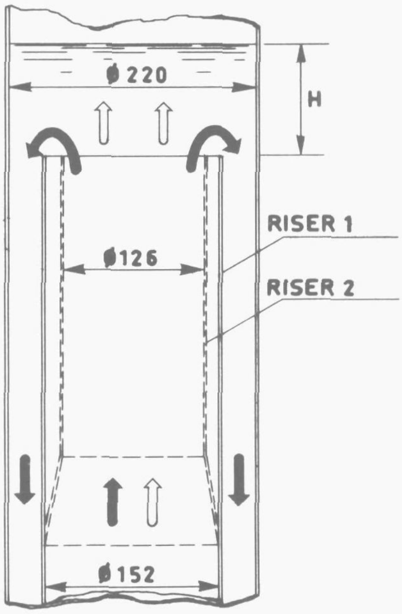

FIGURE 2-1.

Riser downcomer arrangement for gravity separation experiment.

In view of the operating conditions of the real system it was desirable to vary the mixture quality from 4 to 20% and the superficial downcomer water velocity between 0.1 and 1.0 m/sec. The maximum steam flow was limited for the present experiments to 0.556 kg/s by the available boiler capacity. The corresponding maximum downcomer area for 1 m/s downcomer velocity at 4% quality and 70 bar is 0.0182 m^2. The resulting riser and downcomer diameter for equal downcomer and riser area are 0.152 and 0.220 m respectively. As a consequence the superficial steam velocity above the interface, i.e. in the steam dome, is 0.4 m/s which is rather low. The superficial riser mixture velocity also attains a rather low maximum value of 1.85 m/s. However the largest possible model size was considered to be more important than high steam velocities in riser and steam dome, especially because carry-over experiments were not to be included. The effect of low riser velocities was remedied somewhat by a second series of experiments with the same downcomer, but with a necked down riser to give a downcomer to riser area ratio of 2.

The resulting ranges of test variables are presented in table 2-1 together with those of other investigations.

The test runs were coded according to the respective choice of variables.

- Pressure at 50 and 70 bar: P50, P70.
- Riser configuration for area ratio's of 1 and 2: R1, R2.
- Level above riser rim at 0.06, 0.12 and 0.22 m: H6, H12, H22.

The field of test conditions that could be realised is illustrated in figure 2-2 (see page 26). The broken lines give the upper limit of the possible downcomer superficial water velocities set by the maximum available steam flow, for both P50 and P70 series, as a function of the riser quality. Lines of constant total riser mass velocity are added as a third parameter showing how a penalty is paid for the larger model size by the low mass velocity values in the high quality range.

Double scales are provided for the R1 and R2 riser configurations.

Table 2-1.

Geometry				
D_R m	0.129	0.076	0.071-0.339	0.398
D_V m	0.203	0.152	0.129-0.445	0.413
A_D/A_R	1.7	2	1.84-0.85	2.43
H m	0.102-0.482	0.152-0.381	0.25-1.74	> 0.3
x_R %	2×10^{-2}-3×10^{-1}	2-7.24		0.6-4.8
α_R %	10-50	10-50	15-55	
$v_{s\ell D}$ m/s	0.127-0.635	0.127-0.635	0.29-0.635	0.1-0.4
media	air/water	steam/water	air/water	steam/water
system pressure bar	1	41.4;68.9;103.5	1	16-50
investigator	Petrick [20]		Marshall [66]	Skaug [67]
Geometry	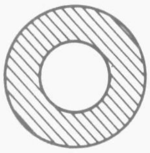	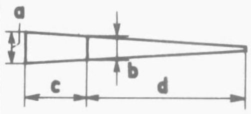		
D_R m	0.456	b = 0.145 d = 1.035	0.323, 0.354	0.152, 0.126
D_V m	0.912	a = 0.210 c = 0.400	0.482	0.220
A_D/A_R	3	0.74, 1.85	1.24, 0.84	1,2
H m	> 0.61	1-2.5	-0.203,+0.304★)	0.06,0.12,0.22
x_R %	0.8-13		? - 16.8	3-20
α_R %		15-58		25-55
$v_{s\ell D}$ m/s	0.06-0.365	0.2-1.5	0.09-0.92	0.05-0.6
media	steam/water	air/water	steam/water	steam/water
system pressure bar	41.4-13.8	1	6.2-87.0	50,70
investigator	Allis Chalmers [49]	Volradt [46]	Comb.Eng. [68]	this thesis

★) *Indicated waterlevel.*

Note:
Downcomer area shaded.

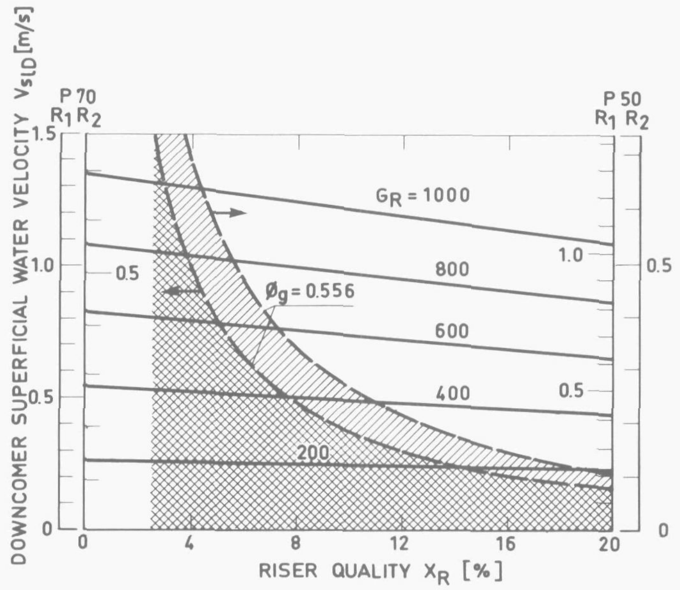

FIGURE 2-2.

Range of test conditions for gravity separation experiment.

2.1.2. Description of 70 bar test facility.

2.1.2.1. Flow sheet and major components.

The 70 bar test facility comprises a pressure vessel with a water and a steam cycle. Steam and water enter the riser in a mixing section simulating the boiling process as encountered in a BWR or a PWR steam generator. Figure 2-3 shows the basic flow sheet of the facility. Steam is raised in a boiler at about 100 bar, and reduced to the test pressure of 70 or 50 bar before being fed into the distributor inside the pressure vessel, where it is mixed with the water also entering the bottom section of the pressure vessel; the mixture flows upwards through a central riser towards the free surface.

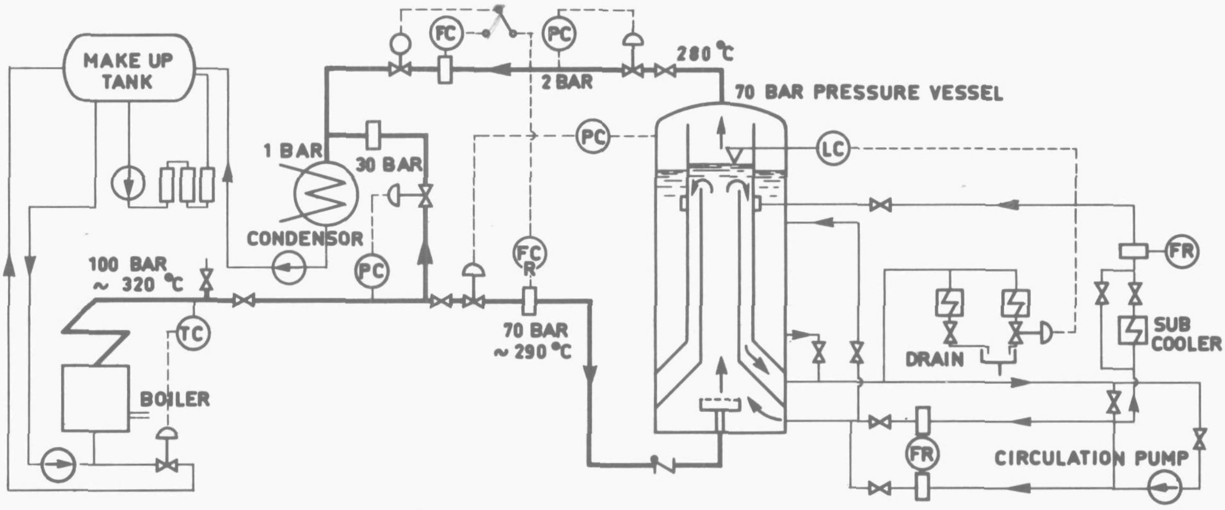

FIGURE 2-3.

Flow sheet of 70 bar test facility.

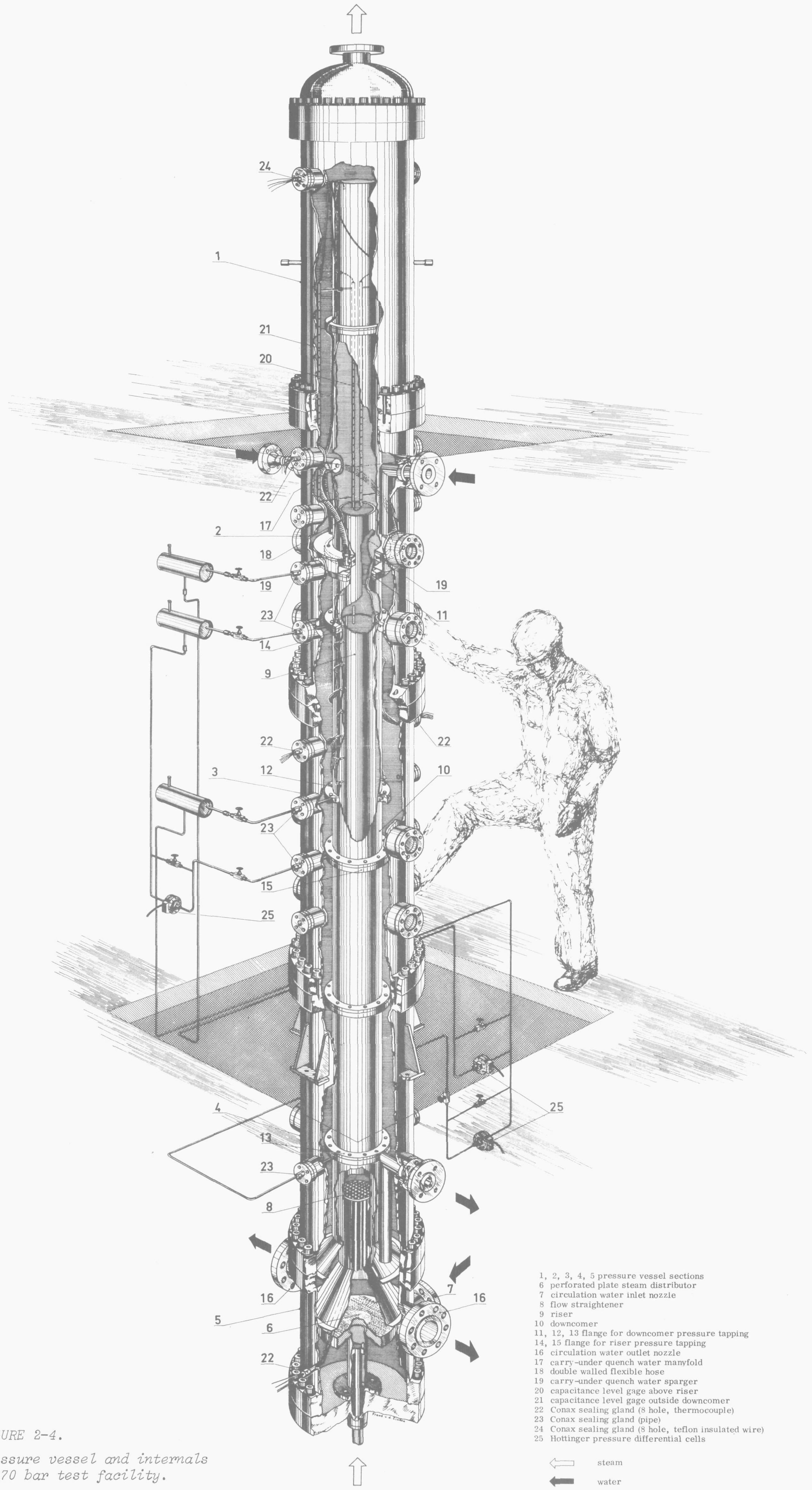

1, 2, 3, 4, 5 pressure vessel sections
6 perforated plate steam distributor
7 circulation water inlet nozzle
8 flow straightener
9 riser
10 downcomer
11, 12, 13 flange for downcomer pressure tapping
14, 15 flange for riser pressure tapping
16 circulation water outlet nozzle
17 carry-under quench water manyfold
18 double walled flexible hose
19 carry-under quench water sparger
20 capacitance level gage above riser
21 capacitance level gage outside downcomer
22 Conax sealing gland (8 hole, thermocouple)
23 Conax sealing gland (pipe)
24 Conax sealing gland (8 hole, teflon insulated wire)
25 Hottinger pressure differential cells

⇦ steam
⬅ water

FIGURE 2-4.

Pressure vessel and internals of 70 bar test facility.

The steam separates from the water and passes through the steam dome towards the steam outlet. Another pressure reducing station consisting of a pressure and a flow regulating valve brings the steam pressure down to the atmospheric pressure of the condensor. Condensate is pumped to a make up tank. A bypass flow from the tank is passed through a mixed bed dimineralisation filter.
The feedwater pump brings the condensate up to boiler pressure again to complete the steam cycle. Several control loops are incorporated in this cycle to obtain a steady pressure and temperature in the test vessel.
The Henschel once through boiler is capable of producing 2 t/h of steam at 125 bar and 400°C and is equipped with an on/off spray cooling system in the steam outlet for temperature control. For boiler conditions of 100 bar and 320°C involving a smaller amount of superheat a better control appeared to be necessary.
The additional control of the boiler exit temperature is effected by a temperature governed valve in the feedwater overflow, while the exit pressure is kept constant by dumping the excess steam to the condensor by means of a valve governed by the boiler pressure. These valves have pneumatic actuators and controllers.
Pneumatic valves are also used for control of the pressure in the test vessel in combination with an electric motor-operated valve governed by either the vessel inlet or outlet flow, operating in het following way.
A deviation of the flow rate causes the electric valve to intervene resulting in a change of the pressure in the 2 bar section of the steam conduit. The pneumatic outlet valve governed by this pressure is actuated and in turn affects the pressure in the test vessel which is corrected by the pneumatic inlet valve. In this way both steam flow and vessel pressure are kept constant.
After separation of the steam at the free interface the water flows down through the annular downcomer and leaves the vessel through two nozzles placed at opposite locations in the wall to enhance symmetric downflow.
Forced circulation is maintained by a Weise 200 t/h circulation pump at 30 m pressure head. Two water return lines of 50 and 100 mm diameter are provided for circulation flow measurement in two ranges. The circulation flow rate is controlled by manually operated valves. The limited steam supply mentioned in the preceding section results in a riser and downcomer assembly with a diameter smaller than that of the test vessel, leaving an annular cavity. To ensure an even temperature distribution during heating up of the test facility this cavity is linked up with the main circulation loop by means of a manually controlled bypass flow through the cavity.
A second bypass with a valve directly connects the pump pressure and suction lines and is used for low circulation flow rates to maintain adequate flow rates through the pump itself.
A third bypass is constituted by a feedwater simulation flow with the purpose of quenching possible downcomer voids. A fraction of the main circulation flow is branched off from the 100 m return line and injected into the downcomer through a sparger after cooling in a shell and tube subcooler.
Flow and temperature are manually controlled by valves at the subcooler exit and in a bypass around it. The level in the riser downcomer assembly is controlled by means of a drain through either a large or a small drain cooler. The small cooler with a capacity of 60 l/h was fitted with a pneumatic valve governed by the test vessel level indicator signal.
A more detailed description of the test vessel and its internals will now be given with reference to figure 2-4, showing an artist's impression of the major component of the facility. The numbers in brackets refer to those in the figure. The vessel is an assembly of 4 interchangeable sections of 1.25 m length and 0.458 m ID (1, 2, 3, 4) and a bottom section of 0.625 m length (5).

The sections are provided with a variety of nozzles for piping, thermocouple and electrical lead vessel wall penetrations.
The steam enters the bottom section (5) through a thermal sleeve and perforated plate distributor (6). Water from the inlet nozzle (7) mixes with the steam and both phases flow upwards through the conical riser inlet, the flow straightener (8) and into the 0.152 m ID, 3.345 m long riser (9). The downcomer (10) is formed by a 0.220 m ID tube placed around the riser also mounted in the bottom section and extending over almost the whole vessel height. The downcomer tube, like the vessel, is an assembly of flanged sections. These flanges also carry the downcomer pressure tappings (11, 12, 13) and the pressure equalisation chambers for the riser pressure tappings (14, 15). Riser and downcomer pressure tappings together with the vessel wall penetrations are shown in figure 2-5.

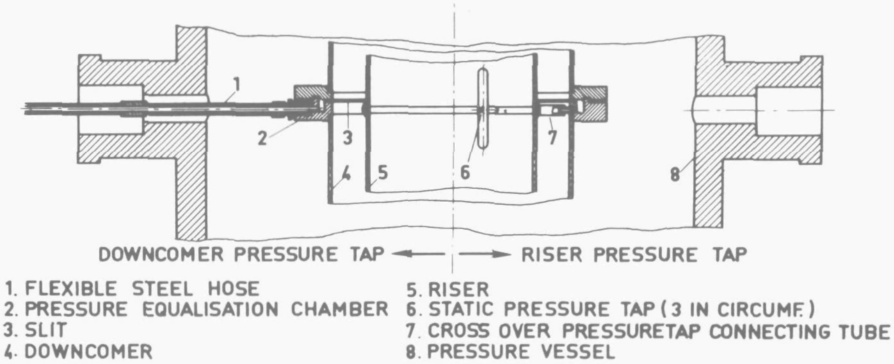

FIGURE 2-5.

Riser and downcomer pressure tappings and connections.

A flexible steel hose connection is used between the downcomer flanges and the vessel wall penetrations to accomodate the differences in thermal expansion of the carbon steel pressure vessel and the stainless steel riser downcomer assembly.
The water that is to be recirculated leaves the vessel by the water outlet nozzles (16).
The carry-under quenching water enters the vessel by means of a manifold (17) from which three flexible steelhoses (18) feed the water into a sparger (19) with 72 1 mm dia holes for even distribution of the water over the downcomer circumference. Manifold, hoses and sparger are double walled with stagnent water between the walls to act as insulation between the relatively cold quench water and the saturated water in the vessel and as thermal sleeve where the vessel wall is penetrated.
A capicitance level gage (20) is attached to the downcomer tube for detection of the two-phase interface above the riser. A similar device (21) is used to monitor the water level in the annular cavity.
Conax sealing glands are used for thermocouple vessel wall penetrations (22), pressure differential measuring lines (23) and the wall penetration of the teflon insulated leads of the level gages (24).

2.1.2.2. Instrumentation.

2.1.2.2.1. Loop instrumentation.

The instrumentation of the water and steam cycle is shown in the diagram of figure 2-6. Distinction is made between loop operational instruments with control panel display and experimental instrumentation pertaining to the experiments proper and linked up with a data acquisition system with punched tape output.

Some of the instruments such as those for flowrate and level detection are used for both purposes, if dual registration does not influence the readings.

In the case of temperate measurement each thermocouple has its own registration instrument, except when monitoring the downcomer subcooling as described in section 2.1.3. A compilation of the instruments indicated by number in figure 2-6 is found in the listing of Appendix 2-A where further particulars are given. An overall view of the control panel and pressure vessel is given in figure 2-7 (see page 30).

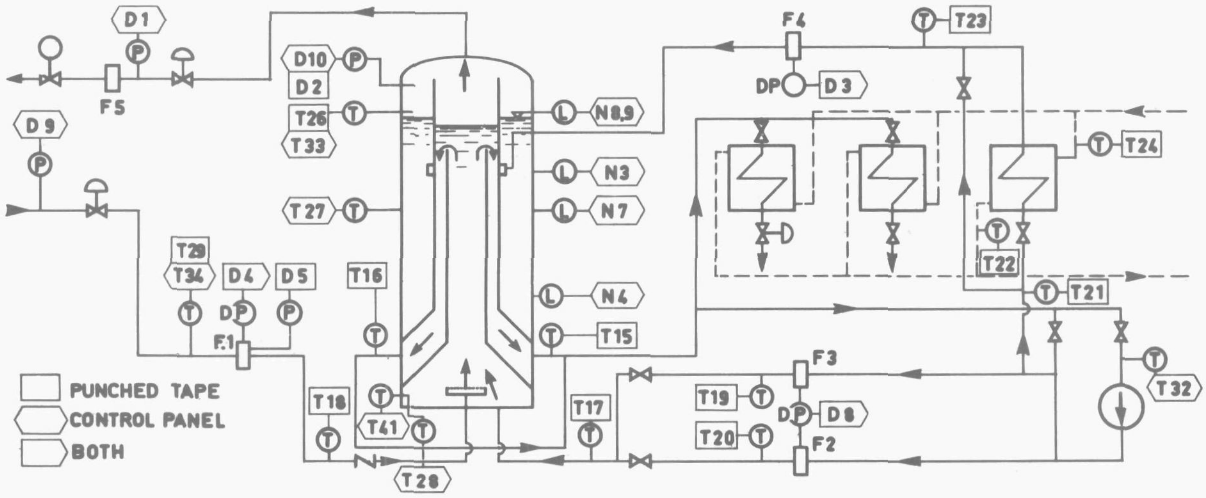

FIGURE 2-6.

Loop instrumentation diagram.

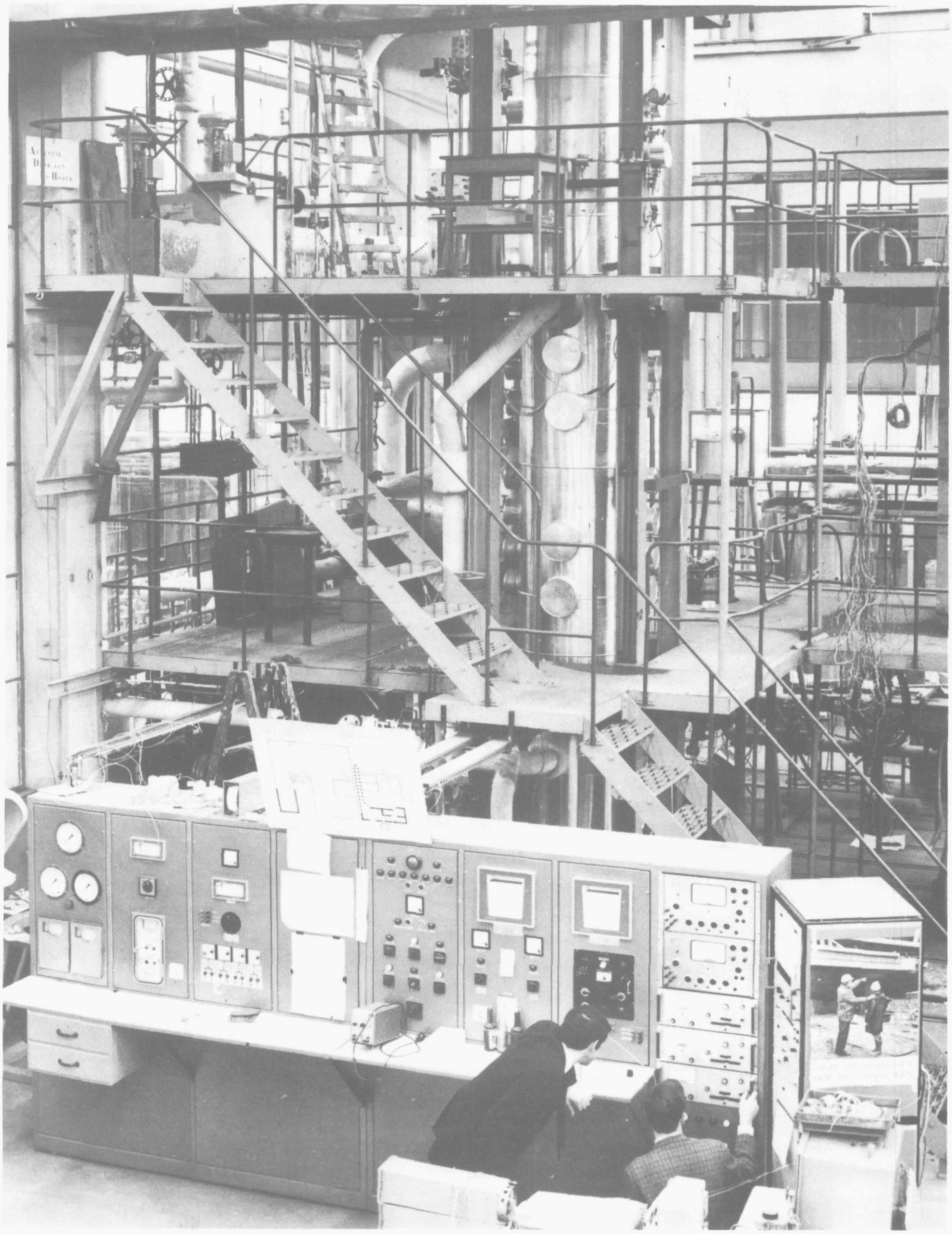

FIGURE 2-7.

Overall view of 70 bar test facility.

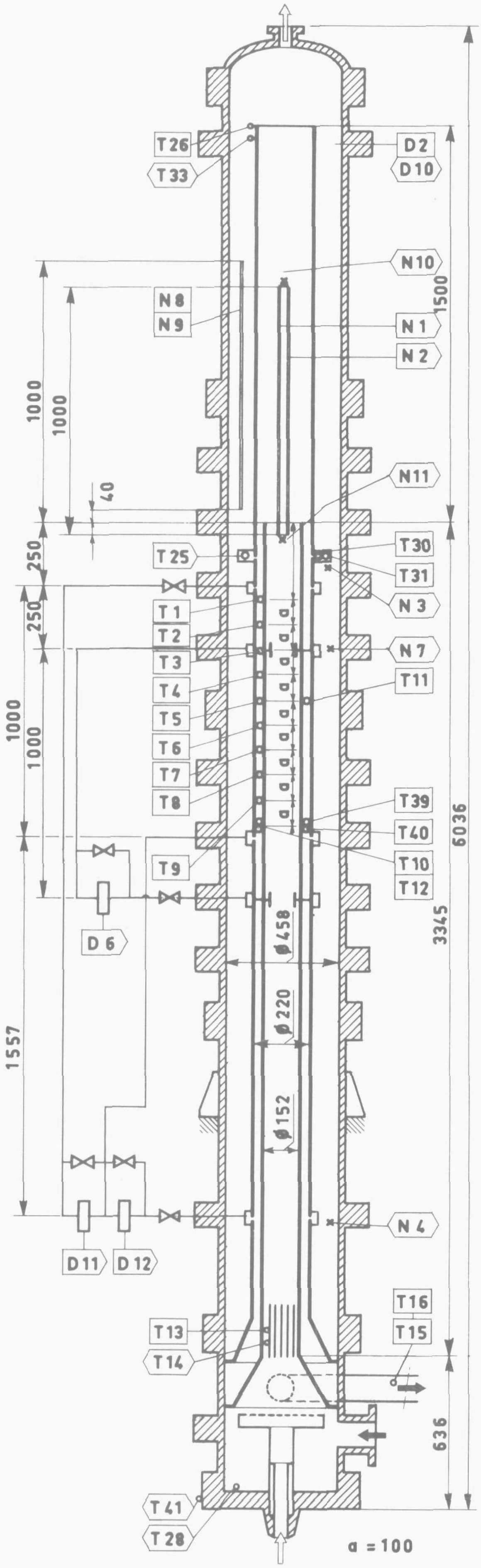

FIGURE 2-8.

Carry-under instrumentation diagram.

2.1.2.2.2. Carry-under instrumentation.

The instrumentation specific for the carry-under measurements will be described in more detail, as its design and use result from the particular measuring technique selected and are closely related to the data reduction procedures described separately in section 2.1.3. The measurements fall into three categories:

- void measurements
- quality measurements
- two-phase level detection

and are described under these headings.

The various measuring stations are shown schematically in figure 2-8, where the numbers again refer to the listing in Appendix 2-A.

Void measurement in downcomer and riser.

The most reliable void measurement technique for obtaining average flow channel values under high pressure conditions was considered to be the hydrostatic head method, based on a momentum balance for a section of the flow channel.

The total pressure drop is equal to the hydrostatic head plus the friction and acceleration losses. For velocities as low as those considered here acceleration and friction losses are of the order of maximum 2% of the total pressure drop, which is thus mainly determined by the hydrostatic head i.e. by the mixture density or void fraction. The measurement is thereby reduced to a differential pressure measurement.

As shown in the diagram of figure 2-8 the pressure drop in the downcomer is measured across a 1.000 m section in the upper region as well as across a 1.557 m section in the lower region. The pressure tappings shown on the left hand side in figure 2-5 are slits in the downcomer wall connected with an annular pressure equalisation chamber in the downcomer flange. The tubing to the differential pressure cells is kept in a horizontal plane where temperature gradients are to be expected. The static head in the riser is measured across a 1.000 m interval in the upper region. Slits are not possible in the riser wall because the associated flanges would obstruct the downcomer area. Static pressure tappings in three 5 mm rods placed at 120° intervals at a distance of 10 mm from the wall are used in stead, and connected to a pressure equalisation chamber in a downcomer flange at the same level by small bore (3 mm) tubes.

The differential pressure cells (D6, D11, D12) incorporate an elastic membrane. Its displacement caused by the differential pressure loading is measured in a Wheatstone bridge composed of two induction coils in the cell and two resistances in the carrier frequency amplifier (Hottinger Baldwin KWS/3-5).

A calibration curve with a reading accuracy of ± 1 mm H_2O was supplied by the manufacturer. Inadvertent overloading of the membrane made later recalibration with a water filled U-tube necessary giving at least the same accuracy.

Quality measurement in the downcomer.

The quality measurement is based on a heat balance over the downcomer region. For this purpose flow rates and enthalpies of water flowing in and out of this region are needed.

Flow measurements are performed for the circulation water and carry-under quench water flow rates by means of venturi tubes (F2, F3, F4) calibrated by the manufacturer (Bopp and Reuter) The foxboro differential pressure cells calibrated with a U-tube manometer are accurate to ± 0.5% of the range. The temperatures required for determining the enthalpies are measured with chromel-alumel mineral insulated, 1.6 mm dia thermocouples and concern the mixture temperature in the riser, the saturation temperature in the steam dome, downcomer temperatures and carry-under quench water temperatures in the sparger and inlet pipe between subcooler and vessel.

The location of the thermocouples in the downcomer is shown in figure 2-8. Thermocouples 10, 12, 39 and 40 are connected in series to increase the output. This is done to increase the sensitivity of the measurement of the downcomer subcooling as well as to give a circumferential average.

The downcomer subcooling is also measured in the return line where the water leaves the vessel.

All thermocouple cold junctions are located in Philips transostats keeping the welds at 50°C within a margin of about 0.05°C.

Separate out-of-loop calibration of the thermocouples was considered useless in view of the expected changes in calibration constants during mounting and soldering in the various locations, the deformation of the sheath in the Conax sealing glands, and aging during operation.

A technique has been used instead that permits the calibration of the whole measuring train including the hot junction, the soldered connections to the chromel-alumel compensation cable, the transostats and the data acquisition system. This "in situ" calibration compares all the thermocouple readings simultaneously with the same "standard temperature" of the loop i.e. the saturation temperature in the steam dome. The technique is shown in principle in figure 2-9. Calibration is either performed at a very low level so that the downcomer thermocouples are in a steam atmosphere or excessive carry-under is created by high circulation rates entraining steam in the water cycle. Thus all thermocouples are at saturation temperature. The system pressure was kept constant by reducing the steam flow to a very small amount and having the steam flow to the vessel governed mainly by the pneumatic inlet valve. When equilibrium is reached pressure variations registered by the strain gage manometer D2 are highly amplified.

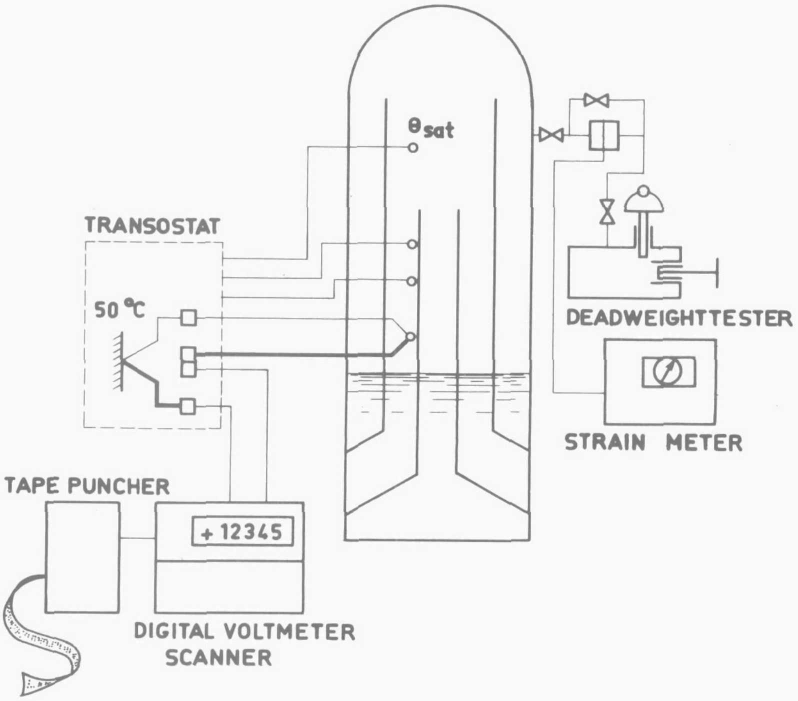

FIGURE 2-9.

"In situ" calibration of thermocouples.

When the variations are within a 0.005 bar margin the steam dome pressure is measured indirectly as indicated in figure 2-9. The nominal system pressure is set on the deadweight tester and the difference between nominal and actual vessel pressure is measured with a Statham strain gage differential pressure cell with a range of 3.3 bar. The calibration of the cell gives an accuracy of ± 0.02 bar or 0.029% of 70 bar, whereas the maximum error of the deadweight tester is 0.1%.
The resulting error in the pressure measurement is $\sqrt{(0.00029)^2 + (0.001)^2}$ = = 0.0012 or 0.073 bar. A pressure difference of one bar at 70 bar is equivalent to about one degree in saturation temperature; consequently the accuracy of the thermocouple calibration is about $0.07^{\circ}C$.
Even greater importance for the accuracy of the heat balance is the simultaneous calibration of the thermocouples against the same value. Any error in the calibration is equal and in the same direction for all thermocouples, the same being true for the corresponding enthalpies. Thus in a heat balance based on enthalpy differences the errors almost cancel out.
To obtain a calibration curve for each thermocouple the system pressure is successively set at three levels: the test pressure and 5 bar above and below it. For each calibration pressure the average of 10 readings it taken. A best fit by the least squares method for a straight line through the three resulting calibration temperatures is calculated by means of a computer program. During each test period the calibration was repeated weekly to correct for any drift in the system.

Two-phase level measurement above the riser.

A dependable level measurement for a two-phase mixture is a necessity but also poses a problem. Normal continuous level measurement based on hydrostatic pressure measurement is impossible due to the a priori unknown mixture density. Acoustic methods pose huge technological problems at elevated temperatures, as do radiation techniques. Electrical resistance probes such as used for level detection in the annular cavity (N3, N4, N7) have the disadvantage of being discontinuous.
As a result a system based on electrical capacitance was chosen consisting of a coaxial capacitor with an insulated inner electrode and a bare outer electrode in direct contact with the two-phase mixture.

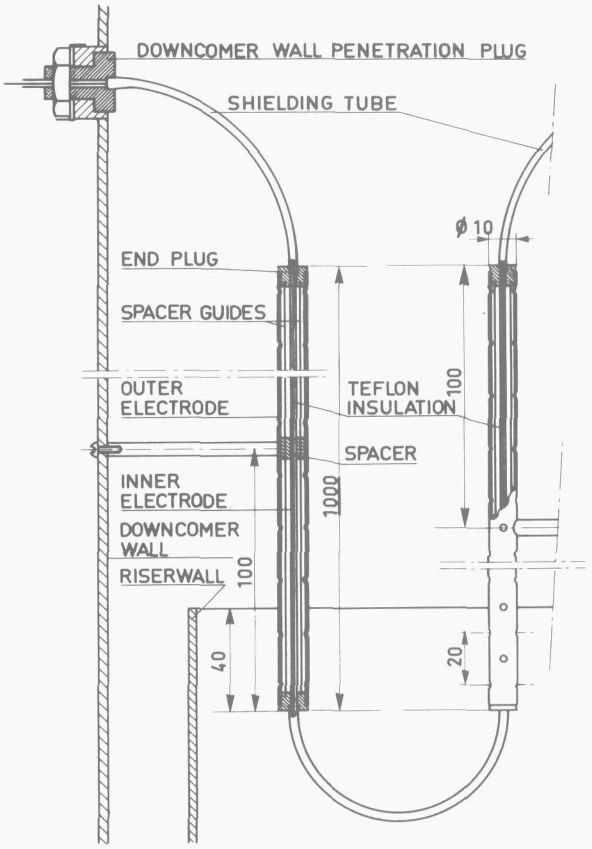

FIGURE 2-10.

Capacitance level gage.

Figure 2-10 shows the electrode design. The inner electrode is a 1 mm copper wire insulated with teflon. The outer electrode consists of a 10 mm ID stainless steel tube with holes drilled in the wall for free passage of the water. Due to density differences between the essentially bubble free water inside the capacitor and the mixture outside a circulation flow is set up.
The outflowing water prevents steam bubbles from entering while the system is replenished through the holes close to the interface resulting in about equal levels inside and outside the tube. Consequently sensitivity to the void fraction of the surrounding mixture is very low. This has been checked by out-of-loop tests with air-water mixtures and under operating conditions. The latter tests and results are described in Appendix 2-B.
The capacitance of the electrodes is a measure for the amount of di-electricum present between the electrodes and hence for the water level. Two outer electrode tubes are used with the same wire passing through both of them. Both ends of the wire penetrate the vessel wall in a multihole conax sealing gland. In this way the closed loop of the teflon ensures the insulation integrity while the change in capacitance is doubled.
The system is completed by an Endress and Hauser silometer, which is essentially a Wheatstone bridge. The unbalance of the bridge due to the level change is read in percentages of the full range, 1 m in this case. Zero and full scale readings are adjustable to compensate for the capacitance of the empty system plus the wires from the electrode to the bridge and the capacitance increase for maximum level.
Readjustment of 0 and 100% is carried out for each new setting of the steam flow. This was done with the aid of electrical resistance probes at high and low level. These probes, when submerged, cause a short circuit indicated by the switching off of a control light. The moment of passing the low and high levels can thus be monitored and the adjustment on the silometer can be made while raising the mixture level.

2.1.2.2.3. Data acquisition.

Measurement of the transducer mV signals is performed by means of a solatron digital voltmeter and scanner. The voltmeter transforms the analog signal into a digital one, which is punched into tape by means of a punch encoder and an ITT Teletype tape puncher. A 5 hole ALCOR-CCIT-code is used.
During the measurement 35 channels of the scanner, corresponding to 35 transducers and thermocouples mentioned in Appendix 2-A, are successively connected with the voltmeter at a rate of 10 channels per second. For each channel the polarity, 5 digits and a comma is punched. The last digit is equivalent to 10 μV corresponding to 0.25 °C.

Ten scans are usually made for each test condition. An ALGOL program was written for data reduction. It is run on a Telefunken TR-4 computer with the punched tape as direct input to the machine.

2.1.2.3. Water chemistry.

Feedwater for the boiler is degassed in the make-up tank and purified in a mixed bed demineralisation filter. The pH is thus kept close to 7 with a conductivity between 10 and 20 μS.

In the test facility Hydrazine is injected into the water cycle to keep the pH at 9.2. Conductivity is about 25 μS. Values above 200 μS are not tolerated. Experience with a leaking condenser tube showed that carry-under behaviour started to change at levels above 1000 μS probably due to frothing effects.

2.1.3. Experimentation.

2.1.3.1. Data reduction.

2.1.3.1.1. Temperature, flow and pressure measurements.

Thermocouple voltages are averaged over 10 scans and are converted to degrees C with use of the calibration constants. Steam and water properties are calculated from the IFC-formulations. Special procedures WIFC and SIFC [95] are incorporated in the data reduction program for this purpose, giving specific volume, enthalpy, entropy and heat for water and steam respectively as a function of temperature and pressure.

The flows measured, steam, circulation water and quench water, are calculated according to the DIN formula [39], with the venturi coefficient provided as a calibration coefficient by the manufacturer. The error in the coefficient is deemed negligible in comparison with the error of the differential pressure cell, calibrated against a waterfilled U-tube and of the order of ± 0.5%. The errors in steam density due to pressure and temperature measurements are ± 0.1 and 0.5% respectively, giving the error in the steam flow as

$$\sqrt{\tfrac{1}{4} \times 0.5^2 + \tfrac{1}{4} \times 0.1^2 + \tfrac{1}{4} \times 0.5^2} = \pm\, 0.4 \ .$$

For the water flow rates the error in density resulting from inaccuracies in pressure are negligible while for temperature errors 0.2% error in the density is to be expected. The resulting error in the flow rates becomes.

$$\sqrt{\tfrac{1}{4} \times 0.5^2 + \tfrac{1}{4} \times 0.2^2} = \pm\, 0.3 \ .$$

Apart from riser and downcomer pressure drop for void fraction determination, other measurements concern absolute pressure of the testvessel and of the steam at the venturi.

The strain gage manometers used are calibrated against a dead weight tester of 0.1% accuracy and have an output of about 100 mV. The last digit of the digital voltmeter of the data acquisition system represents 10 μV or 0.01%. The accuracy of the absolute pressures is therefore ± 0.1%.

The saturation temperature can be derived from this pressure measurement through the IFC-equation for the saturation line. The accuracy of 0.1% would be equivalent to .07°C. Although this way of measuring the saturation temperature of the test vessel is more accurate than the direct way with thermocouples (the last digit of the digital voltmeter represents 0.25°C) this last method was employed to have a consistent set of temperature and pressure measurements in order to avoid discrepancies in the specific enthalpies.

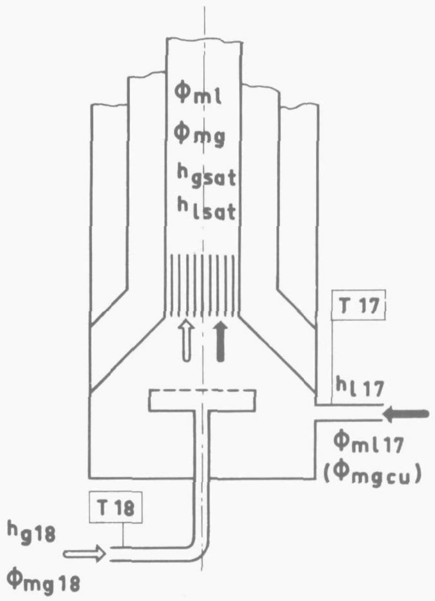

FIGURE 2-11.

Control volume for mixer heat balance.

A correction on the measured steam and water flows is applied for changes of phase when brought together in the mixing section. If the recirculating water is subcooled, which is measured with thermocouple T17, and mixed with superheated steam, measured with T18, the mixture becomes saturated with change of phase taking place. The new steam and water flow rates are found from a heat and mass balance over the control volume of figure 2-11.

Combination of these two balances gives

$$\phi_{mg} = \{ \phi_{mg18} (h_{g18} - h_{\ell sat}) - \phi_{m\ell 17} (h_{\ell sat} - h_{\ell 17}) \} / r \qquad (2\text{-}1)$$

$$\phi_{m\ell} = \{ \phi_{mg18} (h_{gsat} - h_{g18}) + \phi_{m\ell 17} (h_{gsat} - h_{\ell 17}) \} / r \qquad (2\text{-}2)$$

If on the other hand steam is carried under without being condensed the recirculating water is saturated. The carry-under steam flow ϕ_{mgcu} also participates in the mixing process. Although ϕ_{mgcu} is unknown for void fraction measurements the correction can still be performed using the measured downcomer void fraction and a slip correlation for down flow due to PETRICK [20] ★).
The carry-under flow rate is then found from the downcomer velocity, the downcomer void fraction and the slip ratio s_p ★★).

$$\phi_{mgcu} = \frac{v_{s\ell D}}{(1-\langle\alpha_D\rangle)} s_p \rho_{gsat} A_D \langle\alpha_D\rangle \qquad (2\text{-}3)$$

A combination of the mass and heat balance over the control volume of figure 2-11 now yields for the corrected steam and water mass flows

$$\phi_{mg} = \{ \phi_{mg18} (h_{g18} - h_{\ell sat}) + \phi_{mgcu}\, r \} / r \qquad (2\text{-}4)$$

$$\phi_{m\ell} = \{ \phi_{mg18} (h_{gsat} - h_{g18}) + \phi_{m\ell 17}\, r \} / r \qquad (2\text{-}5)$$

★) *As the correction constitutes a small percentage of the flow rates the accuracy of the correlation need not be of great concern now: See also section 2.1.4.3. on downcomer slip.*

★★) *s_p: slip ratio due to Petrick. See section 3.1.2.1. for a definition of the slip ratio.*

2.1.3.1.2. Carry-under measurements.

The void and quality measurements require a series of correlations and corrections based on empirical data obtained from the test loop in separate test runs. These procedures are considered an intrinsic part of the data reduction.

Void fraction in riser and downcomer.

The differential pressure measured by the cells D6, D11 and D12 is a balance of the pressure drop of the mixture over the measuring length against the static head of the cold water in the connecting measuring lines

$$\Delta p_c = \rho_\ell^{\star} \, g \, H - \Delta p_{TP} \tag{2-6}$$

With $\Delta p_{TP} = \{ <\alpha> \rho_g + (1-<\alpha>)\rho_\ell \} \, g \, H + \Delta p_{fr} + \Delta p_{acc}$ and $\rho_\ell^{\star}$ the water density in the tubing to the cell, the average void fraction $<\alpha>$ over the measuring length H becomes

$$<\alpha> = \frac{\Delta p_c - (\rho_\ell^{\star} - \rho_\ell) \, g \, H + \Delta p_{fr} + \Delta p_{acc}}{(\rho_\ell - \rho_g) \, g \, H} \tag{2-7}$$

The friction loss is calculated from levy's correlation ★)

$$\Delta p_{fr} = \frac{1}{(1 - <\alpha>)^2} \, \lambda \, \frac{H}{D_H} \, \tfrac{1}{2} \, \rho_\ell \, v_{s\ell}^{\;2} \tag{2-8}$$

The λ-values for the three channel length's were found from cold water runs [94] for Re numbers in the range of 1.6 to 7×10^4 for the downcomer and 4×10^4 to 1.4×10^5 for the riser.
The actual Re numbers based on water only range from 1 to 2.5×10^5 and 4×10^5 to 10^6 respectively. The tests showed λ to reach a nearly constant value at 5×10^4.
The λ-values used are 0.035 and 0.055 for the upper and lower downcomer region and -0.020 for the riser.
The acceleration loss is considered negligible except for the upper downcomer void measurements. For riser 2 configuration where the downcomer area reduction is to be taken into account. In view of the smallness of this correction the Bernoulli loss of the liquid phase according to

$$\Delta p_{acc} = \tfrac{1}{2} \, \rho_\ell \, (1-<\alpha>)^2 \left(\frac{A_1}{A_2} - 1\right) v_{s\ell D_1}^2 \tag{2-9}$$

was used as an approximation.
The maximum contribution of equations (2-8) and (2-9) amounts to about 4% void. An error of 20% in these equations has at the most an effect of 0.8% void. The error due to the calibration error of the pressure differential cells was already given as ± 1 mm H_2O which is equivalent to 0.14% void.
The total absolute error in the void measurement now becomes

$$\sqrt{0.8^2 + 0.14^2} = 0.81\% \, .$$

★) *See section 3.2.3.1.4. for a justification of the use of this formula.*

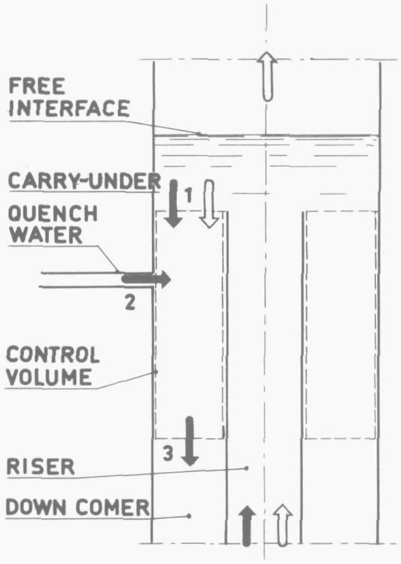

FIGURE 2-12.

Control volume for downcomer heat balance.

Quality in the downcomer.

The heat balance method for the determination of the downcomer quality suffers from inherent inaccuracy, but has to be used for lack of other dependable methods. The basic downcomer heat balance for the control volume given in figure 2-12 is

$$x_D = \frac{\phi_{m\ell 2}\,(h_{\ell 3} - h_{\ell 2}) - \phi_{m\ell 1}\,(h_{\ell 1} - h_{\ell 3})}{\phi_{m\ell 2}\,(h_{\ell 3} - h_{\ell 2}) + \phi_{m\ell 1}\,r} \qquad (2\text{-}10)$$

where x_D is the quality of the mixture at the downcomer inlet, or

$$x_D = \frac{\phi_{mg1}}{\phi_{mg1} + \phi_{m\ell 1}} \qquad (2\text{-}11)$$

The first term in the numerator of equation (2-10) represents the amount of steam condensed and subcooled within the control volume, while second is a measure of the subcooling of the water leaving it at level 3.
For low downcomer qualities the amount of heat involved in both condensation and subcooling are of the same order or magnitude and errors in the downcomer subcooling have a substantial effect on the value of x_D.
Apart form these errors originating from inaccuracies inherent to temperature measurements other heat sources and sinks are to be taken into account: heat flowing from the riser to the downcomer and from the downcomer to the annular cavity around the downcomer, while a third heat sink is constituted by the sparger which forms a part of the downcomer wall as shown in figure 2-4. In theory this sink is accounted for by the enthalpy $h_{\ell 2}$ in equation (2-10). But heat is exchanged with the water in the cavity through the supplying hoses and sparger wall and with the downcomer water through the sparger wall. The exact location of the boundary between the two heat transfer regions cannot be indicated. For the first test series the error introduced by malpositioning of the thermocouples in the sparger was not fully recognized and thermocouples were only located at stations T25, 30 and 31 as illustrated in figure 2-13. These locations will give temperatures of the quench water after having taken up heat from the downcomer. Furthermore thermocouple failure during the tests reduced the number of active thermocouples in the sparger to one.

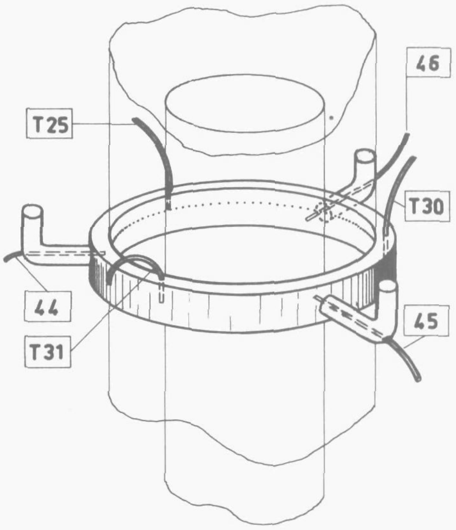

FIGURE 2-13.

Positioning of thermocouples in sparger.

A survey of the additional heat sources and sinks is given in figure 2-14, designated as Q_R, Q_D and Q_S.

Incorporation in equation 2-10 yields

$$x_D = \frac{\phi_{m\ell 2}\,(h_{\ell 3} - h_{\ell 2}) - \phi_{m\ell 1}\,(h_{\ell 1} - h_{\ell 3}) - Q_R + Q_D + Q_S}{\phi_{m\ell 2}\,(h_{\ell 3} - h_{\ell 2}) + \phi_{m\ell 1}\,r - Q_R + Q_D + Q_S} \qquad (2\text{-}12)$$

As shown in figure 2-14 the exit plane 3 of the control volume may be located in the downcomer coinciding with thermocouple 10 or at the exit of the vessel where thermocouples T15 and T16 are placed.

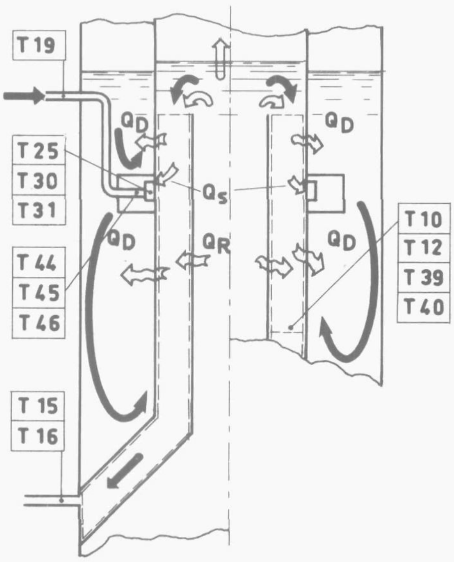

FIGURE 2-14.

Heat sources and sinks for the "long" and "short" downcomer control volume.

In order to establish the value of the sinks Q_R, Q_D and Q_S a separate series of tests were run, where the downcomer quality was known aforehand i.e. equal to zero. For these experiments, designated as XNEP-measurements in contrast to those where carry-under quality and downcomer void fraction were measured, called X- or A-measurements respectively, the conditions were such that no carry-under would occur. Several runs were made but they only became successful when an extra set of thermocouples was installed in the sparger and in the annular cavity. The sparger thermocouples are shown in figure 2-13 numbered T44, 45, 46. A total of 8 thermocouples were placed in the cavity at three levels: above the sparger, at the level of T10 and in the lowest section.

The heat flowing from riser to downcomer, Q_R, was calculated using forced convection correlations, while the heat Q_R from the downcomer to the cavity was based on forced convection at the downcomer side and natural convection in the cavity. The calculations for Q_R and Q_D are presented in Appendix 2-C in more detail. With $h_{\ell 2}$ based on the average readings of T44, 45 and 46 equation (2-12) was evaluated for the "long" and "short" downcomer control volume and checked against the XNEP-measurements. The "long" downcomer heat balance proved to give much more favorable results and was therefore used for the data reduction for all real X-measurements. The inadequacy of the "short" control volume is ascribed to an incorrect measurement of the downcomer subcooling. The four thermocouples spaced along the downcomer circumference and connected in series to give a higher voltage output (designated by T10, 12, 39, 40 in figure 2-14) did not give the expected results. The temperature indicated was too low to make the heat balance give zero downcomer quality for the XNEP-measurements. Because the extra thermocouples in the sparger and cavity were not installed for all real X-measurements, correlations had to be found from the XNEP-experiment to make the results useful for all tests. The cavity temperature had to be correlated with the enthalpy rise of the quench water during its passage through the cavity. The heat transfer mechanisms involved are forced convection inside the flexible steel hoses and natural convection on the outside. A correlation of the form

$$\phi_{m\ell 2}\,\Delta h_{\ell 2} = k\,(\bar{\theta}_C - \theta_{19}) \qquad (2\text{-}13)$$

was established, where $\Delta h_{\ell 2}$ is based on measured temperature at T19 and the average cavity temperature. As shown in Appendix 2-D the temperature difference $\bar{\theta}_C - \theta_{19}$ is predicted better than $\pm$ 5% for both 50 and 70 bar XNEP-experiments. The use of equation (2-13) makes an iterative procedure necessary as the constant k also contains $(\bar{\theta}_C - \theta_{19})$.
The iteration is stopped when the successive calculations differ less than 0.5^oC.
The second correlation concerns the heat transferred to the sparger ring before the water leaves it. This amount of heat is not exactly equal to $\phi_{m\ell 2}\ (h_{\ell 2} - h'_{\ell 2})$ where $h'_{\ell 2}$ is based on T44, 45 and 46. But as $h_{\ell 2}$ is used in equations (2-10) and (2-12) it is the amount missing from these equations. In other words if the extra thermocouples would have been present in all measurements $h'_{\ell 2}$ could have been used instead of $h_{\ell 2}$ in equation (2-12) and Q_S would have been accounted for automatically. Now Q_S is included as a corrective term. This fraction of the total amount of heat transferred to the carry-under quench water between T19 and T25, 30 and 31 was related to the temperatures in the cavity, the sparger and the saturation temperature, as shown in Appendix 2-D. The calculated values of Q_S have an accuracy of $\pm$ 10%.

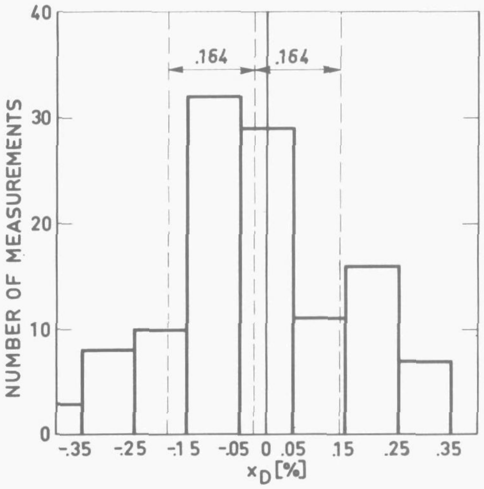

FIGURE 2-15.

Measured x_D values from XNEP-experiment.

Using equation (2-D-1) for Q_R, equation (2-C-6) for Q_D and calculating $\bar{\theta}_C$ from equation (2-D-1) and Q_S from equations (2-D-3) and (2-D-4) the data reduction program calculates x_D from the heat balance as given by equation (2-12). Because the character of the constants given in the appendices mentioned above is that of calibration factors an error analysis treating the separate terms of equation (2-12) is inappropriate. To obtain an impression of the overall accuracy of the heat balance method the calculated results for the XNEP-experiments are given in the form of a histogram in figure 2-15.
The mean value for x_D was found to be -0.024% with a standard deviation of 0.164% quality.

2.1.3.2. Experimental procedure.

The test runs were started after bringing the loop to operating pressure and temperature by supplying steam to the test vessel and circulating the water, which was usually accomplished in three hours. A check of instruments was performed and zero readings adjusted if necessary. Subsequently the steam flow rate was adjusted while the water circulation was set at an amount below the threshold value for carry-under initiation.
The capacitance level gage was then adjusted for minimum and maximum readings. For these conditions a series of tests with increasing water flow according to fixed predetermined increments was carried out. When equilibrium of the loop was reached at a given circulation rate the tape puncher was started and 10 consecutive scans were made.
For void fraction measurements (A-measurements) carry-under initiation and subsequent increase were observed on a recorder showing the mV output of

one of the downcomer pressure differential cells. The test was cut off when the output value exceeded the cell range. The carry-under quench water flow rate was kept equal to the steam flow rate, but, bypassing the subcooler, this water was close to saturation temperature.
During downcomer quality measurements (X-measurements) the same procedure was followed but now both the downcomer void fraction and the subcooling were monitored. When the first carry-under showed on the pressure differential recorder the carry-under quench water temperature was lowered until the voidage disappeared, while keeping the downcomer subcooling less than 1 to 2 degrees. The subcooling was monitored on a μV recorder giving the resulting voltage of the steam dome thermocouple T26 and the one but lowest downcomer thermocouple, T9, connected in series to give a differential voltage proportional to the subcooling.
The test runs were organized in the following scheme. The measurements were performed for three different steam flow rates, 0.25, 0.35 and 0.45 kg/s nominal. A run for different water flow rates was coded X-1,X-2,X-3 or A-1, A-2 and A-3 respectively. An X or A run represents 5 to 25 experiments with an increase in the nominal water flowrate of 0.2 kg/s. Referring to section 2.1.1. for the notation for pressure, riser configuration and level the following experimental program was executed:

TABLE 2-2

R 1							R 2					
P 70				P 50			P 70			P 50		
H 22		H 12	H 6	H 22	H 12	H 6	H 22	H 12	H 6	H 22	H 12	H 6
X/A-1	X/A-1.1	X/A-1	X/A-1	X/A-1	X/A-1	X/A-1	X/A-1	X/A-1	X/A-1	X/A-1	X/A-1	X/A-1
X/A-2	X/A-2.1	X/A-2	X/A-2	X/A-2	X/A-2	A-2	X/A-2	X/A-2	X/A-2	X/A-2	X/A-2	X/A-2
X/A-3	X/A-3.1	X/A-3	X/A-3	X/A-3	X/A-3		X/A-3	X/A-3	X/A-3	X/A-3	X/A-3	X/A-3

For R1/P70/H22 more than three steam flow rates were tested; also intermediate values of 0.3, 0.4 and 0.5 kg/s were investigated denoted by X/A-1.1, X/A-2.1 and X/A-3.1, as shown in Table 2-2.

2.1.4. Results.

2.1.4.1. Carry-under.

The primary experimental test results, i.e. downcomer quality and void fraction, can be presented in several ways, depending on which parameter is given prime importance. The superficial downcomer water velocity related to to the downcomer inlet area was chosen as the independent variable, being a known variable of any circulating system and a direct cause of the entrainment process in contrast to the also relevant but secondary parameter, the circulation rate ⋆).

⋆) circulation rate $= \frac{\phi_{m\ell R} + \phi_{mgR}}{\phi_{mgR}} = \frac{1}{x_R}$

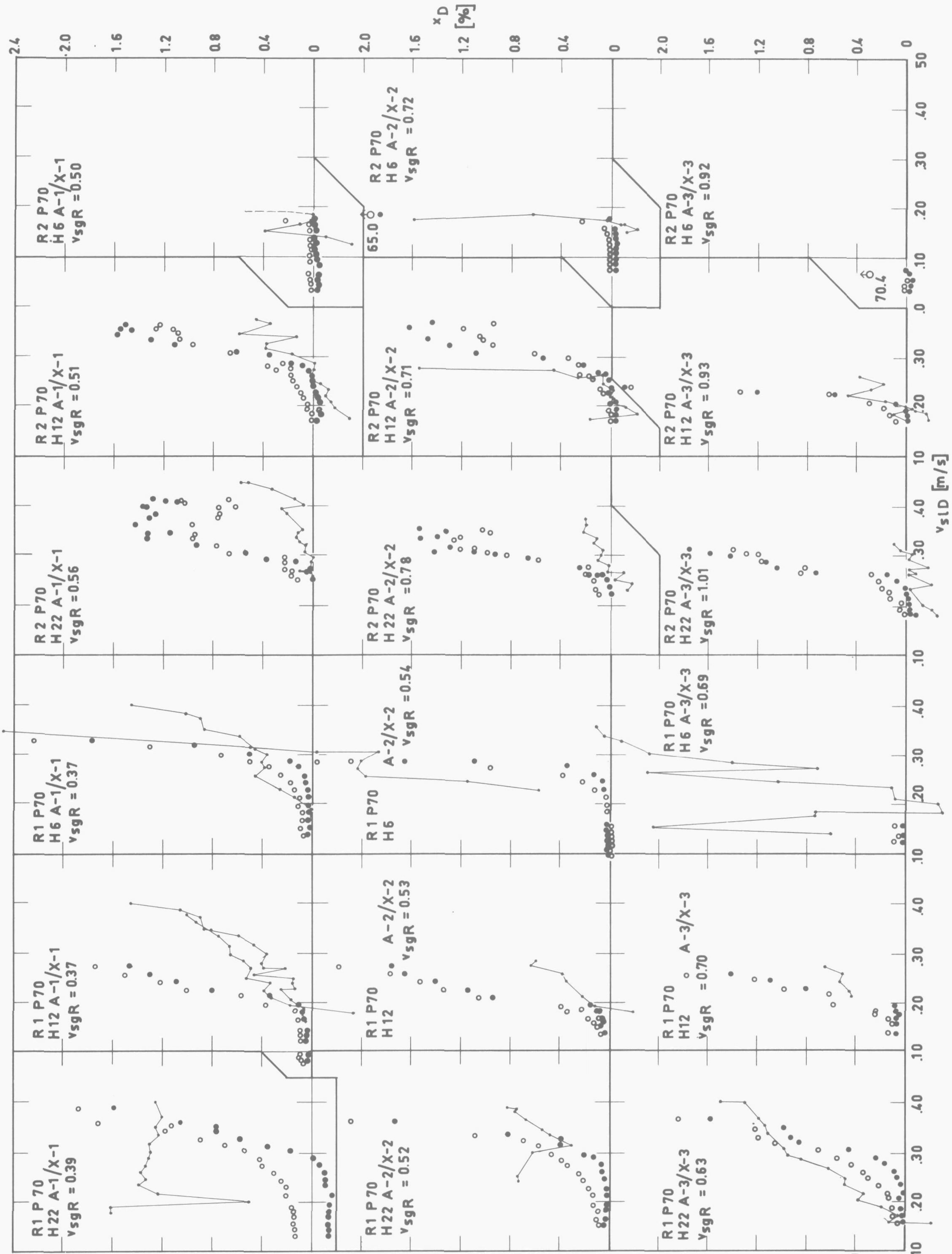

FIGURE 2-16.
Measured downcomer quality and void fraction as a function of superficial downcomer water velocity at 70 bar.

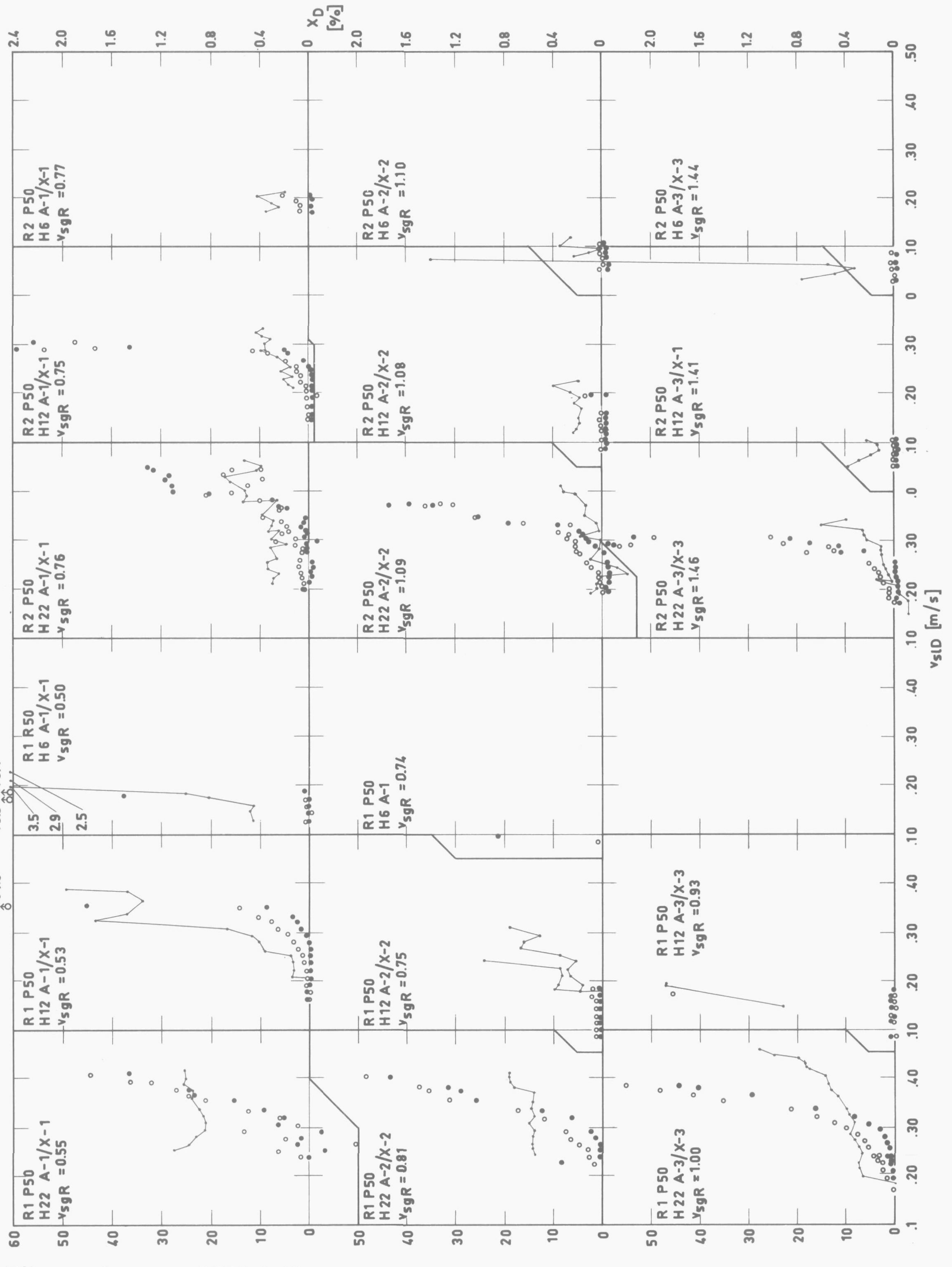

FIGURE 2-17.
Measured downcomer quality and void fraction as a function of superficial downcomer water velocity at 50 bar.

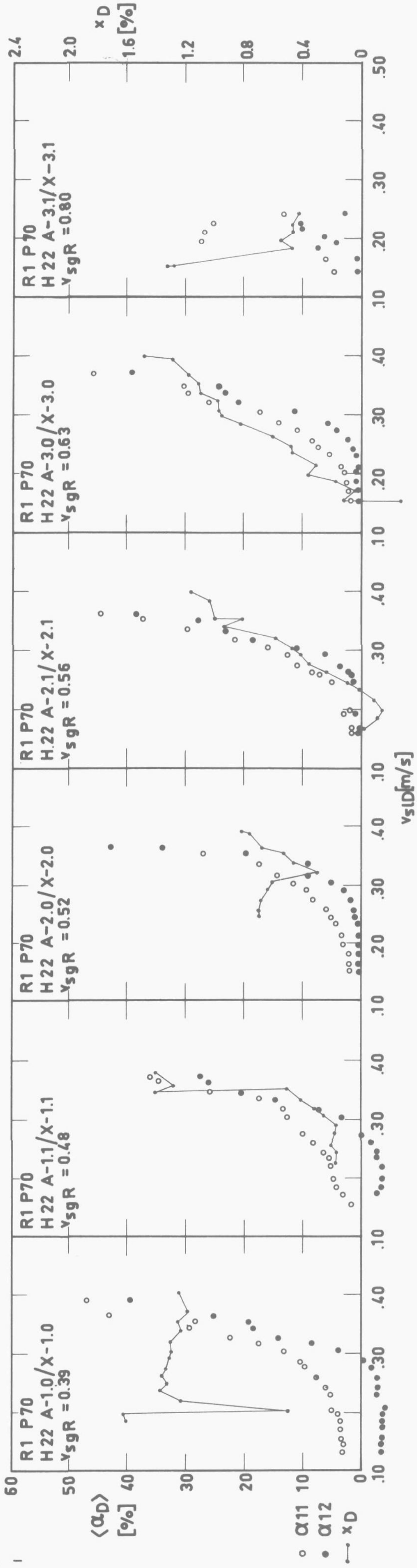

Furthermore it facilitates a direct comparison of different geometries and dimensions. A better comparison is also possible if all or a large portion of the experimental data could be plotted in one graph.
For this reason all the P70 and all the P50 data are grouped in the two figures 2-16 and 2-17 (see page 42 and 43) with the exception of the intermediate data for R1/P70/H22 which are given together with the X/A-1, X/A-2 and X/A-3 data in figure 2-18. The downcomer void fraction for the upper region α11 and the lower region α12, as well as the downcomer quality x_D are plotted as a function of superficial downcomer water velocity. The individual graphs for each test run are arranged to show the influence of level in horizontal direction and riser steam flow in vertical direction. The superficial riser steam velocity indicated in the graphs is related to the riser exit area.

FIGURE 2-18.

Measured downcomer quality and void fraction as a function of superficial downcomer water velocity at 70 bar.

2.1.4.2. Riser and downcomer slip ratio.

An important phenomenon in two-phase flow is the relative motion of both phases, called the slip and characterized by the slip ratio s ★). The mean cross sectional value <s>, being the ratio of the mean true velocities $<u_g>$ and $<u_\ell>$, is related to the quality and void fraction $<\alpha>$ by the definition of quality formulated at the cross section under consideration.

$$<s> = \frac{<u_g>}{<u_\ell>} = \frac{x}{1-x}\;\frac{1-<\alpha>}{<\alpha>}\;\frac{\rho_\ell}{\rho_g} \qquad (2\text{-}14)$$

When gravity is the major force causing the slip, the lighter phase is expected to have the larger velocity for upflow and lag behind for downflow. In other words <s> will be greater than 1 in upflow and smaller than one in downflow. For high mixture velocities the relative velocity between u_g and u_ℓ will become smaller relative to the mixture velocity and <s> will assymptotically tend equal 1. If on the other hand the liquid velocity is zero (stagnant liquid) the gas phase rises and <s> is + ∞ or - ∞ if the coordinates are assumed for up or downflow respectively.

Slip ratio's based on experimental riser qualities and void fractions are presented in figures 2-19 and 2-20 for 70 and 50 bar.

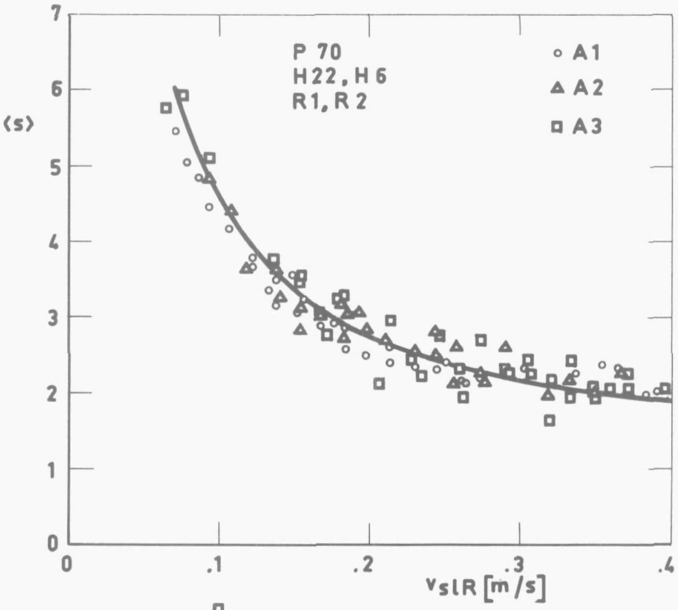

FIGURE 2-19.

Slip ratio as a function of superficial water velocity for upflow from 70 bar experiments.

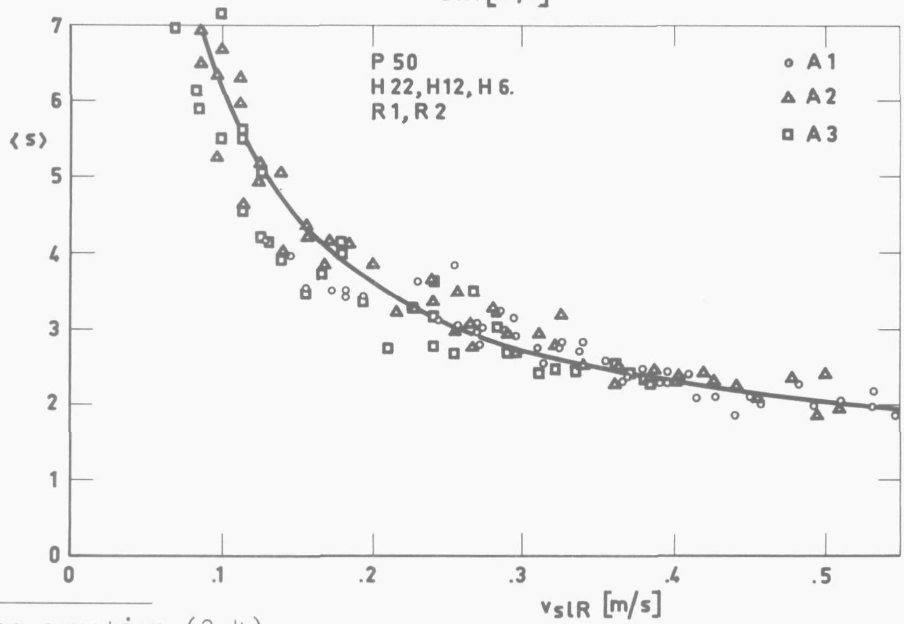

FIGURE 2-20.

Slip ratio as a function of superficial water velocity for upflow from 50 bar experiments.

★) See equation (3-4)

<s> is plotted as a function of the superficial riser water velocity. As evident from these plots the above described trend for <s> is followed. The simplest relation that would satisfy this trend would be:

$$<s> = k_1/v_{s\ell} + k_2 \qquad (2\text{-}15)$$

where k_2 has to be equal to 1 in order to let <s> be 1 for $v_{s\ell}$ equal to ∞. The value of k_1 is found from the experimental data and the resulting expressions for the slip ratio for 70 and 50 bar respectively read:

$$<s>_{70} = 0.35/v_{s\ell} + 1 \qquad (2\text{-}16)$$

$$<s>_{50} = 0.52/v_{s\ell} + 1 \qquad (2\text{-}17)$$

As shown in figures 2-19 and 2-20 the experimental data agree very well with these relations.
Equation (2-14) was also evaluated for the measured downcomer qualities and void fractions. The quality was corrected for the increased water velocity, due to the quench water, in the region where the downcomer voids were measured. The results are plotted in figure 2-21 and 2-22. The data points show a large scatter and the expected trend in <s> is not evident at all. For low velocities slip ratios even larger than 1 were found, whereas values ≤ 0 were expected. Apparently the high slip ratio values are due to another phenomenon.

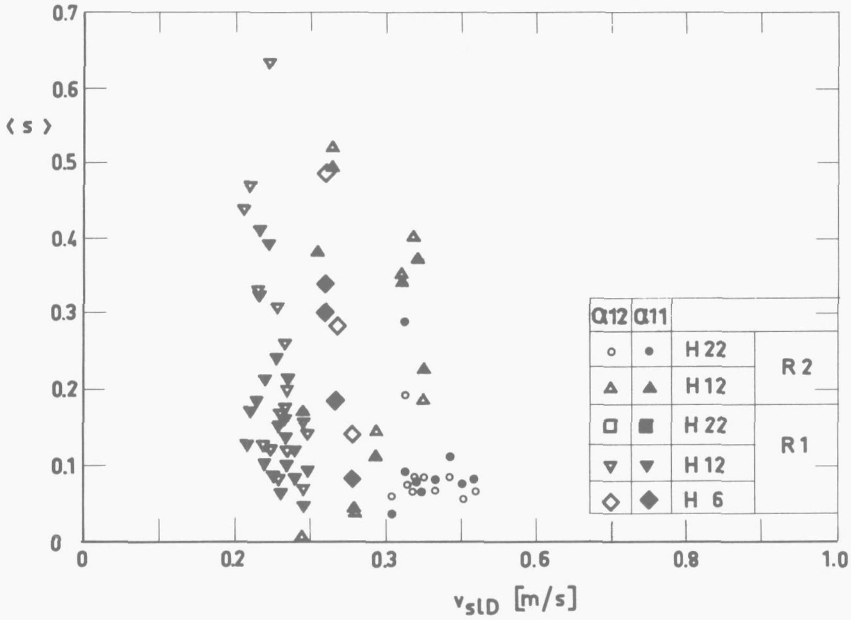

FIGURE 2-21.

Slip ratio as a function of superficial water velocity for downflow from 70 bar experiments.

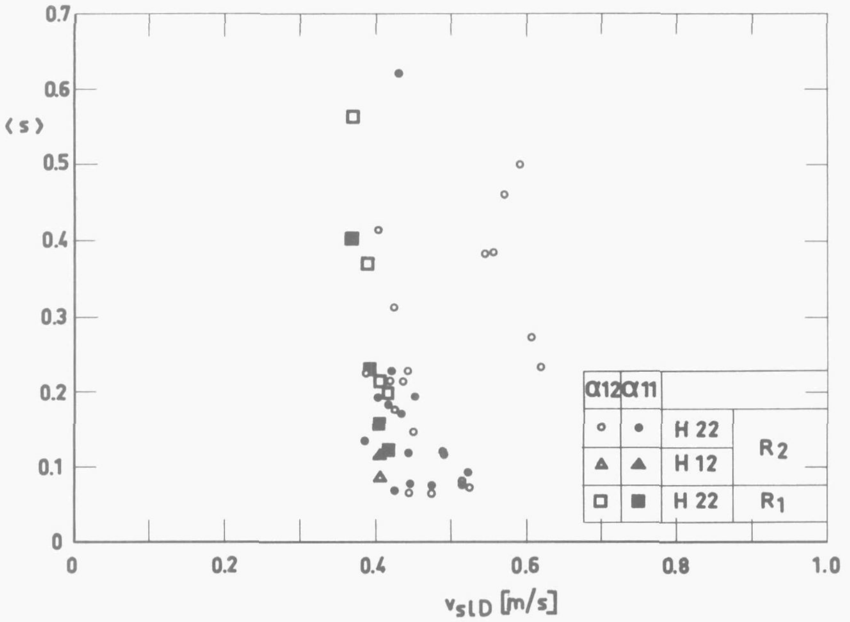

FIGURE 2-22.

Slip ratio as a function of superficial water velocity for downflow from 50 bar experiments.

2.1.4.3. Discussion

Several aspects of the experimental results need further discussion. After going into the general behaviour of the experimental curves shown in figure 2-16 and 2-17, effects of level, steam flow rate, pressure and riser geometry will be treated as well as the downcomer slip.

General behaviour.

Looking at the void fraction data all curves show a velocity range for which no carry-under occurs. Beyond a critical velocity the void fraction in the upper downcomer, α11, begins to increase, followed after a certain interval by the void fraction in the lower downcomer region, α12. As the downcomer velocity is further increased α12 tends to equal the α11 values. Both values grow with increasing downcomer velocity until they exceed the instrument range. An exception is formed by high level tests with riser 2, where the void fraction did not increase further beyond a certain level. These test runs had to be stopped when the carry-under initiated pump oscillations.
The critical velocity at which the void fraction in the lower region begins to deviate from zero will be called the threshold velocity ⋆).
The subsequent increase may be gradual or steep, becoming more abrupt with decreasing level.
Some of the behaviour may be explained by the peculiarities of two-phase flow. If the threshold velocity is regarded as the rise velocity of a dense bubble swarm in stagnant water, this velocity is higher than for a single bubble or a very "dilute" swarm as will be explained later in section 3.2.3.2.4. At a certain liquid velocity some bubbles will be drawn into the downcomer, but as the population increases the rise velocity, due to decreased drag

---

⋆) *The results of runs R1 P70 H22 A-1 and A-1.1 show α12 values below zero that must be attributed to errors in the zero adjustment of the instrument.*

forces, will increase and a tongue of bubbles will be formed penetrating into the downcomer. The liquid velocity distribution at the downcomer inlet will show the highest value near the riser wall and decrease towards the downcomer wall due to the 180° turn. It may thus be that the bubbles entrained in the high velocity region rise again in the outer region, stabilizing the tip of the tongue at a certain level.

The tip moves downwards with increasing liquid velocity resulting in an increasing $\alpha 11$ untill the bubbles reach the $\alpha 12$ region and net carry-under takes place.

VOLLRADT [46] performed carry-under experiments using a full size pie shaped section of small included angle, cut from a BWR riser and downcomer.

Using air-water mixtures and "sandwiching" the flow model between plate glass windows he could observe the flow patterns. From his observations he concluded that the velocity distribution showed a maximum near the downcomer wall diminishing towards the riser rim. In this region he saw a large eddy filled with a two-phase mixture. Although the photographs presented by Vollradt have lost quality in the reproduction process they show his conclusions to be not quite correct. The eddy near the riser rim is probably a flow separation zone of considerable size. The velocity of the flow between this zone and the downcomer wall should then have a distribution with a maximum near the separation zone and diminish towards the wall.

Vollradt also observed the two-phase tongue penetrating the downcomer having a well defined and stationary boundary between the mixture and the water in the downcomer before net carry-under occurred.

The flow pattern at the downcomer entrance is of course much more complicated than sketched above and eddies will be forming in the region of the 180° turn as the water flows from the riser to the downcomer. Therefore the assumption of a simplified model to explain the carry-under behaviour must include a region where the flow separates from the sharp rim of the riser as shown in figure 2-23, and contracts at the downcomer inlet.

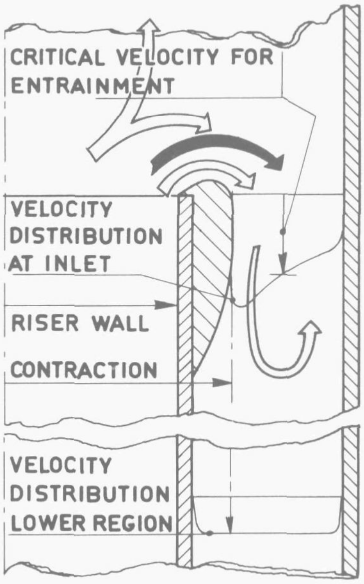

FIGURE 2-23.

Flow pattern at downcomer entrance.

Due to the contraction the critical superficial downcomer velocity for the beginning of entrainment is lowered. Downstream of it the flow will again fill the downcomer area and have a more uniform and lower velocity, even lower than the critical velocity for entrainment. When with increasing superficial downcomer velocity the velocity at the wall also increases above critical no bubbles can escape anymore.

Now a situation is created where steam is carried under at the downcomer inlet but cannot be entrained any further. There is but one place to go and that is the flow separation zone which becomes filled with steam and grows downwards as more steam is entrained. The high velocity over the top will prevent the slug from escaping to the surface unless the buoyancy forces become too large and it breaks away.

This phenomenon has been observed by MARSHALL [66] in air-water experiments and was called the "double interface condition". In his tests the flow separation zone filled up with air, creating a new interface in the downcomer that moved downwards. Beyond the downcomer velocity at which the double interface was created the carry-under increased sharply.

For a severe contraction at the downcomer inlet the effect may result in a very abrupt change from no to substantial carry-under. If on the other hand the contraction is small it may create a transition regime after which the steamfilled flow separation zone empties again through entrainment and the carry-under behaviour shows a much more gradual increase. Vollradt reports no double interphase contition but periodic breaking away of air slugs from the separation zone. If the double interphase is only stable for small scale experiments more favorable carry-under behaviour can be expected for the full size system. Furthermore the velocity profile may be less skewed for the large system, reducing the incentive to create a double interphase. A very sharp increase in void is shown in the P70 R1 H6, the P50 R1 H6 and two of the P50 H1 H12 runs while the P70 R1 H12 runs exhibit a more gradual increase. If these curves correspond to double interface conditions it is clear that the phenomenon is a function of level and steam flow rate.

Another effect also influences the carry-under experiments. As the circulation is increased the jet issuing from the riser is projected to greater heights. For high levels this fountain is submerged, but a point may be reached where the top of the fountain penetrates the level set by the controller. During the test runs the level is controlled by draining off water. When the fountain height determines the level gage indication draining has no effect on the level above the riser, while only water from the downcomer is drained.

At this instance water and entrapped steam undergo a free fall into the downcomer, which is accompanied by a stepwise increase in the downcomer void fraction to 100 percent. This fountain effect was especially observed for the low level R2 test runs and may have obscured or coïncided with a double interface condition. The measured downcomer qualities for most of the tests follow the general trend described above, although the scatter of the data points is much larger. Some curves however do not start at zero quality and seem to be in contradiction with the behaviour apparent from the void measurements. This effect is most evident for the R1 H22 runs.

This seeming incongruity can be explained by the advancing two-phase tongue at the onset of carry-under. If the tongue penetrates past the sparger which is situated 0.17 m below the riser rim the steam is condensed and the heatbalance registers carry-under. This effect is called "false" carry-under, for further reference. The fact that the narrow downcomer of the R1 experiment promotes this effect as shown by the experimental data corroborates this hypothesis.

Effect of level.

The effect of the two-phase level above the riser on carry-under is important from a practical point of view. As long as the fountain effect is not present (a decreasing danger with increasing system size) a change of level has two effects. It influences the radial velocity from the riser to the downcomer and consequently the radial transport of steam to the downcomer and the distance the steam has to rise to reach the surface and escape from entrainment. These two effects are contradictory.

For different levels the radial superficial water velocity over the riser rim relative to the superficial water velocity in the downcomer is:

TABLE 2-3

	H22	H12	H6	
$\frac{v_{s\ell\ rad}}{v_{s\ell D}}$	0.175	0.321	0.643	R1
	0.279	0.512	1.025	R2

As shown in Table 2-3 the variation in radial velocity is fairly large. In view of the large influence of the downcomer velocity the effect of this variation was expected to be strong. This is not borne out by the experiments however (not including the fountain effects). Comparing the R1 P70 runs for different levels it seems that the threshold velocity shows a minimum for the H12 experiments, an effect which does not hold for the R2 runs: the threshold velocity is about equal for H22 and H12. For P50 the effect is not visible due to fountain effects for the H6 runs. The reduction in residence time through increased radial velocity which is needed for the bubble to escape to the surface is apparantly balanced by the shorter distance to be covered when the level is decreased.

Effect of steam flow rate.

The effect of the steam flow rate is surprisingly low for the range considered. The more extensive series of P70 R1 H22 give the results for 6 steam flows. The threshold velocity is about constant at 0.22 m/s while the void fraction curves are slightly steeper with increasing steam flow. The downcomer void fraction at 0.35 m/s downcomer velocity is 19, 21, 20, 28, 28% for α12 respectively. The last run for the highest steam flow shows very erratic results; the maximum boiler capacity was reached for those conditions and the control system became unstable.
The downcomer quality appears to go through a minimum when varying the steam flow. Values of 1.25, 1.41, 0.52, 1.01, 1.12% are shown for the first 5 runs respectively at a superficial downcomer velocity of 0.35 m/s. The amount of "false" carry-under measured at low velocities as a result of the two-phase tongue decreases with increasing steam flow. This trend is also evident in the other runs. PETRICK [20] also reports a minimum in the downcomer quality for varying steam flow. His results and corresponding data from this expetiment are plotted in figure 2-24, where the ratio of downcomer over riser quality is given as a function of riser quality. Although the effect is stronger in Petrick's data the agreement is reasonable. An explanation may be found in the two opposing effects of increasing void fraction in the separating plenum. A higher void fraction increases the amount of steam available for entrainment but reduces the drag forces on the bubbles. This last effect could also explain the stronger incentive to form a two-phase tongue at lower riser qualities which penetrates deeper into the downcomer.

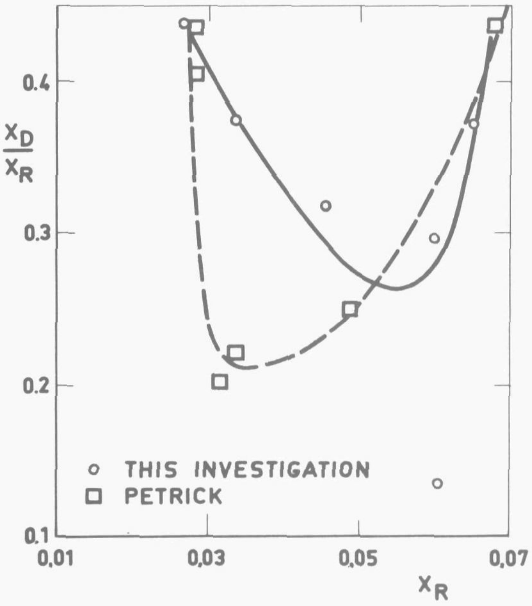

FIGURE 2-24.

Carry-under as a function of riser quality for a superficial downcomer water velocity of 0.35 m/s.

Effect of pressure.

The experimental riser slip ratio's for 50 and 70 bar system pressure presented in figures 2-19 and 2-20 suggest that the effect of rising pressure would be an increase in carry-under due to increased drag forces. However, no such marked effects were found for carry-under.

The threshold velocities show a slight increase from 0.22 m/s for P70 R1 H 22 to 0.25 m/s for P50 R1 H22 and 0.28 m/s for P50 R1 H12. The threshold for both pressures is higher for the R2 measurements. An average value of 0.26 m/s is found for P70 and 0.29 for P50.

Where the downcomer qualities are the same for both pressures the P50 void fractions are somewhat lower which is in agreement with the higher riser slip ratio's and reduced steam to water density ratio at 50 bar.

This effect should also be evident in the downcomer slip but the large scatter due to the "false" carry-under measured for the lower downcomer velocities abscures this tendency.

A stronger fountain effect is found for P50 especially at low levels resulting from the greater specific volume of the steam at the lower pressure and consequently higher velocities of the jet at the riser exit. For P50 the effect was found in 10 runs whereas only in 5 for P70.

Effect of riser geometry.

The necked down geometry of R2 gives an improvement in carry-under performance over R1 as long as the conditions for a fountain effect are avoided. For low steam flow rates the void fraction and quality reach a certain plateau beyond which they do not increase. At higher steam flow rates this plateau disappears which may be caused by a postponed fountain effect. It should be noted that for the same superficial downcomer velocity at the entrance the downcomer void fraction for R2 must be lower as a result of the 1.43 times higher downcomer velocity in the region of the reduced area. For this reason a double interphase is less likely to form. The flow contraction at the inlet should be of the same order and the bubbles entrained at the top are carried down in the narrow downcomer section.

Comparison of the experiments with other investigations mentioned in Table 2-2 presents difficulties. Only one investigator [20] measured the downcomer quality for steam-water mixtures and only four performed steam-water experiments at all. Furthermore those experiments were not performed very systematically.

The level, for example, was not kept constant during a test rund and (or) not reported. This should explain the different threshold velocities that can be deduced from the various references and are listed below

PETRICK [20]	69 bar	0.33 m/sec
SKAUG [67]	50 bar	0.26 m/sec
CEND [68]	85 bar	0.21-0.27 m/sec
A-C [49]	69 bar	0.18 m/sec

Down comer slip.

The unexpected results obtained for the downcomer slip ratio and shown in figures 2-21 and 2-22 can be explained in the light of the above discussion on the two-phase tongue penetrating into the downcomer. The "false" carry-under results ★) in a quality too high with respect to the void measurements made further downstream of the sparger. The slip ratio calculated from these

---

★) *For an explanation of the term "false" see the definition at the end of "General behavior" in this section.*

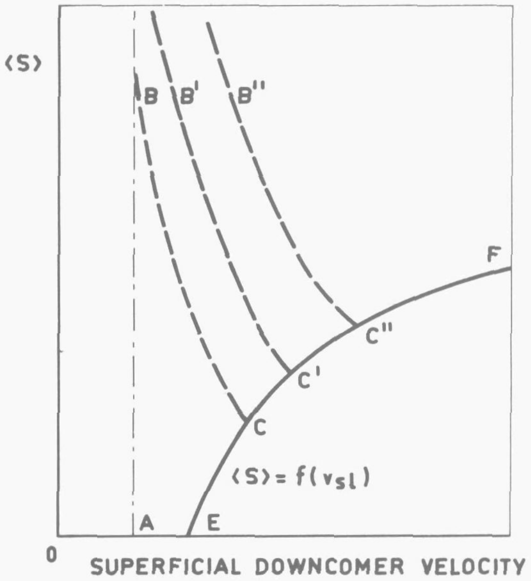

FIGURE 2-25.

Trend in the measured downcomer slip ratio for increasing superficial downcomer velocity.

data is consequently too high but decreasing with increasing downcomer velocity i.e. for a diminishing effect of "false" carry-under. This trend is illustrated in figure 2-25. Below the threshold velocity, indicated by point A in the figure, no tongue can theoretically be formed and with no carry-under, "false" on otherwise, the slip ratio is zero until A is reached. Then, depending on the void fraction of the tongue some high value of the slip ratio is found, indicated by B, B' and B''.

With increasing downcomer velocity the contribution of the "false" carry-under diminishes until the point for net carry-under, C, is reached. From there on the true slip ratio curve is followed which increases with increasing velocity. Going back to figure 2-21 and 2-22 this trend is only vaguely evident. The data points cover lines corresponding to B-C but no substantial rise after reaching C is seen.

PETRICK [20] performed some additional experiments to his carry-under tests to investigate the down flow slip behavior. The mixture was directed downwards from the riser to a downcomer of equal diameter by means of a 180° bend. In this way no separation could take place and the quality of the mixture was known with greater accuracy. He measured slip ratio's for superficial velocities up to 1.4 m/s. His results follow the trend of the curve indicated in figure 2-25 by E-F. Some of his data points for 69 bar are plotted in figure 2-26 together with those of figure 2-19. The combination of both sets of data points, follows the expected trend better despite the large scatter.

If the downcomer slip is the result of the same forces which act in upflow it should be possible to use the same type of function for up and downflow.

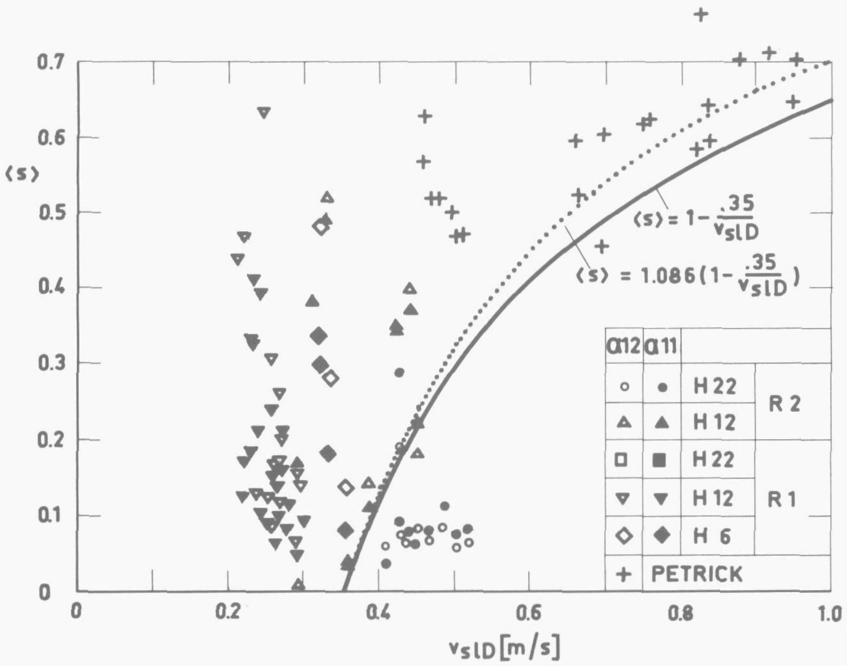

FIGURE 2-26.

Comparison of correlation for down flow slip ratio with experimental data from 70 bar experiments.

For downflow the slip ratio should go to unity increasing the velocity to infinity and become zero for zero gas velocity, which should happen at the critical velocity for entrainment.
The simplest form that satisfies these demands is

$$<s> = 1 - \frac{k_1}{v_{s\ell D}} \qquad (2\text{-}18)$$

The curve according to equation (2-18) with k_1 equal to 0.35, as for the riser, is shown in figure 2-26 to give reasonable agreement with the author's data as well as with those of PETRICK [20], although it somewhat underpredicts the latter's data. However when using a value of $k_1 = 0.52$ the same relation is seen from figure 2-27 to underpredict all the data even when taking the "false" carry-under data into account. This may be due to a diameter effect: 0.152 m for the riser and 0.062 m for the downcomer. The Froude number as given in Petrick's correlation:

$$<s> = 0.63 \left\{ \frac{v_{s\ell D}^{2}}{g D_D} \right\}^{0.4} \left\{ \frac{x}{1-x} \frac{\rho_\ell}{\rho_g} \right\}^{0.2} \qquad (2\text{-}19)$$

is sometimes used to incorporate this effect for upflow. Most authors [20], [45], [96], [97] find the effect to die out above a certain value e.g. 0.05 [96] or 0.0762 [20], [45], [97].
Taking 0.0762 as maximum the correction of the riser slip ratio's according to equation (2-19) is $(0.0762/0.062)^{0.4}$ = 1,068 and the results are plotted in figures 2-26 and 2-27. The agreement with Petrick's data is better but the correction term results in slip ratios above 1 for velocities above 4.5 and 6.6 m/s respectively.

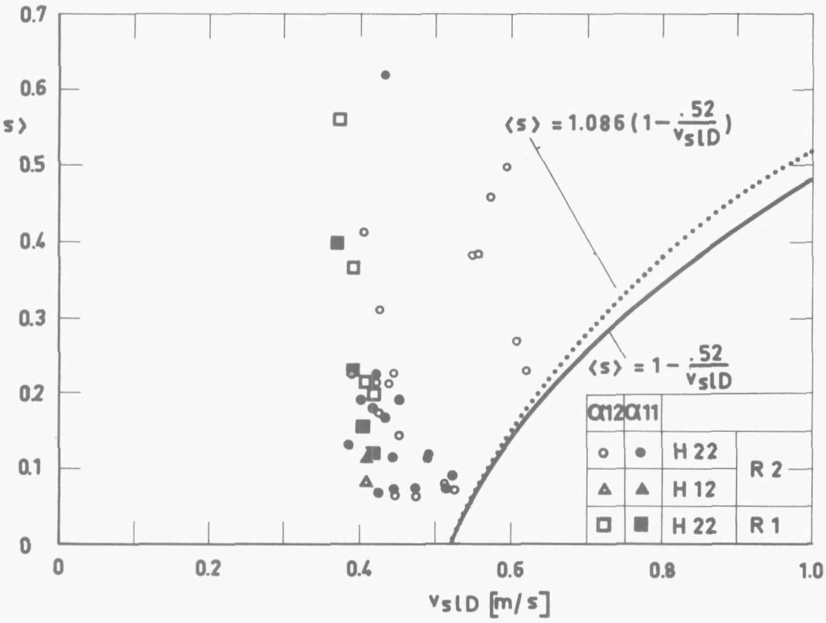

FIGURE 2-27.

Comparison of correlation for down flow slip ratio with experimental data from 50 bar experiments.

The choice of parameters used in equation (2-19) which correlates slip data obtained at 41.4, 69 and 103.56 bar was based on a slip correlation for upflow derived by MARCHATERRE and HOGLUND [45], who used the same parameters. Petrick states that the density effect is contained in the last term; therefore in comparing two flows at different pressure having the same void fraction the difference in slip is given by the last term.

It would be interesting to see whether the pressure effect found in this experiment could also be correlated by this expression while it is about the only one existing for downflow conditions. However, an investigation of equation (2-19) shows Petrick's statement to be unfounded. This becomes evident when writing equation (2-19) in terms of superficial velocities instead of quality

$$\langle s\rangle = 0.63 \left\{ \frac{v_{s\ell D}^{2}}{gD_D} \right\}^{0.4} \left\{ \frac{v_{sgD}}{v_{s\ell D}} \frac{\rho_g}{\rho_\ell} \right\}^{0.2} \left\{ \frac{\rho_\ell}{\rho_g} \right\}^{0.2} \qquad (2\text{-}20)$$

showing that <s> is independent of pressure for equal flowrates, or

$$\langle s\rangle \neq \langle s\rangle (p), \; (v_{s\ell D} = \text{const}, \;\; v_{sgD} = \text{const}) \qquad (2\text{-}21)$$

Combining equation (2-19) and (2-14) <s> can be eliminated:

$$\frac{x}{1-x} \quad \frac{\langle\alpha\rangle}{1-\langle\alpha\rangle} \frac{\rho_\ell}{\rho_g} = 0.63 \left\{ \frac{v_{s\ell D}^{2}}{gD_D} \right\}^{0.4} \left\{ \frac{x}{1-x} \frac{\rho_\ell}{\rho_g} \right\}^{0.2}$$

and

$$\frac{\langle\alpha\rangle}{1-\langle\alpha\rangle} = 0.63 \left\{ \frac{v_{s\ell D}^{2}}{gD_D} \right\}^{0.4} \left\{ \frac{v_{sgD}}{v_{s\ell D}} \right\}^{-0.8} \qquad (2\text{-}22)$$

It is clear form equation (2-22) that also

$$\langle\alpha\rangle \neq \langle\alpha\rangle (p), \; (v_{s\ell D} = \text{const}, \;\; v_{sgD} = \text{const}) \qquad (2\text{-}23)$$

This leads to the conclusion that according to Petrick's correlation the slip ratio and void fraction are both constant for constant flow rates regardless of the pressure. This is not acceptable on physical grounds and not in agreement with the experimental data.
It is not possible therefore to give a general correlation of the data taking into account the pressure effect according to the expression used in equation (2-19).
Moreover the downcomer slip ratio's show such scatter no independent analysis can be based on these data only. The difference for both pressures for the riser slip is much more outspoken and must serve as an indication for the trends and effects for downflow.

2.1.5. Conclusions.

Carry-under experiments are presented, giving downcomer quality and void fraction as a function of interface level, riser steam and water flow rates, riser to downcomer area ratio at system pressures of 50 of 70 bar.
Based on the experimental results a physical interpretation of the various effects is formulated.
Within the range of variables tested the effect of level is weak, except when interacting with the level control as described in section 2.1.4.3.

As expected the downcomer water velocity turned out to constitute the main influence on carry-under. All experiments showed a threshold for the superficial downcomer water velocity which varied between 0.22 to 0.28 m/s. The results obtained with the necked down riser give lower carry-under rates than for the straight riser.

The downcomer void fraction shows a maximum for constant riser steam flow and increasing water flow for some experiments with the necked down riser.

The effect of steam flow rate is small. In accordance with PETRICK's [20] findings a minimum in the carry-under with increasing steam flow was found.

Although carry-under was somewhat lower at 50 than at 70 bar the effect was not sufficiently marked to suggest a definite influence of pressure at these two levels.

Slip ratio's for riser and downcomer are shown. While the riser data could be correlated by a simple expression the downcomer slip ratio's are subject to considerable scatter due to experimental inaccuracy and "false carry-under". This last phenomenon, a considerable downcomer quality where the void fraction measurements indicated no net carry-under, is attributed to the relatively high position of the quench water sparger and the small experimental scale.

2.2. Separation by centrifugal force.

2.2.1. Range of process parameters.

The choice of separator type, i.e. the venturi upcomer cyclone, has already been elucidated in chapter 1. It was also made clear that the investigation on separation by centrifugal force was intended to be of a preliminary nature. This explains why only air-water experiments were performed, the results of which are not directly applicable to reactor conditions, even though there are indications from the work performed at AEG [48] on downcomer cyclones that overall separator efficiencies can be extrapolated on a basis of volumetric flow rates. However, the aim of the experiments was not this kind of extrapolation but rather to provide an insight into the two-phase flow phenomena underlying the separator behaviour, which have to be understood prior to designing separator performance tests. Small scale atmospheric experiments are better suited for this purpose.
From earlier experiments [64], [65] it had become clear that three distinct regions can be discerned in the upcomer cyclone, each with its own specific function and associated problems. With reference to figure 1-6 the first region consists of the separator inlet where the guide vanes are located. There the rotation is imparted to the mixture. The stronger the mixture rotation the larger are the forces that move the steam to the center. On the other hand the higher velocities in the guide vanes result in higher friction losses and a reduction of bubble diameter through increased bubble breakup with respect to coalescence. These very small bubbles have an adverse effect on separation performance and optimal design of the guide vanes with regard to both friction losses and bubble diameter is to be sought.
In the second region, indicated as the vortex tube, the separation proper takes place. It is a tube of constant or varying circular cross section. The rotating mixture flows upward while the gas phase migrates to the center of the tube, forming a gas core. If separation is complete an annular rotating flow regime is established with a water layer free of bubbles. The length of tube needed to reach this point is of course determined by the rotation and the forces resisting the radial movement of the gas phase. This separating length is an important parameter for the reactor designer as it is directly reflected in the vessel height. Whereas the vane design has very little influence on the dimensions of the first region it is of great importance to the separating length.
The third region is the outlet section of the separator, where the vortex finder for the gas core is located to remove the separated gas phase and where the liquid phase leaves the separator. Proper design of the outlet

section to avoid re-entrainment of the phases, carry-over of liquid and carry-under of gas, is probably the most complicated problem.

Because the flow phenomena in this section are the least understood an empirical solution to the re-entrainment problem seems the only solution at present.

The second of the three regions, the vortex tube is the main subject of the present work, where the air-water experiment should furnish the means to test a theoretical approach to the separation process. Nevertheless overall efficiencies have been obtained from the test separators and will be shown.

The number of relevant variables, is much larger than in the case of gravity separation as a result of the more complex geometry of the test separator. The range of variables pertaining to BWR core requirements were presented in chapter 1 with special reference to figure 1-8. Based on equal velocities the air-water experiments should be carried out with water velocities (related to the vortex tube inlet cross section) varying from 2 to 3 m/s, whereas the air velocity should be varied from 3 to 7 m/s. These air velocities could not be obtained during the tests due to severe re-entrainment. The highest air velocity that could be run was 1.4 m/s. Translated to the example of chapter 1 (the Browns Ferry Plant) this means running the reactor at 44% power and 2.2% core exit quality.

The submersion of the separator or level above the separator outlet is a further variable that may have an influence on separator behaviour.

This parameter was not varied however because it mainly affects the static pressure in the water outlet path and is of importance for the outlet section but has no basic influence on the separation process in the vortex tube.

All the geometrical parameters are laid down in the design of the two venturi separators tested and described in the next section. The difference between the two is in the length of the convergent vortex tube.

As a consequence the throat length as well as the throat diameter is different and the vortex finder had to be adapted. In conclusion table 2-4 gives the range of variables.

TABLE 2-4.

	separator 1	separator 2
superficial water velocity at inlet vortex tube	2-3	2-3 m/s
superficial air velocity at inlet vortex tube	0.3-1.4	0.3-0.9 m/s
vortex tube length	0.295	0.530 m
vortex tube diameter at inlet	0.100	0.100 m
angle of convergence	$5^{\circ}58'$	$5^{\circ}58'$

2.2.2. Description of test separators.

The test separators consist of a cylindrical inlet section of 0.1 m I.D, a convergent vortex tube and an outlet section with vortex finder and diffuser with an outlet diameter of 0.1 m I.D. as shown in figure 2-28.

The swirl generator is made of brass and has 8 blades formed from flat plate, with an inlet angle of zero degrees with the vertical and an outlet angle of 45 degrees, measured at the separator wall.

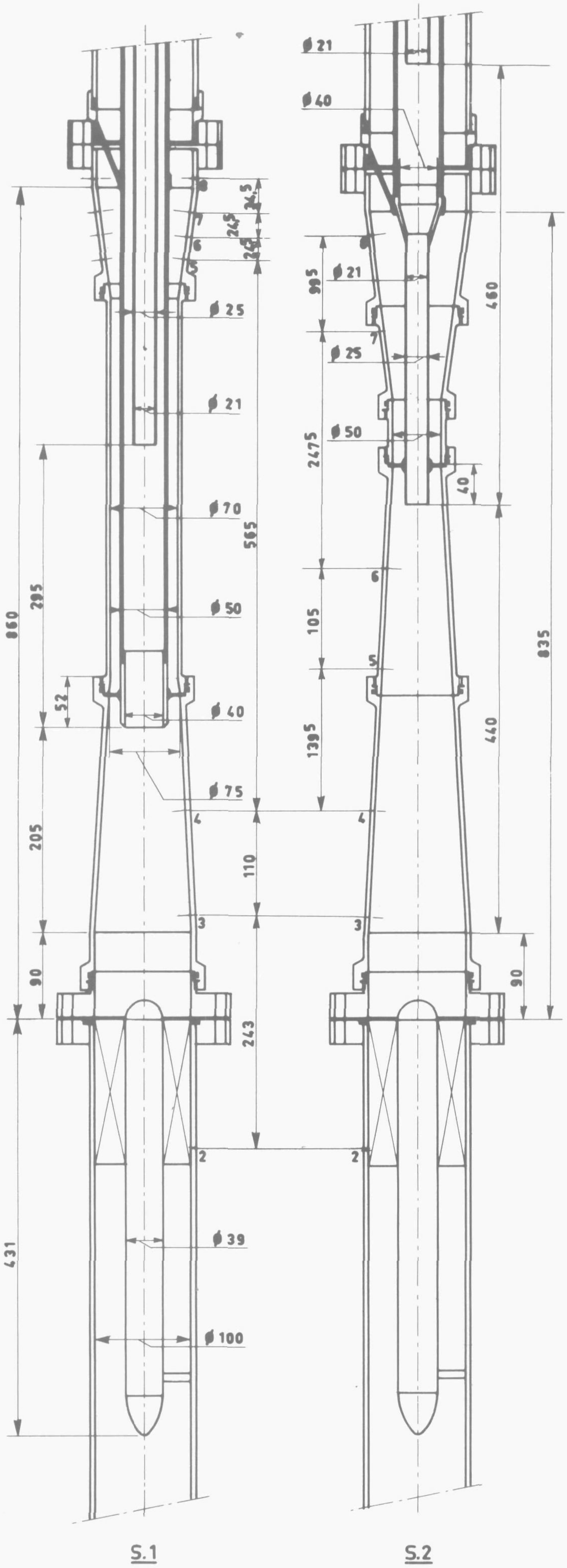

FIGURE 2-28.

Test separators S1 and S2.

Earlier experiments [65] with separators with a cylindrical vortex tube and 4-bladed swirl generators of 45 degrees outlet angle had shown an appreciable reduction of pressure loss over the same type with outlet angles of 60 and 75 degrees.
The objective of the convergent vortex tube being the "bladeless" augmentation of the rotation, the 45 degree outlet angle was chosen here.
A development of the blades at the wall and at the central hub, to which they are soldered, is given in figure 2-29 (see page 58).
The venturi itself - convergent vortex tube, divergent outlet section and throat - is composed of sections screwed together to make up different configurations with the same parts. Pressure tappings are provided at several locations as shown in figure 2-28.
The vortex finder is extending through the throat for reasons explained later. Its diameter was chosen on the basis of visual observations of the gas core.
A second tube was placed inside the vortex finder after initial runs to reduce the heavy carry-over that occurred.

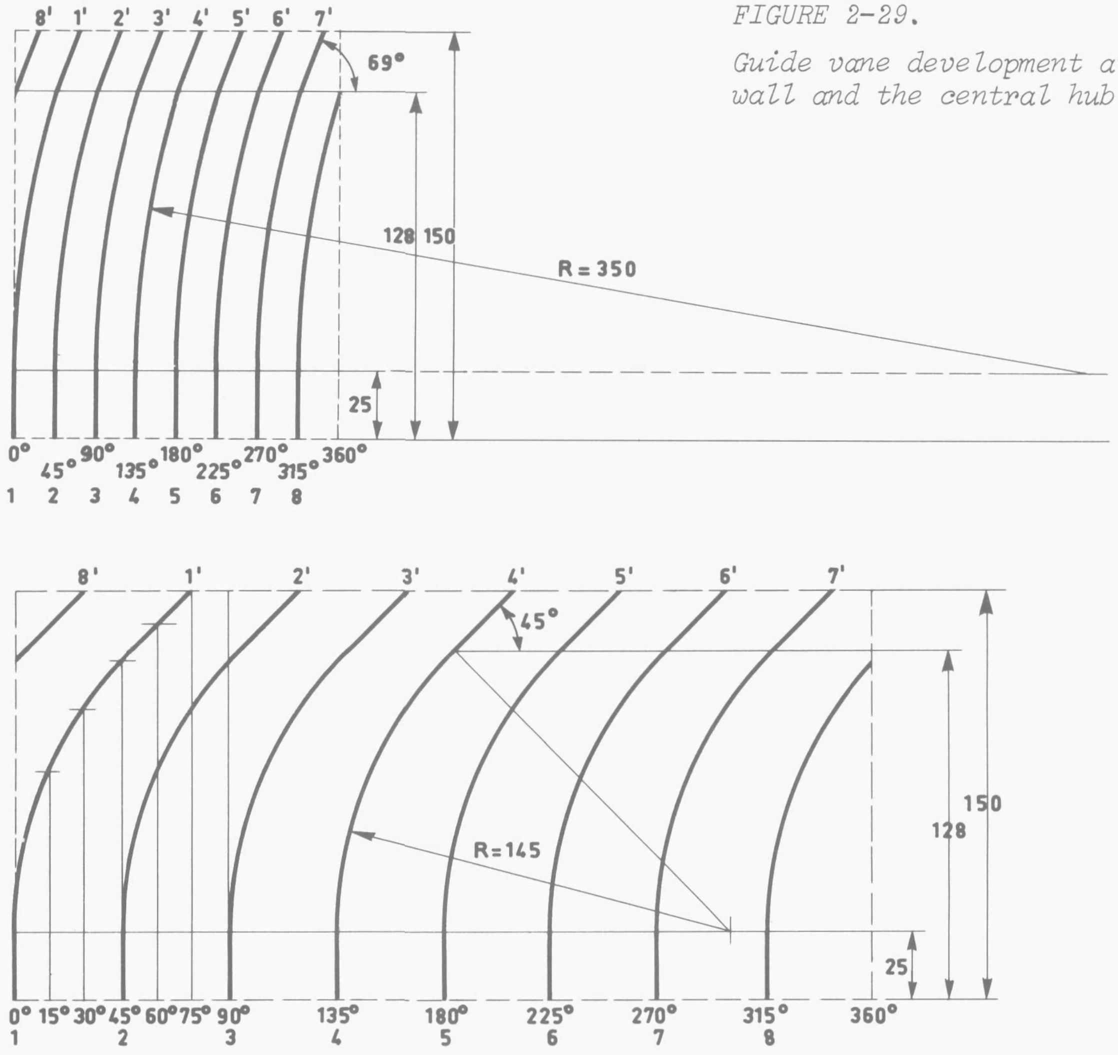

FIGURE 2-29.

Guide vane development at the wall and the central hub.

The flow pattern in the vortex finder was a swirling annular flow and the purpose of the second tube is to remove the gas core and let the water pass between this tube and the vortex finder, thus acting as a second vortex finder.

2.2.3. Description of test facility.

2.2.3.1. Flow sheet.

The atmosferic air-water test facility is shown schematically in figure 2-30. Air and water are mixed in an annular mixer (1). The air is evenly distributed over the annulus by means of a restriction of porous material before entering the flow channel through holes in the wall.
Above the mixer a flow straightener is situated. The mixture flows upwards through a 0.1 m ID calming section of 2.63 m and enters the swirl generator (3). After passing through the test separator the water flows into a tank (4) with a free surface and on into a downcomer to the settling tank (5).
A shield (6) is provided to prevent the air carried under by the water to escape to the free surface so that it is entrained to the settling tank.
In this (1 m diameter 1.5 m long) tank the water velocity is reduced to a very low value and the air rises and collects at the top where it enters a measuring bell (7). The water is drawn from the tank and circulated back to the mixer by a Delta centrifugal pump (8) capable of delivering 40 kg/s at 23 m head.

Water and air flowing in the annulus between the inner and outer vortex finder are reversed in direction by a hood (12) and returned into the tank.

The air admitted to the mixer is drawn from a 30 bar (13) utility air supply system and reduced in pressure in two stages (14). The loop filled with tap water is held at constant temperature by continuous overflow (15) and supply. A traversing unit (16) for a γ-scource and detector is provided to make scans over the length of the separator.

All parts of the test facility in contact with water were made of corrosion-resistant materials. Clear perspex was used for the test separators, trovidur for the piping and stainless steel for the tanks. The pump has a bronze casing and impeller.

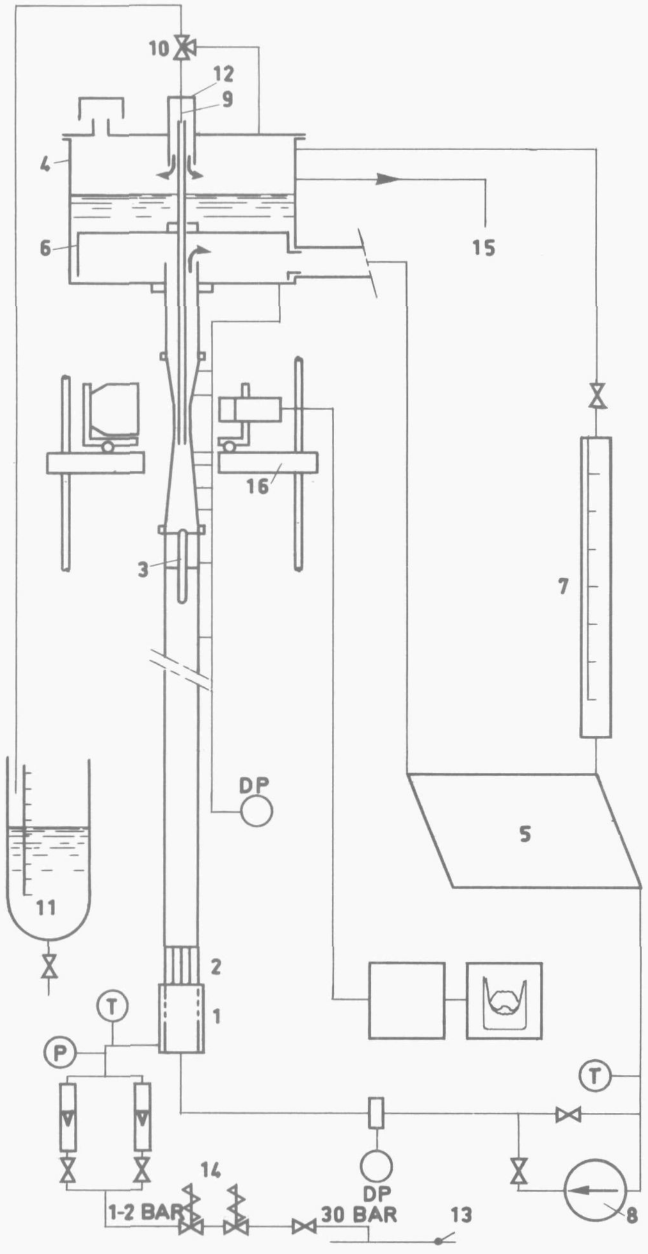

FIGURE 2-30.

Atmosferic air-water separator test facility.

2.2.3.2. Instrumentation.

2.2.3.2.1. Loopinstrumentation.

Details of the instrumentation indicated in the diagram of figure 2-31 are presented in the listing of Appendix 2-E.

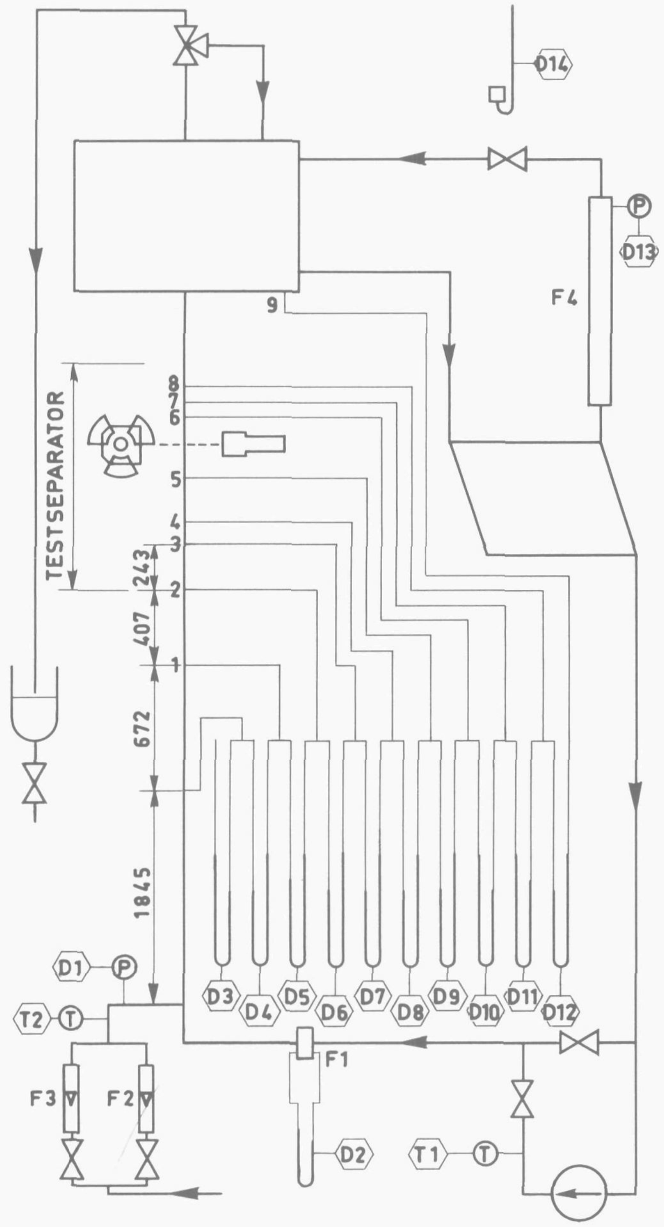

FIGURE 2-31.

Loop instrumentation for separator tests.

The venturi tube for the water flow rate was manufactured from brass according to the DIN standards [39] within the tolerances described therein and can be expected to give an accuracy of ± 1.9% in the calculated venturi coefficient. The rotameters for the air flow were calibrated by the manufacturer to an accuracy of ± 1%. U-tube manometers were filled with Merriam fluid. The error in the density is ± 2%. The error in the reading of the scale is ± 0.5 mm but due to increased fluctuations of the fluid at higher differential pressures the error is about ± 1% of the indicated value in the range used.

2.2.3.2.2. Void fraction measuring equipment.

Local void fractions are measured by a γ-ray attenuation technique. This method has become standard [73] in two-phase flow investigation due to the advantage of giving the most accurate results without introducing any obstructions in the flow channel. This in contrast to methods based on void fraction dependant electrical resistance [74], [70] or impedance of the mixture [36], [69], [71], using needle or plate electrodes. The same is true for other probe methods as hot-wire anemometry [75] and isokimetic sampling [76]. Calibration of these probes is sometimes a problem and often relies on the γ-ray method [46]. In view of the common use the technique will only be discussed briefly.

A collimated γ-beam is directed through the flowing mixture and a detector registers the reduced radiation intensity. The absorption of photons from the beam is a measure of the amount of material present in the beam and hence of the average density along the beam path.

By moving the source perpendicular to the test section axis, the average absorption along successive chords can be measured. To avoid inclusion of the effects of absorption in channel walls, or any material which is not part of the two-phase mixture, a scanning of the empty test section and filled with water is made before the scan with the flowing mixture. These extra scans constitute both a repeated calibration and a means to exclude the effect of absorption in foreign material.

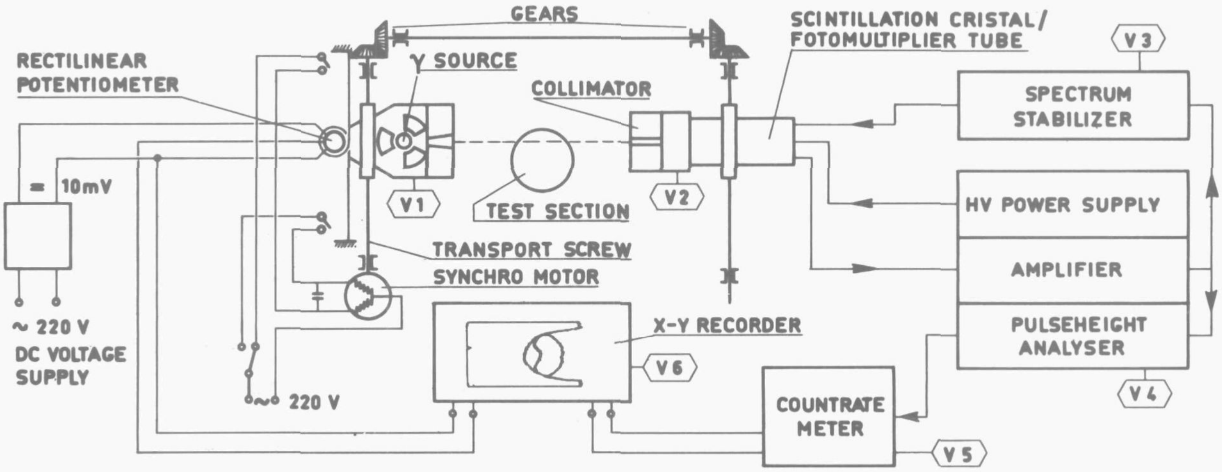

FIGURE 2-32.

System lay-out for traversing γ-ray void fraction measuring equipment.

As shown schematically in figure 2-30 and 2-32 the γ-source and detector are mounted on a traversing mechanism that can slide up and down along the test section to make scannings at any desired level over a range of 2 m. The source holder and detector are moved in a horizontal plane by a set of transport screws driven by an electric motor.

In addition to careful workmanship to remove all slack from the mechanism, the precaution was taken to make each traverse in the same direction to assure the same alignment every time. As shown in the diagram of figure 2-32 the scanning motion is stopped by end switches. A change in motion is effected by reversal of polarisation of the drive motor.

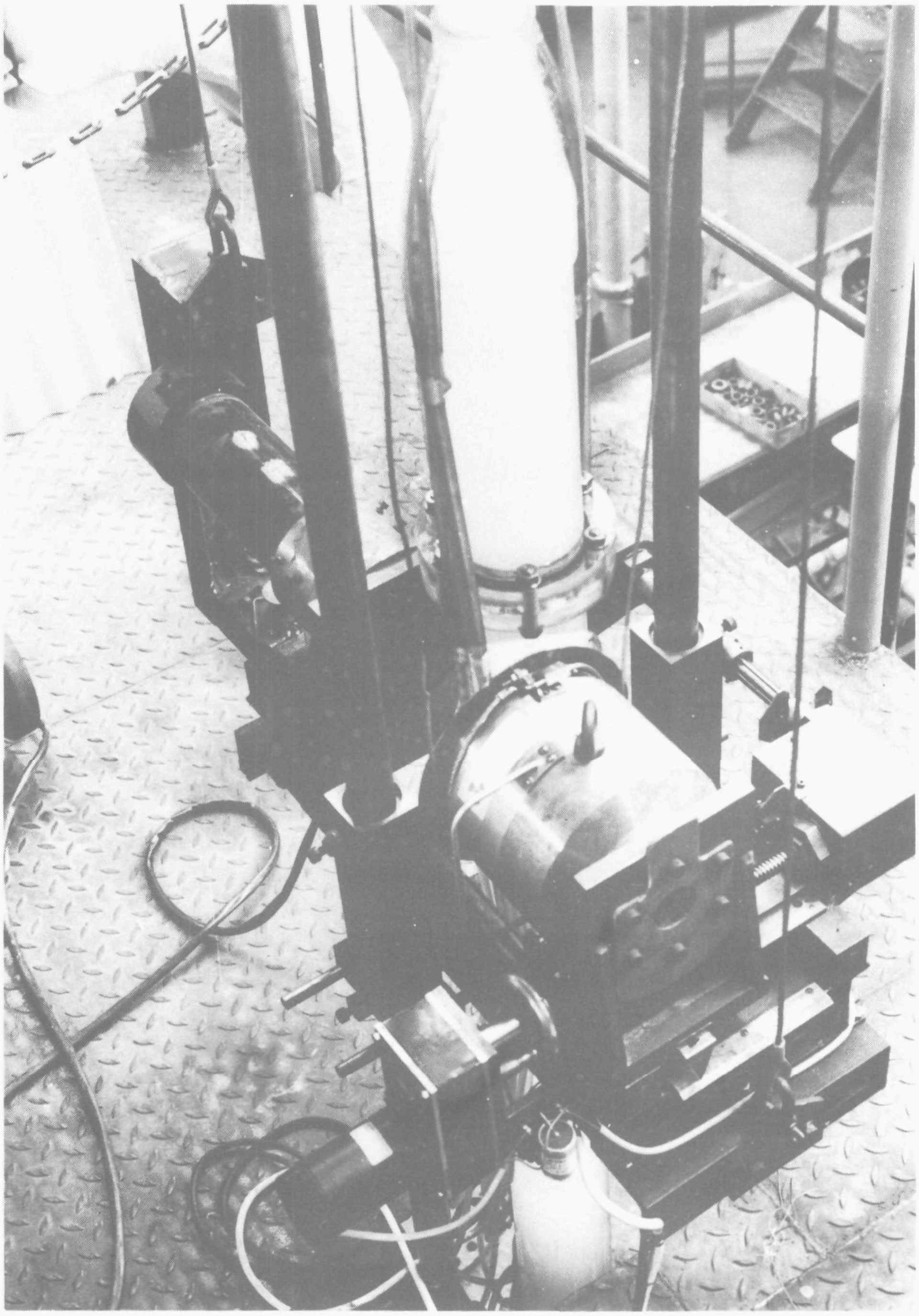

FIGURE 2-33.

View of γ-source and detector on traversing mechanism and test section.

A view of the source holder and detector mounted on the traversing mechanism is shown in figure 2-33. The source travel is measured by a potentiometer fed by 10 mV. An output voltage proportional to the distance traveled governs the motion of one coordinate of an x-y recorder.
For the γ-source a Cs^{137} isotope of 0.1 Curie strength is chosen. The energy of the photons is 0.66 MeV, which is too low for pair production (1.02 MeV threshold) when interacting with matter, leaving only Compton scatter and photo-effects to be considered.

Using a very narrow beam the detector will count only those photons that are not absorbed or scattered from the beam. This would greatly reduce the count rate and cause very long counting times. With more practical beam dimensions photons that are back-scattered into the beam are also detected but these have lost energy during interactions. Their energy spectrum would be depending on the geometry (read: void fraction) of the material outside the beam. In order to acheave an unequivocal measurement only dependent on the mean density of the chord the detector must discriminate between the photons of original and those of lower energy.

The equipment corresponding to these demands is shown schematically in figure 2-32. The detector is a scintillation counter consisting of a NaI-cristal and photomultiplier tube. A lead collimator with a window of 3 mm wide, 6 mm high and 80 mm long is fitted in front of the crystal, thereby reducing the back-scatter but not suppressing it.

A voltage of about 810 V is supplied to the multiplier tube. The measured pulses representing photons of various energy are amplified and fed into the pulse height analyser. All pulses below a discrimator level set at the lower side of the peak corresponding to photons of original energy are cut off and only pulses over a narrow span containing the peak are counted in the count rate meter.

Fluctuations in photomultiplier or amplifier gain might shift the pulse spectrum along the pulse height scale resulting in the counting of pulses from scattered photons. To eliminate these effects a spectrum stabilizer is incorporated in the system. A characteristic line or peak in chosen from the spectrum at the amplifier output and the location on the pulse height scale is monitored. If the peak shifts an output voltage proportional to the shift is fed back to the photomultiplier tube, counteracting the effects that initiated the shift.

The output voltage from the count rate meter which is now solely dependent upon the source strength, the distance between the source and detector and the absorption along the beam is recorded on the x-y recorder, together with the motion of the traversing mechanism. The result is a recording of mean chord density as a function of the test section radius.

A typical example is reproduced in figure 2-34 (see page 64) showing the "full", "empty" and "mixture" scans. To minimize the statistical error in the amount of photons produced by the source a strong scource is recommendable. There is a limit of about 2×10^4 cps to the count rate, set by the detector. For the configuration described above the 0.1 Curie source gives a maximum count rate of 1.76×10^4.

Further details concerning the instrumentation for the void fraction measurement is given in Appendix 2-E where the numbers correspond with those given in figure 2-32.

2.2.3.2.3. Data acquisition.

Instrument readings were taken by hand and punched on cards as input for the data reduction program written in ALGOL for the IBM 360/65 computer. An exception is constituted by the void measurements. The measured radiation intensities for 41 chords have to be measured from the traces of the three scans made at each location. In figure 2-34 these three lengths I_g, I_ℓ and I_m, that are proportional to the radiation intensities of the air only, water only and mixture scans respectively, are indicated for one of the 41 chords. To expediate the tedious work of the multiple measurements the following semi-automatic system to convert the readings to punched tape was devised [72]. The same x-y recorder is used together with two adjustable voltage supply units to move the pen along the previously recorded trace. The voltage applied to the γ-intensity coordinate is registered by the Solartron data acquisition system described in section 2.1.2.2.3.

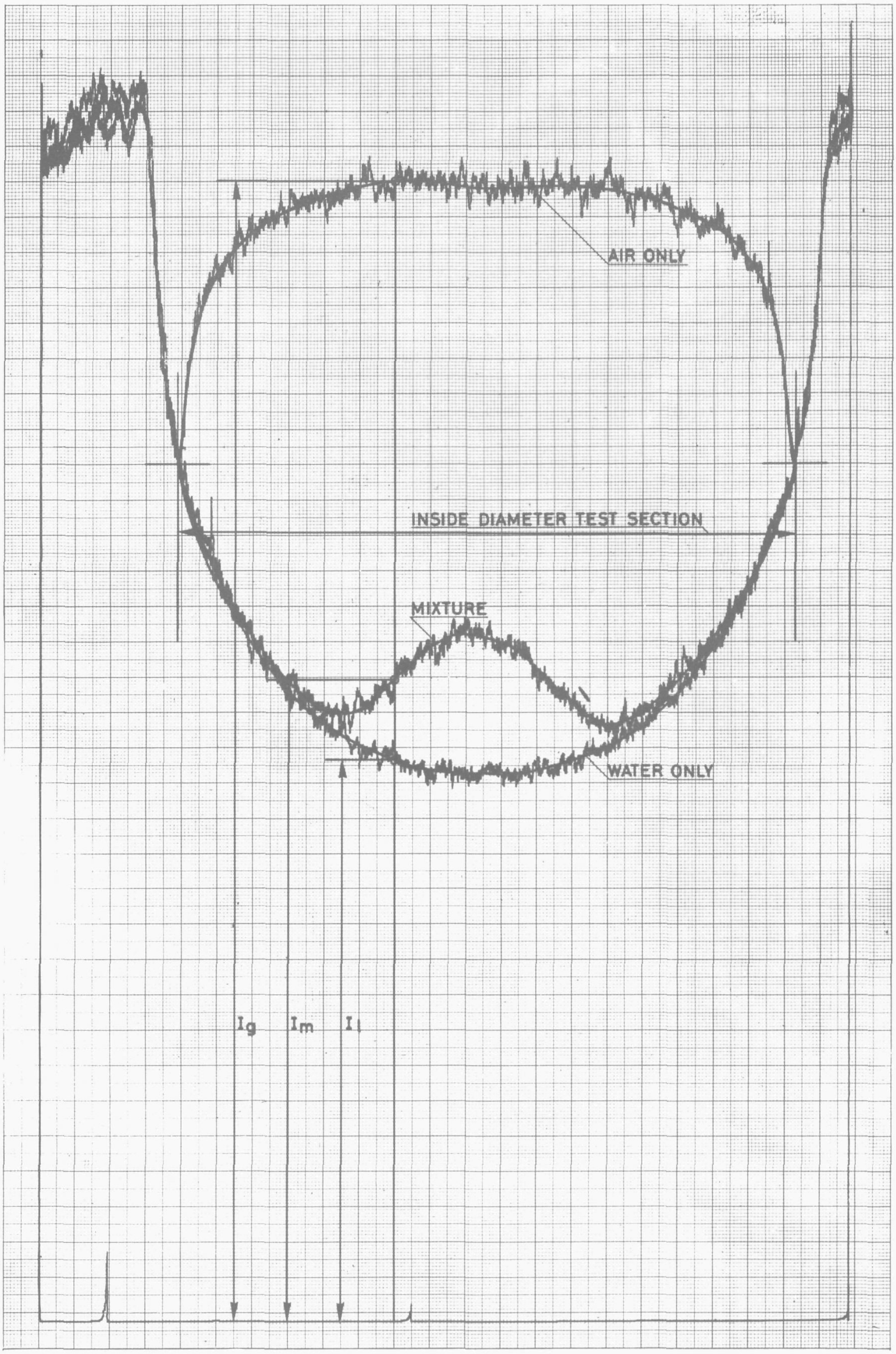

FIGURE 2-34.

Typical recording of mean chord density showing "empty", "full" and "mixture" scans.

The pen is successively placed over the appropriate places and the voltage punched on tape. The tape is later converted to cards to be added to the other data cards for computer input.

2.2.4. Experimentation.

2.2.4.1. Data reduction.

2.2.4.1.1. Flow and pressure measurement.

The standard DIN formula [39] is used for calculation of the water flow rate from the venturi pressure loss measurements. The error in the flow due to the errors in the venturi coefficient, the manometer fluid density and the manometer reading becomes

$$\sqrt{1.9^2 + \tfrac{1}{4} \times 2^2 + \tfrac{1}{4} \times 0.5^2} = \pm\ 2.2\%$$

The air flow rate measured with the rotameters is corrected for the amount of water vapor which is taken up by the dry air when mixed with the water. The absolute pressure in the test section upstream of the vanes at pressure tap 1 is taken as reference pressure. Pressure tap locations are indicated in figure 2-31. The air in the rotameter has a relative humidity of 5% and if ϕ_{mgr} is the mass flow measured, the amount of dry air is $\phi_{mgr}/1.0002$ *). The mass flow of saturated wet air in the test section is

$$\phi_{mgts} = (1 + \zeta)\ \phi_{mgr}/1.0002 \qquad (2\text{-}24)$$

where ζ, the relative humidity at saturation, is given by BAEHR [32]

$$\zeta = 0.6220\ \frac{p_{sat}}{p_{ts} - p_{sat}} \qquad (2\text{-}25)$$

The saturation pressure of the water vapor is taken at test section temperature and found in steam tables [32], [33].
The volumetric air flow rate at test section reference pressure is found by dividing ϕ_{mgts} by the density of wet air as given by BAEHR **) [32]:

$$\rho_g = (348.3 \times p_{ts} - 131.6 \times p_{sat}) / T \qquad (2\text{-}26)$$

The calibration of the rotameter is given by the manufacturer for a calibration gas at standard conditions. Pressure and temperature measurements at the rotameter locations are needed to obtain the flow rate. The error due to these corrections is ± 1%. The error in scale reading is mostly due to pulsations originating from the mixer and is of the order of ± 2%. The error in the mass flow rate resulting from these effects and from the calibration accuracy of ± 1% becomes

$$\sqrt{1^2 + 2^2 + 1^2} = \pm\ 2.5\%$$

The error in ζ is neglected because of the small effect of this correction.

---

*) *at 5% relative humidity the amount of water vapor is* 0.2×10^{-3} *kg/kg dry air.*

**) *see also equation (3-46); pressures: in equation (2-26) in bars.*

The error in the volumetric flow rate is dependent on the density of the air in the test section, which is dependent on the error in T and p_{ts}, as follows from equation (2-26). The overall error in p_{ts} is dependent on the absolute errors in the barometer reading and the manometer readings of D3 and D4, but the approximate value is $\pm$ 0.3%. The error in the gas density is

$$\sqrt{0.3^2 + 0.1^2} = \pm 0.32\%$$

The resulting error in the volumetric flow rate becomes $\sqrt{2.5^2 + 0.32^2} =$ $= 2.5\%$

The carry-over and carry-under flow rates are determined by the rate of change of the level in the measuring tank and bell respectively. The accuracy of the time measurement for the carry-under flow rate is strongly dependent on the flow rate itself and the surface oscillations in the bell. The accuracy of the time measurement varies between 0.5 and 10% for the lowest and highest carry-under flow rates measured. The carry-under flow rate is converted to the test section reference pressure and the overall error due to errors in bell dimensions, rate of fall of the level, pressure in the measuring bell and the test section pressure respectively is

$$\sqrt{2^2 + 0.5^2 + 2^2 + 0.34^2} = \pm 3.0\%$$

at the lowest and

$$\sqrt{2^2 + 10^2 + 2^2 + 0.34^2} = \pm 10.4\%$$

at the highest flow rate.

The carry-over flow rate accuracy is determined by the error in the tank dimensions and the time of rise measurement, hence the error is

$$\sqrt{2^2 + 1^2} = 2.2\% .$$

The pressures at the various locations are found by adding the differential pressures. The error for each interval is composed of an uncertainty in the fluid density of 2% and an error in the scale reading, giving

$$\sqrt{2^2 + 1^2} = 2.2\%$$

The absolute error for the average reading of 400 mm is 8,8 mm or 0.0176 bar. The accumulated effect for pressure tap 9 is

$$\sqrt{9} \times 0.0176 = 0.0528 \text{ bar},$$

to which the error in the absolute pressure at tap 0 has to be added of about 0.0051 bar:

$$\sqrt{0.0051^2 + 0.0528^2} = 0.053 \text{ bar}.$$

2.2.4.1.2. Void fraction measurements.

As stated in section 2.2.3.2.2. γ-ray attenuation techniques have become standard in two-phase flow investigation. A review of the method is given by SCHROCK [73]. It is usual to assume that the linear absorption coefficient for γ-photons passing through a two-phase mixture can be written, in analogy to the mixture density, as

$$\mu_m = \alpha\mu_g + (1-\alpha)\,\mu_\ell \qquad (2\text{-}27)$$

The attenuation law for the radiation reads

$$\frac{I_x}{I_o} = e^{-\mu x} \qquad (2\text{-}28)$$

where μx is the additive result of the absorption coefficients and absorber thicknesses placed in the beam while x is the total thickness. Substition of the corresponding expressions for μx in equation (2-28) for a "full", "empty" and "mixture" scan results in a relation for the void fraction

$$\langle\alpha\rangle = \frac{\ell n \dfrac{I_m}{I_\ell}}{\ell n \dfrac{I_g}{I_\ell}} \qquad (2\text{-}29)$$

where I_m, I_ℓ and I_g are proportional to the lengths indicated in figure 2-34. The void fraction according to equation (2-29) is the average value along a chord. However, the experimental results must be converted to radial void distributions. Before this can be done it is necessary to know the general form of this relationship. Various distributions are assumed in the literature [83]. In the present case the distribution function is not known a priori and a polynomial approximation is chosen. The general form is

$$\alpha(r) = c_o + c_2 r^2 + c_4 r^4 + \ldots c_{2n} r^{2n} \qquad (2\text{-}30)$$

where 2n may be as high as 16 to include all possible profile shapes. On grounds of axial symmetry only even powers are admitted and the term proportional to r is also left out to make the profile continuously differentiable at the center line. The mean value of $\langle\alpha\rangle$ along chord k is found from integration of equation (2-30) and division by the chord length L_k

$$\frac{1}{L_k}\int_k \alpha(r)dk = \int_k \frac{c_o}{L_k}dk + \int_k \frac{c_2}{L_k} r^2 dk + \ldots + \int_k \frac{c_{2n}}{L_k} r^{2n} dk \qquad (2\text{-}31)$$

or

$$\langle\alpha\rangle_k = c_o a_{ko} + c_2 a_{k1} + \ldots + c_{2n} a_{kn} \qquad (2\text{-}32)$$

where

$$a_{ki} = \frac{1}{L_k}\int_k r^i dk \qquad (2\text{-}33)$$

The value of the coefficients c_i can be found by the method of the least squares if the void fraction is measured over a sufficient number of chords. The deviation between $\langle\alpha\rangle_k$ and the measured values $\langle\alpha_m\rangle_k$ is

$$\delta_k = \langle\alpha_m\rangle_k - \langle\alpha\rangle_k \qquad (2\text{-}34)$$

The best fit of the polynominal to the void profile is found for a minimum of $\sum_1^N \delta_k^2$, where N is the number of chords, involved in the calculation.

A minimalization scheme for this purpose was devised [78] based on the measured void fractions over 41 chords ★). After calculation of the coefficients for the 8 possible polynomials the optimal degree is chosen by comparing the standard deviations

$$\sqrt{\frac{\sum_{1}^{41} \delta^2}{41-2n}} \qquad (2\text{-}35)$$

where 2n is the polynomial degree.

The relative error in the measured void fraction over the chords becomes larger the further it is removed from the channel axis. The void fraction at the channel wall should become zero but the test results showed a sharp increase in the calculated profile very close to the wall, which is attributed to these errors. The selection of the degree is based on the standard deviation. The boundary errors make a considerable contribution to the standard deviation and a polynomial of higher degree is selected than would be required by the true shape of void profile. An attempt was made to remedy this deficiency by weighting the error δ_k with α_k, thereby reducing the effect of the larger errors in the wall region. No appreciable improvement was obtained however.

It is difficult to indicate the scource of all the errors involved in the profiles obtained. If a single value has to be given to evaluate the reliability of the technique the standard deviation seems to be a good indication. It does not incorporate systematic errors of the attenuation measurement itself however, such as deviations from the assumptions underlying equation (2-29) and deviations from ideal collimation of the beam. Another error is introduced by differences in the air density at various test section pressures as compared to the atmosferic pressure of the air during an "empty" scan. The error caused by this latter effect is smaller than 0.75% [78].

Void measurements of perspex mock-ups of various shapes and distributions have been reported [73] to incorporate errors in the range of 5 to 10%. These errors may partly be caused by deviation from the assumption of equation (2-27).

Another source of errors is found in the accuracy of the computer, where the higher degree polynomials involve calculations with ill-conditioned matrices. Furthermore these matrices contain numbers in the order of 10^{10} The calculation of the polynomial coefficients c_o, c_1, etc. is based on adding and subtracting these numbers and absolute errors of 0.05 are involved in each operation if the computer operates with numbers of 12 digits, which is the case for the Telefunken TR-4 originally used. An impression of the errors resulting from these effects was obtained [78] in an attempt to fit a homogeneous void fraction distribution equal to 1 by various polynomials. The overall absolute error in the calculated void fraction was 0.003 for a 12th degree, 0.08 for a 14th degree and 0.12 for a 16th degree polynomial. The fitting of real void profiles will give increasingly better results for higher degrees up to the point where the computer accuracy is of the same order as the statistical variation in the measured values. This appeared to be the case for the 14th and 16th degree and the TR-4 discarded these polynomials. Sufficient improvement was found by changing to an IBM-360/65 computer, using numbers of 16 digits, to make the selection of the degree insensitive to these errors up to the 16th degree.

★) *The number of chords was chosen for easy adaptation to the graph paper division of the recorder and for obtaining sufficient statistical information.*

An estimation of the real error in the local void fractions obtained through the combination of measurement and curve fitting is difficult to make due to the lack of an absolute standard. In view of the precautions taken with regard to beam collimation it seems reasonable to assume an error in the measured mean chordal void fraction of about 5%. To this the local error of the polynomial fit must be added when looking at local void fractions. Integrated polynomial values along the chords showed a nearly constant average absolute error of 0.02 for all scans. This absolute error is smaller than the true local error as errors of opposite sign are partly cancelled out by the integration. This is demonstrated by a comparison of the cross sectional average void fraction obtained by integration of the polynomial and by direct summation of the measured chordal values. Agreement better than 1% was always found, justifying the assumption that for cross sectional average void fractions computational errors need not be taken into account. The absolute computational error in the local void fraction however is probably larger than the average chordal value of 0.02 but smaller than the maximum absolute chordal error of 0.07 (also found constant for all scans). Assuming 0.05 as absolute local computational error total average relative errors in local void fractions from 7% to 50% can be expected depending upon the void fraction.

2.2.4.2. Experimental procedure.

Separation efficiency and pressure loss measurements [77] were taken over the range of parameters given in section 2.2.1. For carry-over measurement the effluent from the central vortex finder was diverted to the collecting tank by means of a three way cock, where the water was allowed to accumulate for 50 seconds and the level rise was measured. The carry-under measurement was started by closing the valve on top of the measuring bell and clocking the time for the level to fall over a distance of 750 mm. Subsequently the pressure, flow and temperature readings were taken. The void fraction profile measurements were performed in separate runs for a limited number of test conditions. With regard to the requirements set forth in said section only the highest air flows are of interest. The test conditions chosen for this purpose are given below in Table 2-5.

TABLE 2-5

	separator 1			separator 2		
superficial water velocity at inlet m/s	2.0	2.5	3.0	2.0	2.5	3.0
superficial air velocity at inlet m/s	0.8	1.0	1.2	0.7	0.8	0.6

Four scans at various levels were made for each test condition for separator 1 and six for separator 2, which has a longer converging section. These locations coincide with the pressure tap locations 1, 3 and 4 and with 1, 3, 4, 5 and 6 respectively; the fourth and sixth scan were taken 1 cm below the vortex finder entrance. The three scans necessary at each location were performed in direct succession to avoid errors in readjustment of the traversing locations.

2.2.5. Results.

2.2.5.1. Separating efficiencies.

The efficiency of separators can be expressed in various ways. For dust or droplet cyclones it is usual to formulate a collection efficiency as the percentage of the particulate phase collected or separated. This efficiency is a good measure of cyclone performance where only the separating effect of one phase is regarded. The objective of steam-water separators is to obtain both phases in as pure a form as possible.

Furthermore the reactor designer specifies limits to the entrainment in the separated phases. This is usually done in terms of a maximum allowable quality in the downcomer, and a minimum allowable quality of the steam leaving the separator. It would be a logical step to formulate two separating efficiencies relating these qualities to the separator inlet quality. For the carry-under

$$\eta_D = 1 - \frac{x_D}{x_R} \qquad (2\text{-}36)$$

and for the carry-over

$$\eta_E = 1 - \frac{1-x_E}{1-x_R} \qquad (2\text{-}37)$$

For η_E the liquid qualities, (1-x), are considered instead of the steam qualities to obtain an efficiency of unity for the ideal case that pure steam, $x_E = 1$, is issued from the separator.

Direct comparison of air-water and steam-water separation results on the basis of these efficiencies becomes impossible on grounds of the large differences in gas density of the two systems. Requiring the quality based on mass flow rates of the air-water mixture at the separator inlet to be equal to that under reactor conditions would result in widely different volumetric qualities. Figure 2-35 gives the volumetric quality as a function of the quality for different density ratios. The quality region of interest for BWR's of 6 to 14% involves a range for β from about 57% to 77% respectively. The corresponding range for air-water mixtures lies in the interval between 98 and 99%. The important difference between these two volumetric quality ranges lies in the difference in flow pattern. Whereas the lower range would involve slug or froth slow depending on the mixture velocity the high values for the air-water mixture suggest mist flow. In other words where the steam was the disperse phase in the first case the liquid would be so in the second case, changing the nature of the interaction forces between phases that govern the separation process.

With regard to the flow patterns a comparison on a void fraction basis would be more justified, but the often unknown phase slip is a handicap and the volumetric quality must be regarded as second best.

The efficiencies now become

$$\eta_D = 1 - \frac{\beta_D}{\beta_R} \qquad (2\text{-}38)$$

and

$$\eta_E = 1 - \frac{1-\beta_E}{1-\beta_R} \qquad (2\text{-}39)$$

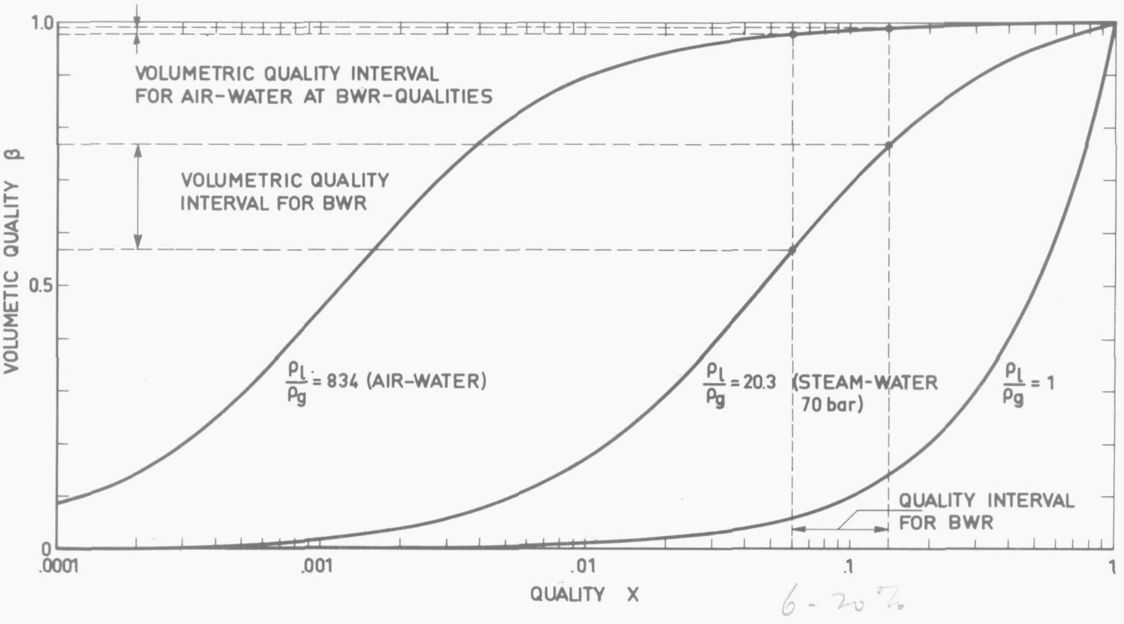

FIGURE 2-35.

Relation between qualities based on mass and volumetric flow rates.

These are in fact the same efficiencies as used by BOHNET [79] for the separation of liquid-liquid suspensions in hydrocyclones.
The disadvantage of having two criteria was overcome by VAN ROSSUM [80] and EBBENHORST TENGBERGEN [81] by defining a compound efficiency based on both the entraining and antrained flow rates leaving the separator.

$$\eta_c = \left| \frac{\phi_g - \phi_{cu}}{\phi_g} - \frac{\phi_{co}}{\phi_\ell} \right| = \left| \frac{\phi_{cu}}{\phi_g} - \frac{\phi_\ell - \phi_{co}}{\phi_\ell} \right| \qquad (2\text{-}40)$$

This formulation also excludes any density effect as both volumetric and mass flow rates will give the same result. The flow rates at either the water or steam exit of the separator may be taken.
Upon substitution of the qualities

$$x_R = \frac{\phi_{mg}}{\phi_{mg} + \phi_{m\ell}} \qquad (2\text{-}41)$$

$$x_D = \frac{\phi_{mcu}}{\phi_{mcu} + \phi_{m\ell} - \phi_{mco}} \qquad (2\text{-}42)$$

$$x_E = \frac{\phi_{mg} - \phi_{mcu}}{\phi_{mg} - \phi_{mcu} + \phi_{mco}} \qquad (2\text{-}43)$$

in equation (2-40) and rearranging the efficiency becomes

$$\eta_c = 1 - \frac{x_R}{x_E}\,\frac{(1 - x_E)}{(1 - x_R)} - \frac{x_D}{1 - x_D}\,\frac{\dfrac{1 - x_R}{x_R} - \dfrac{(1 - x_E)^2}{(1 - x_R)}\,\dfrac{x_R}{x_E{}^2}}{\dfrac{x_E - x_D}{x_E\,(1 - x_D)}} \qquad (2\text{-}44)$$

Substition of β for x in equation (2-44) makes no difference. For small values of $(1 - x_E)$ or $(1 - \beta_E)$ and x_D or β_D equation (2-44) may be approximated by

$$\eta_c = 1 - \frac{x_R\ (1 - x_E)}{x_E\ (1 - x_R)} - \frac{x_D\ (1 - x_R)}{x_R\ (1 - x_D)} \qquad (2\text{-}45)$$

The maximum allowable downcomer quality is often set at 0.2% and the minimum allowable steam quality at 90% [47], [55]. The corresponding minimum allowable efficiencies are given in figure 2-36 as a function of volumetric riser quality. The curves for η_D and η_E drop off to zero for riser qualities equal to the allowable β_D and β_E values respectively; under these hypothetical conditions the specifications require no separation at all for one of the phases, while the efficiency curve for the other phase tends to equal the allowable quality specification. The compound efficiency η_c is also shown and appears to be intermediate between η_E and η_D more or less following η_D for the lower riser qualities and η_E for the upper half of the scale. Closer agreement is found for the case one of the phases is separated completely. Using η_c as a criterion it must therefore be mentioned that it gives a "weighted measure" of the separator performance giving carry-under behavior more weight for low values of β_R and shifting it to carry-over retention at high β_R. Almost equal weight is given to both phenomena for the β_R interval of interest for BWR's.

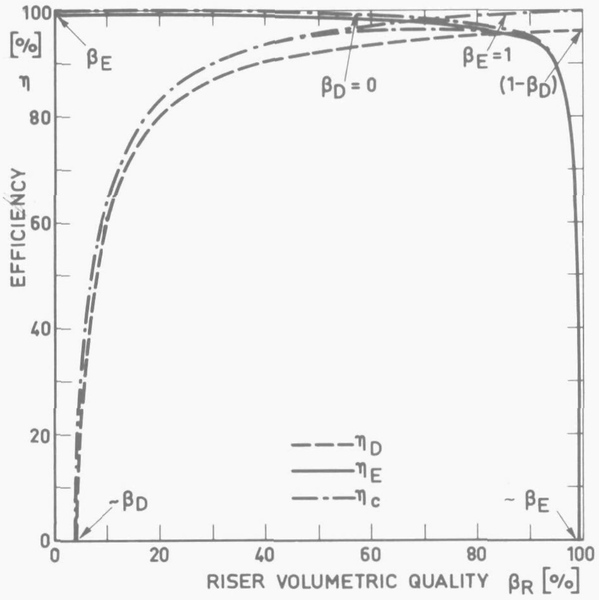

FIGURE 2-36.

Minimum allowable efficiencies.

The measured carry-under and carry-over data were plotted in terms of the above efficiencies. Figure 2-37 gives the results for separator 1 and figure 2-38 for separator 2. As already mentioned in section 2.2.1. the volumetric inlet quality could not be extended above 32% due to entrainment problems. Apart from that the efficiency pertaining to carry-over is too low for all tests compared with the minimum efficiency curves drawn in both figures for comparison. Carry-under performance meets the specifications, only for a limited inlet quality range for separator 1. Visual observations made it clear that reentrainment occurred at the entrance of the vortex finder. Separation in the vortex tube, indicated as region two, will be discussed later together with the results of the radial void profiles, and axial pressure distribution.

2.2.5.2. Axial pressure distribution and total pressure drop.

A number of differential pressures along the separator were measured, for which the pressure tap locations are indicated in figure 2-28. Tap 1 is located upstream of the guide vanes in the stand pipe and tap 2 at the inlet of the vanes. For separator 1 the converging section comprises taps 3

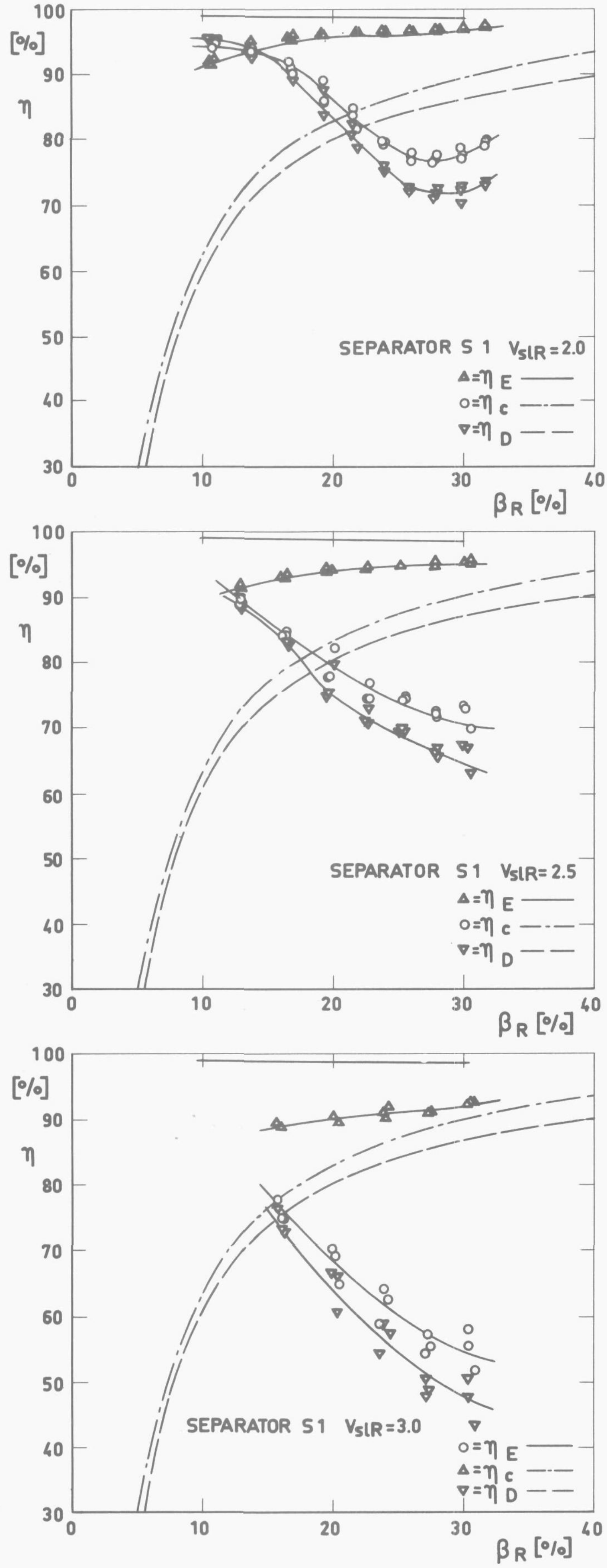

FIGURE 2-37.

Measured efficiencies for separator 1.

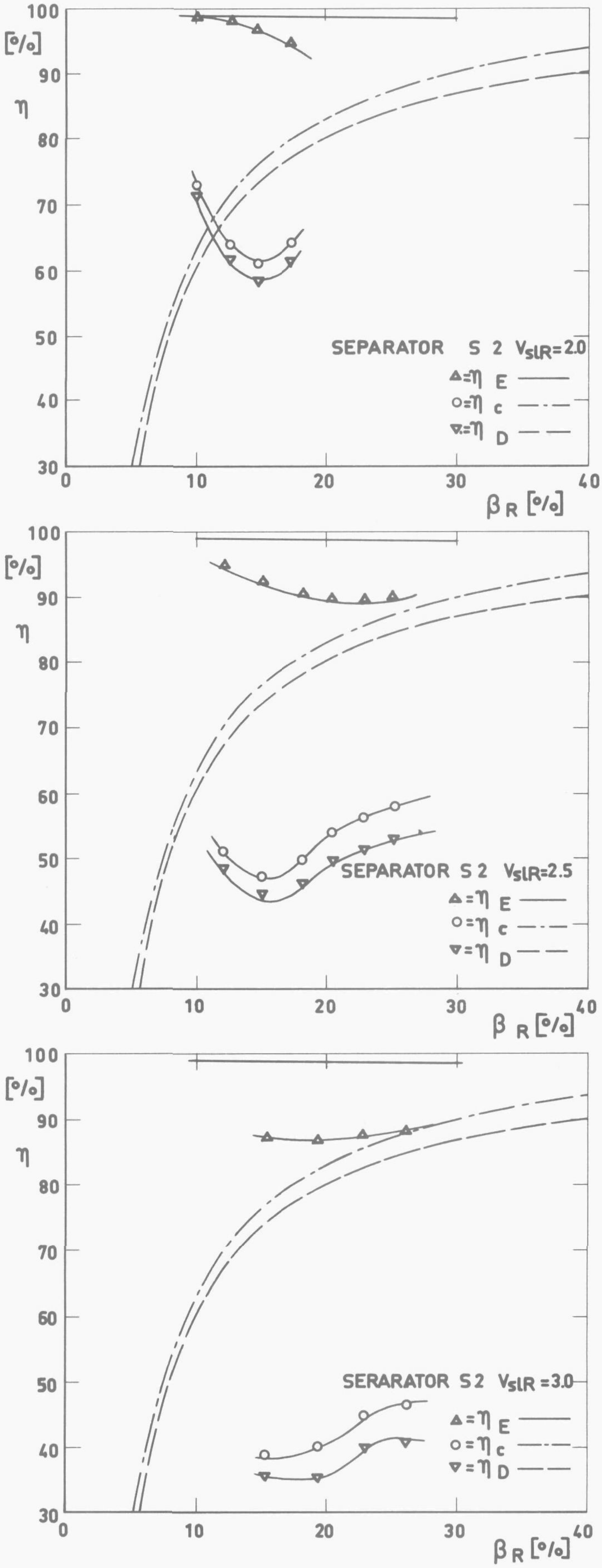

FIGURE 2-38.

Measured efficiencies for separator 2.

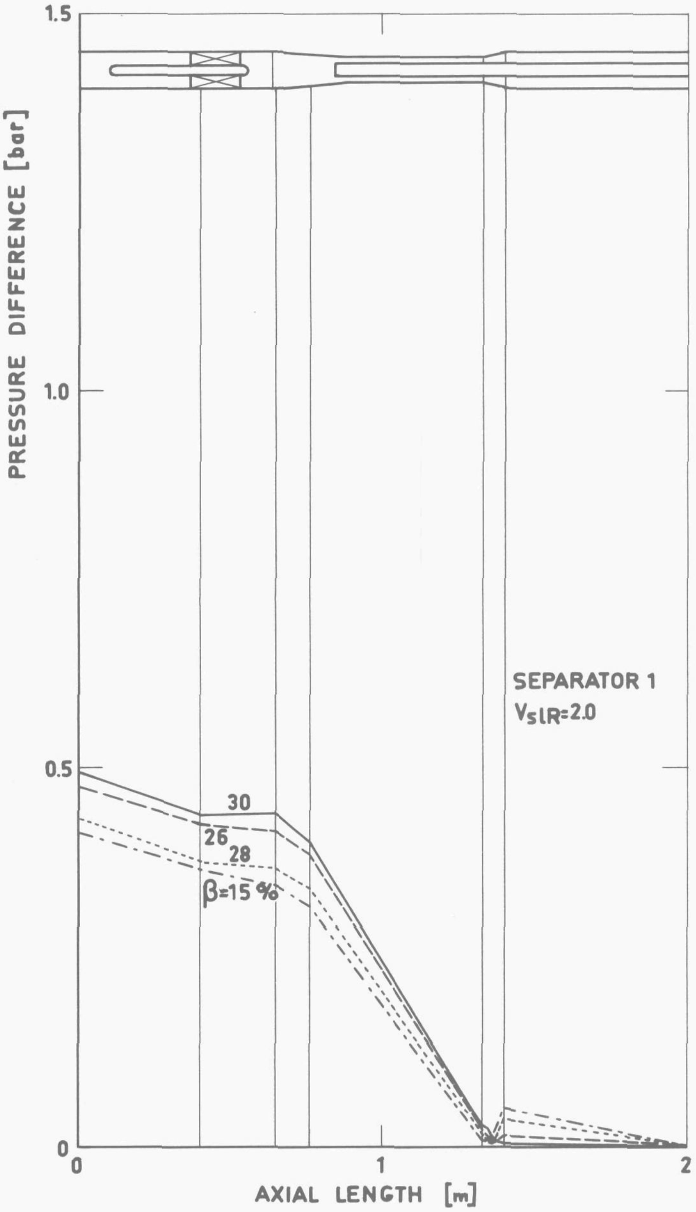

FIGURE 2-39.

Axial pressure distribution along separator 1 for $v_{s\ell R} = 2.0$ m/s.

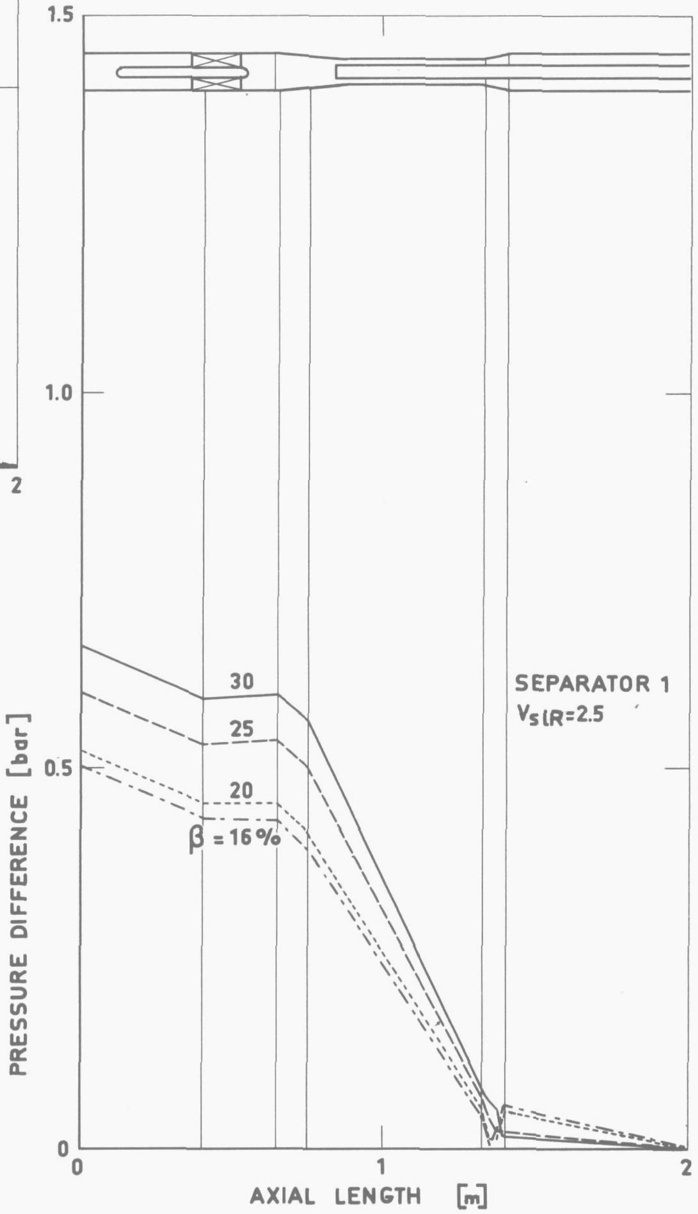

FIGURE 2-40.

Axial pressure distribution along separator 1 for $v_{s\ell R} = 2.5$ m/s.

and 4 while the longer converging section of separator 2 comprises taps 3, 4, 5 and 6. The rest of the taps up to number 8 is found in the diverging outlet section while tap 9 is located in the outlet tank where all rotational energy is dissipated.

The results were plotted as pressure differences with respect to tap 9. The axial wall pressure profile thus obtained incorporates friction, acceleration and static head differences as well as the effects of the increased wall pressure due to rotation. The distributions for separator 1 are given in figures 2-39, 2-40 and 2-41, those for separator 2 in figures 2-42, 2-43 and 2-44 (see page 76). A schematized pressure profile is drawn through the measured points.

Figures 39 through 2-44 suggest that any attempt to improve the separator pressure losses should be concentrated on the outlet section. This can not be done without looking at the pressure drop over the gas exhaust tube which is approximately equal to the pressure drop from tap 4 or 6 to 9 increased by the static head corresponding to the submergence of tap 9 under the free surface and equal to 0.04 bar. This loss is caused by two-phase friction in the gas exhaust and an improved pressure loss over the water outlet section must be accompanied by a reduced carry-over performance.

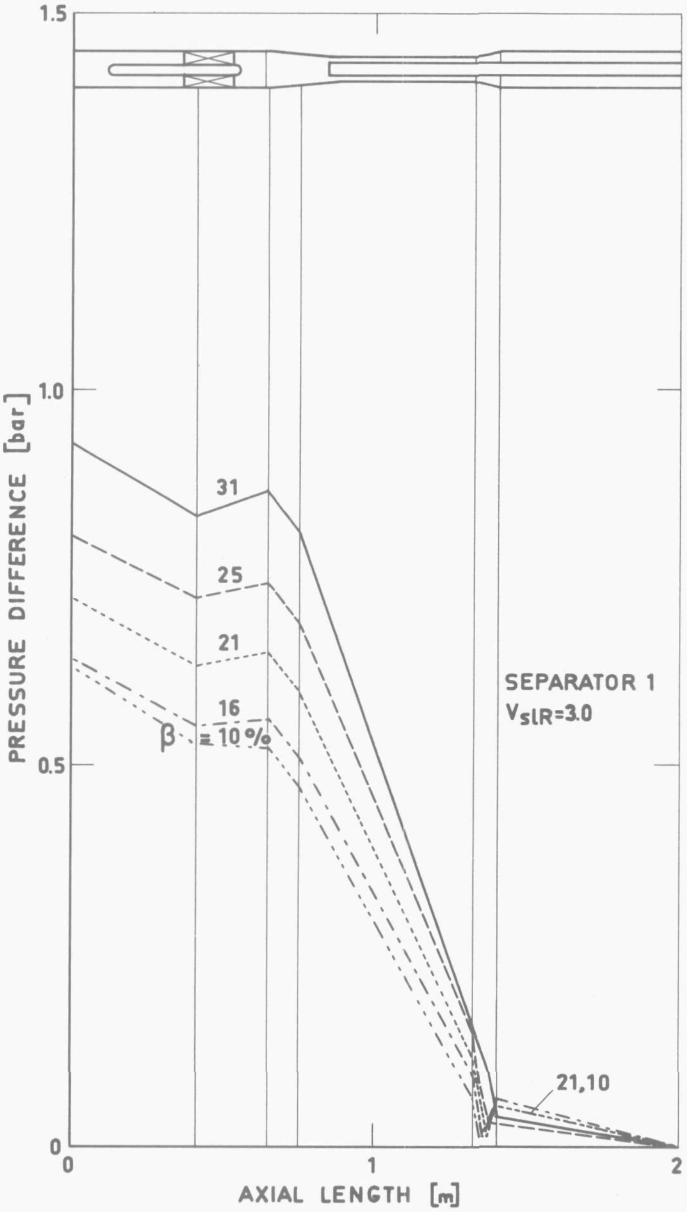

FIGURE 2-41.

Axial pressure distribution along separator 1 for $v_{s\ell R} = 3.0$ *m/s.*

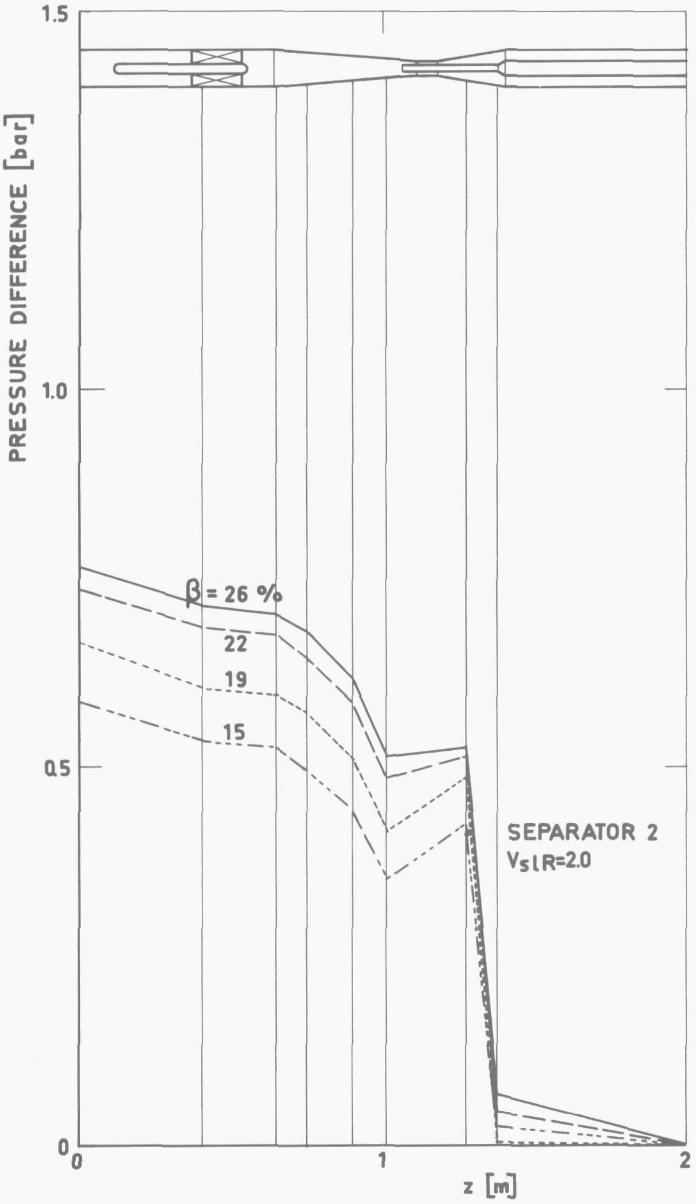

FIGURE 2-42.

Axial pressure distribution along separator 2 for $v_{s\ell R} = 2.0$ *m/s.*

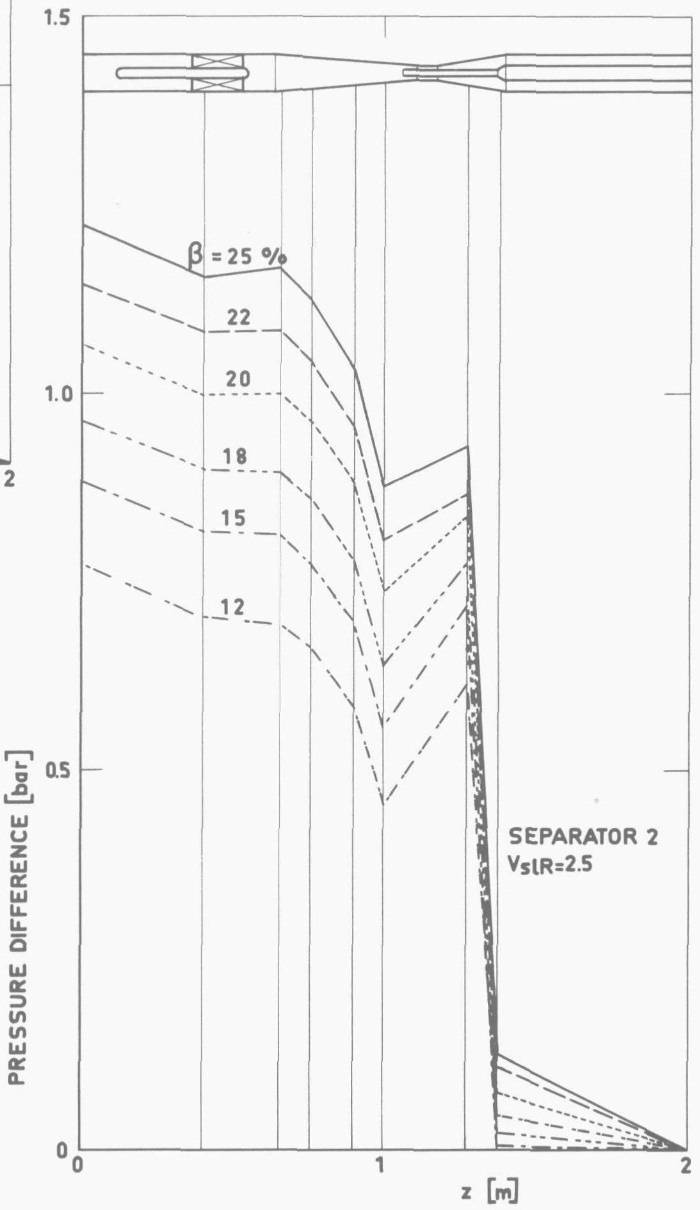

FIGURE 2-43.

Axial pressure distribution along separator 2 for $v_{s\ell R} = 2.5$ *m/s.*

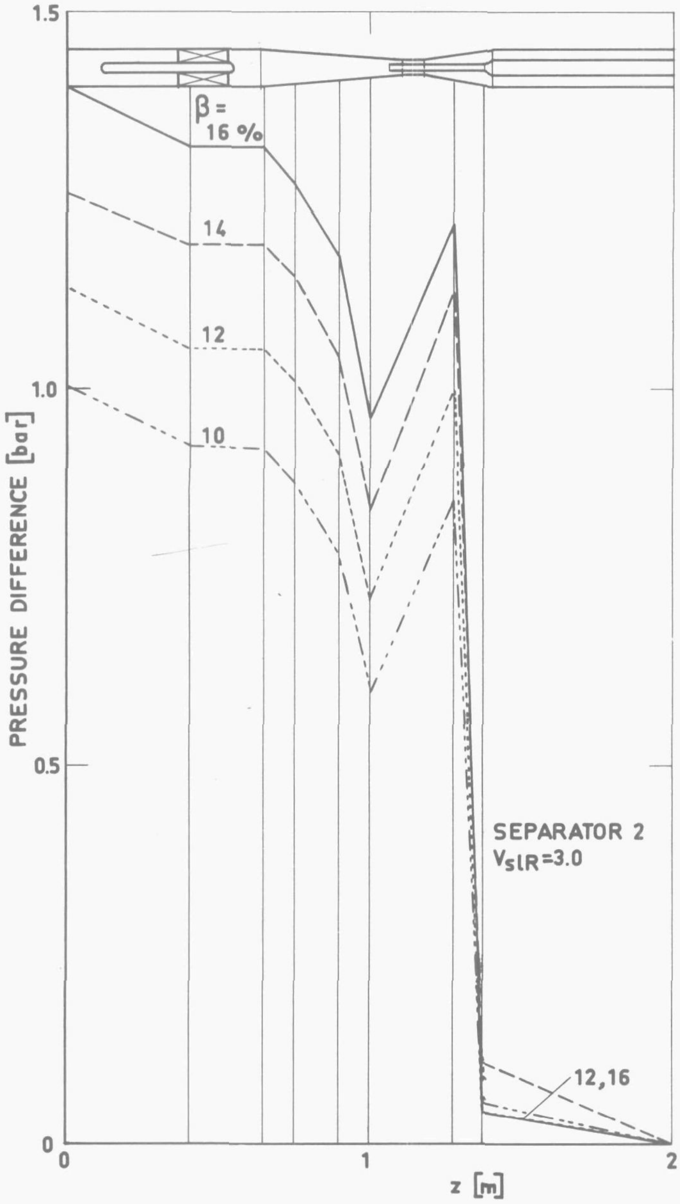

FIGURE 2-44.

Axial pressure distribution along separator 2 for $v_{s\ell R}$ = 3.0 m/s.

No specifications regarding allowable total separator pressure loss are found in literature. A possible means of judging the measured pressure loss is a comparison with those of other separators even if they have different geometries. AEG en GE give pressure losses from the mixing plenum above the reactore core to the steam space above the steam exit for the downcomer and the upcomer cyclone respectively. Values for the air-water and steam-water tests of AEG [48], [55] are given in figure 2-45 as a function of the specific separator vortex tube loading in t/m^{2}h mixture ★).

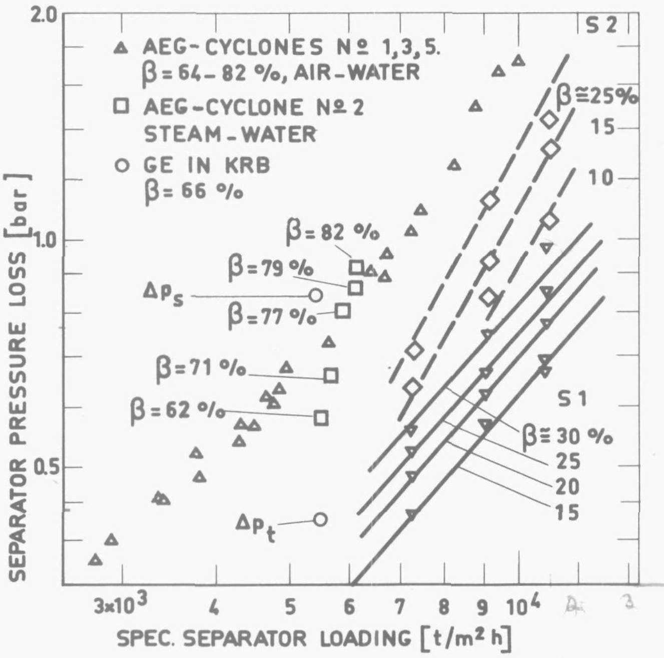

FIGURE 2-45.

Comparison of pressure losses of test separators 1 and 2 with those for AEG and GE cyclones.

★) *This way of plotting is used by AEG. The GE results are given as a function of total volumetric flowrate. All values were transformed to the same basis for comparison.*

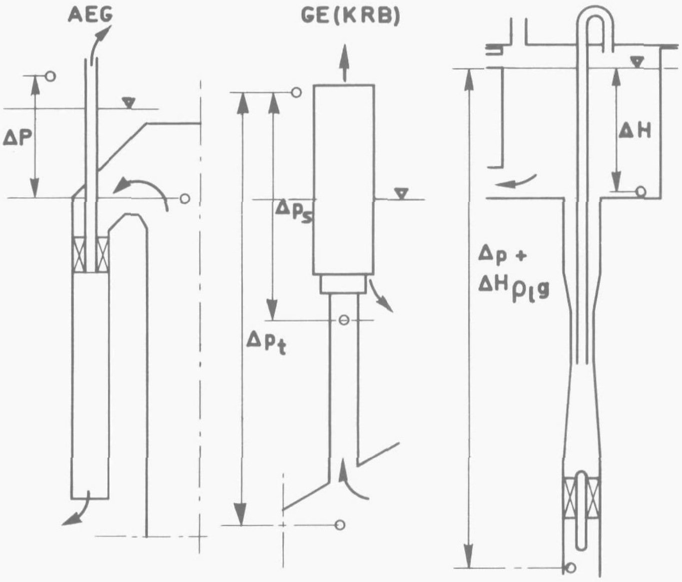

FIGURE 2-46.

Pressure tap locations for separator pressure losses of figure 2-45.

From measurements [82] in the KRB reactor equipped with GE upcomer cyclones, the separator pressure loss at nominal reactor power is given as measured from the plenum and from the stand pipe. The measured values for the venturi separators 1 and 2 are shown for various values of β_R. Figure 2-46 shows the geometry of the three separator types and the location of the pressure tappings.

The venturi separators show favorable results in comparison with the others but some differences in behaviour should be mentioned. In contrast to the AEG air-water results a marked influence of mixture quality was found.
The AEG steam-water results for a cyclone of similar design as used for air-water show a different gradient although pressure losses of the same magnitude were found ★).
A remarkable difference in pressure loss is found for the GE-separator [82] depending upon whether the measurement includes the stand pipe (~ 1.5 m) or not. Although it is not clear from [82] what the exact location of the pressure taps is it is reasonable to compare the venturi cyclone results with the lower of the two GE values because no plenum entrance losses were included in this investigation.

2.2.5.3. Void fraction profiles.

Radial void fraction distributions obtained from the γ-ray scans are given in figures 2-47 through 2-52 (see pages 78 and 80). The profiles are plotted from the calculated polynomial distribution functions for the separator inlet conditions given in Table 2-5.
The void profile at pressure tap 1 location describes the inlet conditions. The profile is rather flat, which is usual at lower void fractions ★★).
The average slip ratio-except for one condition (separator 2, $v_{s\ell R} = 2.0$, $v_{sgR} = 0.7$ m/s) - is less than zero which must be attributed to a "Bankoff effect" ★★★).
The profiles in the vortex tube show a concentration of gas in the center of the tube as a result of the separation.

★) *An influence of quality on the steam-water results is also reported [55] although there is no evidence of this in figure 2-46 due to the lack of data points given.*

★★) *This trend is also found elsewhere and will be further discussed in section 3.2.2.2.*

★★★) *A definition is given in 3.1.2.1.*

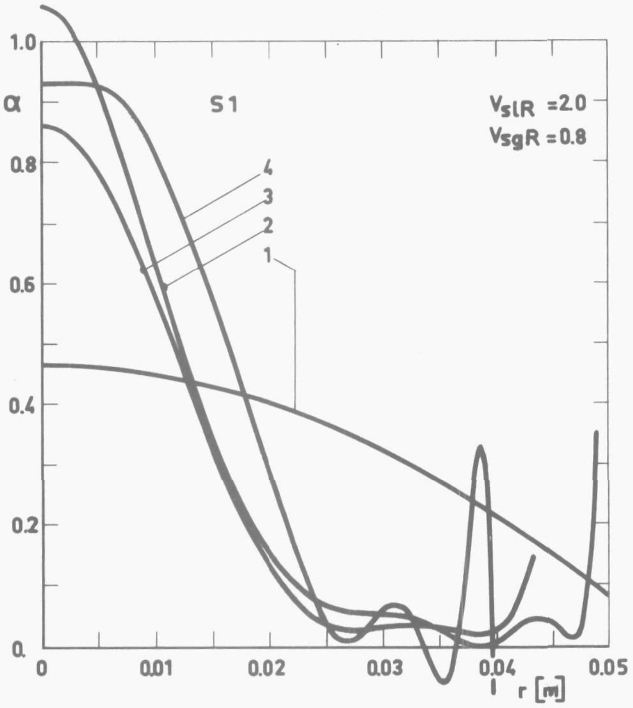

FIGURE 2-47.

Measured void fraction profiles in separator 1 for $v_{s\ell R} = 2.0$ *m/s.*

FIGURE 2-48.

Measured void fraction profiles in separator 1 for $v_{s\ell R} = 2.5$ *m/s.*

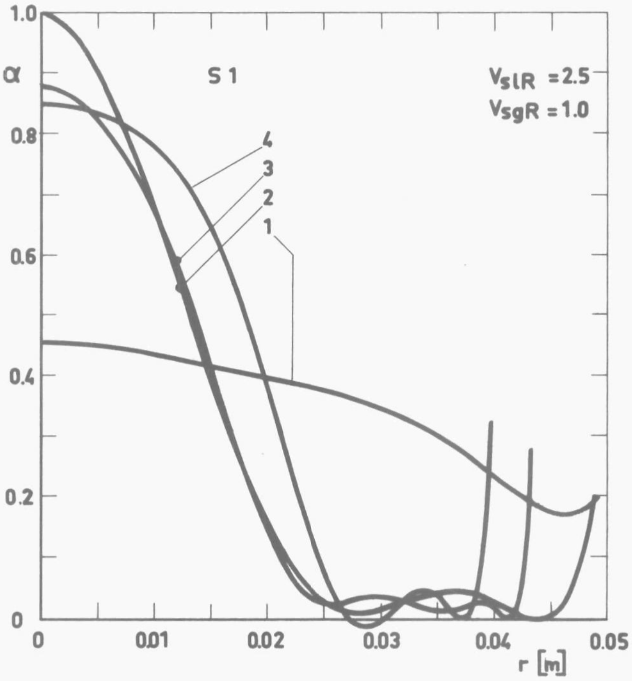

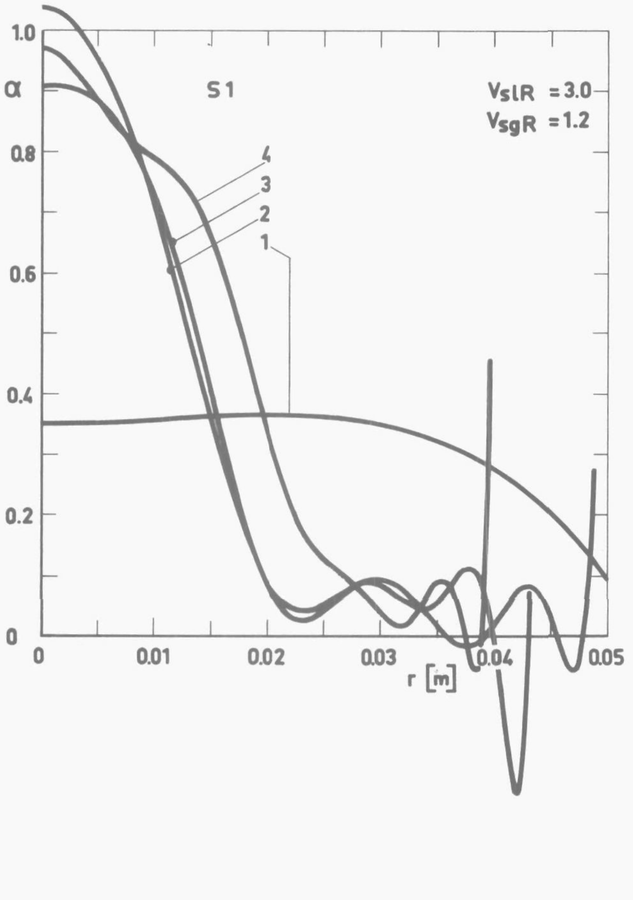

FIGURE 2-49.

Measured void fraction profiles in separator 1 for $v_{s\ell R} = 3.0$ *m/s.*

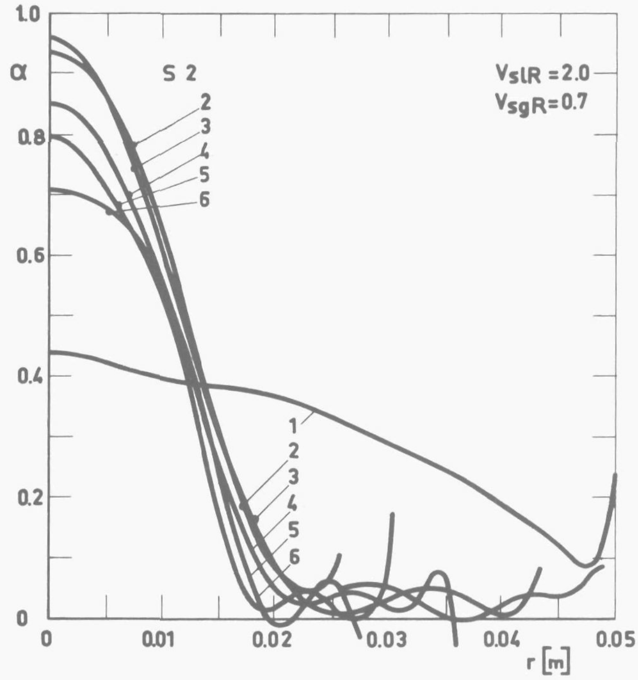

FIGURE 2-50.

Measured void fraction profiles in separator 2 for $v_{s\ell R}$ *= 2.0 m/s.*

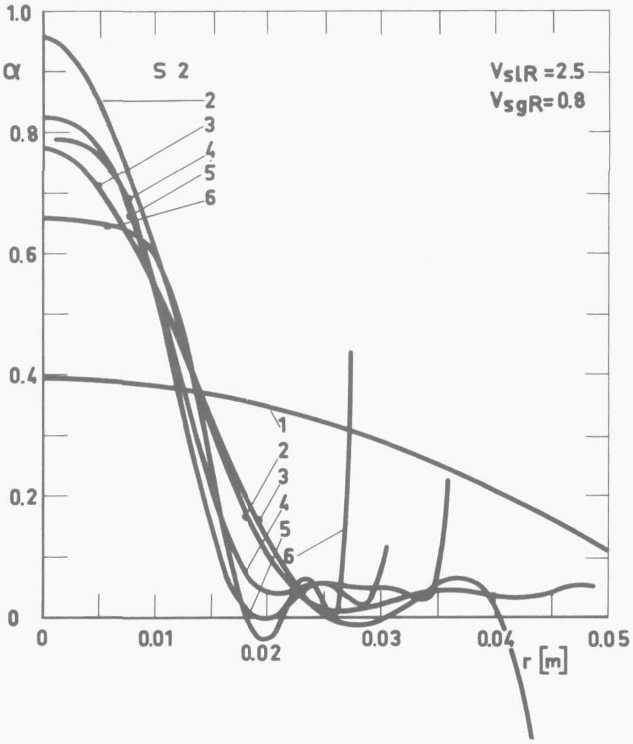

FIGURE 2-51.

Measure void fraction profiles in separator 2 for $v_{s\ell R}$ *= 2.5 m/s.*

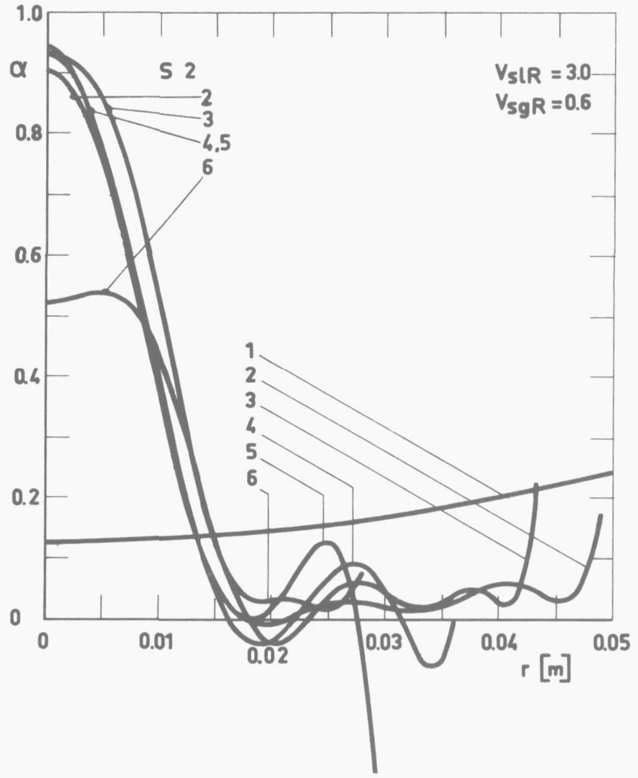

FIGURE 2-52.

Measure void fraction profiles in separator 2 for $v_{s\ell R}$ *= 3.0 m/s.*

It is remarkable that in most scans no pure air core ($\alpha = 1$) or gas free water annulus ($\alpha = 0$) is found but that on the other hand most of the separation has taken place before the first scan above the vanes. Apparently an entrainment or remixing phenomenon takes place in the air core. The scans show a constant diameter air core and therefore a thinning ring of water with a very low gas content. The limitations of the γ-ray attenuation technique must also be mentioned here and an error band of 5 to 10 vol. percent must be taken into account when drawing conclusions. Furthermore the inherent experimental inaccuracies make the polynomial distribution function cross the zero line in trying to fit the experimental data. A much lower degree polynomial would, in this region, probably give a much better fit, but the higher degree is dictated by the necessity to describe the steep void increase near the core. The increasing error towards the wall due to the very short chord length is demonstrated by the sudden sharp void increase of "boundary layer" thickness at the wall, where, instead, the void should go to zero. Nothwithstanding these experimental and computational errors most scans show some air- a few percent by volume - in the water ring outside the gas core that seems to be very hard to separate out. Visual observation is in agreement with this finding: apart from the mass of bubbles in the center some long spiralling chains of small bubbles could be seen "orbiting" around the central cloud. These small bubbles probably collected in the wakes formed by the trailing edge of the vanes.
The very small bubbles, 1 mm and less, have a much larger flow resistance than the larger bubbles of the main stream, which were in the order ⋆) of 5 to 10 mm.

2.2.5.4. Discussion.

A survey of the experimental results shows a low separator efficiency coupled with pressure losses open to improvement in contrast to a fairly good separation in the vortex tube. The origin of this seeming contradiction is located in the gas and water outlet section, where a mixing phenomenon takes place and hence a reentrainment of the separated phases.
In the original design the vortex finder did not extend through the throat into the converging section, but was intended to remove the gas in the diviverging section. However, the first trials showed this to be impossible because the gas core disintegrated once it entered the diffusor. No gas at all would enter the vortex finder and all the air would be "carried under" with the upflowing water around it. Moving the vortex tube downward into the throat would push the end of the gas core in front of it until the converging section was reached; only here the gas core could be forced to enter the vortex finder. An illustration of the phenomenon is given in photographs reproduced in figures 2-53 and 2-54, taken in the throat section of separator 1.

⋆) *For a discussion of this effect the reader is referred to section 3.1.2.2.*

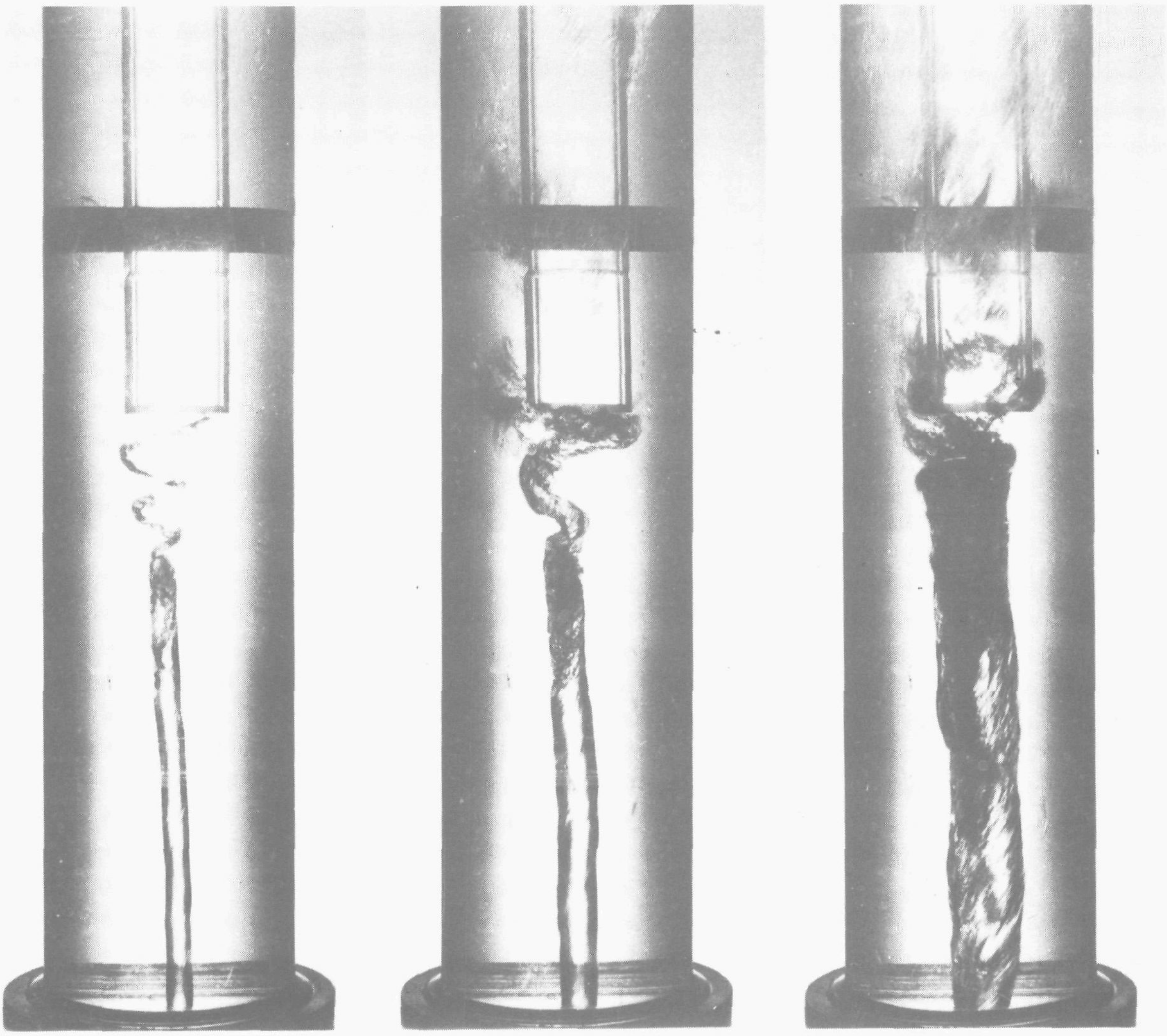

a. $V_{slR}=2$, $\beta_R \ll 1\%$ b. $V_{slR}=2$, $\beta_R < 1\%$ c. $V_{slR}=2$, $\beta_R \approx 1\%$

FIGURE 2-53.a,b,c,d.

Gas core in the throat of separator 1 for increasing volumetric qualities, with the vortex finder positioned in the throat.

Figure 2-53.a shows the gas core with almost no air admitted to the loop. The abrupt ending of the core is shown. The spiral of air extending from the top of the stationary core could not be seen by eye as it rotated at a very high speed giving the impression of a cone of very small bubbles. The liquid within the vortex finder and spiral was almost stationary. The subsequent pictures with increasing air flow show some water falling back into the core (the dark region in the top of the gas core) but no bubbles entering the vortex finder. Visual observations made it clear that no rotation of the main stream was transferred to the mixing zone as the water in the vortex tube was stationary. At higher inlet qualities as shown in figure 2-53.d. some air enters the vortex finder. Figure 2-54 (see page 84) shows the separation zone in the converging section. Figure 2-53.c. corresponds to the same conditions as for figure 2-47. The abrupt way of diameter reduction of the gas core is quite similar in appearance to the hydraulic jump phenomenon encountered in open channel flow.

In fact the same conditions apply as for the open channel: a layer of flowing fluid with a free surface and a force field perpendicular to the

d $V_{slR} = 2$, $\beta_R = 26$ %

direction of motion. While the gravity field acts as such in the open channel the centrifugal force field has this function for the rotating system. YIH [84], [85] has shown the hydraulic jump to exist in a rotating fluid, but he used a rotating cylinder with a relatively thin liquid film falling down the cylinder wall. Although his test conditions are different from those of the separator the same basic forces act on the system.
BINNIE [86] describes the sudden decrease in diameter of an air core entrained in the swirling flow in a vertical tube ending in a 90° bend. An hydraulic jump was formed upstream of the bend, without completely destroying the core.
KEDL [87] describes experiments with an axial flow separator of constant diameter, where the air core desintegrates before reaching the vortex finder and the separated air is remixed with the water in very small diameter bubbles.
The photograph presented [87] shows a picture very similar to figure 2-53 without the spiral, and to those in Binnie's work. Kedl gives no explanation for the collapse, whereas Binnie considers it to be an hydraulic jump.
The hydraulic jump in open channel is described in many textbooks on fluid flow e.g. STREETER [88]. The phenomenon exists thanks to the possibility for the fluid to flow at two different depths at a given throughput possessing equal energy: deep flow with a low velocity head and high pressure head and shallow flow where these heads are reversed in magnitude. For decreasing energy of the flow the difference in depth decreases and a minimum energy is reached when both possible depths coincide: the critical depth. The Froude number pertaining to this condition is equal to unity or

$$Fr^{\star} = \frac{u}{(gh)^{\frac{1}{2}}} = 1 \qquad (2\text{-}46)$$

where u is the velocity and h the depth of flow.
An hydraulic jump occurs when supercritical flow (Fr > 1) suddenly changes to subcritical (Fr < 1) with the accompanying changes in depth and a turbulent mixing zone. An energy balance over the jump yields the dissipated energy as the difference of the energy before and after the jump. A momentum balance gives the change in depth by equating momentum flux and external forces before and after the jump [88].
Having established that the conditions in the separator correspond to those in stratified flow in the presence of a gravitational field, it is still necessary to show the flow is supercritical. A Froude number for swirling flow can be defined if the gravitational constant g is replaced by u_t^2/r for the centrifugal force

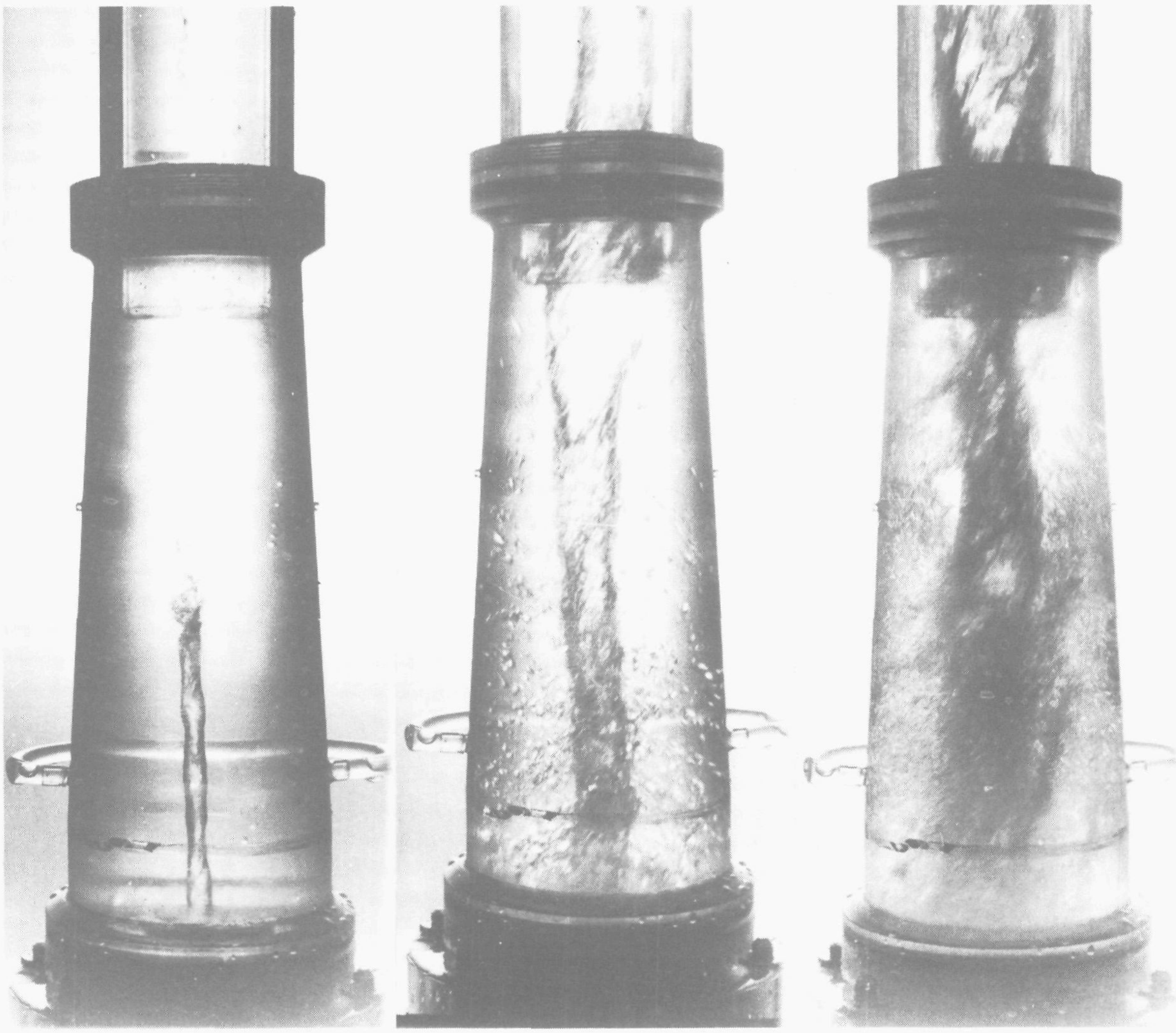

a. $V_{slR}=2$, $\beta_R \ll 1$ % b. $V_{slR}=2$, $\beta_R=18$ % c. $V_{slR}=2$, $\beta_R=26$ %

FIGURE 2-54.a,b,c.

Gas core in the converging section of separator 1 for increasing volumetric qualities with the vortex finder protruding through the throat.

$$Fr = \frac{u_z}{\left(\frac{u_t^2}{r}\,h\right)^{\frac{1}{2}}} \tag{2-47}$$

For the separator u_t and u_z are no independent variables. Assuming solid body rotation ⋆) and an homogeneous distribution of the axial velocity over the radius the tangential velocity can be written as $u_{z1}\ tg\theta$ and the Fr-number at the entrance of the vortex tube as

$$Fr_{w1} = \frac{u_{z1}}{u_{z1}\,tg\theta_w\left(\frac{R_1-r_{c1}}{R_1}\right)^{\frac{1}{2}}} = \frac{\cot\theta_w}{\left(1-\frac{r_c}{R_1}\right)^{\frac{1}{2}}} \tag{2-48}$$

⋆) *see section 3.3.2.3.*

where u_{z1} is the axial velocity at the exit of the guide vanes, R_1 the radius of the vortex tube θ the angle between the resultant of the axial and tangential velocities and the vertical, r_{c1} the radius of the gas core at that location and w indicates the wall. For vane angles of 45 degrees and smaller the Fr-number is always greater than one and under the simplifying conditions no subcritical flow can be realised. Slip would have a decreasing effect on the velocity u_{z1} and u_{t1}, but it is reasonable to assume that the effect is equal for both u_z and u_t. For the test separators the γ-scans show r_{c1} to be about 0.4 R_1.

The corresponding Fr-number becomes 1.29. The force field for swirling flow is not constant and at the core interface the value of the Fr-number changes to

$$Fr_{c1} = \frac{\cot\theta_w}{\left[\frac{r_{c1}}{R_1}\left(1 - \frac{r_{c1}}{R_1}\right)\right]^{\frac{1}{2}}} \tag{2-49}$$

According to equation (2-49) the Fr-number increases to 3.1 for the example given. The conditions for a hydraulic jump, though a weak one, according to the relatively low values of Fr, are present but the question remains how the Fr-number is affected when traveling up the converging section. Both the axial and the tangential velocity change as well as the depth of the liquid layer.

The change in rotation can be estimated on a basis of conservation of angular momentum and Fr-numbers at a level close to the vortex finder entrance are derived in Appendix 2-F.

$$Fr_{w2} = \frac{\dfrac{1 - (\frac{r_{c1}}{R_1})^2}{1 - (\frac{r_{c2}}{R_2})^2}(1 - \beta_1)\cot\theta_w}{\dfrac{R_2}{R_1}\,\dfrac{1 + (\frac{r_{c1}}{R_1})^2}{1 + (\frac{r_{c2}}{R_2})^2}\left[1 - \frac{r_{c2}}{R_2}\right]^{\frac{1}{2}}} \tag{2-50}$$

$$Fr_{c2} = \frac{\dfrac{1 - (\frac{r_{c1}}{R_1})^2}{1 - (\frac{r_{c2}}{R_2})^2}(1 - \beta_1)\cot\theta_w}{\dfrac{R_2}{R_1}\,\dfrac{1 + (\frac{r_{c1}}{R_1})^2}{1 + (\frac{r_{c2}}{R_2})^2}\left[\frac{r_{c2}}{R_2}\left(1 - \frac{r_{c2}}{R_2}\right)\right]^{\frac{1}{2}}} \tag{2-51}$$

For the γ-scan of figure 2-47 r_{c1} is 0.4 R_1 and r_{c2} is 0.6 R_2; with these values the Fr-numbers at the inlet of the vortex finder become 7.6 $(1-\beta_1)$ and 10.6 $(1-\beta_1)$. For the volumetric qualities of the tests it is clear that the Fr-number increases going into the diverging section, thus adding to the probability of a stronger jump.

Two conclusions can be drawn from the rather rough analysis of the Fr-numbers: increasing both the mixture quality and the vane exit angle decreases Fr. Only a decrease below unity would exclude a jump. With a β_1 value of 77% as required by reactor conditions (corresponding to 14% quality at 70 bar) θ_w would have to be 72 degrees to bring Fr from 10.6 down to 1. Further experimental work must show whether this requirement is sufficient to prevent the formation of a jump and to obtain adequate separation at the vortex tube entrance.

Another aspect of the efficiency of the separate removal of the two phases is the often quoted pressure drop balance [47], [49] of the gas and water outlet paths, or adjustment of over- and underflow as it is called in hydrocyclone practice for separation of emulsions [79], [80]. A shift in the pressure drop balance will improve the efficiency for one phase but reduce it for the other phase. For primary upcomer [47] and downcomer cyclones where carry-under performance is of prime importance the water discharge is usually throttled to meet the carry-under specifications. For the present test separators that have shown both efficiencies to be insufficient a discussion of this aspect is inappropriate at this stage.

The pressure curves of figures 2-39 through 2-49 give no clear indication of the cause of the severe drop in the outlet section. It is noted that measured pressure curves show the wall pressures and, because of the superimposed radial pressure profile, give no direct indication of the pressure recovery or loss in the diffuser. This radial pressure difference in the throat can be estimated from the approximation given in Appendix 2-G.

For two test conditions for separators 1 and 2 showing the highest pressure loss the pressure difference is shown to be 0.073 and 0.175 bar respectively, which is much smaller than the pressure differences between taps 4 and 5 for separator 1 and between 7 and 8 for separator 2. The curves therefore do show a severe loss.

A possible cause for this loss might be the diffuser of 14.6°, a value much too large for single-phase flow. For two-phase flow however the optimum angle of divergence is found in this range e.g. KORSTANJE [89] found a diffusor efficiency of about 45% for 15° diffusers having an area ratio of 2 using low pressure steam-water mixtures at 10% void. HENCH and JOHNSTON [90] measured pressure recovery in 2-dimensional diffusers with air-water and report about 30% for a 10° diffuser at an area ratio of 4. The area ratio for separator 1 is 3.1 and 5 for separator 2. For the conditions in Appendix 2-G the pressure recovery based on superficial water velocities of 12.5 and 16 m/s in the throat would amount to 0.23 and 0.39 bar for 30% efficiency separator 1 and 2 respectively.

It can be concluded therefore that the pressure losses are not due to the large diffuser angle employed for both separators. The outlet section thus remains an area for further investigation.

2.2.6. Conclusions.

Experimental results are given for two venturi type upcomer separators for air-water mixtures. Efficiency, pressure drop and radial void fraction distributions in the vortex tube are presented in graphical form.

These experiments, meant as a forerunner for steam-water testing, display some basic problems connected with the venturi design. Hydraulic jump and/or diversion of the flow around the vortex finder give rise to remixing phenomena of the separated phases, causing unsatisfying efficiencies at too low gas loadings. Reduction of guide vane pressure loss obtained by a small vane exit angle (45°) and "bladeless" augmentation of the rotation in the converging section of the venturi design is lost by expansion losses in the diffuser section.

The overall pressure drop is still acceptable in comparison with other designs.
Void fraction profiles in the vortex tube show the separation to be adequate before the remixing zone is reached.

3. ANALYSIS

3.1. Introduction.

3.1.1. General philosophy.

The quotation at the beginning of this thesis, taken from Levy's invited lecture at the Exeter symposium [1] on two-phase flow in 1965. served and still serves to illustrate the fact that in many cases two-phase flow phenomena are discussed as extrapolations from the knowledge of single-phase flow. This is not due to a lack of experimental work in the field, because the literature on two-phase flow has vastly expanded since that date, but apparently the complexity of the problem, indicated by Levy as interphase phenomena, has prevented fundamental analysis to bring about the much wanted understanding of the physics involved.

Two obstructions seem to be in the way. Firstly, any model of some value will probably be very complex, because of the discontinuous flow structure and the moving phase boundaries. The second barier lies in the testing of the model, where it is necessary to solve the equations that are often given in differential form. The more complex the model the more difficult it is to find methods of solution that must provide the predictions that are to be verified experimentally. The increasing availability however of large computers and an also increasing program library enable the investigator to limit the amount of simplifying assumptions and try out more hypotheses where tedious and time consuming calculations prevented him from doing so in the past.

Levy's plea for more fundamental analysis has a consequence however. The designer of hardware is only remotely interested in the pure physics of the problem at hand but even more so in formulae and criteria, that give him a practical answer to his questions. Apart from pure science for the sake of science, all other studies must ultimately give off results for practical use.

To illustrate the above differences in approach, two rather arbitrarily chosen examples are given.

A now almost classical example of a single-phase extrapolation is the calculation of frictional pressure loss according to LOCKHART and MARTINELLI [2]:

$$\left(\frac{dp}{dz}\right)_{TP} = \Phi_L^{\,2} \left(\frac{dp}{dz}\right)_{L.O.} = \Phi_G^{\,2} \left(\frac{dp}{dz}\right)_{G.O.}$$

The pressure gradient of the two-phase mixture flowing through a pipe is correlated with the singel-phase pressure loss due to either the gas or the liquid flowing alone in the pipe.

The two-phase multipliers Φ_G^2 and Φ_L^2 are a function of a parameter χ that is based on the gas and liquid properties. The practical value of such a design formula is evident. And although it is about the first correlation of its kind and numerous new correlations have followed, the work of Lockhart and Martinelly is still widely used in chemical and nuclear engineering. What is more, it is often claimed to given the best results as borne out by the comparitive study of DUCKLER e.a. [4].

The work of BANKOFF [3] may be quoted as an example of the analytical approach. The model predicts the average slip of the phases at a cross section of the flow channel. The two-phase mixture is treated as a single fluid of variable density. This implies that the local phase velocities are equal i.e. that no local phase slip can occur.

By introducing velocity and concentration profiles the weighted average gas and liquid velocities can be calculated and hence the average slip ratio ⋆).
The foregoing classification has the purpose to provide the arguments for the course taken in the present work. Although a parameter study of the separation process presented as correlations of dimensionless groupings might yield more practical results for direct use by the designer, it was felt that it would involve a large amount of experimental work and have the disadvantage to be restricted to the range of variables tested and giving but little insight in the two-phase phenomena involved.

The main attraction of the more analytical approach is exactly its possibility to provide this insight, while the experimental work can be less extensive because it becomes more of a check on the theory. The outcome of the analysis may also be valid beyond the bounds of the experiment.

Another important reason why the analytical study was chosen, lies in the size restraints imposed on the experiments. It is virtually impossible to build a full size mock-up of the reactor system for actual pressure and temperature conditions. This leaves out an all-important variable for the parameter study. The analysis on the other hand is better suited to extrapolate from the laboratory experiment to the real size, simply because the true analysis which encompasses all phenomena is generally applicable to any size or choice of fluid properties, and even if the underlying assumptions diminish this applicability the analysis still has the advantage, of giving the functional relationship between the parameters of influence, whereas dimensional analysis in case of a parameter study only produces the governing dimensionless groupings leaving the function to be found by trial and error.

It should be mentioned that the theoretical advantage of an analysis is often bought at the expense of equations that are difficult to solve.

The result will be a compromise between completeness and mathematical simplicity resulting in a series of simplifying assumptions decreasing its domain of validity.

3.1.2. Phase interaction.

3.1.2.1. Relative motion of dispersed phase.

It is now necessary to present such principles and basic relations as are required for the analysis of the separation process. It is substantially a transport problem, where one phase moves relative to the other.

Of many aspects of two-phase boundaries, only the interphase forces will be considered here. The process may be considered as adiabatic and isothermal and change of phase due to pressure variations will be shown to have negligible influence. The relative motion of the phases, i.e. the slip, is either defined by the slip velocity

$$u_r = u_g - u_\ell$$

⋆) *The average slip ratio as defined in section 3.1.2.1. is thus dependent on the functions that describe the profiles and which can be verified experimentally. The paradox of this example lies in the name of the model: single fluid variable density model. This would classify it as a single phase extrapolation. In reality however it recognizes the non-homogeneous distribution of the phases in space and gives analytical relations for this distribution. Subsequently the model postulates an extremum of another typical two-phase characteristic, the equality of the local velocities which in general are different. In spite of this last limitation the model is truly analytical.*

or by the slip ratio

$$s = \frac{u_g}{u_\ell}$$

If velocities u_g and u_ℓ are true local phase velocities the slip is a local parameter. However, in most cases where the slip ratio is used, i.e. for two-phase pipe flow, the average values over a cross section are taken to evaluate the slip ratio.
In general the radial distribution of the phases and their velocities are not uniform over the cross section of the flow channel. The distribution of the phases in space is defined by the void fraction α where

$$\alpha = \frac{\text{volume occupied by gas}}{\text{total volume occupied by gas and liquid}} \tag{3-1}$$

If α is assumed to be a continuous function in space, which implies the physical impossibility that both phases are present at the same point in space but is nevertheless customary, the void fraction is often defined at a channel cross section as the area fraction occupied by gas

$$\alpha = \frac{dA_g}{dA} \tag{3-2}$$

If in a special case the velocity profiles of gas and liquid are indentical the local slip velocity is zero, or

$$s = \frac{u_g}{u_\ell} = 1 \tag{3-3}$$

Due to the nonuniform radial distribution of α, however, the average slip ratio at a cross section may differ from 1 because

$$\langle s\rangle = \frac{\int u_g dA_g}{A_g} \frac{A_\ell}{\int u_\ell dA_\ell} = \frac{\int \alpha u_g dA}{A\ A_g} \frac{A\ A_\ell}{\int (1-\alpha) u_\ell dA} = \frac{\phi_{vg}}{\langle\alpha\rangle} \frac{\langle 1-\alpha\rangle}{\phi_{v\ell}} \neq \langle \frac{u_g}{u_\ell} \rangle \tag{3-4}$$

This is the slip ratio as defined by BANKOFF [3] and the paradox, $\langle s\rangle \neq s$, will be called the "Bankoff effect" for future reference.

For the present case local slip is essential. It is in fact the separation itself. The analysis must consequently be based on the forces that govern the movement of the disperse phase relative to the continuous phase. In view of the delimitations of the present investigation given in section 1.2. the gas phase is always taken to be the disperse phase. It is further postulated that the equation of motion for a "particle" which may either be a bubble or a solid particle of this disperse phase can be written as

$$\frac{d}{dt} (\rho_g V_g u_{g_i}) + \frac{d}{dt} (B \rho_\ell V_g u_{r_i}) + V_g \frac{\partial p}{\partial x_i} + \rho_g V_g g \frac{\partial x_i}{\partial x_g} +$$

$$+ C_D A_g \tfrac{1}{2} \rho_\ell\, u_{r_i} \left| u_{r_i} \right| = 0 \tag{3-5}$$

The first and second term are the acceleration forces of the real and virtual mass of the "particle" or bubble. The third is the pressure gradient force and the fourth is an external body force for instance the gravity force. The last term represents the drag on the bubble caused by its relative movement. Equation (3-5) is written in Lagrange notation. For stationary motion of the bubble the equation in Euler notation becomes

$$u_{gk} \frac{\partial}{\partial x_k} (\rho_g V_g u_{g_i}) + u_{gk} \frac{\partial}{\partial x_k} (B\rho_\ell V_g u_{r_i}) + V_g \frac{\partial p}{\partial x_i} +$$

$$+ \rho_g V_g g \frac{\partial x_i}{\partial x_g} + C_D A_g \tfrac{1}{2} \rho_\ell u_{r_i} |u_{r_i}| = 0 \qquad (3\text{-}6)$$

The force balance of equation (3-6) is the mathematical representation of the interphase phenomena with which this analysis has to deal.
The equation states that the bubble motion is governed by a driving force (the pressure gradient force), two resisting forces (the drag force and the virtual mass force) and a body force that may be due to the resultant of a gravitational and a centrifugal field. Of these the drag force and virtual mass force require a more extensive discussion.

3.1.2.2. Drag force.

The drag force in equation (3-6) is presented in the notation usual for the drag of a submerged body. The problem is thus reduced to finding an appropriate drag coefficient for given body dimensions. As the bubble dimensions are also unknown or at best known to lie between two extreme values the problem is somewhat more complicated. Furthermore the bubble shape together with a number of other influences have an effect on the value of C_D. Comparison of the drag coefficient for a dense swarm of bubbles in a flowing system to that of single solid sphere in stagnant liquid shows the following affecting differences can be listed
- single bubbles in stagnant liquid: fluid character and bubble parameters
- single bubbles in flowing liquid: turbulence of the main stream
- effect of adjacent bubbles
- bubble swarms in stagnant and turbulent liquid.

These differences, and the effect of acceleration on the drag coefficient, will now be discussed in some detail.

Single bubbles in stagnant liquid: fluid character and bubble parameters.

Literature on the rise of single bubbles in stagnant liquid is fairly extensive. In the case of laminar flow ($Re_b < 1$) [13], [14] analytical solutions have been given that are modifications of Stokes' law for the solid sphere. HADAMARD [5] and RYBCYNSKI [6] give the solution for the viscous flow around a fluid sphere, resulting in:

$$C_D = \frac{24}{Re_b} \frac{2\eta_\ell + 3\eta_g}{3\,(\eta_\ell + \eta_g)} \qquad (3\text{-}7)$$

The flow around the sphere induces an internal circulation in it which reduces the tangential shear force.

For negligible viscosity of the sphere as compared to the surrounding fluid equation (3-7) reduces to

$$C_D = \frac{2}{3} \cdot \frac{24}{Re_b} = \frac{2}{3} \cdot C_{D_{STOKES}} \tag{3-8}$$

These relations only hold for laminar flow. LEVICH [7] calculated the pressure distribution around a fluid sphere for Re-numbers up to 300. Postulating irrotational flow outside the boundary layer and zero shear stress at the bubble surface he found

$$C_D = \frac{48}{Re_b} = 2\ C_{D_{STOKES}} \tag{3-9}$$

Most of the work for higher Re-numbers is experimental. Results of some of these investigations are plotted in figure 3-1 for air-water systems.

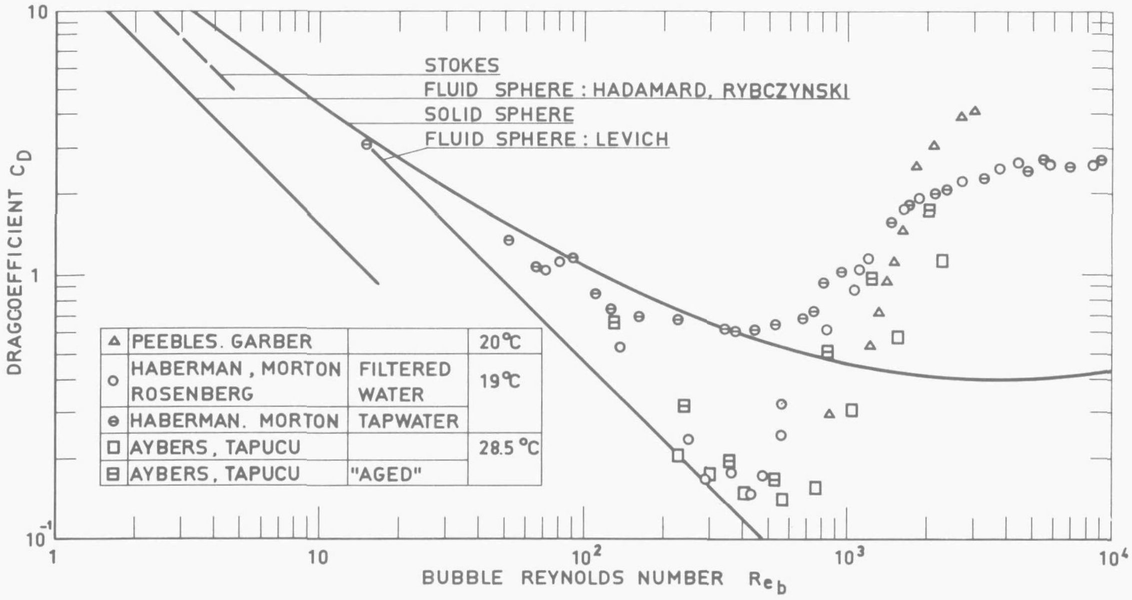

FIGURE 3-1.

Drag coefficient for spheres and air bubbles as a function of their Reynolds number.

The function of the drag coefficient versus Re-number shows three distinct regions. For comparison Stokes' law, equations (3-8) and (3-9) and the drag curve for a solid sphere are drawn in. Up to a Re-number of about 500, the bubble behaviour is seen to lie in between that of a solid and a fluid sphere. In this region no separation of the boundary-layer of the solid sphere is to be expected; the drag is due to friction only. Bubbles would be expected to behave more like fluid spheres the larger the Re-number is, as the internal circulation which reduces the shear stress becomes more and more pronounced. Deviation from the fluid sphere values appears when the bubble begins to deform. This commences above Re ≈ 300 [8], [9]. Data of HABERMAN and MORTON [8] and ROSENBERG [10], for filtered water, both investigations being performed at David Taylor Model Basin, as well as those from AYBERS and TAPUCU [9] more or less follow the fluid sphere line up to Re ≈ 300 and show an increasing drag at higher Re-numbers.

Another reason why bubbles do sometimes not behave like fluid spheres is demonstrated by Haberman and Morton's experiment with tap water. The explanation is found in the concentration of surface active impurities on the bubble surface. These impurities are able to "hold" water molecules at the surface thus creating the same conditions for development of a boundary layer as in the case of a solid surface.
The effect is very clear for the data of Haberman and Morton. Aybers and Tapucu found the velocity of rise decreased to an asymptotic value after having reached a maximum. The corresponding increase in C_D was also attributed to surface active impurities. This formation of higher impurity concentration at the surface or "aging" of the bubble takes place as the bubble moves through the liquid gradually forming a boundary layer. Thus the bubble velocity gradually decreases as it moves upwards. When the bubble begins to deform again higher values of C_D are found.

A second region is found between Re ≈ 500 and Re ≈ 5000. The experiments all show a rapid increase in drag coefficient in this region, which is explained by separation of the flow and shedding of vortices.
The bubbles take a spheroidal form. The motion which was rectilinear in the first region now becomes either helical or oscillating in a plane. This motion is caused by alternate shedding of a vortex simular to the Karman vortex street. The influence of impurities has disappeared because the shear force becomes larger than the forces that maintain the impurities at the surface [8]. The drag is now mainly determined by the deformation and the wake formed. The scatter in experimental data from different investigations is understandable as the deformation is strongly dependent on surface tension and thus of temperature, which varied from 19 to 28.5°C for different investigations. The discrepancy between the C_D-values of Aybers and Tapucu for maximum rise velocity and that for "aged" bubbles cannot be explained by an "aging" effect. As will be shown in section 3.1.2.2. the bubble shape is changing during acceleration. The bubble may not have reached its largest deformation upon reaching its maximum rise velocity after initial acceleration. A subsequent decrease in velocity can be attributed to further deformation as well as the surface oscillations mentioned by the authors [9].

The third region for Re > 5000 shows a constant value for the drag coefficient. The bubbles assume a mushroom like shape with a spherical dome. These spherical cap bubbles were first investigated by DAVIES and TAYLOR [11] who found their rise velocity solely dependent on the dome radius

$$u_p = 1.02 \sqrt{g r_d} \tag{3-10}$$

where $r_d = 1.15\ d$
corresponding with

$$C_D = 2.6 \quad . \tag{3-11}$$

The David Taylor Model Basin data [8], [10] coincide with equations (3-10) and (3-11). The values for C_D found by PEEBLES and GARBER however are higher, which they attribute to a possible wall effect of the test tube for the larger bubbles (largest bubble diameter of 11.5 mm in a 26 mm tube).
It should be mentioned here that the above discussion is far from complete. Only some of the air-water data available in literature are given in figure 3-1, the sole objective of this section being to give a general description of bubble behaviour. Furthermore the region of interest is the second region between Re ≈ 500 and 5000.

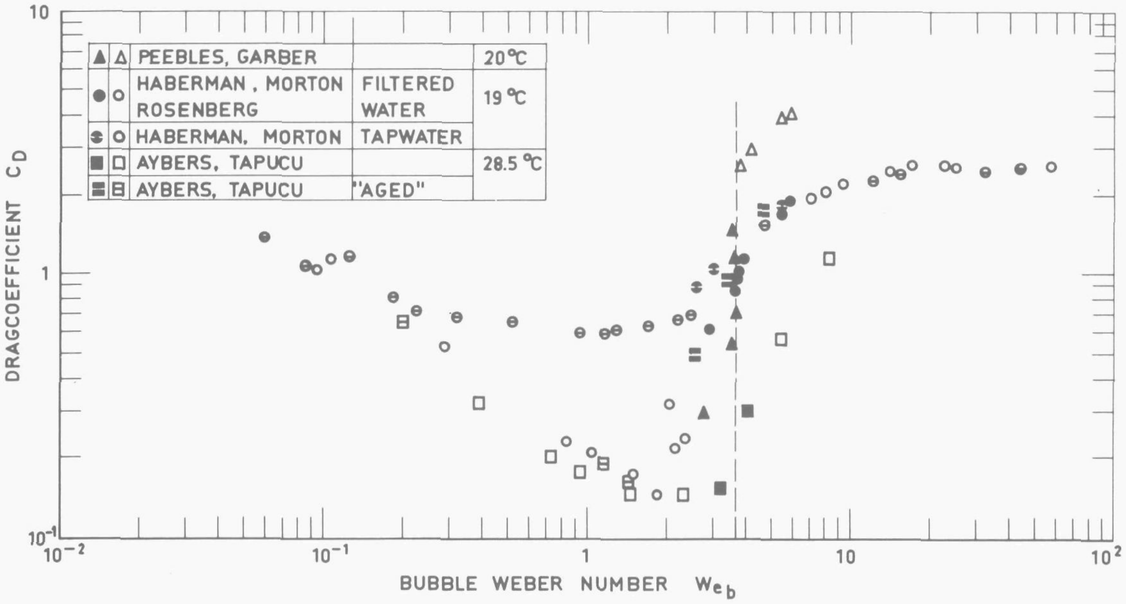

FIGURE 3-2.

Drag coefficient for bubbles as a function of their Weber number.

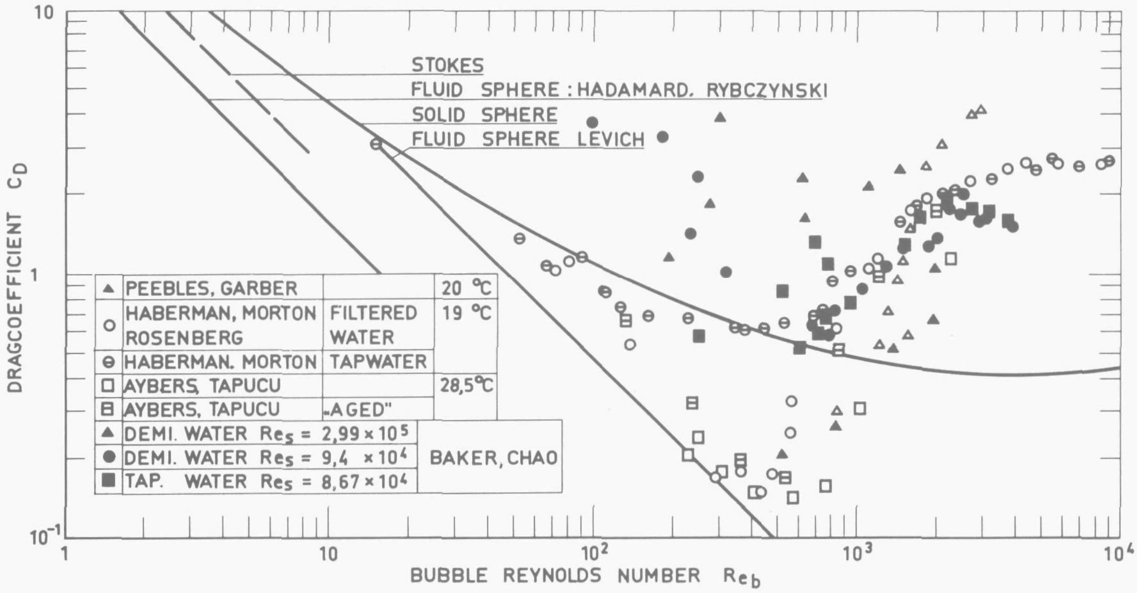

FIGURE 3-3.

Comparison of bubble drag coefficients for rising bubbles in stagnant and flowing water.

Peebles and Garber observed that in the interval Re ≈ 750-1300 the bubble Weber number remained constant at a value of 3.65. RIETEMA and RYPKEMA [12] found a value of 3.6 from results of their own experiments and of others. Although this interval does not cover the second region completely it is an interesting phenomenon that emphasizes that the drag in the interval mentioned is strongly deformation controled. To verify if the same trend is followed by the experimental points of figure 3-1 all the data were

replotted as a function of the We-number. The solid points in figure 3-2 fall in the interval Re ≈ 750-1300.
The first impression is that a better correlation of the data is obtained this way, showing less scatter. Apparently the strong influence of bubble deformation on drag applies to all the points shown. The findings of Peebles and Garber, We = constant, is not very markedly corroborated by the solid points.
A clear deviation of the "aged" drag coefficient of Aybers and Tapucu for Re > 1000 from the other data is shown, indicating a not fully developed bubble deformation for these values.

Single bubbles in flowing liquid: turbulence of the main stream.

BAKER and CHAO [21] studied the rise velocity of single bubbles in a turbulent stream. Demineralized and tap water was circulated in a closed loop and single air bubbles were allowed to rise in a vertical section of this loop. The system Re-number was varied in the range $5.15 \times 10^4 - 3.86 \times 10^5$. The relative bubble velocities were measured for various bubble diameters. Some of their data are plotted in figure 3-3 in the form of drag coefficients. This figure also contains the data of figure 3-1 for comparison. The influence or turbulence is not very clear.
The authors of [21] conclude that there is a slight shift to the right of the minimum of the drag curve as compared to stagnant water. The drag coefficients in the second region are consequently somewhat lowered, the more so for higher values of Re_s. For Re_b-numbers below 800 the scatter is large and no influence of turbulence can be discerned. Above $Re_b \approx 2000$ the results converge to values lower than for stagnant water.
Furthermore it can be seen that the values of Baker and Chao for tap water show agreement with HABERMANN and MORTON's [8].

Effect of adjacent bubbles.

For a single bubble rising in a stagnant liquid the first two terms of equation (3-6) are zero and the equation reduces to

$$-\frac{\pi}{6} d^3 \cdot \rho_\ell g + \frac{\pi}{6} d^3 \cdot \rho_g g + C_D^{\infty} \cdot \frac{\pi}{4} d^2 \cdot \tfrac{1}{2} \cdot \rho_\ell (u_r^{\infty})^2 = 0 \qquad (3\text{-}12)$$

where C_D^{∞} and u_r^{∞} are the values pertaining to the single bubble. In applying equation (3-6) to a swarm of bubbles of the same size the pressure gradient is no longer given by $\rho_\ell g$ as in equation (3-12) but by the mixture density.

$$-\frac{\pi}{6} d^3(\alpha\rho_g + (1-\alpha)\rho_\ell)g + \frac{\pi}{6} d^3 \rho_g g + C_D^{\alpha} \frac{\pi}{4} d^2 \quad \tfrac{1}{2}\rho_\ell (u_r^{\alpha})^2 = 0 \qquad (3\text{-}13)$$

The drag coefficient and rise velocity for the swarm are different from the single bubble case and are denoted by C_D^{α} and u_r^{α}.
The effect of neighbouring bubbles on the drag coefficient will be investigated by taking the ratio $C_D^{\alpha}/C_D^{\infty}$ from equations (3-12) and (3-13).

$$\frac{C_D^{\alpha}}{C_D^{\infty}} = \frac{\frac{4}{3} d \frac{\rho_\ell - \rho_g}{\rho_\ell} \frac{(1-\alpha)}{(u_r^{\alpha})^2}}{\frac{4}{3} d \frac{\rho_\ell - \rho_g}{\rho_\ell} \frac{1}{(u_r^{\infty})^2}} = (1-\alpha) \left(\frac{u_r^{\infty}}{u_r^{\alpha}} \right)^2 \qquad (3\text{-}14)$$

Several authors have investigated the rise velocity or relative velocity in swarms of "particles". A simple approximation of the ratio of relative velocities can be made by considering a cubic arrangement of equal bubbles. The relative motion of the bubble causes liquid to be displaced from the front, which has to flow around the bubble. This back flow in unhindered in the case of a single bubble but becomes more and more difficult for an increasing bubble population.
If it is assumed that the relative bubble velocity of the swarm is reduced by the increased backflow, which is proportional to the liquid flow area, a bubble velocity relative to the average true liquid velocity (which is zero for stagnant liquid but finite for a flowing system) can be obtained for the cubic arrangement of spherical bubbles mentioned above from the following formula (also given by MERTES and RHODES [22]):

$$\frac{u_r^\alpha}{u_r^\infty} = 1 - 1.209\ \alpha^{2/3} \tag{3-15}$$

The backflow is equation (3-15) is related to the minimum free flow area in the unit cell. Taking the average free area in the cell somewhat higher values are obtained [22]

$$\frac{u_r^\alpha}{u_r^\infty} = \frac{(1-\alpha)}{(1-\alpha) + 1.209\ \alpha^{2/3}} \tag{3-16}$$

Both equations (3-15) and (3-16) are gross oversimplifications of the real flow system, but serve a purpose in comparison with experimental results. Substitution of these equations in equation (3-14) gives respectively

$$\frac{C_D^\alpha}{C_D^\infty} = \frac{(1-\alpha)}{(1-1.209\ \alpha^{2/3})^2} \tag{3-17}$$

and

$$\frac{C_D^\alpha}{C_D^\infty} = \frac{\{(1-\alpha) + 1.209\ \alpha^{2/3}\}^2}{(1-\alpha)} \tag{3-18}$$

MARRUCCI [23] derived the relative velocity of a spherical bubble belonging to a swarm by taking a spherical cell, with the bubble in the centre. For a relative movement of the two spheres the energy dissipation of the liquid flowing between them is related to the work done by the drag force. Marrucci then divides the drag force so obtained by the single bubble drag force according to LEVICH [7] and finally arrives at

$$\frac{u_r^\alpha}{u_r^\infty} = \frac{(1-\alpha)^2}{1-\alpha^{5/3}} \tag{3-19}$$

Upon substitution of equation (3-19) in (3-14) one finds

$$\frac{C_D^{\alpha}}{C_D^{\infty}} = \frac{(1-\alpha^{5/3})^2}{(1-\alpha)^3} \tag{3-20}$$

Equations (3-17), (3-18) and (3-20) are drawn in figure 3-4. Mertes and Rhodes give experimental data on the relative velocity of glass and catalyst beads in water for various particle Re-numbers. A graphical representation is given of the ratio of the relative velocities of the swarm and a single particle. By substituting these experimental values in equation (3-14) corrsponding drag coefficient ratio's are found, which are plotted in figure 3-4. A good agreement of Marrucci's equation with equation (3-18) is observed for lower void fractions. Comparison with the values for the solids shows the effect for high particle Re-numbers is best predicted by Marrucci. The predictions fail for low Re-numbers where the drag is mainly viscous. The reduction in particle boundary layer thickness can apparently not be described by the assumptions that underly the above predictions. In the region where the drag coefficient for solid particles tends to become independent of the Re-numbers the experimental points are bracketed between the curves of equations (3-17) and (3-18).

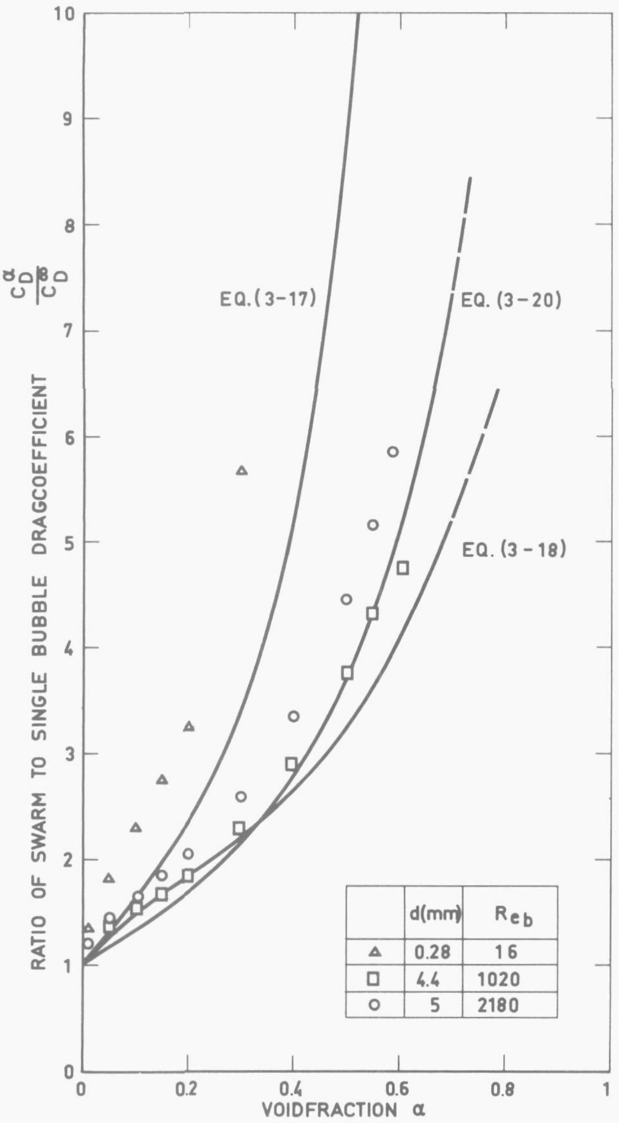

FIGURE 3-4.

Effect of neighbouring bubbles and solid particles on the drag coefficient.

An effect that is not accounted for in the equations is the wake of the particle. For high solid fractions the particles will be flowing in the wake of the particles ahead thereby decreasing the drag for the swarm. If the interparticle spacing becomes too small no wakes can be formed. For solid fractions above 0.065 the particles are already less than a diameter apart while they are touching at solid fraction of 0.52 assuming cubic arrangement.

Marrucci's assumption that the wakes of the bubbles may be neglected should be valid for solid fractions above a value somewhat below 0.5.

It should be remembered that the experimental points in figure 3-4 are for solid particles that do not deform or coalesce with increasing void fraction. Corresponding values of the ratio of drag coefficients for bubbles can not be shown because the bubble diameter is unknown and changes with void fraction. The effects shown in figure 3-4 would thus be obscured by the other phenomena as increased coalescence due to increasing contact probability. The ultimate consequence is a transition to other flow regimes such as slug or annular flow.

Bubble swarms in stagnant and turbulent liquid.

In most cases the bubble diameter - or the equivalent diameter of a sphere with equal volume as generally used is unknown in a flowing mixture or even in a swarm of bubbles rising through stagnant liquid.

If single bubbles are generated from nozzles and orifices there is a correlation between orifice diameter, gas rate and liquid and gas properties, especially surface tension [15], [16]. The influence of the pore size on the bubble diameter when forming a swarm of bubbles from a filter of porous material is much less if not negligible. VERSCHOOR [17] observed that the bubbles fromed at a glass filter were 10 to 100 times larger than the pores from which they emerged. He also found almost no influence of surface tension in bubble dimensions for such swarms. Lowering the surface tension from 70 × 10^{-3} (water) to 22.6 × 10^{-3} by use of a different fluid (methanol) made no difference. By contrast the addition of 0.1% Teepol to water, also resulting in a lowering of the surface tension to 29 × 10^{-3}, caused a drastic reduction of the bubble diameter. This apparent contradiction may be explained by the fact that in the latter case the coalescence is prevented by the higher concentration of the solute at the boundaries as compared to the rest of the water. Verschoor mentions this effect is in agreement with the findings of other authors.

The diameter of bubbles in a swarm or a flowing mixture can be regarded as the result of continuous coalescence and breaking up of the bubbles. Both processes are random in nature and, given the time, will reach an equilibrium.

Two bubbles coalesce when, touching, they remain in contact long enough for the liquid to drain from the film until it is so thin it breaks.

MARRUCCI e.a. [18] calculate a draining time of 10^{-3} sec. This would imply that coalescence occurs almost instantaneously. Addition of surface active additives such as Teepol or inorganic salts like KCl, NaCl and Na_2SO_4 prolongs the draining time. Marrucci e.a. measured the film draining time of two simultaneously formed bubbles from adjacent orifices for different concentrations of KCl. The rest time was in the order of 10^{-3} sec as long as the concentration stayed below 0.03 g moles/liter then gradually increasing to 0.1 sec at 0.1 g moles/liter.

HOWARTH [19] measured coalescence fequency ⋆) of liquid drops in a stirred tank. In this case the coalescence is not controlled as in Marrucci's experiment and due to the random movement of the drops the time available for coalescence is much shorter. Addition of 0.05 g mole/liter NaCl lowered the coalescence frequency by a factor 5.

Apart from confirming the influence of surface active additives Howarth's experiments show that coalescence is also dependent on turbulence (generated by stirring) and void fraction. Both increase the probability that bubbles come into contact. The coalescence frequency is for instance found to be proportional to $\alpha^{0.5}$. The breaking up of the bubbles is also governed by the turbulence. Howarth assumes that the drops grow until they have reached a maximum stable dropsize which is solely dependent on the turbulence intensity.

⋆) *Number of coalescences per unit time or reciprocal of mean lifetime of droplet between coalescences.*

Values of the average bubble sizes in flowing systems are scarce for air-water and non-existent for steam-water mixtures. PETRICK [20] has measured bubble size spectra in air-water mixtures for up and downflow.

The data were taken from photographs, for void fractions up to 35% and true water velocities in the range of 0.3 to 1.2 m/sec.

Although these values are rather low for practical purposes, figure 3-5, which is taken from [20], shows a fairly good correlation of the average bubble size with the true water velocity.

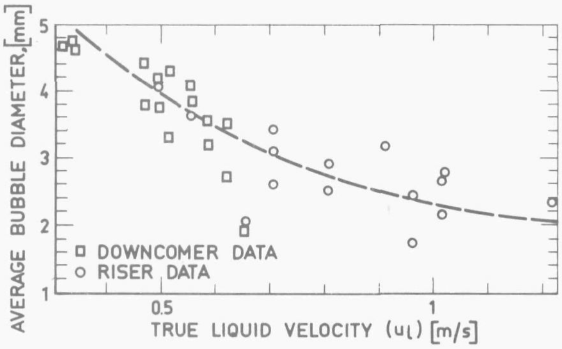

FIGURE 3-5.

Average bubble diameter as a function of true water velocity.

However, an attempt to replot the data as a function of relative bubble velocity or the corresponding We-number failed to give such correlation. As seen from figure 3-5 no distinction can be made between up and downflow, whereas the relative bubble velocity is quite different for both cases. This overriding influence of the water velocity, i.e. the turbulence of the main stream, seems to be in agreement with Howarth's assumption with regard to the maximum stable dropsize. Unfortunately a comparison of the data of Howarth and Petrick on a Re-number basis is not possible because Howarth does not give absolute values of drop diameters as a function of impeller speed. The impeller Re-numbers ranged from 10^4 to 5×10^4 while the mainstream Re-numbers of Petrick varied from 4×10^4 to 1.5×10^6. Moreover the different properties of the liquid-liquid and air-water system would make a comparison difficult.

With some reservation the conclusion can be drawn that the "particle" size in the flowing mixture is primarily determined by the turbulence of the continuous phase and thus by the main stream Re-number. If very steep velocity gradients exist, however, the bubbles may be broken up by shearing forces. In accelerating flow the bubbles are "stretched" in the direction of their motion, which promotes further breaking-up. It is reasonable to state however that the formation of the bubbles e.g. on sieve plates or by evaporation is not decisive for the eventual bubble size unless coalescence is greatly impeded by surface active additives.

In view of the above determination of the bubble drag force based on a drag coefficient - vs - bubble diameter correlation is not feasible.

Acceleration with respect to surrounding liquid.

In the foregoing only steady flow conditions have been considered. A change in bubble velocity with respect to the surrounding liquid may occur however, when the driving and resisting forces acting on the bubble are not in equilibrium. Examples can be found in the process of bubble formation at an orifice, where the bubble accelerates from rest to its terminal velocity or in a gas-liquid mixture flowing through a restriction. In such cases the question arises whether the drag force is affected by the unsteady character of the flow around the bubble.

HUGHES and GILLILAND [24] reviewing the available literature, find an increase in the drag coefficient of drops, and solid spheres depending on the acceleration. For very low Re-numbers where inertia of the surrounding fluid in negligable a mathematical solution of the unsteady flow equations around a sphere due to Bassett is presented. The correction of the drag coefficient given for high Re-numbers appears to be fully attributed to the virtual mass force. Apparently correction on the drag coefficient proper is only necessary for very low Re-numbers, which fall outside the field of interest ★). The "virtual mass effect", which seems to be the only significant addition to the nonsteady bubble resistance, is the subject of the next section.

3.1.2.3. Virtual mass.

The effect of the virtual mass accounted for in equation (3-6) by the second term is an inertia force and thus a force resisting any change in the relative motion of the disperse phase. While there are no doubts about its effect on "particle" motion, the physical explanation of the phenomenon is less clear cut. Although treated as an increase in inertia of the particle for the duration of the relative particle acceleration and hence named "virtual" or "added" mass, it is in fact the inertia of the surrounding liquid disturbed by the relative movement of the particle that is responsible for the effect. An observer, moving with the particle, would notice the flow is unsteady in case the particle velocity changes with respect to the undisturbed flow. The pressure distribution he would measure at the particle surface will be different from that for steady flow. For the latter case this pressure distribution is solely a result of the irreversabilities of the flow constituting the hydraulic resistance that is called the particle drag. For the accelerating bubble a component resulting from the unsteady part of the velocity distribution around the bubble is added to the pressure distribution.
The inertia forces of the liquid are thus imparted to the particle by pressure forces at the phase boundaries of the mixture. From this indirect nature of the virtual mass force stems a controversy as to how the momentum balance equation for a mixture should be composed. This problem shall be dealt with in section 3.2.1.
Let us first consider the problem in its simplest from: the unsteady motion of a sphere in an unbounded fluid. For frictionless irrotational flow the pressure distribution over the surface of the sphere can be calculated. The velocity potential for a doublet and a parallel flow is substituted in the Bernoulli equation which is subsequently integrated over the surface of the sphere giving the resulting pressure force on the sphere. The calculus is given in many handbooks on fluid dynamics, for instance in [25]. The resulting acceleration force on the sphere is

$$F_{acc} = (\frac{\pi}{6} d^3 \rho_p + \frac{\pi}{12} d^3 \rho_f) \frac{du_p}{dt} \qquad (3\text{-}21)$$

The outcome, equation (3-21), makes it clear why the name virtual or added mass is used. The real mass of the sphere is increased by an amount equal to half the liquid displaced, and the equation of motion for the submerged sphere can be written according to Newton's second law if this mass correction is made. The analysis makes use of the velocity potential which is dependent on the form of the submerged body. The more streamlined the body the smaller the virtual mass and vice versa.
Equation (3-21) can also be written as

$$F_{acc} = \frac{\pi}{6} d^3 (\rho_p + B.\rho_f) \frac{du_p}{dt} \qquad (3\text{-}22)$$

★) *An indirect effect is constituted by the bubble deformation as already mentioned in the discussion on bubble size in the flowing mixture. An elongation of the bubble in the flow direction may occur reducing the form drag.*

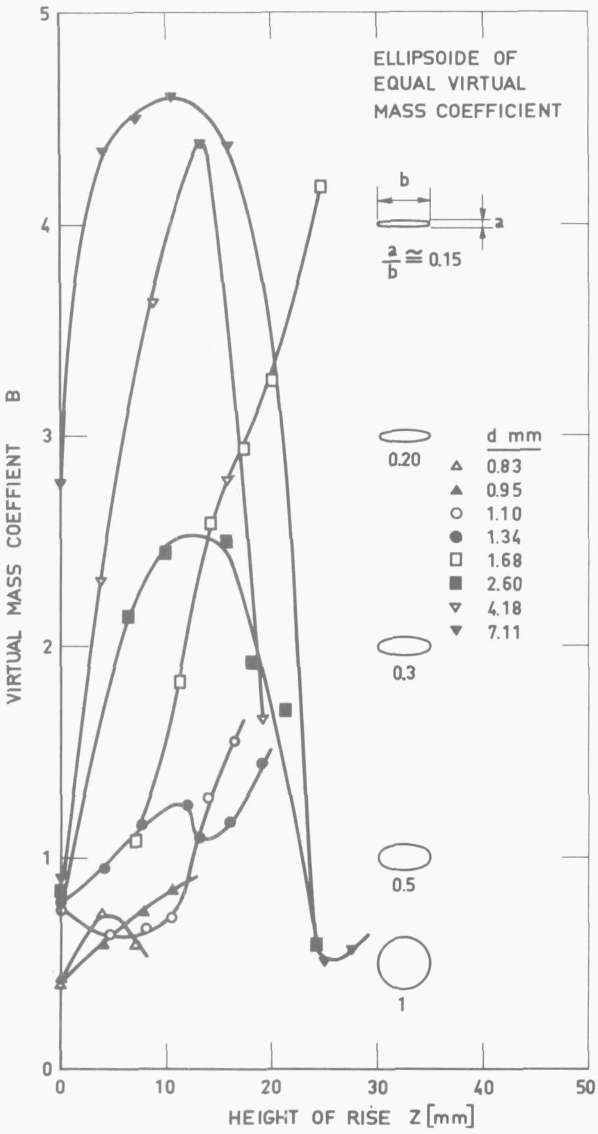

FIGURE 3-6.

Calculated virtual mass coefficients from experiments with rising bubbles.

where B is the virtual mass coefficient equal to 0.5 for a sphere.
In case the surrounding fluid is not unbounded or more than one sphere is present the potential function will also take a different form resulting in a different value for B. For a real two-phase mixture it becomes virtually impossible to find an expression for the potential function and an exact solution for B is out of the question; the value of B has to be found from experiment.
Taking the accelerating bubble as an example to illustrate the effect of deformation on B, measured values of u, $\frac{du}{dt}$ and C_D are to be inserted in equation (3-5) in order to find the corresponding values of the virtual mass coefficient. Such experimental data can be obtained from the acceleration part of the velocity-distance curves for rising bubbles of AYBERS and TAPUCU [9].

By putting

$$\frac{du}{dt} = \frac{du}{dz} \cdot \frac{dz}{dt} = \frac{1}{2} \frac{du^2}{dz}$$

equation (3-5) reduces to

$$B = \frac{2g - \frac{3}{2} \frac{C_D}{d} u^2}{\frac{du^2}{dz}} \qquad (3\text{-}23)$$

Measured values of u^2 are replotted as a function of the vertical position coordinate z. The slope of this plot together with C_D value's for the appropriate Re-numbers calculated for the terminal velocities of [9] were taken to evaluate equation (3-23) for several bubble diameters during their initial motion. Figure 3-6 shows the result. Ellipsoīdes of corresponding B-value [26] are also depicted to illustrate the bubble deformation. Some interesting observations can be made from this diagram. First it is clear that on the average the virtual mass increases with bubble diameter, which is clearly a result of increased deformation. Furthermore most of the bubbles show a growing value of B, at least at the start, as they rise. This indicates that the bubble is closet to spherical (B = 0.5) at the moment of release and that deformation sets in as the relative velocity becomes larger. For bubble diameters above 1.68 mm a maximum appears in the value of B. Apparently the bubble returns to a more spherical shape. Although it should be mentioned that the error in equation (3-23) becomes larger on coming close to the terminal velocity, the trend of the curves in figure 3-6 seems to be pertinent. Moreover the return to spherical shape of the three bubbles in question is in accordance with the values of the drag coefficient for "aged" bubbles calculated from [9] and shown in figure 3-1 and 3-2, which fall below the data of others. The conclusion given in section 3.1.2.1., that the bubbles had not reached their "terminal deformation" is corroborated. Oscillations of bubble forms are also to be seen in the photographs of PATTLE [27] and a photograph presented in the discussion of the conference papers [15], [17], [27].

An attempt to correlate the B-values with the We-number fails. A good correlation was shown in case of the drag coefficient, where deformation also plays a role but where the bubble form is more or less stable. For bubble form oscillations as presented in figure 3-6 the We-number is not the only correlating parameter.

In general it can be said the virtual mass coefficient increases with bubble diameter. Acceleration may have a flattening effect on small bubbles, therby further increasing B. Larger bubbles may be elongated, decreasing B. This last effect can be seen in the photographs of MUIR and EICHHORN [28] where an air water mixture flows through a converging diverging nozzle. As the bubble approaches the throat the bubble is streched, taking a more spherical form again upon entering the diffuser.

The presence of other bubbles has an effect on the virtual mass, a phenomenon that was also found for the drag coefficient but even less literature exists than in the latter case. ROSE and GRIFFITH [30] have performed experiments from which an idea may be formed concerning the effect of the presence of other bubbles. They measured the momentum flux of an air water mixture ejected from a pipe on a turning Tee thus diverting the flow at right angles from its original direction. The force on the Tee, which is equal to the momentum flux of the two-phase jet, was measured.

For a homogeneous flow with no slip, locally and averaged over a cross section, the momentum flux is given by

$$M = \rho_m v^2_{sm} A \qquad (3\text{-}24)$$

Introducing a momentum multiplier MM

$$MM = \frac{M}{G^2 A} \qquad (3\text{-}25)$$

Allowing for slip between the phases, PRINS [31] showed that the momentum flux should also contain a term accounting for the virtual mass.
The momentum multiplier as defined by equation (3-25) becomes

$$MM = \frac{x^2}{\alpha}\left[\frac{\rho_g + B\rho_\ell}{\rho_g^{\,2}}\right] + \frac{1-x}{1-\alpha}\left[\frac{\rho_g - x(\rho_g + B\rho_\ell)}{\rho_\ell \rho_g}\right] \qquad (3\text{-}26)$$

Experimental data of ROSE and GRIFFITH [30] for x, α and MM can be inserted in equation (3-26) to give the virtual mass coefficient pertaining to the flow conditions ofthe mixture upon entering the measuring Tee as shown in figure 3-7.

Compared with the high values of the virtual mass for single bubbles figure 3-7 shows a strong influence of the void fraction. The value of B rapidly falls off with the void fraction and becomes zero for α > 0.5.

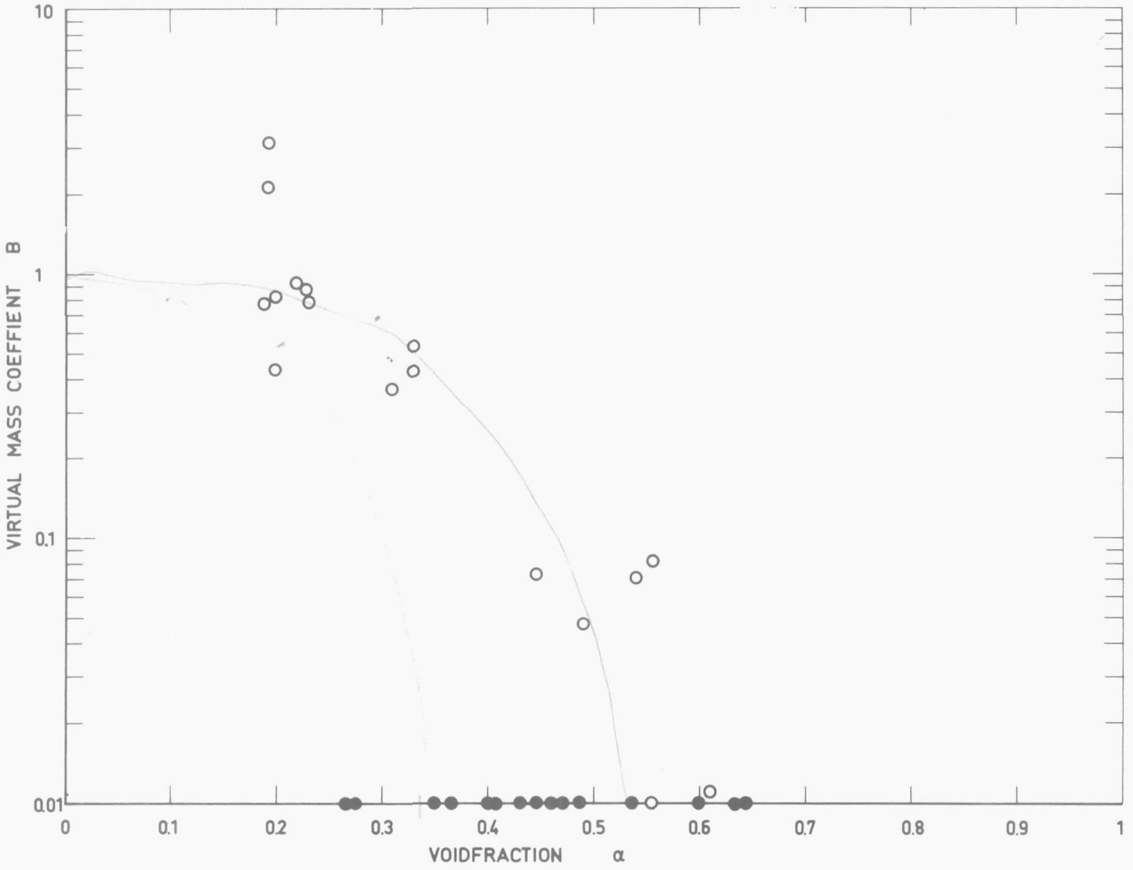

FIGURE 3-7.

Influence of void fraction on virtual mass.

The accuracy of this curve is rather low, however, due to the scatter in the experimental momentum flux values and the errors involved reading the graphs in [30]. The solid points indicate negative calculated values of B, which are plotted as B = 0 in figure 3-7, because it is physically impossible to have a negative virtual mass. As an example of the order of magnitude that is to be expected for B in a flowing mixture figure 3-7 serves a purpose.

3.1.3. Outline of analysis.

After having illustrated the interactions and effects for concurrent gas and liquid flow where the gas is the disperse phase, the equations of motion for the phases in the separation process remain to be given.
For axisymmetric flow the process can be described in a two coordinate system. The pertinent set of equations will be called the two dimensional model. As will be clear from the foregoing sections two important parameters are still quantitatively unknown. The drag coefficient divided by the "bubble diameter" and the virtual mass coefficient in a flowing mixture.
For the purpose of obtaining these an auxiliary investigation was started, comprising a one-dimensional model based upon the same interaction forces as in the two-dimensional model and an experiment that could be considered as one-dimensional.

The results of these auxiliarly tests will subsequently be used when solving the two-dimensional model equations.

3.2. One-dimensional model.

3.2.1. Basic equations.

In order to derive the one-dimensional conservation equations some simplifying assumptions must be made. An immediate consequence of the one-dimensional character are the following two assumptions:

- Both phases are uniformly distributed over a channel cross section. This implies that no Bankoff slip can be taken into account, which has consequences when comparing this model with experimental data.
- Changes in cross sectional area are gradual enough to have no influence on the first assumption. No flow separation in a divergent channel or contraction following an area reduction is assumed to occur.

A listing of the remaining, more general, assumptions contains the following items:

- The flow is steady. All variables are independent of time in the Eulerian coordinate system.
- High Re-numbers. Apart from the drag forces of the disperse phase and wall friction all viscous effects are neglected.
- No heat exchange takes place with the channel wall; adiabatic flow.
- The gas phase is not contributing to the wall friction.
- The phases are in thermodynamic equilibrium. The gas phase acts as a perfect gas for air-water mixtures and is assumed incompressible for high pressure steam-water mixtures.
- Change of state of the gas phase is isothermal
- The liquid is considered incompressible.

3.2.1.1. Conservation of mass.

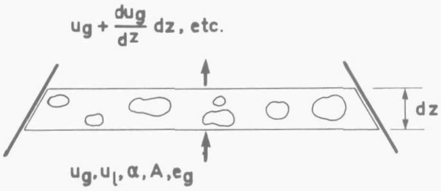

FIGURE 3-8.

Control volume for mass considerations.

Figure 3-8 shows a section dz of a one-dimensional channel of variable cross section A.

The mass inside the control volume remaining constant in time the balance equation yields

$$\frac{d}{dz}\left(\rho_g \alpha A u_g\right) + \rho_\ell \frac{d}{dz}\left((1-\alpha) A u_\ell\right) = 0 \qquad (3\text{-}27)$$

The mixture quality is introduced by the definition

$$x = \frac{\rho_g \alpha A u_g}{\phi} \qquad (3\text{-}28)$$

Substitution of equation (3-28) in (3-27) and subsequent integration gives

$$\rho_\ell (1-\alpha) A u_\ell = (1-x)\phi \qquad (3\text{-}29)$$

It should be noted that in the one-dimensional channel no difference can be made between local and average values at a cross section. The <>-signs are therefore dropped when applying conservation laws to figure 3-8.

3.2.1.2. Conservation of momentum of the gas phase.

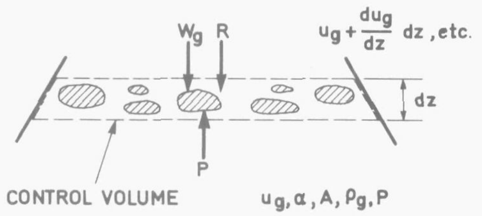

FIGURE 3-9.

Control volume for momentum considerations of gas phase.

The momentum balance equation of the gas phase is essentially equal to the equation of motion for a single particle given in equation (3-6).
The particle volume is replaced by the total volume of the gas within the control volume designated by the shaded areas in figure 3-9. The boundaries for the gas phase are the gas-liquid interfaces within the control volume. The void fraction $<\alpha>$ being the amount of gas in a unit volume, the gas volume considered, dropping the <>-signs, now becomes $\alpha A dz$.
Conservation of momentum requires that the change of momentum inside the control volume, which is zero, is equal to the net momentumflux in- and out the control volume plus the sum of all external forces.
One of the external forces is the virtual mass force. It was shown in section 3.1.2.2. that the effect of this force could be regarded as that of a, virtual, amount of water travelling with the gas. Although not correct in a strict physical sense, this liquid envelope concept of the virtual mass makes it possible to regard it as part of the momentumflux. The advantage of this representation is that the problem of unknown liquid velocity potential for the flow around the bubbles is evaded. The amount of liquid in the envelopes is $B\alpha\rho_\ell$ per unit volume, having a momentum of $B\alpha\rho_\ell(u_g-u_\ell)$.
The other forces are weight W_g, pressure force P and the resistance force R, all given per unit volume. If n is the number of gas bubbles per unit volume the drag force per unit volume becomes

$$R = n \cdot C_D \frac{\pi}{4} d^2 \cdot \tfrac{1}{2}\rho_\ell(u_g-u_\ell)\,|u_g-u_\ell| \qquad (3\text{-}30)$$

where the number of bubbles must be equal to the fraction of gas in a unit volume divided by the bubble volume, thus

$$n = \alpha / \frac{\pi}{6} d^3 \qquad (3\text{-}31)$$

combining equations (3-30) and (3-31)

$$R = \frac{3}{4}\alpha \frac{C_D}{d} \rho_\ell(u_g-u_\ell)\,|u_g-u_\ell| \qquad (3\text{-}32)$$

The momentum equation for the section of figure 3-9 now reads

$$-\frac{d}{dz}(\alpha A \rho_g u_g^2)dz - \rho_\ell \frac{d}{dz}(B\alpha A u_g(u_g-u_\ell))dz + PAdz - W_g Adz - RAdz = 0 \qquad (3\text{-}33)$$

with

$$P = -\alpha \frac{dp}{dz} \qquad (3\text{-}34)$$

and

$$W_g = \alpha g \rho_g \qquad (3\text{-}35)$$

Substitution of equations (3-32), (3-34) and (3-35) in (3-33) gives the momentum equation for the gas phase

$$\frac{d}{dz}(\alpha A \rho_g u_g{}^2) + \rho_\ell \frac{d}{dz}(B\alpha A u_g(u_g - u_\ell)) =$$

$$= -\alpha A \frac{dp}{dz} - \alpha A \rho_g g - \frac{3}{4}\alpha A \frac{C_D}{d} \rho_\ell (u_g - u_\ell)\,|u_g - u_\ell| \qquad (3\text{-}36)$$

3.2.1.3. Conservation of momentum of the liquid.

The momentum balance for the liquid in the control volume is derived in the same manner as was done for the gas. The liquid is now represented by the shaded area in figure 3-10.
The boundaries are the external boundaries of the control volume and the internal gas-liquid interfaces. The momentum equation for the steady state is now written as

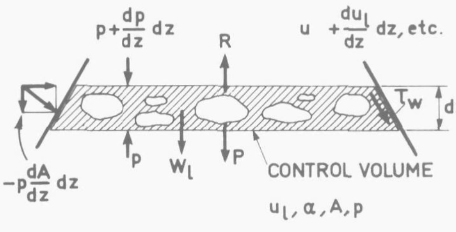

FIGURE 3-10.

Control volume for momentum considerations of liquid phase.

$$-\rho_\ell \frac{d}{dz}((1-\alpha)Au_\ell{}^2)\,dz - \frac{d}{dz}(pA)dz + p\frac{dA}{dz}dz - PAdz - W_\ell Adz +$$

$$+ RAdz - \tau_w Odz = 0 \qquad (3\text{-}37)$$

With $W_\ell = (1-\alpha)\rho_\ell g$ (3-38)

and equations (3-32) and (3-34) equation (3-37) becomes

$$\rho_\ell \frac{d}{dz}((1-\alpha)Au_\ell{}^2) = -(1-\alpha)A\frac{dp}{dz} - (1-\alpha)A\rho_\ell g +$$

$$+ \frac{3}{4}\alpha A \frac{C_D}{d}\rho_\ell(u_g - u_\ell)\,|u_g - u_\ell| - \tau_w O \qquad (3\text{-}39)$$

The above derived momentum equations are based upon the liquid envelope concept as far as the virtual mass is concerned. Some inconsistency could be noted, however, with regard to the treatment of the virtual mass force and the other forces: the pressure force and the drag force. For the last Newton's third law is applied, and consequently P and R in equations (3-33) and (3-37) are equal but of opposite sign. It seems controversial therefore that the virtual mass force is ommitted from equation (3-37). HINZE [34] has in fact called attention to this controversy. If the virtual mass force is included in the equation for the liquid the whole effect would cancel out in the equation of the mixture, which is the sum of the gas and liquid equations. If on the other hand equations (3-33) and (3-37) are used it is evident that, in case of an accelerating flow, not only the rate of change of the slip is influenced by the virtual mass but its effect could also be measured as an increase in pressure drop. This last approach was shown to be correct by HINZE [34], who considered a control volume containing liquid and a spherical particle, both moving in the same direction with different speeds.

The momentum balance equation for the control volume in the direction of motion is

$$F = \frac{dM}{dt} + M_{out} - M_{in} \tag{3-40}$$

The force F is the resultant of the pressure forces at the boundary. Assuming irrotational frictionless flow the Bernoulli equation gives the pressure at the boundary and F is found from integration over the surface. In this example the momentum flux in and out of the control volume is equal and cannels out leaving only the term $\frac{dM}{dt}$. The velocity potential for the liquid flow together with the Bernoulli equation are then used to compute the surface integral of the pressure force F. From the velocity potential the liquid velocity is obtained with which the momentum of the liquid inside the control volume is found.
Finally Hinze arrives at the momentum equation for the, aforementioned, control volume

$$-\frac{4}{3}\pi Q_c^{\,3}\left(\frac{dp}{dx}\right) = \rho_\ell \frac{4}{3}\pi(Q_c^{\,3} - Q_p^{\,3})\frac{du_{\ell\infty}}{dt_\ell} + \rho_p \frac{4}{3}\pi Q_p^{\,3}\frac{du_p}{dt_p}$$

$$+ \rho_\ell \frac{2}{3}\pi Q_p^{\,3}\left(\frac{du_p}{dt_p} - \frac{du_{\ell\infty}}{dt_p}\right) \tag{3-41}$$

Where $u_{\ell\infty}$ is the velocity of the undisturbed liquid and Q_c the radius of the control volume. Equation (3-41) clearly shows that the equation for the system-liquid and particle contains the virtual mass in the last term. Furthermore this term in independent of Q_c, which proves that the mixture momentum equation for any control volume, including the section of the flow channel that served to derive equations (3-33) and (3-37) should contain the virtual mass term and consequently the liquid equation cannot.
Furthermore equation (3-41) shows that Newton's law is not violated because the effect of the virtual mass is felt at the external boundaries of the liquid control volume. Strict formulation should in fact show, by applying Newton's law, the virtual mass force working on the external boundary as well as on the gas-liquid interface but with opposite sign.
The conclusion is that the liquid envelope concept is physically acceptable for deriving the momentum equations.
The question may still arise, however, in what respect the drag force R is different from the virtual mass force and does appear in the equation for the liquid. The relative movement of the particle or bubble causes a velocity defect in the liquid velocity profile behind it. The associated momentum defect for the system of equation (3-40) is according to HINZE [34]

$$M_{out} - M_{in} = -\rho_\ell \int_{\Delta A_c} u_{\ell\infty} \cdot u_\ell \, dA_c = -R_p \tag{3-42}$$

where the drag force of the single particle is designated by R_p.
Substitution in equation (3-40) shows that the drag force will only appear in the equation for the mixture and that for the gas phase and that there is indeed no difference between drag and virtual mass in this respect.
It is however customary to omit the drag force in the equation for the mixture while the momentum defect caused by the gas slip is tacitly assumed to be accounted for in the momentum flux of the liquid.

3.2.1.4. Conservation of momentum of the mixture.

The conservation equation for the mixture is found by adding equations (3-36) and (3-39)

$$\frac{d}{dz}(\rho_g \alpha A u_g{}^2) + \rho_\ell \frac{d}{dz}((1-\alpha)A u_\ell{}^2) + \rho_\ell \frac{d}{dz}(B\alpha A u_g(u_g-u_\ell)) =$$

$$- A\frac{dp}{dz} - A(\alpha\rho_g + (1-\alpha)\rho_\ell)g - \tau_w 0 \qquad (3\text{-}43)$$

Although not mentioned in the list of assumptions at the beginning of section 3.2.1. it is clear that no momentum transfer due to change of phase is accounted for in the equations of the separate phases. This effect is postulated to be negligible for both the air-water and the high pressure steam-water mixtures.
The above assumption only holds if the change in mixture quality or the momentum transfer associated with it is negligible. This is shown by two representative examples in Appendix 3-A.

3.2.2. Method of solution.

The system of mass- and momentum equations constitute a set of four independent simultaneous first order differential equations viz. two of the three equations (3-36), (3-39) and (3-43) and two mass balances, because the two terms of equation (3-27) are separately equal to zero when no change of phase occurs. There are also four unknowns: u_g, u_ℓ, α and p. By elimination of the velocities u_g and u_ℓ, with the use of equations (3-28) and (3-29), where the quality is now a constant for the whole channel, the number of equations is reduced to two, with α and p as unknowns. The highly non-linear character of these equations make numerical integration necessary. The Runge-Kutta method, described in most handbooks on numerical analysis, was selected for this purpose.
In order to apply this method the equations were written in the form

$$\frac{d\alpha}{dz} = f(\alpha,p,A,\frac{dA}{dz},\rho_g,\frac{d\rho_g}{dp},B,\frac{C_D}{d},z,\text{constants}) \qquad (3\text{-}44)$$

$$\frac{dp}{dz} = f(\alpha,p,A,\frac{dA}{dz},\rho_g,\frac{d\rho_g}{dp},B,\frac{C_D}{d},z,\text{constants}) \qquad (3\text{-}45)$$

The differentials $\frac{d\rho_g}{dz}$ and $\frac{dA}{dz}$ must also be written in terms of local variables. According to the list of assumptions the gas either behaves as an ideal gas undergoing an isothermal change of state or is saturated steam so so that the values of ρ_g and $\frac{d\rho_g}{dp}$ can be taken from the steam tables [33].
In the former case, where the gas is saturated wet air, the density is given by BAEHR [32] as

$$\rho_g = \frac{p}{R_{gd}T} - (\frac{1}{R_{gd}} - \frac{1}{R_{gw}})\frac{p_{sat}}{T} \qquad (3\text{-}46)$$

Differentiation of equation (3-46) gives

$$\left(\frac{d\rho_g}{dp}\right)_T = \frac{1}{R_{gd}T} \qquad (3\text{-}47)$$

The derivative $\frac{dA}{dz}$ could be found from a function of the cross sectional area in terms of the coordinate z. For the sake of simplicity the channel is subdivided into a series of segments Δz that are small enough for the area to be approximated by a linear relationship. Thus the area in the i-th segment, lying between coordinates z_i and z_{i+1} is

$$A_z = A_i \{1+(\sigma_i-1)\frac{z-z_i}{\Delta z_i}\} \qquad (3\text{-}48)$$

where

$$\sigma_i = \frac{A_{i+1}}{A_i} \qquad (3\text{-}49)$$

accordingly

$$\left(\frac{dA}{dz}\right)_i = \frac{A_i(\sigma_i-1)}{\Delta z_i} \qquad (3\text{-}50)$$

A computer program was written to perform the integration procedure outlined above. The program, called VAPOM, was written in ALGOL. It requires the starting values for the variables at the begin of the flow channel as input together with the constants pertaining to the mixture and channel geometry. A starting value for the integration step length for each section must also be given. The program halves the step length h automatically until the values of α and p found after a given number of steps calculated with step length h deviate no more than a specified percentage ε from the values obtained with step length 2h. This feature was deemed necessary to avoid too large errors when the gradient of the variables α or p becomes large. The program can be run for the conditions of the experiments suggested in section 3.1.3., to compare the calculated and experimental void fraction and pressure as a check on the expressions for C_D/d and B that are to be fed into the program. Apart from these expressions a correlation for the wall shear stress τ_W appearing in equations (3-39) and (3-43) has still to be given.
The auxiliary experiments to be described in the next sections deal with a direct measurement of the wall shear stress and the evaluation of C_D/d and B-values from the flow through channels of variable area.

3.2.3. Auxiliary experiments.

3.2.3.1. Wall shear stress measurements.

3.2.3.1.1. Principle of measuring technique.

Direct measurement of the wall friction from pressure difference measurements is not possible in two-phase flow. The alternative is to measure the shear force exerted on the channel wall as a result of the friction of the flowing mixture. A portion of the channel wall is suspended freely from the rest of the wall and kept in alignment with it. The force to keep the free section axially in place is then related to the shear force.

ARMAND [35] measured the shear force of air-water mixtures exerted on a 5 m long suspended section of a 26 mm diameter tube. MALNES [36] describes a similar method, where a 2.05 m section of a 24.7 mm bore tube is used. In Both instances the force on the suspended section was measured by means of a mechanical force balancing system.
CRAVEROLO c.s. [37] developed an hydraulic technique for balancing and measuring the shear force on a 80 mm section of a 25 mm diameter tube. The section can move freely up and down, guided in three ring seals, two near the ends and one halfway the section. By controlling the pressure in the two annular spaces formed by the seals, the section and the external housing, the section can be positioned between the stationary tube sections.
The first two systems have the disadvantage of averaging the friction over a considerable length. Because the void fraction for air-water mixtures may change over the height due to the expansion of the air, correlation of the results may be difficult. Also in the method of Malnes the ends of the suspended section are guided in the surrounding housing by an annular gap, through which water flows as a result of pressure differences over this gap, which influence the results. Armand used bellows to connect the suspended section with the stationary tube.
Furthermore the three experiments pertain to small bore tubes, while the hydraulic diameter for the flow through cyclones are much larger. The force balance for a suspended section is given in figure 3-11.a.

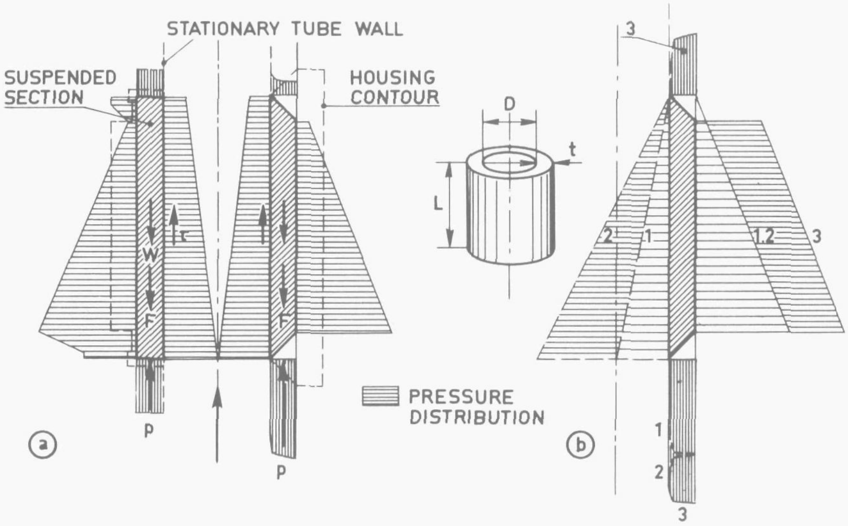

FIGURE 3-11. Forces and pressure distribution on the measuring section of shear stress meter.

The figure shows the pressure distribution over the surface of the suspended section by shaded area's. The pressure in the housing is constant and due to the hydrostatic head of the stagnant water. The pressure inside the flow channel is dependent on the hydrostatic head and the frictional pressure drop which is not constant. The housing contour given in the far left side corresponds to the situation of references [36], [37] where the pressure in the flow channel also acts on the end faces of the suspended section. Disregarding friction due to flow through the seals the force balance is

$$W \pm F = \tau\pi\, DL + \left(\frac{dp}{dz}\right)_{TPF} \pi\, DtL \qquad (3\text{-}51)$$

It is clear that not only the balancing force F has to be measured but also the pressure gradient in the flow and that an error in the pressure gradient has a direct effect on the accuracy of the shear stress.
In the design of the shear stress meter for the present investigation an

attempt was made to overcome the errors due to flow through the seals and the pressure working on the end faces of the suspended section. The consequence of omitting the seals is a different alignment and guiding system that will be described in the next section. Furthermore even though the axial gaps between the connecting tubes and suspended section were made small a leakage flow between housing and flow channel sets in.
The resulting force is now perpendicular to the balancing force F, however, and has no contribution to the force balance of equation (3-51), but the pressure distribution in the radial gap is unknown, making it impossible to determine the buoyancy force, represented by the last term in equation (3-51). To remedy this problem the end faces of suspended section and connecting tubes were bevelled off at 45°C, as shown in the right hand side if figure 3-11.a. The pressure in the widening gap is now essentially the housing pressure. By applying Bernoulli's equation for the flow through the gap it is found that the deviation of the actual pressure in the gap from the housing pressure is about 8% of the pressure difference existing between the housing and the channel. By taking a zero reading of the balancing force F with the test loop and housing filled with water and no flow through the test section the shear stress can be calculated from the measurements of F under flow conditions using

$$F = \tau \pi DL \tag{3-52}$$

Figure 3-11.b shows that an increase of the housing pressure does not disturb the force balance of the suspended section because the increase is the same on both end faces, thus cancelling out. Slight overpressure was sustained during the experiments to ensure a purge flow of water from the housing to the test tube.

3.2.3.1.2. Experimental equipment.

The shear stress meter [38] consists of a measuring section having the same inside diameter as the connecting tubes, i.e. 0.114 m, and 0.35 m of height. The suspended section was made of aluminium of 1 mm wall thickness with a 1 mm perspex liner to give it the same inner surface as the rest of the perspex loop.
Three circular ribs on the outside carry two sets of flat springs as shown in figure 3-12. The spring mounts of the springs labeled A can move in three perpendicular directions to adjust aligment.
The mounts themselves can be moved up and down together to obtain equal axial gaps at the top and bottom of the suspended section for zero conditions.

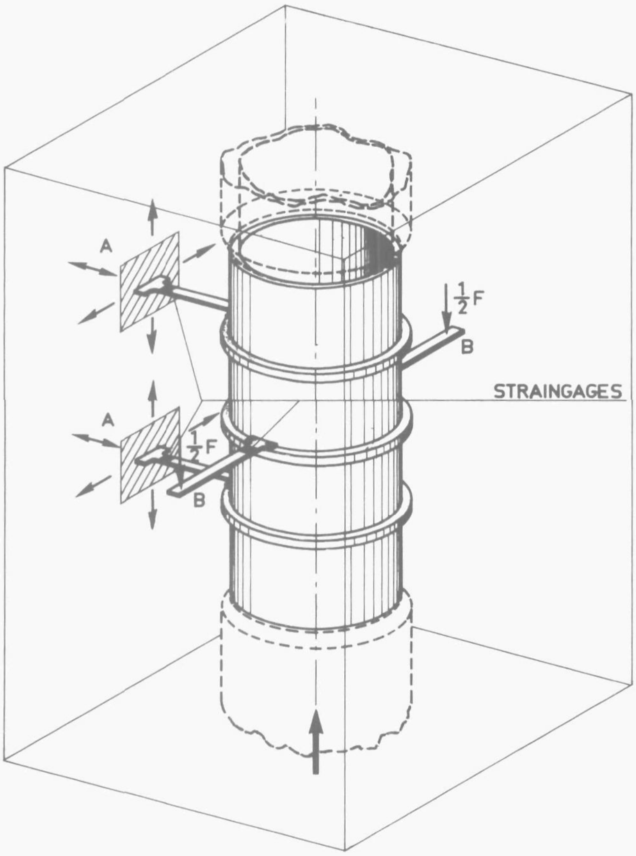

FIGURE 3-12.

Measuring section of shear stress meter.

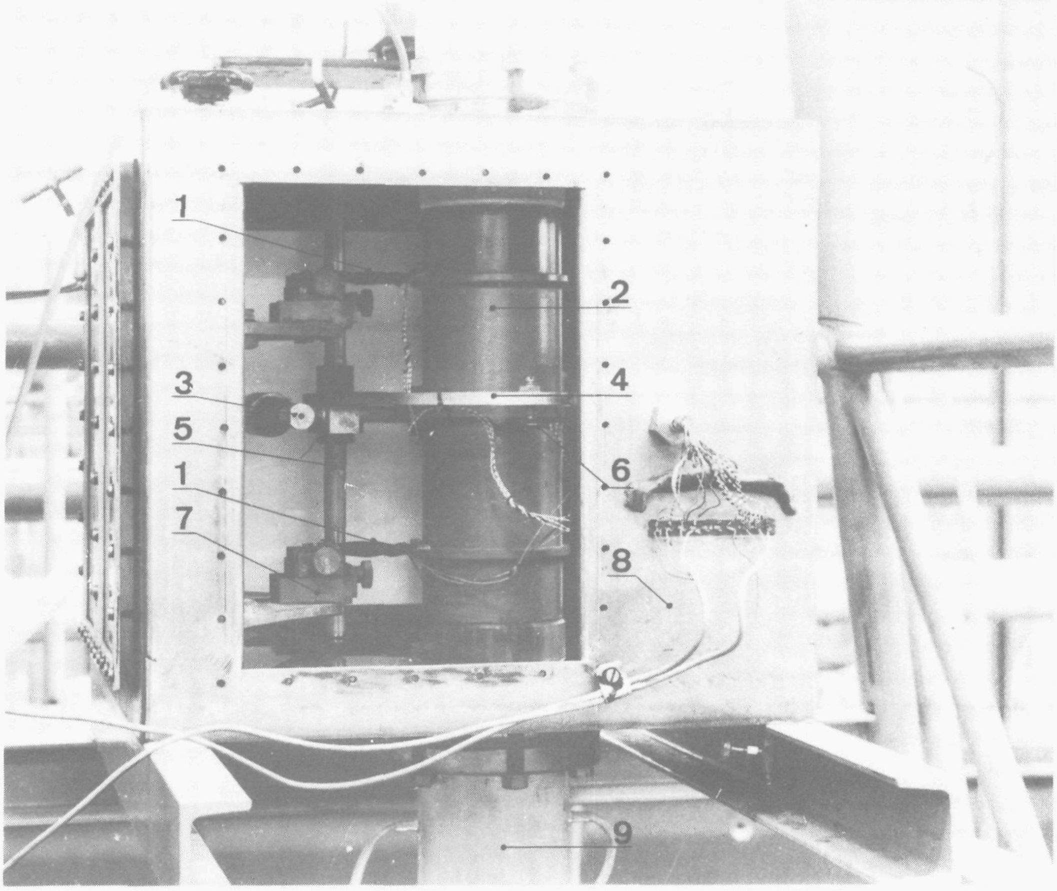

1 SPRINGS "A"
2 SUSPENDED MEASURING SECTION
3 BALANCING FORCE RING SUPPORT
4 BALANCING FORCE RING
5 POSITIONING SPINDLE FOR
BALANCING FORCE RING
6 SPRING "B"
7 ALIGNMENT ADJUSTMENT
8 HOUSING
9 CALMING SECTION

FIGURE 3-13.

Shear stress meter.

Two other springs, labeled B, that are fitted perpendicular to the A-springs carry the balancing force F. This is done by means of a ring placed around the suspended section, which can be moved up and down on a spindle and has two point contacts on the ends of springs B. The springs were made of steel with a cadmium anti-corrosion layer. Springs A are 1 cm wide, 6 cm long and 1.5 mm thick, while springs B have the same width and length but are 0.8 mm thick.

Strain gages were glued to the springs at locations shown in figure 3-12. For greater output gages were used on both sides of the springs to measure both tensile and compression strain. The two sets of four gages are connected to form two complete bridges A and B. Unbalance of each bridge during spring deflection is measured with Peekel electronic strain meters. Figure 3-13 gives an impression of the suspended section and housing. In order to obtain the value of the applied balancing force F the spring-strain gage system B was calibrated. One end of the beam of a pair of scales was connected to the suspended section, after removing the connecting tubes, while weights were placed on the scale of the other end. Thus the section was pulled upwards by the weights.

The force-strain relation proved to be linear and could be expressed by

$$F = (\frac{19}{130}\,\varepsilon + \tfrac{1}{2})\ 0.0098\ [N] \qquad (3\text{-}53)$$

where ε is the microstrain read from the strain meter. The scatter in the data was ~ 1% for $F < 0.3$ N and less than 0.5% for larger forces.
It should be noted here that the shear forces measured were very small, ranging from 0.125 to 2.25 N.
The test rig in which the shear stress measurements were made has a recirculation loop for water, while air is mixed with the water and vented to the atmosphere after passing through the test section. The water is circulated by a KSB-centrifugal pump of max. 110 m^3/h with a max. pressure head of 31 m. As illustrated in figure 3-14 the water flows through a venturi flowmeter of VDI [39] design. Upon entering the test section the water is mixed with air and flows vertically upwards. An annular mixer is employed from which the air is blown through small holes in the tube wall into the water stream.

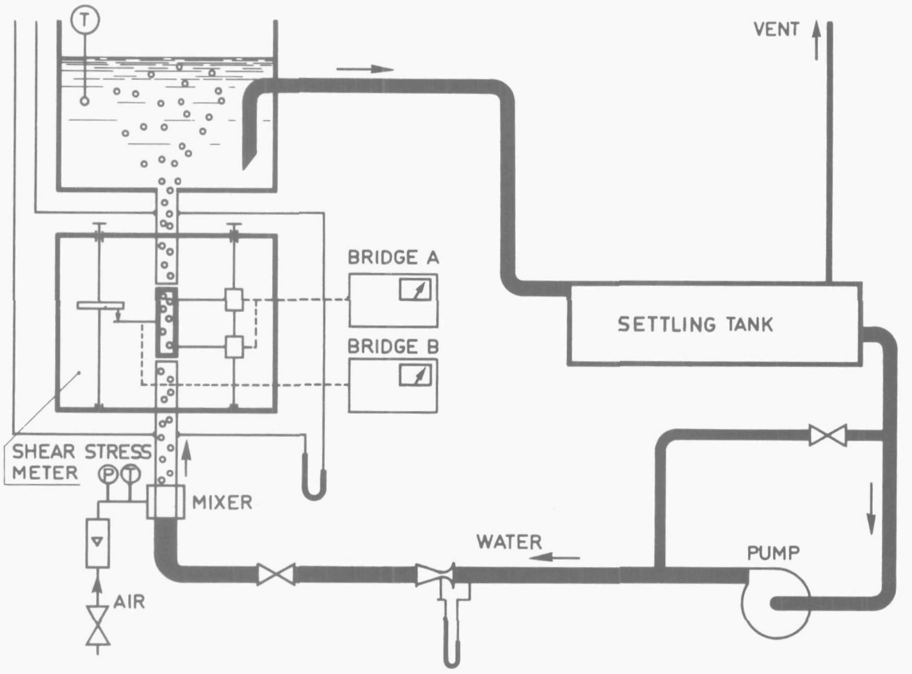

FIGURE 3-14.

Air-water test loop for shear stress measurements.

A flow straightener is situated immediately downstream of the mixer to prevent any swirl in the test section. The test section between mixer and suspended section is 1 m long. After passing through the shear stress meter the mixture enters into a tank where part of the air is separated by gravity. The water with the remaining air flows into a settling tank where the air escapes before the water enters the pump. The water flow was adjusted by means of a valve and a pump-bypass. The air admitted to the mixer from a compressed air system is measured by a Fisher and Porter rotameter, maximum flow rate 20 Nl/s.
The pressure drop at the location of the shear stress meter was measured with waterfilled open manometer tubes. For small pressure drops a Van Essen U-tube manometer with nonius scale and filled with epichlorehydrine of 1100 kg/m^3 density was used.

3.2.3.1.3. Experimental procedure.

Prior to the measurements the suspended section was positioned halfway between the connecting tubes, leaving an axial gap of 0.45 mm on both sides. A zero reading for the springs A was then taken. Subsequently the pump was started and air admitted to the mixer. After setting the desired flow rates the balancing force was applied to the springs B by lowering the ring-mechanism until the suspended section was again in its zero position as indicated by the strain meter for bridge A. The strain meter for bridge B was then read together with the other measuring points. For a certain water flow rate a series of air flows were adjusted and readings taken. These series were repeated 5 times to check on reproducebility.

3.2.3.1.4. Results.

The range of superficial water velocities in the test section over which the measurements [40] were taken lies between 0.8 and 2.2 m/s. The lower limit was set by the very low shear stress and accordingly larger errors. The upper limit was due to the settling tank where entrainment of air to the pump and subsequent disturbance of the water and air flow measurements occured at higher water velocities.

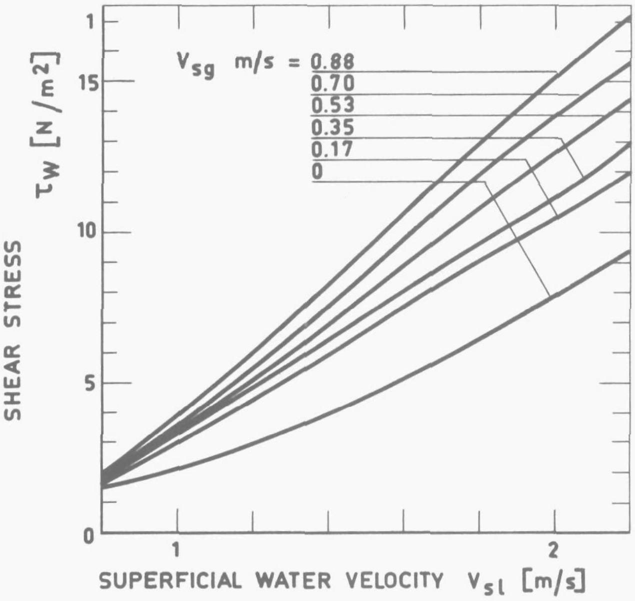

FIGURE 3-15.

Measured shear stress as a function of superficial water velocity for single and two-phase flow.

The air flow had to be limited to a maximum superficial velocity in the test section of 0.88 m/s. Void fractions up to 32% could be realized: at higher flow rates the flow regime became pulsating, inducing vibrations of the suspended section that made the strain meter readings unreliable. Furthermore the amplitude had to stay within the range of the axial gap tolerance of 0.45 mm. Recordings of the strain meter were taken on a Philips Schwarzer Oszilloscript which showed that for the above range of variables the maximum amplitude of the vibrations was 0.176 mm as compared to a 0.9 mm tolerance of the gaps. The Re numbers for the test section based on the average water velocity lie between 10^5 and 4×10^5. The quality of the mixture that can be calculated from the measured air and water flows ranged from 0.0001 to 0.014. The estimate of the average void fraction $<\alpha>$ was obtained from equation (3-43), assuming the acceleration pressure drop to be zero and inserting measured values of $\frac{dp}{dz}$ and τ_W. The measured shear stresses are presented in figure 3-15 where τ_W is plotted as a function of the superficial water velocity with the superficial gas velocity as parameter including the single phase values. To evaluate these results a comparison was made with the well-known Martinelli frictional pressure drop correlation which is discussed in section 3.1.1. [2]. The results of this comparison are shown in figure 3-16 for superficial air velocities of 0.53 and 0.88.

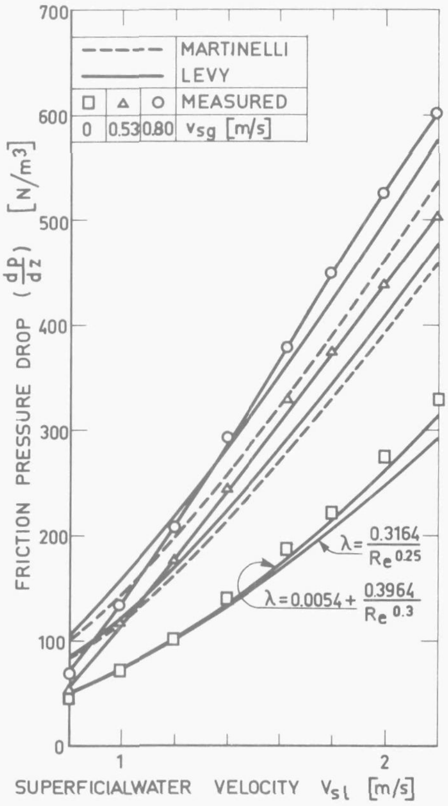

FIGURE 3-16.

Comparison of measured frictional pressure drop with predictions according to MARTINELLI [2] and LEVY [41].

The agreement is fairly good but for values of $v_{s\ell} < 1.2$ the measured values are closer to the single phase curve than the correlation. A better agreement was found with the simple correlation of Levy [41], which postulates that the two-phase multiplier is

$$\phi_{TP}^2 = \frac{1}{(1-\alpha)^2} \qquad (3\text{-}54)$$

This implies that the only effect of the presence of the gas-phase is to increase the water velocity. The friction pressure drop is thus correlated by the single phase friction factor corresponding to the single phase Re-number based on the true average liquid velocity

$$\left(\frac{dp}{dz}\right)_{TP} = \frac{\lambda}{D}\,\frac{1}{2}\,\rho_\ell\, u_\ell^2 \qquad (3\text{-}55)$$

Curves according to equation (3-55) with the measured single phase friction factors are also shown in figure 3-16.

For comparison of the single phase measurements values for λ were taken from the Blasius correlation [42]

$$\lambda = 0.3164\ Re^{-0.25}\ (3 \times 10^3 < Re < 10^5) \qquad (3\text{-}56)$$

and from Hermann [42]

$$\lambda = 0.00540 + 0.3964\ Re^{-0.3}\ (2 \times 10^4 < Re < 2 \times 10^6) \qquad (3\text{-}57)$$

The Blasius correlation shows an underprediction of the experimental data which is to be expected for $Re > 10^5$.
A crossover of the experimental two-phase curves and those predicted by equation (3-55) occurs at the lower water velocities. Whereas the flow may be considered fully developed for the single phase flow after a L/D ratio of 10 [14], which is corroborated by the agreement with equation (3-56) this may not be the case for two-phase flow and the deviation from the Martinelli and Levy correlations could be a result of this phenomenon. Comparison with other experiments where the entrance effects have died out should throw some light on this matter. The good agreement with equation (3-55) suggests a plot of the friction factor versus the Re-number based on u_ℓ. This kind of plot is also given by MALNES [36] for his data and provides a basis for comparison. Both sets of experimental points are presented in figure 3-17 (see page 116). The data of Malnes, for a 25 mm tube, and the those of the present investigation, for a tube of 114 mm, cover adjacent ranges of Re-numbers and show good connection. The calming section for the small diameter tube is 40 D. The low friction factors for the region of

Re between 7 × 10^4 and 2 × 10^5 are apparently systematic for two-phase flow and it seems reasonable to conclude that the short calming section for the larger tube had no appreciable influence on the wall friction. An influence of the gas flow rate is still evident but seems te become smaller at higher Re-numbers. The friction factors of drawn steel tubing [42] having a slight, wavy roughness, seem to fit the 0.114 m tube rather well suggesting that a sort of equivalent wall roughness can be ascribed to the presence of the gas bubbles. In case of large diameter vertical tubes the friction pressure loss is but a small part of the total pressure drop, the hydrostatic pressure drop giving the main contribution. For instance for a superficial liquid velocity of 2 m/sec and a void fraction of 26% the friction pressure drop is but 7% of the hydrostatic pressure drop. This percentage is 40 for a 25 mm tube for otherwise equal conditions. A great accuracy in determining the two-phase friction factor is therefore not required for large diameters. The use of a single phase friction factor correlation and the Levy two-phase multiplier may be 25 to 30% in error but has the advantage of being simple and easy to use.

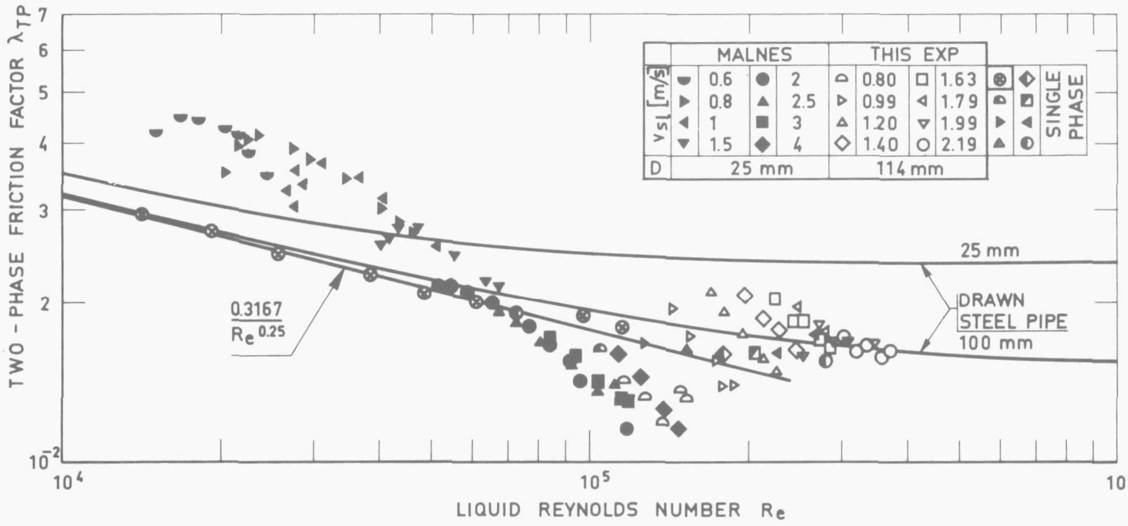

FIGURE 3-17.

Comparison of experimental friction factors of this experiment with those of MALNES [36] on a Reynolds number basis.

Extrapolation of these results to high pressure steam water mixtures seems dangerous. The friction pressure drop for a 70 bar steam-water mixture in a 114 mm tube at the same conditions as above is, according to the MARTINELLI-NELSON [43] correlation, 4% of the hydrostatic pressure drop. This would indicate that the use of Levy's multiplier at least for void fractions below 30%, is permissible.

The study of friction pressure drop presented here is superficial. Many more correlations than the two with which the measurements are compared here exist, such as can be found in the review given by TONG [44]. The Martinelli correlation was chosen because its use is widespread and has proven to give reliable results [4].

3.2.3.1.5. Conclusions.

Two-phase and single-phase wall shear stress measurements presented for superficial water velocities of 0.8 to 2.2 m/sec with void fractions up to 32% are in agreement with the calculation procedure proposed by LEVY [41].

It is suggested that this method be used for Re-numbers above 10^5 and large diameter tubes. The single-phase friction factor is to be chosen according to the Re-number involved and the condition of the tube concerning diameter and roughness. For Re-numbers of 10^5 and below large errors (30-60%) are involved which have increasing effect on the total pressure drop for decreasing tube diameter.

3.2.3.2. Void fraction measurement in accelerating flow.

3.2.3.2.1. Principle of measuring technique.

Unlike the wall shear measurements no tools are available for direct measurement of the interaction forces and an indirect method has to be introduced. The physical principles that constitute the one-dimensional model developed in section 3.2.1. deal with two interaction forces, the drag force and the virtual mass force. The effect of these forces appears in the slip and the rate of change of slip between the phases and the pressure distribution in the flow direction. Thus the slip or void fraction and pressure drop are indirect measures for the interaction forces and their relation is given by the momentum balances (3-36), (3-39) and 3-43).
Measurement of axial void and pressure distribution and subsequent substitution of these values in the integrated momentum balances would yield values for the interaction forces. Unfortunately the momentum equations are not accessible to exact solution and numerical techniques as described in section 3.2.2. have to be employed. Such solutions for various assumed values of the interaction forces have to be compared with the experimental results and the appropriate values are found by trial and error.

The design of the test section forms an integral part of the measuring technique. The pressure gradient in a channel of constant cross sectional area is comparatively small and almost constant. The slip comes close to an equilibrium value and after a long entrance region a pseudo-fully developed flow is established. Especially for vertical low pressure gas-liquid mixtures expansion of the gas, implying an increase in void fraction and subsequent change in flow pattern, prevents the flow from even becoming fully developed. The changes are very gradual, however, and only the drag force has any effect in the one-dimensional concept of the flow. It is clear that even for the pseudo-fully developed region the cross-sectional mean slip as defined by equation (3-4) is also a result of a possible "Bankoff effect". When the radial void and velocity distributions do not change in the flow direction, i.e. for pseudo-fully developed flow and limited channel lengths, this effect can be accounted for by a modified interphase drag force. For the entrance region, which is characterized by changes in the radial void and velocity profiles and for profiles that correspond to a slip below unity this can not be done. Keeping the purpose of this experiment in mind it is clear that the "Bankoff effect" must be excluded from the drag force to make the results useful for the local slip effects in the two-dimensional model. For this reason a constant area channel is in principle not suitable. Moreover it would give no information regarding the virtual mass force.
A converging or diverging section of the channel serves both purposes. The change in void profile cannot be completely excluded, but is reduced by making the section short without violating the one-dimensional character of the flow too much. In this light a converging section is better suited than a diffuser, where stall effects may disturb the flow in the case of a short length.
The measuring technique is thus shown to consist of a converging flow channel, a set of momentum equations and void and pressure measurements.
A continuous recording of the axial void distribution is difficult to achieve but instead the average void fraction is measured for a number of

successive channel cross sections. The γ-ray attenuation technique described in section 2.2.3.2.2. and 2.2.4.1.2. was used for this purpose. Pressure measurements were made at the same levels.

3.2.3.2.2. Experimental equipment.

The measurements are carried out in the air-water loop used for the separator experiments of section 2.2. using the same instrumentation. The swirl vanes and separator were removed and the latter replaced by a converging test section. Instead of the free surface tank employed in the separator test configuration a large cylindrical tank with tangential inlet for the mixture was used to separate the air. The two converging test sections (c.s. 1 and c.s. 2) used shown in figure 3-18. The test sections are of circular cross section with an inlet area equal to that of the separators.

TABLE 3-1

	c.s. 1	c.s. 2	
diameter at inlet	.10	.10	m
diameter at outlet	.07	.05	m
length of converging section	.10	.10	m
angle of convergence	$17^{\circ}1'$	$28^{\circ}6'$	
area ratio	2.04	4.00	

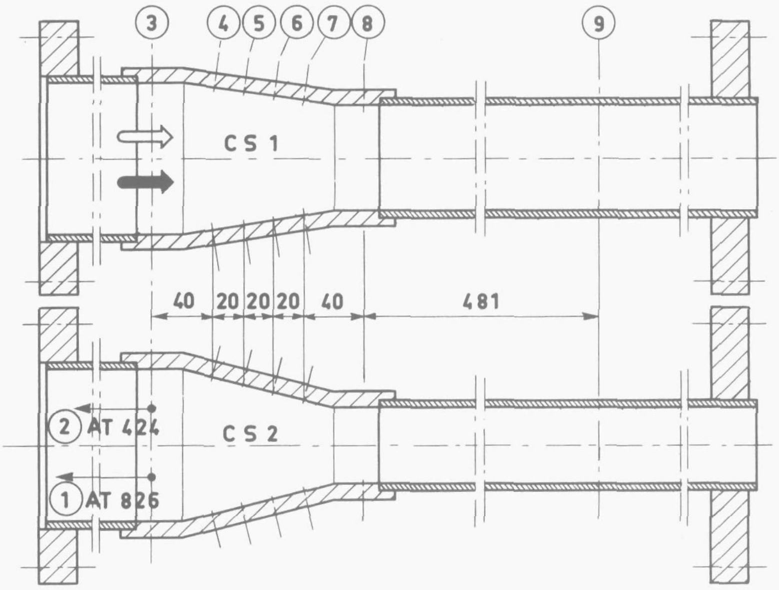

FIGURE 3-18.

Converging test sections showing pressure tap and γ-scan locations.

The locations of 7 of the pressure and void measuring levels are indicated in figure 3-18. Two holes were drilled on opposite places in the tube wall at each level for pressure equalisation. Measuring levels 1 and 2 are identical with those of the separator tests.

3.2.3.2.3. Experimental procedure.

The experimental procedure is essentially the same as that for the separator tests as far as void, pressure and flow measurements are concerned.

3.2.3.2.4. Results.

The results for the two test sections consist of void profiles for 9 levels and the axial pressure distribution for a total of 17 test conditions [78], [91]. The tests were performed for three different air inlet velocities for each of three inlet water velocities as given in table 3-2.

TABLE 3-2

$v_{s\ell}$	v_{sg} c.s.1	v_{sg} c.s.2	
1	0.5, 1.5, 3.0	0.4, 1.4, 2.5	m/s
2	0.4, 1.5, 2.7	0.4, 1.1, 1.5	m/s
3	0.4, 1.4, 2.5	0.3, 0.8	m/s

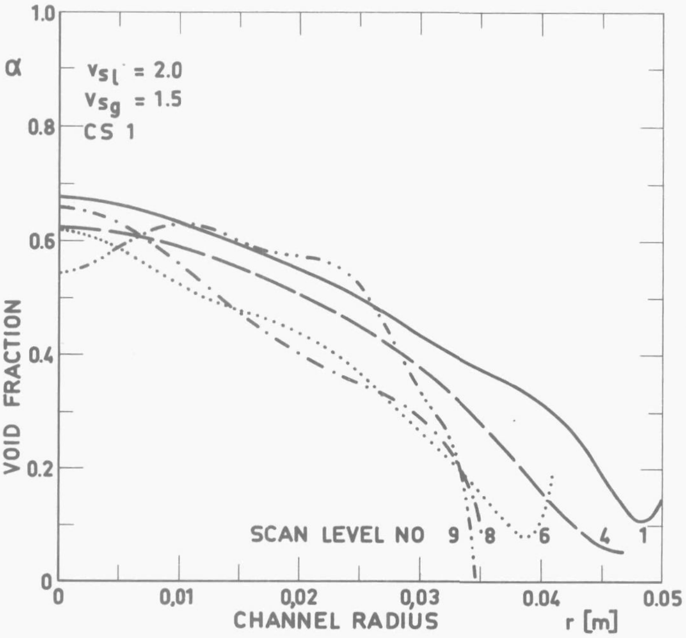

FIGURE 3-19.

Example of measured void fraction profiles at different levels having a maximum in the center of the channel.

The void profiles for these conditions revealed some remarkable differences.
The profiles were all more or less parabolic in shape even though they showed various bumps and dents, and have a maximum in the centre of the channel, except for the conditions in boxes in table 3-2 (high water and low air velocity), which showed the maximum of the profile near the wall. The slip for these conditions, and these only, is below one. An example of both types of profile is given in figure 3-19 and 3-20. The "camel back" profiles could be an indication of developing flow, a result from the mixer geometry, but the same

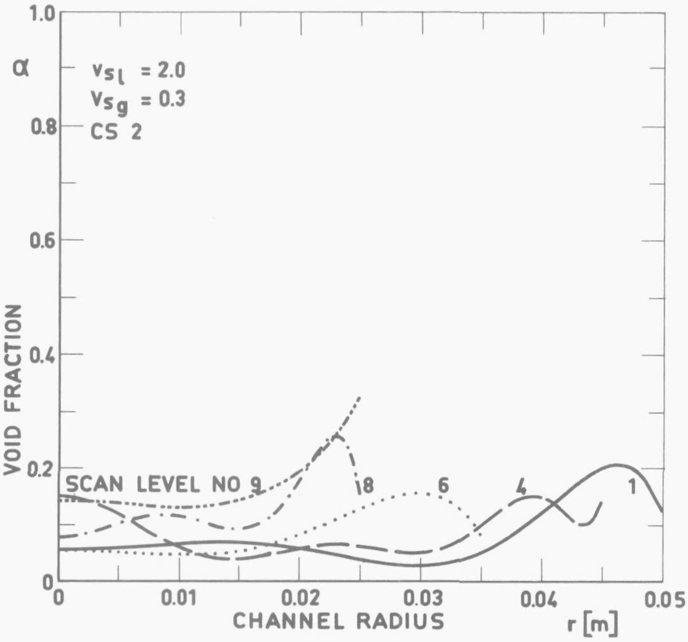

FIGURE 3-20.

Example of measured void fraction profiles at different levels having a maximum near the wall.

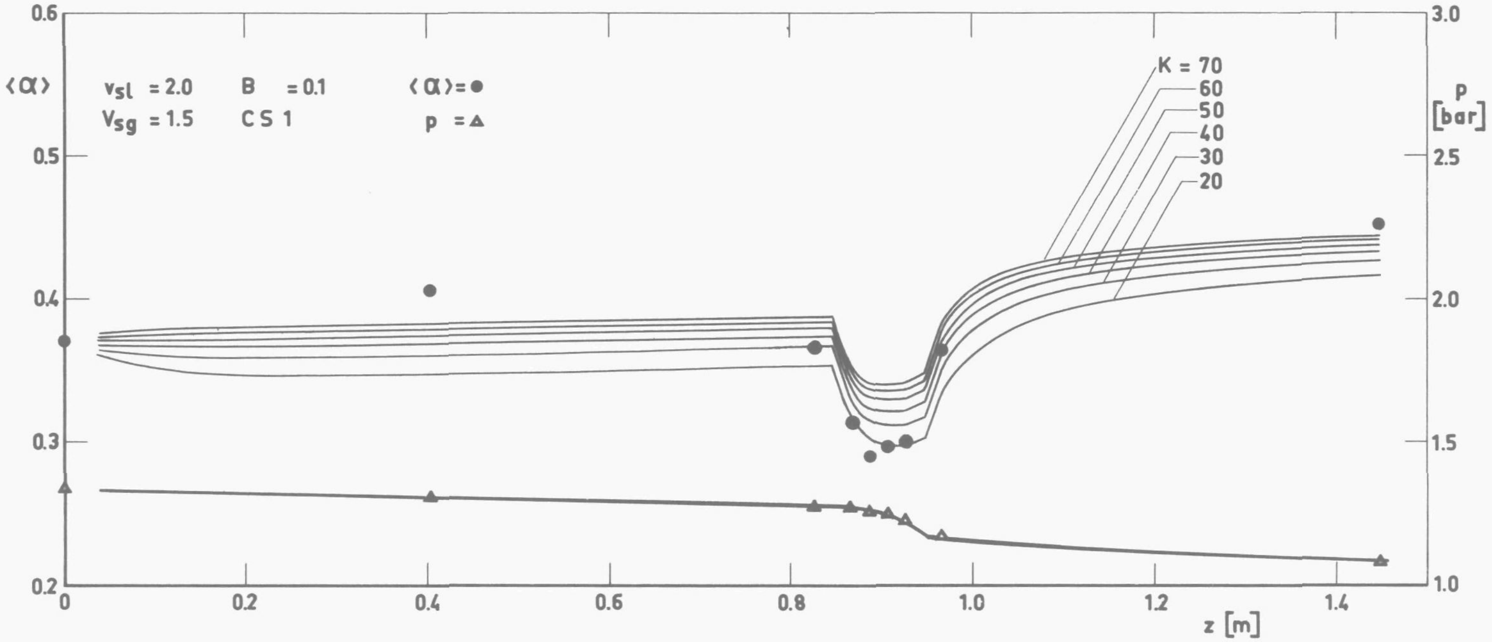

FIGURE 3-21.

Comparison of calculated axial void fraction and pressure profiles for different values of drag force with experiments for test conditions of figure 3-19.

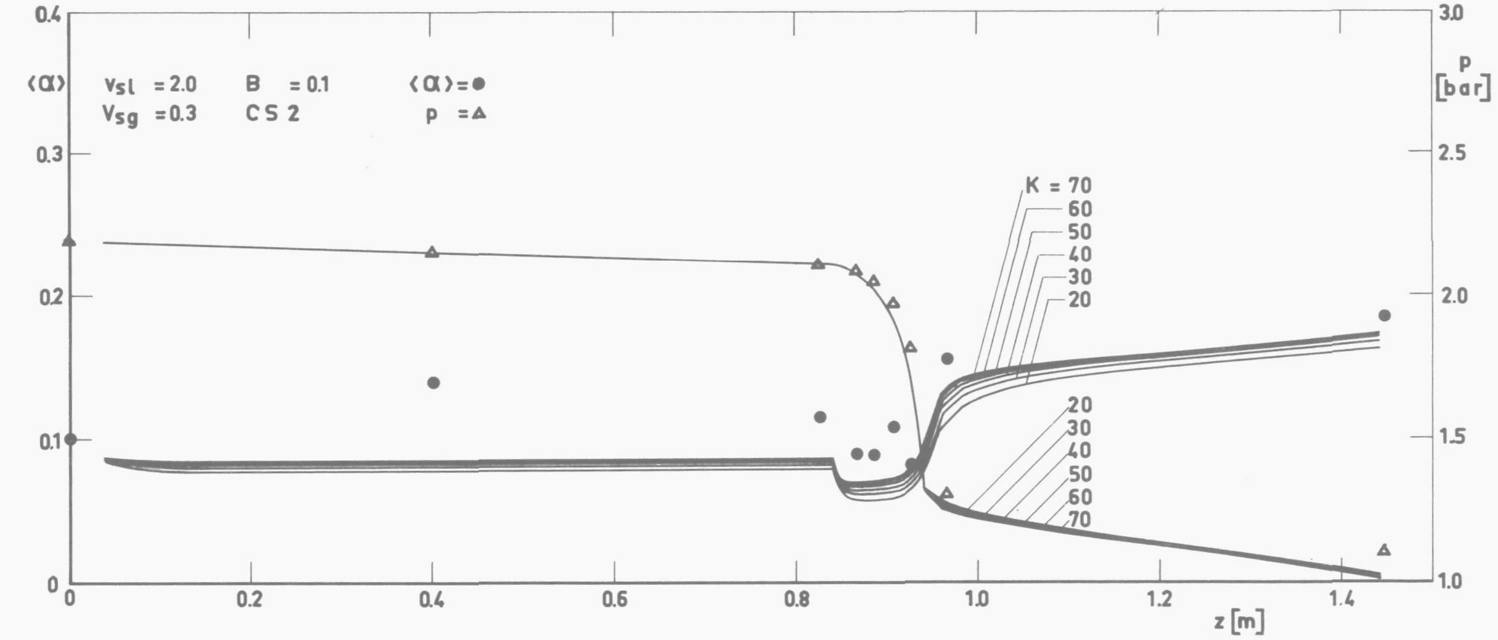

FIGURE 3-22.

Comparison of calculated axial void fraction and pressure profiles for different values of drag force with experiments for test conditions of figure 3-20.

profiles have been found by OLSEN [92] for (much) longer L over D ratios (84 versus 30) and for both air admission through a porous section of the tube wall and in the center. Furthermore the "camel back" persists downstreams of the converging section. PETRICK and KUDIRKA [93] have also found profiles of this shape. They, however, assume developing flow to be the reason. Both conclusions may not be mutually exclusive but in either case the low slip values are due to the "Bankoff effect".

The computer program VAPOM mentioned in section 3.2.2., provided with output procedures for the Calcomp plotter was run for the conditions of table 3-2. A drag force relation as suggested by HENCH and JOHNSTON [90] was used, where $\frac{C_D}{d}$ of equation (3-32) is correlated with the void fraction

$$\frac{C_D}{d} = K(1-\alpha)^3 \qquad (3\text{-}58)$$

For the "churn turbulent" flow regime which lies between ideal bubble flow and froth or slug flow Hench and Johnston take K equal 54.9 m^{-1}. The virtual mass coefficient B was initially assumed constant. The program was run for several values of K and B. An example is given in figures 3-21 and 3-22 which are for the same conditions as figures 3-19 and 3-20, also showing the experimental data for $\langle\alpha\rangle$ and p. Although these examples are for a single value of $B = 0.1$ it can be seen that no single value for K will fit both the constant area and the converging section. A new series of runs was then made starting at the entrance of the converging section and taking the measured values of location 3 as staring values. From these plots of calculated and measured axial distributions the value of K was found to be 30.

It is remarkable that the trend of equation (3-58) seems to be completely the opposite of that suggested by MERTES and RHODES [22] for solid particles and MARRUCCI's [23] analysis for bubbles. Equation (3-58) can, like equations (3-17) or (3-20), also be written as a ratio of drag coefficients by taking $K = C_D^{\infty} / d^{\infty}$

$$\frac{C_D^{\alpha}}{C_D^{\infty}} = \frac{d^{\alpha}}{d^{\infty}} (1-\alpha)^3 \qquad (3\text{-}59)$$

Agreement with these equations could only be possible if the effective bubble diameter would increase strongly with increasing void fraction. If for example d^{∞} is taken 3.3 mm the corresponding C_D^{∞} becomes 0.1 for K = 30. For a void fraction of 0.60 equation (3-20) gives 5.18 for $C_D^{\alpha}/C_D^{\infty}$. The bubble diameter d^{α} is then: $d^{\alpha} = 0.0033 \times 5.18/0.064 = 0.27$ m. This enormous increase in bubble diameter is very unrealistic; the bubble becomes larger than the flow channel. In comparison with the behaviour with solid particles the drag coefficient is apparently considerably more reduced by other effects such as bubble deformation and internal circulation than it increases due to the reduced liquid flow area as the void fraction increases.

After having established the drag force the selection of the virtual mass coefficient could be undertaken. An example of the plots for K = 30 and various B-values is shown in figures 3-23 and 3-24 (see page 122), again for the same conditions as the preceeding four figures.

Only the four data points lying within the converging section were considered for the determination of B. The value of B that made the numerical solution go through a data point was plotted as a function of the void fraction $\langle\alpha\rangle$ itself. The result is shown in figure 3-25 (see page 123). The black data points were found to be smaller than zero. There appears to be a considerable scatter as was the case in figure 3-7. Taking into

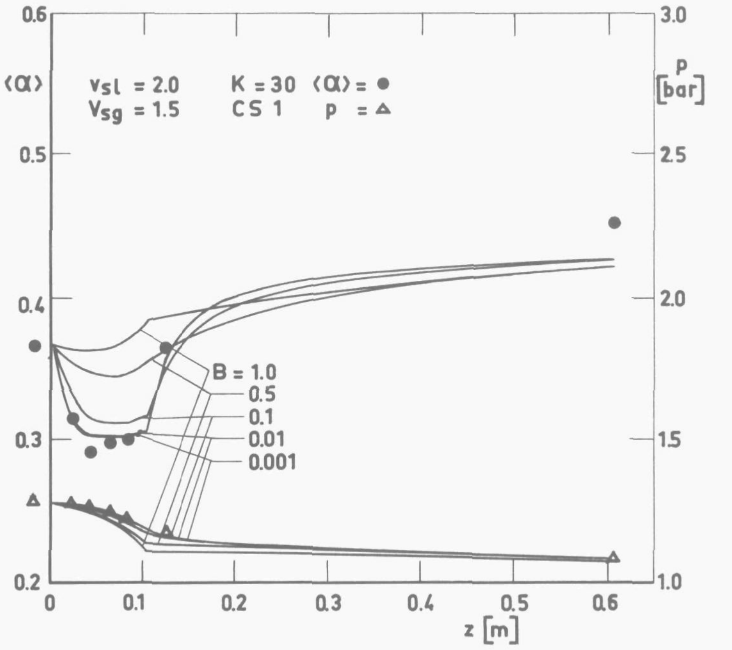

FIGURE 3-23.

Comparison of calculated axial void fraction and pressure profiles for different values of virtual mass with experiments for test conditions of figure 3-19.

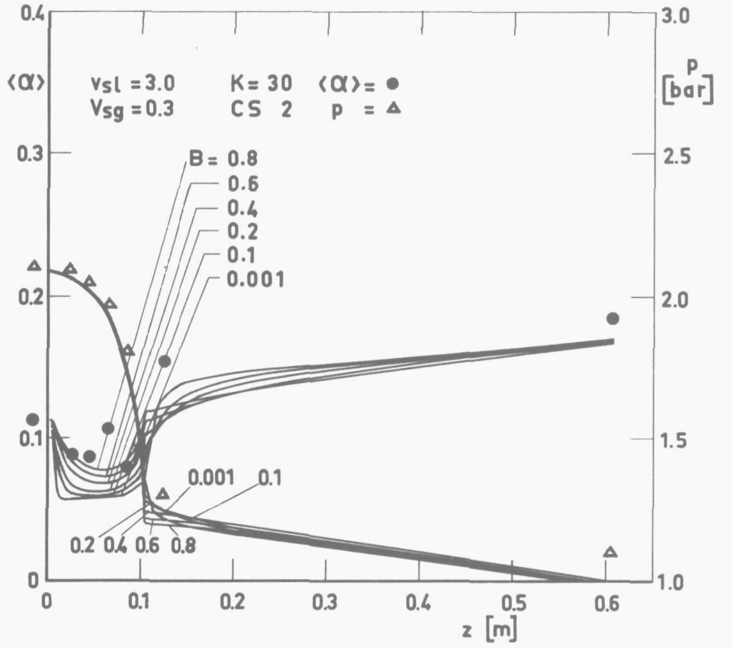

FIGURE 3-24.

Comparison of calculated axial void fraction and pressure profiles for different values of virtual mass with experiments for test conditions of figure 3-20.

account the weak effect of a variation of B on the numerical solution and the errors involved in the void measurement as well as the comparitively small change in slip in the converging section the scatter is not worse than could be expected.

For the range of void fractions investigated the results are correlated by

$$B = 3.155(1-\alpha)^{10.85} \qquad (3\text{-}60)$$

It must be emphasized that this correlation should always be used in combination with an interphase drag force based on

$$\frac{C_D}{d} = 30(1-\alpha)^3 \qquad (3\text{-}61)$$

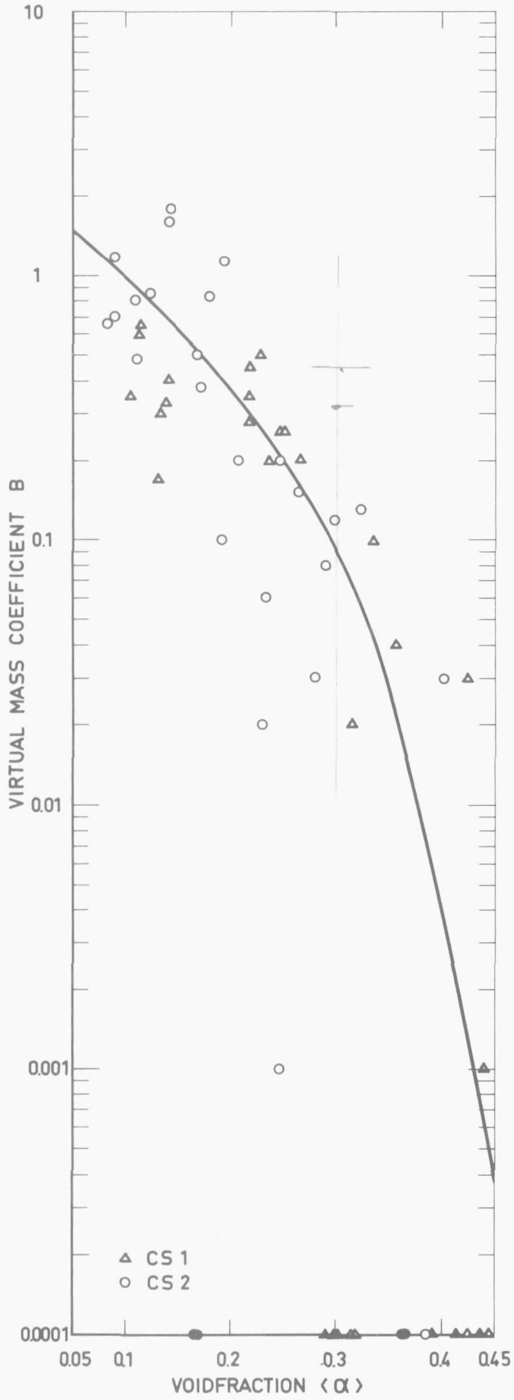

FIGURE 3-25.

Experimental virtual mass coefficients as a function of void fraction.

Furthermore both equations are valid for local considerations only, because equation (3-60) incorporates no "Bankoff effect".

A discrepancy between figure 3-25 and 3-7 is apparent, the last figure giving higher values for B. The reason for this may be found in the void fractions given by ROSE and GRIFFITH [30] and used for the calculation of B from their data. They measured the void fraction upstream of the tube outlet plane for which the calculations are made. These void fractions are probably higher than actually found at the tube outlet and would result in an overestimation of B as can be seen from equation (3-26).

The trend in both figures is the same however and the steep fall of B with increasing void fraction is in agreement with the liquid envelope concept for virtual mass: the envelope must eventually vanish as the void fraction approaches 1. As pointed out in relation with the influence of adjacent bubbles on the drag force, spherical bubbles in a cubic arrangement would be touching at a void fraction of 0.52. No substantial liquid envelope could exist at that or higher void fractions. In fact a highly reduced virtual mass coefficient would be expected at values somewhat below 50 percent, which is in agreement with the present findings.

3.2.3.2.5. Conclusions.

The interphase drag force in an accelerating two-phase air-water mixture can be expressed in a form due to HENCH and JOHNSTON [90] making use of equation (3-58). The applicability of this correlation demonstrates a basically different trend in the influence of adjacent bubbles on the bubble drag force from that for solid particles. The constant K given as 54.9 in [90] probably also incorporates a "Bankoff effect". It was possible to eliminate this effect for the accelerating flow and within the range of test variables K was found to be 30.

The virtual mass coefficient derived from the measurements is correlated by the same type of power function as used in equation (3-58). The exponent is found to be much higher, 10.58 versus 3, than for the drag force.

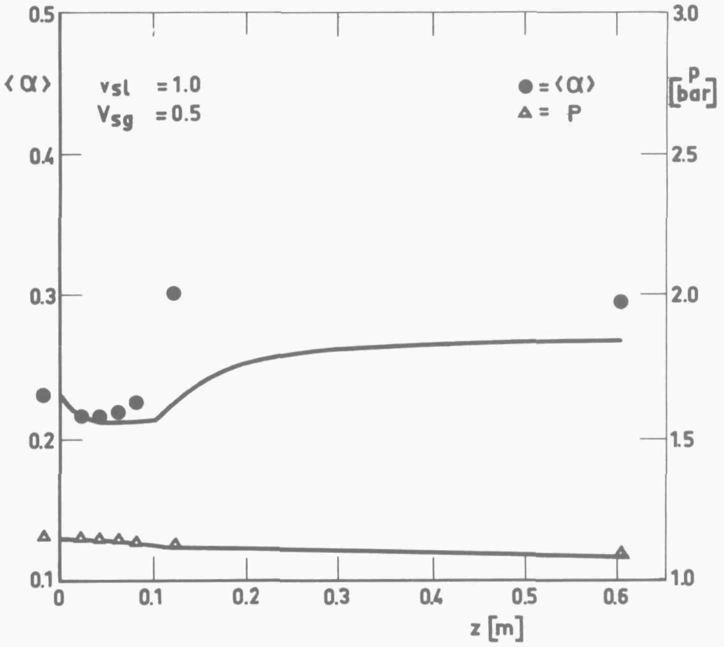

0.5
0.4
0.3
0.2
0.1
⟨α⟩
vsl = 1.0
Vsg = 0.5
● = ⟨α⟩
△ = p
p [bar]
3.0
2.5
2.0
1.5
1.0
0
0.1
0.2
0.3
0.4
0.5
0.6
z [m]

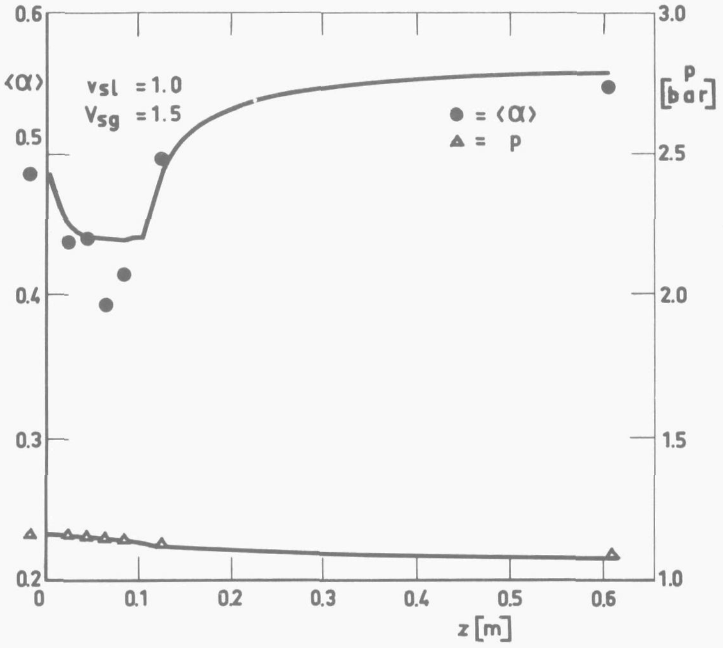

0.6
0.5
0.4
0.3
0.2
⟨α⟩
vsl = 1.0
Vsg = 1.5
● = ⟨α⟩
△ = p
p [bar]
3.0
2.5
2.0
1.5
1.0
0
0.1
0.2
0.3
0.4
0.5
0.6
z [m]

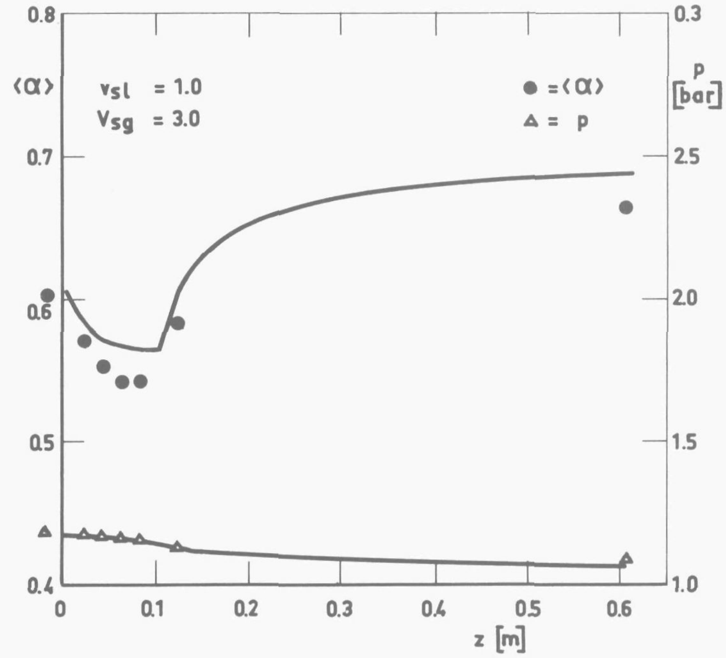

0.8
0.7
0.6
0.5
0.4
⟨α⟩
vsl = 1.0
Vsg = 3.0
● = ⟨α⟩
△ = p
p [bar]
0.3
2.5
2.0
1.5
1.0
0
0.1
0.2
0.3
0.4
0.5
0.6
z [m]

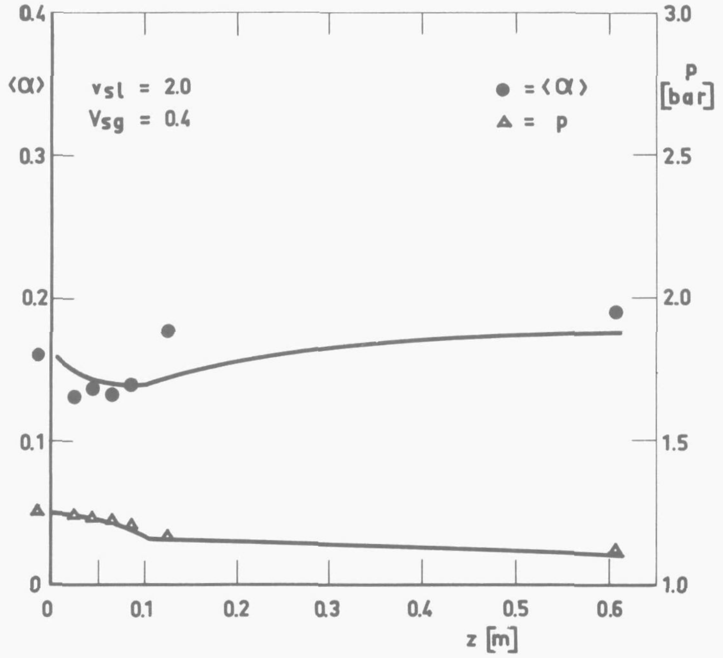

0.4
0.3
0.2
0.1
0
⟨α⟩
vsl = 2.0
Vsg = 0.4
● = ⟨α⟩
△ = p
p [bar]
3.0
2.5
2.0
1.5
1.0
0
0.1
0.2
0.3
0.4
0.5
0.6
z [m]

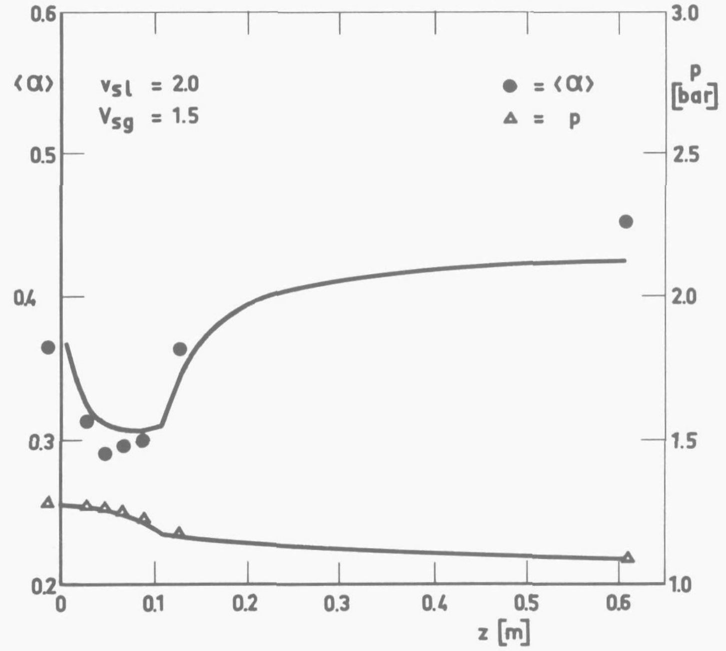

0.6
0.5
0.4
0.3
0.2
⟨α⟩
vsl = 2.0
Vsg = 1.5
● = ⟨α⟩
△ = p
p [bar]
3.0
2.5
2.0
1.5
1.0
0
0.1
0.2
0.3
0.4
0.5
0.6
z [m]

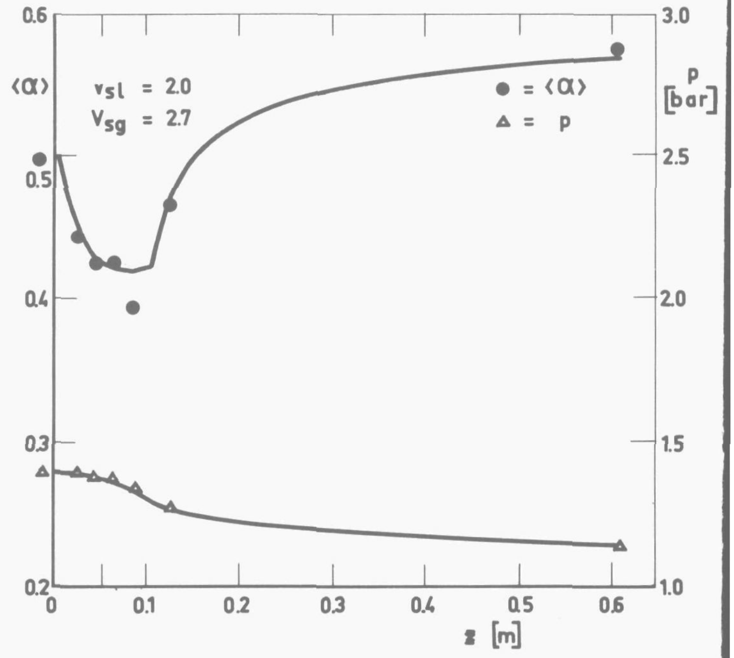

0.6
0.5
0.4
0.3
0.2
⟨α⟩
vsl = 2.0
Vsg = 2.7
● = ⟨α⟩
△ = p
p [bar]
3.0
2.5
2.0
1.5
1.0
0
0.1
0.2
0.3
0.4
0.5
0.6
z [m]

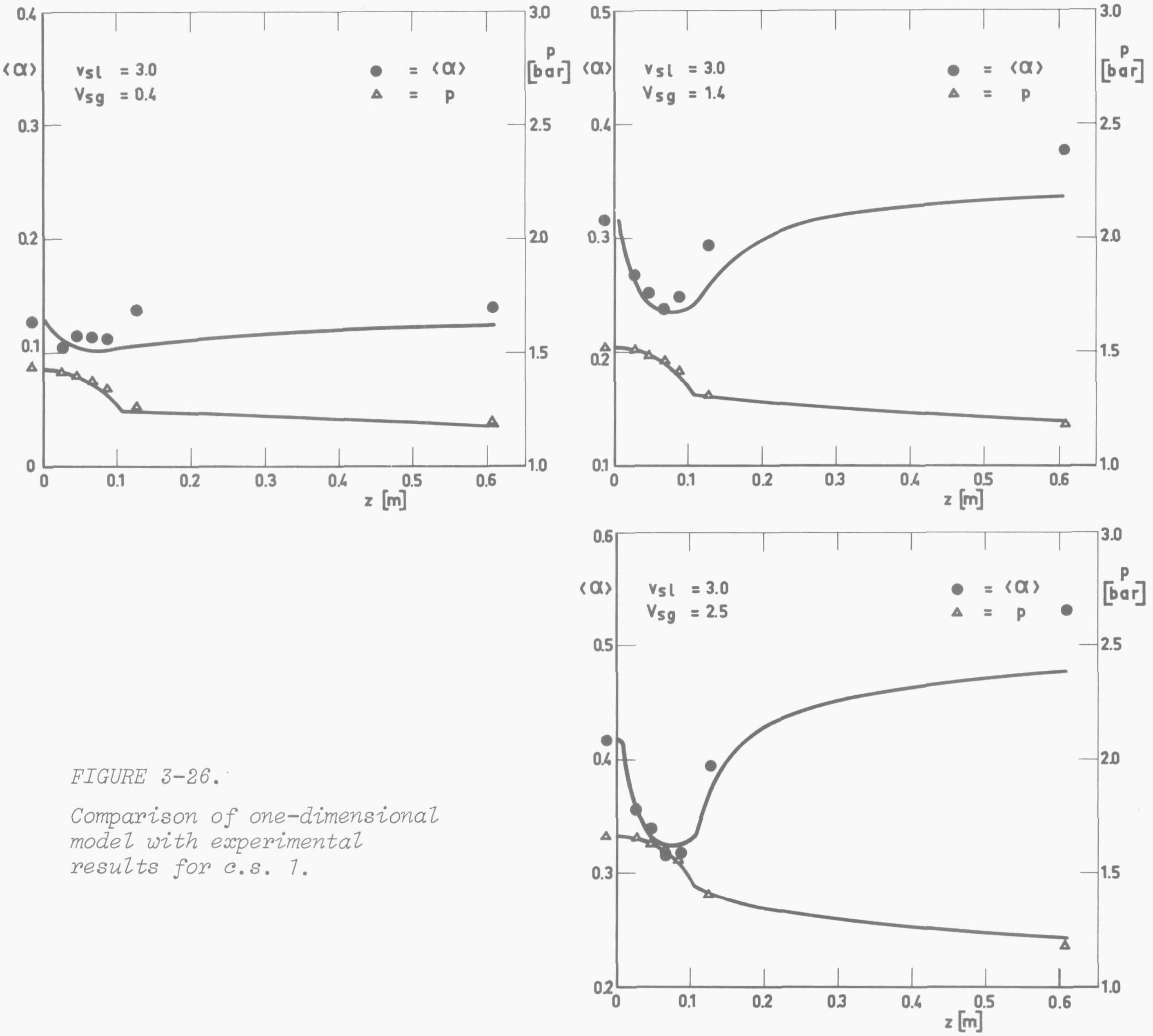

FIGURE 3-26.

Comparison of one-dimensional model with experimental results for c.s. 1.

The virtual mass effect dies out much faster with increasing void than the drag force. The expression for the virtual mass coefficient equation (3-60) is only valid in combination with a drag force based on equation (3-61).

3.2.3.3. Comparison of one-dimensional model and auxiliary experiments.

In order to obtain an overall impression of the capabilities and shortcomings of the one-dimensional model, computer runs were made for the 17 test conditions of the converging channel experiments. Friction losses were calculated by Levy's method, using the findings of the shear stress measurements. Equations (3-60) and (3-61) were used for calculation of the virtual mass and interfacial drag force. For reasons explained before the program was started at the entrance of the converging section using the measured data of level 3 as starting values.
The results for the void fraction $<\alpha>$ and the pressure p are shown in figure 3-26 (see page 124 and 125) and figure 3-27 (see page 126 and 127).

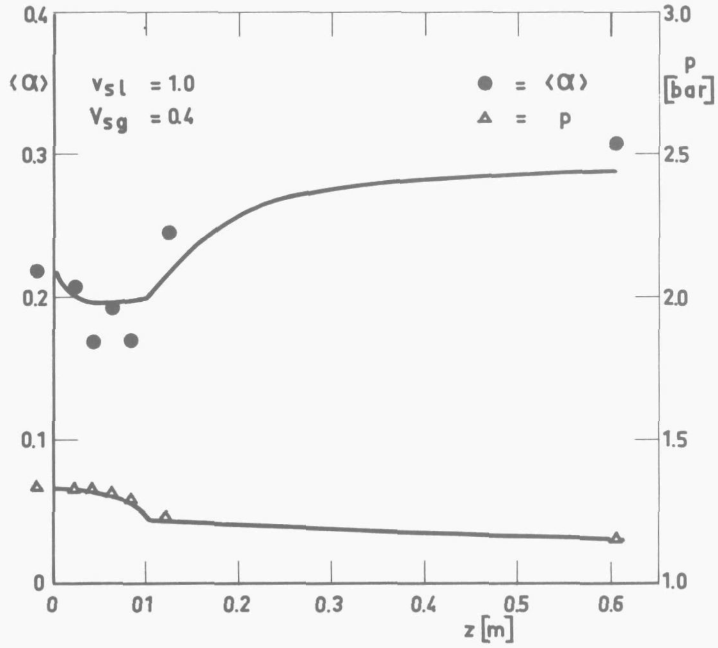

⟨α⟩
0.4
0.3
0.2
0.1
0
v_{sl} = 1.0
V_{sg} = 0.4
● = ⟨α⟩
△ = p
p
[bar]
3.0
2.5
2.0
1.5
1.0
0
01
0.2
0.3
0.4
0.5
0.6
z [m]

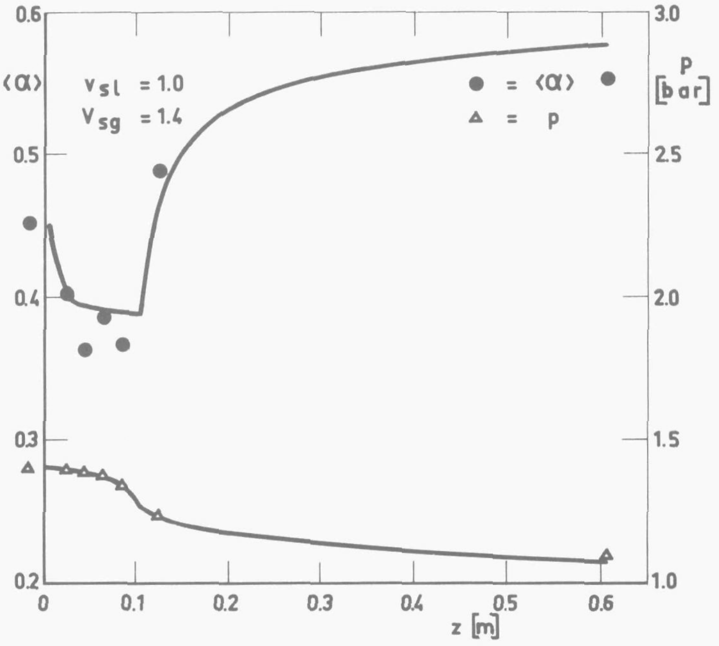

⟨α⟩
0.6
0.5
0.4
0.3
0.2
v_{sl} = 1.0
V_{sg} = 1.4
● = ⟨α⟩
△ = p
p
[bar]
3.0
2.5
2.0
1.5
1.0
0
0.1
0.2
0.3
0.4
0.5
0.6
z [m]

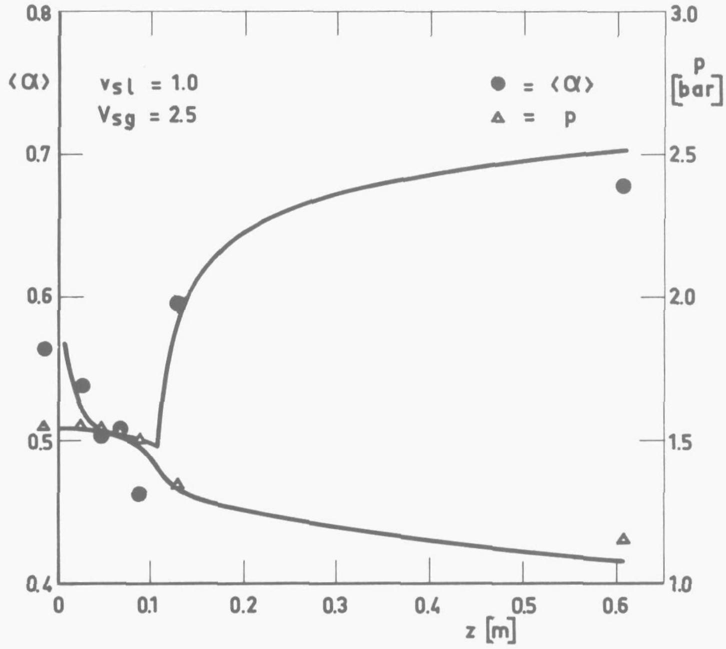

⟨α⟩
0.8
0.7
0.6
0.5
0.4
v_{sl} = 1.0
V_{sg} = 2.5
● = ⟨α⟩
△ = p
p
[bar]
3.0
2.5
2.0
1.5
1.0
0
0.1
0.2
0.3
0.4
0.5
0.6
z [m]

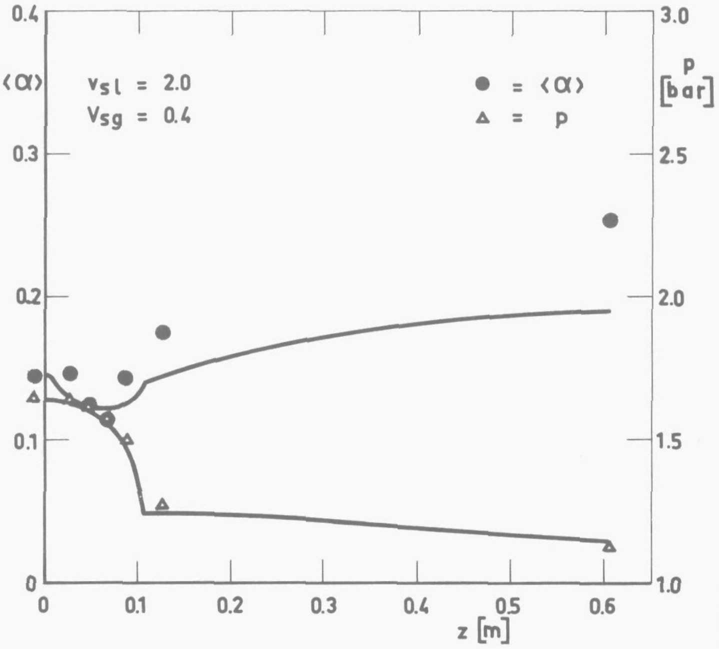

⟨α⟩
0.4
0.3
0.2
0.1
0
v_{sl} = 2.0
V_{sg} = 0.4
● = ⟨α⟩
△ = p
p
[bar]
3.0
2.5
2.0
1.5
1.0
0
0.1
0.2
0.3
0.4
0.5
0.6
z [m]

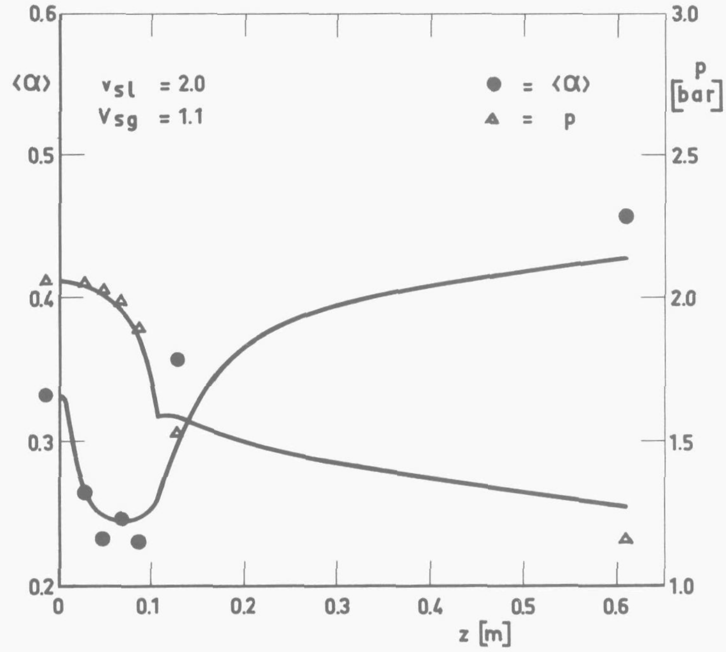

⟨α⟩
0.6
0.5
0.4
0.3
0.2
v_{sl} = 2.0
V_{sg} = 1.1
● = ⟨α⟩
△ = p
p
[bar]
3.0
2.5
2.0
1.5
1.0
0
0.1
0.2
0.3
0.4
0.5
0.6
z [m]

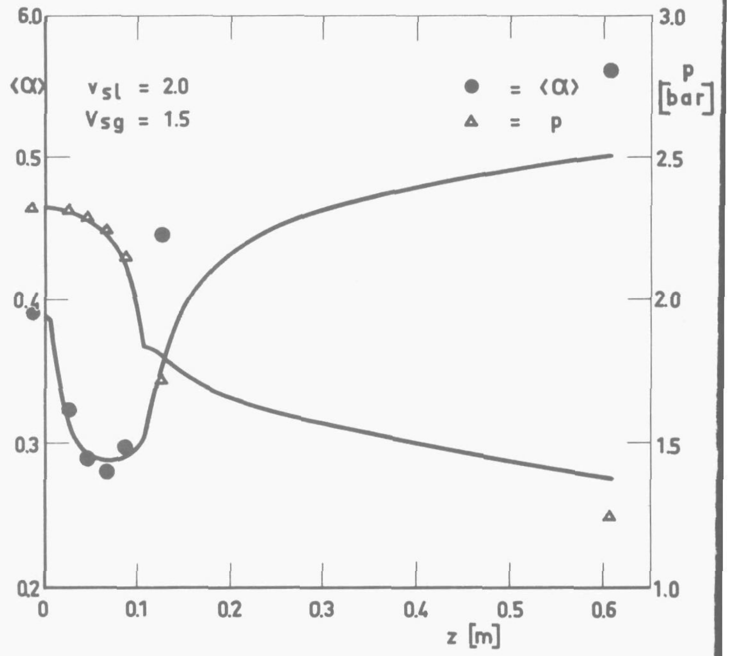

⟨α⟩
6.0
0.5
0.4
0.3
0.2
v_{sl} = 2.0
V_{sg} = 1.5
● = ⟨α⟩
△ = p
p
[bar]
3.0
2.5
2.0
1.5
1.0
0
0.1
0.2
0.3
0.4
0.5
0.6
z [m]

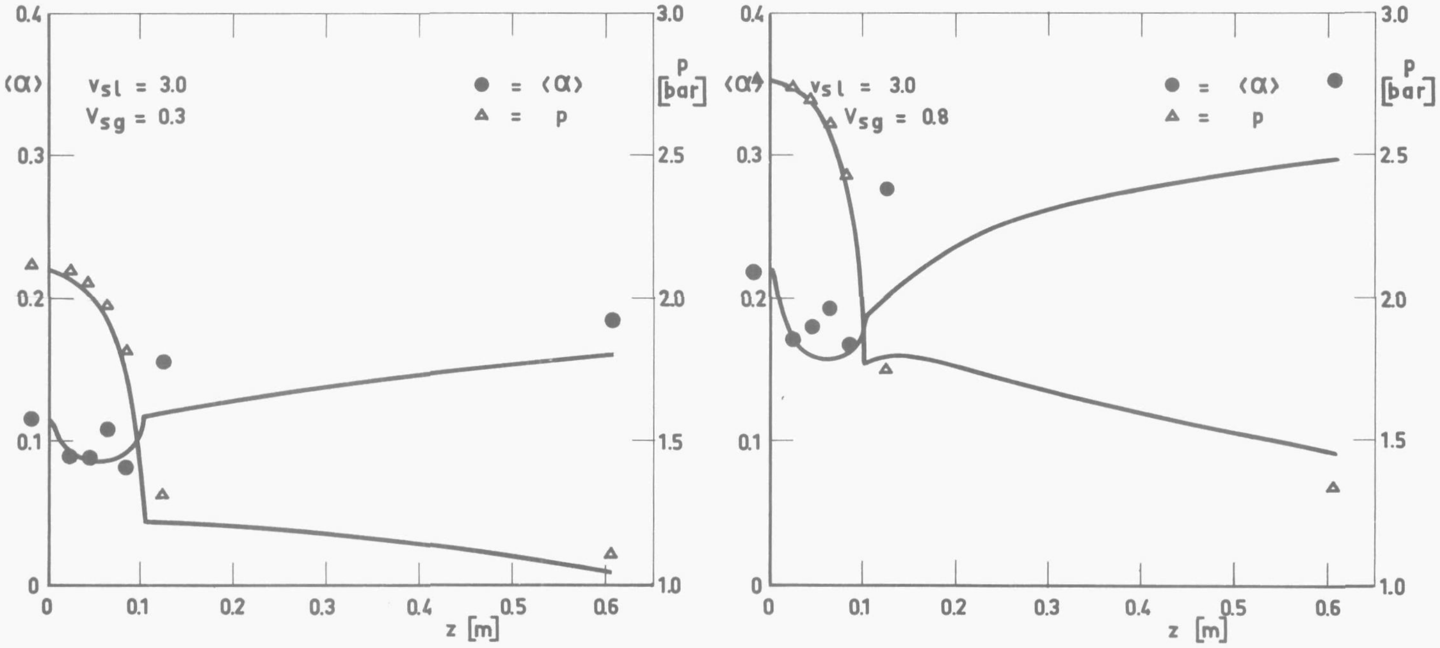

FIGURE 3-27.

Comparison of one-dimensional model with experimental results for c.s. 2.

The axial void distributions in the converging section are reasonably well predicted by the model, while there are no differences worth mentioning between c.s. 1 and c.s. 2.

Although the model was made to fit the accelerating flow only, it is interesting to see how well the void fraction in the following tailpipe is predicted. Two effects may cause deviations. Firstly, whereas the radial profiles are assumed "frozen" in the short length of the converging section, changes may be expected in the longer tailpipe introducing the "Bankoff effect" again.

Secondly, the flow will contract further upon leaving the converging section and then show a more abrupt expansion to fill the pipe again than experienced in the calculations, where the pipe geometry is followed.

Inspections of figures 3-26 and 3-27 reveals that there is a tendency for the lower inlet void fractions to underpredict the void fractions in the tailpipe. This tendency spreads to higher void fractions for increasing water velocities. Although more flow contraction can be expected for c.s. 2, this is not reflected in the amount of the deviation. The axial pressure profiles are well predicted, but where the major part of the pressure drop consists of acceleration loss this is not surprising. Deviation of the predicted void fraction from the true values is reflected in the true liquid velocity and hence in the pressure drop as demonstrated by the results. Larger deviations are to be expected for c.s. 2 due to the higher velocities and two-dimensional effects. This is also evident in figure 3-27.

The pressure profile in the tailpipe is best predicted if the void profile is accurately followed and vice versa. If the pressure of level 8 is over or underpredicted is dependent on the void fraction calculated at the end of the converging section. If the predicted void fraction is increasing again before entering the tailpipe the calculated pressure loss is too high. This is shown in the results for c.s. 2 for the lowest void fractions.

3.3. Two-dimensional model.

3.3.1. Introduction.

Both the riser-downcomer deometry for gravity separation and that of the vortex tube of the venturi separator are rotational symmetric and an extension of the one-dimensional equations to the two-dimensional rotational symmetric case would apply to both flow problems. However no methods of solution for such a set of differential equations is available in literature. An attempt was made to modify a method known to give results for single phase equations.

Because the investigation of the axial separator was set up as a preliminary study it was thought to be better suited to try out this method, which is to be regarded as a mathematical experiment. Furthermore, the turning flow in the riser-downcomer geometry is an extra complication and would prohibit the use of the method envisaged. Nevertheless in order to provide a means to predict carry-under a qualitative approach to the gravity separation problem based on the findings of the one-dimensional analysis will be given in section 3.4.

The following description of the two-dimensional model comprises several steps. First the basic balance equations for mass and momentum, which constitute the model proper are formulated. It appears to be necessary to replace the rotation by a centrifugal force field in order to arrive at the equations required. The tangential velocity distribution, although not appearing directly in the two-dimensional description, is introduced indirectly, being the source of this force field. The method of solution forms an integral part of the model and is based on the N-strip method [61]. This method, which makes it possible to transform a set of nonlinear partial differential equations into a set of ordinary differential equations, requires that the equations can be written as a system of divergence expressions. This requirement can not completely be satisfied however.

A formal description of the N-strip method, up to the point where ref. [61] is followed, is given. The modification necessary to arrive at the same result, a set of ordinary differential equations, are then presented as well as the method of solution for this set.

The above outlined course did not produce the desired result in solving the two-dimensional equations. A discussion of the numerical instabilities encountered, their couses and possible remedies is given in chapter 5.

3.3.2. Basic equations.

The same assumptions, that are made in section 3.2.1., are taken to be valid for the two-dimensional model, with the exception of the first two which specify a one-dimensional character. Although this relaxation of the limitations of the model will allow for the radial as well as the axial velocity distribution, including a possible "Bankoff effect", no attempt is made to incorporate a proper description of the boundary layer. This is justified where the main purpose is to represent the transport process of the gas phase in the bulk of the flow.

As a result the boundary conditions at the solid wall of the flow channel are of the simplest form. The constitutive equations of the model are again the conservation laws of mass and momentum in essentially the same form as in sections 3.2.1.1. through 3.2.1.4. but derived for rotational symmetric flow which permits a two-dimensional description according to the control volume of figure 3-28.

The number of unknowns is six: α, p, u_{gz}, u_{gr}, $u_{\ell z}$, $u_{\ell r}$. The number of consistent equations to describe this system should therefore also be six: a mass balance and two momentum balances for each phase. Instead of taking momentum balances for gas and liquid separately those for the mixture and

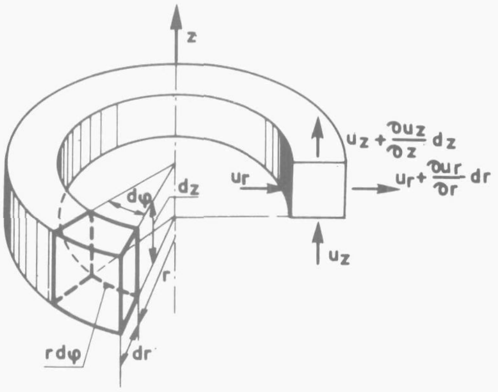

FIGURE 3-28.

Control volume for rotational symmetric flow.

liquid only were used, anticipating the method of solution, to obtain a more compact formulation. Physically this makes no difference. It is further assumed that both liquid and mixture equations are valid throughout the channel. This means that no sharp boundary is assumed to exist between the gas core and the surrounding two-phase region and liquid is still present in the core. On the other hand, even though the void fraction may get extremely small in the outer liquid layers, totally gas free water will not be found.

3.3.2.1. Conservation of mass.

The mass-balances for the separate phases for the element $rd\phi drdz$ of figure 3-28 give for the rotational symmetric case:

gas phase

$$\frac{\partial}{\partial r}(\alpha\,\rho_g\,u_{gr}) + \frac{\alpha\,\rho_g\,u_{gr}}{r} + \frac{\partial}{\partial z}(\alpha\,\rho_g\,u_{gz}) = 0 \qquad (3\text{-}62)$$

liquid phase

$$\frac{\partial}{\partial r}((1-\alpha)\,\rho_\ell\,u_{\ell r}) + \frac{(1-\alpha)\rho_\ell u_{\ell r}}{r} + \frac{\partial}{\partial z}((1-\alpha)\,\rho_\ell\,u_{\ell z}) = 0 \qquad (3\text{-}63)$$

3.3.2.2. Conservation of momentum.

For the conservation laws for the momentum in r and z directions the same interaction forces between the phases are taken into account as for the one-dimensional model. If the liquid phase is considered as the continuous phase, as has been done for the one-dimensional case, and assumed to be turbulent, the "turbulence stresses" may be accounted for by a "turbulence viscosity" $\varepsilon\ [m^2/s]$.

In accordance with the assumptions of section 3.2.1. the flow is frictionless, i.e. $\eta = 0$, but the wall shear force is introduced as an external force acting on the control elements adjacent to the wall i.e. for $r = r_{wall}$.

The contribution of the wall shear on these outer elements becomes, after division by $rdrd\phi dz$:

$$\frac{\tau_w\ rd\phi dz}{rdrd\phi dz} = \frac{\tau_w}{dr} = \frac{\tau_w\ 2\pi r}{2\pi rdr} = \frac{\tau_w\ 0}{A_{ring}} \qquad (3\text{-}64)$$

For a channel of variable cross section the wall shear has components in r and z direction.

Letting $\delta = 1$ for $r = r_{wall}$ and $\delta = 0$ for $r \neq r_{wall}$ the momentum equations for the element $rd\phi drdz$ of figure 3-28 and division by $rdrd\phi dz$ read liquid phase

r direction

$$\frac{\partial}{\partial r}\left((1-\alpha)\,\rho_\ell\, u_{\ell r}{}^2\right) + \frac{(1-\alpha)\rho_\ell u_{\ell r}{}^2}{r} + \frac{\partial}{\partial z}\left((1-\alpha)\,\rho_\ell\, u_{\ell r}\, u_{\ell z}\right) =$$

$$-\,(1-\alpha)\,\frac{\partial p}{\partial r} + (1-\alpha)\rho_\ell f_r + R_r + \rho_\ell \varepsilon \left\{\frac{\partial^2 u_{\ell r}}{\partial r^2} + \frac{1}{r}\,\frac{\partial u_{\ell r}}{\partial r} - \frac{u_{\ell r}}{r^2} + \right.$$

$$\left.\frac{\partial^2 u_{\ell r}}{\partial z^2}\right\} - \frac{\delta\, \tau_{wr}{}^0}{A_{ring}} \qquad (3\text{-}65)$$

z direction

$$\frac{\partial}{\partial r}\left((1-\alpha)\,\rho_\ell\, u_{\ell z}\, u_{\ell r}\right) + \frac{(1-\alpha)\rho_\ell u_{\ell z} u_{\ell r}}{r} + \frac{\partial}{\partial z}\left((1-\alpha)\,\rho_\ell\, u_{\ell z}{}^2\right) =$$

$$-\,(1-\alpha)\,\frac{\partial p}{\partial z} - (1-\alpha)\,\rho_\ell f_z + R_z + \rho_\ell \varepsilon \left\{\frac{\partial^2 u_{\ell z}}{\partial r^2} + \frac{1}{r}\,\frac{\partial u_{\ell z}}{\partial r} + \right.$$

$$\left.\frac{\partial^2 u_{\ell z}}{\partial z^2}\right\} - \frac{\delta\, \tau_{wz}{}^0}{A_{ring}} \qquad (3\text{-}66)$$

The equations for the mixture incorporate contributions from the gas phase. This being the disperse phase the contribution of the disperse phase to the "turbulence stresses" can be neglected, in the same way that the wall shear is wholly attributed to the liquid phase. The resulting equations become

mixture

r direction

$$\frac{\partial}{\partial r}\left(\alpha\rho_g\, u_{gr}{}^2 + (1-\alpha)\,\rho_\ell u_{\ell r}{}^2\right) + \frac{\alpha\rho_g u_{gr}{}^2 + (1-\alpha)\rho_\ell u_{\ell r}{}^2}{r} +$$

$$\frac{\partial}{\partial z}\left(\alpha\rho_g\, u_{gr}\, u_{gz} + (1-\alpha)\,\rho_\ell\, u_{\ell r}\, u_{\ell z}\right) + \frac{\partial}{\partial r}\left(B\alpha\rho_\ell\, u_{gr}\,(u_{gr} - u_{\ell r})\right) +$$

$$\frac{B\alpha\rho_\ell\, u_{gr}\,(u_{gr} - u_{\ell r})}{r} + \frac{\partial}{\partial z}\left(B\alpha\rho_\ell\, u_{gz}\,(u_{gr} - u_{\ell r})\right) =$$

$$-\,\frac{\partial p}{\partial r} + \left(\alpha\rho_g + (1-\alpha)\,\rho_\ell\right) f_r + \rho_\ell \varepsilon \left\{\frac{\partial^2 u_{\ell r}}{\partial r^2} + \frac{1}{r}\,\frac{\partial u_{\ell r}}{\partial r} - \frac{u_{\ell r}}{r^2} + \right.$$

$$\left.\frac{\partial^2 u_{\ell r}}{\partial z^2}\right\} - \frac{\delta\tau_{wr}{}^0}{A_{ring}} \qquad (3\text{-}67)$$

z direction

$$\frac{\partial}{\partial r}(\alpha\rho_g\, u_{gr}\, u_{gz} + (1-\alpha)\rho_\ell u_{\ell r} u_{\ell z}) + \frac{\alpha\rho_g\, u_{gr}\, u_{gz} + (1-\alpha)\rho_\ell u_{\ell r} u_{\ell z}}{r} +$$

$$\frac{\partial}{\partial z}(\alpha\rho_g\, u_{gz}^{\,2} + (1-\alpha)\,\rho_\ell\, u_{\ell z}^{\,2}) + \frac{\partial}{\partial r}(B\alpha\rho_\ell\, u_{gr}\,(u_{gz} - u_{\ell z}) +$$

$$\frac{B\alpha\rho_\ell\, u_{gr}\,(u_{gz} - u_{\ell z})}{r} + \frac{\partial}{\partial z}(B\alpha\rho_\ell\, u_{gz}\,(u_{gz} - u_{\ell z})) =$$

$$-\frac{\partial p}{\partial z} - (\alpha\rho_g + (1-\alpha)\rho_\ell)\, f_z + \rho_\ell \varepsilon\, \{\frac{\partial^2 u_{\ell z}}{\partial r^2} + \frac{1}{r}\frac{\partial u_{\ell z}}{\partial r} + \frac{\partial^2 u_{\ell z}}{\partial z^2}\} -$$

$$\frac{\delta\,\tau_{wz}{}^0}{A_{ring}} \qquad (3\text{-}68)$$

In the above equations f_r and f_z represent the force field. When the direction of flow is taken vertically as is customary in cyclones, f_z represents the gravitational and f_r the centrifugal acceleration thus:

$$f_z = g \qquad (3\text{-}69)$$

$$f_r = \frac{u_t^{\,2}}{r} \qquad (3\text{-}70)$$

In contrast to the constant value of the gravitational force the centrifugal force is dependent on both the radius and the tangential velocity u_t. In orde to solve the conservation equations knowledge of the radial distribution of the tangential velocity is required.

3.3.2.3. The centrifugal force field.

Unfortunately the radial distribution of u_t in an axial cyclone for gas-liquid mixtures is not known with great accuracy. Although many measurements have been taken in solid-gas and solid-liquid cyclones with tangential inlet these results are not easily applicable to axial flow cyclones as a result of the differences in flow patterns for the two types. This is illustrated schematically in figure 3-29. The inward flow of the carrier fluid in the tangential cyclone causes a radial transport of angular momentum resulting in an increasing tangential velocity towards the center. This radial flow is substantially lower in the axial cyclone and directed in the opposite way, to displace the radially migrating gas phase.

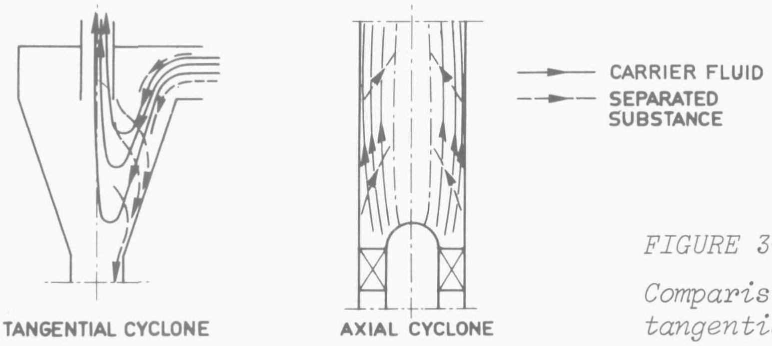

FIGURE 3-29.

Comparison of flow patterns in tangential and axial cyclones.

TER LINDEN [57], KELSALL [58] and RIETEMA [59] measured the tangential velocity in tangential inlet cyclones where the carrier fluid was a gas.
They and also BRADLEY [60] who experimented with hydrocyclones, found distributions of the general form:

$$u_t\, r^n = C \qquad (3\text{-}71)$$

For n = 1 the ideal potential flow distribution is found. The value of n in the experiments lies between 0.5 and 0.8. Close to the wall the velocity drops off to zero, while in the centre of the cyclone the velocity must have a finite value. In the experiments mentioned above a core rotating as a solid body was found, or in terms of equation (3-71): n = -1. Experiments performed at Allis Chalmers Co. [102] on axial flow cyclones show tangential velocity profiles with a much larger core of more or less solid body rotation and a gradial transition near the wall to a distribution obeing $u_t r^{0.5}$ = const.

For the sake of simplicity and in view of the foregoing two extreme cases are considered in this analysis: solid body rotation (n = -1), which is the type of rotation that is forced on the system by the shape of the swirl vanes and potential flow swirl (n = 1).
Through the radial force field f_r a new unknown C is added to the original set of six unknowns. Once the tangential velocity distribution function (3-71) is assumed to remain the same throughout the cyclone the value of C is governed by an angular momentum balance.

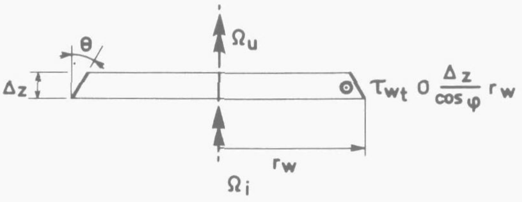

FIGURE 3-30.

Control volume for angular momentum considerations.

Consider a section of the cyclone body of height Δz as shown in figure 3-30. For steady state conditions the net angular momentum flux into the volume equals the torque exerted by the wall friction:

$$\Omega_i - \Omega_u - \tau_{wt} . 0\, \frac{\Delta z}{\cos\,\theta}\, r_w = 0 \qquad (3\text{-}72)$$

where the angular momentum flux Ω is given by

$$\Omega = \int_0^{r_w} \{\, \alpha\rho_g\, u_{gz}\, u_{gt} + (1-\alpha)\, \rho_\ell\, u_{\ell z}\, u_{\ell t} \,\}\, r\; 2\,\pi r\; dr \qquad (3\text{-}73)$$

The slip between the tangential gas and liquid velocity components is neglected. In contrast to the axial and radial directions there is no pressure gradient in tangential direction to act as a driving force to initiate phase slip. Furthermore the effects of the corriolis force on the rotating mixture are neglected. Thus for $u_{gt} = u_{\ell t}$ equation (3-73) becomes with the aid of equation (3-71).

$$\Omega = 2\,\pi\, C \int_0^{r_w} \{\, \alpha\rho_g\, u_{gz} + (1-\alpha)\, \rho_\ell\, u_{\ell z} \,\}\, r^{-n+2}\, dr \qquad (3\text{-}74)$$

3.3.3. Boundary conditions.

For the system of basic equations a set of 6 boundary conditions has to be formulated. In anticipation of the method of solution these are chosen at the solid wall of the vortex tube.
The first condition is that both phase velocities have to become zero at the wall. Both r and z components have to be zero, thus

$$u_{\ell z_n} = u_{\ell r_n} = u_{gz_n} = u_{\ell z_n} = 0 \tag{3-75}$$

A further requirement is that the void fraction is zero at the wall, implying

$$\alpha_n = 0 \tag{3-76}$$

In agreement with the condition that only the liquid contributes to wall friction effects the sixth boundary condition states

$$\frac{d\,u_{\ell s}}{dn} = \frac{\tau_w}{\eta_\ell} \tag{3-77}$$

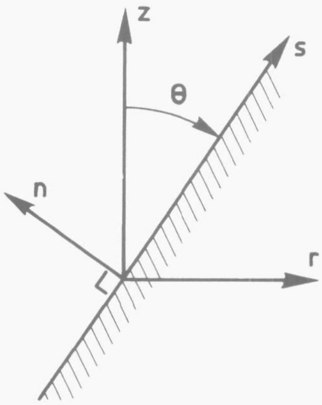

FIGURE 3-31.

Coordinate system at the wall.

where s is in the direction of the wall and n normal to it. If the wall makes an angle θ with the positive z direction as indicated in figure 3-31

$$u_{\ell s} = u_r \sin\theta + u_z \cos\theta \tag{3-78}$$

and

$$\frac{d\,u_{\ell s}}{dn} = \left(\frac{\partial u_r}{\partial r}\frac{\partial r}{\partial n} + \frac{\partial u_r}{\partial z}\frac{\partial z}{\partial n}\right)\sin\theta +$$

$$+ \left(\frac{\partial u_z}{\partial r}\frac{\partial r}{\partial n} + \frac{\partial u_z}{\partial z}\frac{\partial z}{\partial n}\right)\cos\theta = \frac{\tau_w}{\eta_\ell} \tag{3-79}$$

3.3.4. Simplified equations.

In view of the complexity of the momentum equations simplifications will be made with regard to the turbulence terms that constitute the momentum transfer in the liquid as well as for the wall shear stress. By omitting these terms from the equations the new set of momentum equations becomes:

liquid phase

r direction

$$\frac{\partial}{\partial r}((1-\alpha)\,\rho_\ell\,u_{\ell r}{}^2) + \frac{(1-\alpha)\,\rho_\ell\,u_{\ell r}{}^2}{r} + \frac{\partial}{\partial z}((1-\alpha)\,\rho_\ell\,u_{\ell r}\,u_{\ell z}) =$$

$$-\,(1-\alpha)\frac{\partial p}{\partial r} + (1-\alpha)\,\rho_\ell f_r + R_r \tag{3-80}$$

z-direction

$$\frac{\partial}{\partial r}\left((1-\alpha)\,\rho_\ell\,u_{\ell z}\,u_{\ell r}\right) + \frac{(1-\alpha)\,\rho_\ell u_{\ell z} u_{\ell r}}{r} + \frac{\partial}{\partial z}\left((1-\alpha)\,\rho_\ell\,u_{\ell z}{}^2\right) =$$

$$-\,(1-\alpha)\,\frac{\partial p}{\partial z} - (1-\alpha)\,\rho_\ell f_z + R_z \qquad (3\text{-}81)$$

mixture

r direction

$$\frac{\partial}{\partial r}\left(\alpha\rho_g\,u_{gr}{}^2 + (1-\alpha)\,\rho_\ell\,u_{\ell r}{}^2\right) + \frac{\alpha\rho_g\,u_{gr}{}^2 + (1-\alpha)\,\rho_\ell u_{\ell r}{}^2}{r} +$$

$$\frac{\partial}{\partial z}\left(\alpha\rho_g\,u_{gr}\,u_{gz} + (1-\alpha)\,\rho_\ell\,u_{\ell r}\,u_{\ell z}\right) + \frac{\partial}{\alpha r}\left(B\alpha\,\rho_\ell\,u_{gr}\,(u_{gr} - u_{\ell r})\right) +$$

$$\frac{B\alpha\rho_\ell\,u_{gr}\,(u_{gr} - u_{\ell r})}{r} + \frac{\partial}{\partial z}\left(B\alpha\rho_\ell\,u_{gz}\,(u_{gr} - u_{\ell r})\right) =$$

$$-\,\frac{\partial p}{\partial r} + (\alpha\rho_g + (1-\alpha)\,\rho_\ell)\,f_r \qquad (3\text{-}82)$$

z direction

$$\frac{\partial}{\partial r}\left(\alpha\rho_g\,u_{gr}\,u_{gz} + (1-\alpha)\,\rho_\ell\,u_{\ell r}\,u_{\ell z}\right) + \frac{\alpha\rho_g\,u_{gr}\,u_{gz} + (1-\alpha)\rho_\ell\,u_{\ell r}\,u_{\ell z}}{g} +$$

$$\frac{\partial}{\partial z}\left(\alpha\rho_g\,u_{gz}{}^2 + (1-\alpha)\,\rho_\ell\,u_{\ell z}{}^2\right) + \frac{\partial}{\partial r}\left(B\alpha\,\rho_\ell\,u_{gr}\,(u_{gz} - u_{\ell z})\right) +$$

$$\frac{B\alpha\rho_\ell\,u_{gr}\,(u_{gz} - u_{\ell z})}{r} + \frac{\partial}{\partial z}\left(B\alpha\rho_\ell\,u_{gz}\,(u_{gz} - u_{\ell z})\right) =$$

$$-\,\frac{\partial p}{\partial z} - (\alpha\rho_g + (1-\alpha)\,\rho_\ell)\,f_z \qquad (3\text{-}83)$$

Due to these simplifications the boundary conditions proposed in the proceeding sector have to be adapted to the new requirements.
No fluid can penetrate the wall and the condition

$$u_{\ell n} = u_{gn} = 0 \qquad (3\text{-}84)$$

remains.
The velocity component directed along the wall can no longer be zero because the wall friction has been dropped from the equations and the flow must be regarded as a slip flow. Physically this would mean that the boundary layer is excluded from the control area. Only the core, which in case of single phase flow would have a nearly flat velocity profile, is considered and the axial velocity at the boundary between core and boundary layer has a finite but a priori unknown value.
The corresponding new condition, is

$$\frac{\partial u_{\ell s}}{\partial n} = \frac{\partial u_{gs}}{\partial n} = 0 \qquad (3\text{-}85)$$

As the radial velocity at the wall is zero no diffusion of axial momentum normal to this wall is possible. From diffusion considerations the normal gradient in the velocities $u_{\ell s}$ and u_{gs} must be zero at the solid wall. At boundary layer distance from the wall, however, a finite radial velocity may exist. By excluding the boundary layer from the control volume the assumption of zero gradients is no longer justified completely. Assuming zero or about zero normal velocities within the boundary layer region the error in the boundary condition of equation (3-85) may be tolerated.
The assumption of zero void fraction was abandoned as well and replaced by

$$\frac{\partial \alpha}{\partial n} = 0 \qquad (3\text{-}86)$$

again this condition can be defended on grounds of diffusion and assuming zero normal velocity.
The sixth boundary condition to complete the set prescribes the gradient of the pressure at the wall as given by the radial force field which is imposed on the flow:

$$\frac{\partial p}{\partial n} = \rho_m \frac{u_t^2}{R} \qquad (3\text{-}87)$$

3.3.5. Integration by the N-strip method.

3.3.5.1. Description of the method.

Despite the simplifying assumptions the basic equations representing the model constitute a set of highly nonlinear first order partial differential equations for which no standard method of solution exists, numerical or otherwise. ZANDBERGEN [61] proposed a method by which a set of such equations for single phase flow (momentum equations for the flow of an ideal gas around a circular cone) could be reduced to a set of ordinary differential equations by dividing the flow field into a number of strips. This so called N-strip method approximates the solution of the original set by a method of integral relations using interpolation functions based on the value of the variables on the strip boundaries.
For the two dimensional case, which is of interest here, the set of equations is to be written as

$$\frac{\partial P_i}{\partial x} + \frac{\partial Q_i}{\partial y} = S_i \qquad (3\text{-}88)$$

where i indicates the i-th equation. The flow field is divided as indicated in figure 3-32.

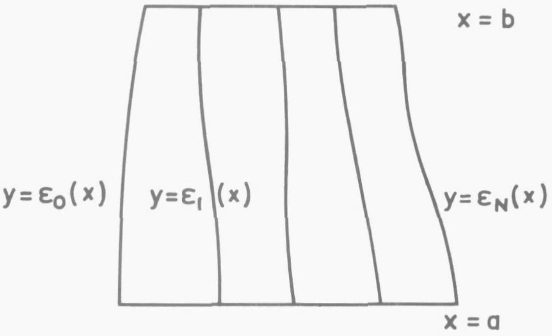

FIGURE 3-32.

Division of flow field in strips.

It is now assumed that $\frac{\partial P_i}{\partial x}$ and S_i can be written as functions of y at a certain value x by an interpolation formula of the form

$$\frac{\partial P_i}{\partial x} = \sum_{j=0}^{n} g_{ij}\ (y)\ \frac{\partial P_i^{\ j}}{\partial x} \tag{3-89}$$

with the only condition for the interpolation function g_{ij} that

$$g_{ij}\ (\varepsilon_k) = \delta_{jk}\ \text{(Kronecker delta)} \tag{3-90}$$

and where $\frac{\partial P_i^{\ j}}{\partial x}$ is the value at the j-th strip boundary:

$$\frac{\partial P_i^{\ j}}{\partial x} = (\frac{\partial P_i}{\partial x})_{y=j} \tag{3-91}$$

The strip method postulates that the equations (3-88) are satisfied approximately by the integral relations

$$\int_{\varepsilon_o}^{\varepsilon_k} \frac{\partial P_i}{\partial x}\, dy + \int_{\varepsilon_o}^{\varepsilon_k} \frac{\partial Q_i}{\partial y}\, dy = \int_{\varepsilon_o}^{\varepsilon_k} S_i\, dy \tag{3-92}$$

for each of the n regions $y = \varepsilon_o(x) \rightarrow y = \varepsilon_k(x)$.

Assuming g_{ij} independent of i (i.e. the same type of interpolation function for all the equations of the set (3-87)) and writing the integral of the interpolation function as

$$\int_{\varepsilon_o}^{\varepsilon_k} g_j\ (y)\ dy = a_{kj} \qquad\qquad k = 1 \ldots\ldots n \tag{3-93}$$

equation (3-92) becomes

$$\sum_{j=0}^{n} a_{kj}\ \frac{\partial P_i^{\ j}}{\partial x} + Q(\varepsilon_k) - Q(\varepsilon_o) = \sum_{j=0}^{n} a_{kj}\ S_i^{\ j} \tag{3-94}$$

Transformation of $\frac{\partial P_i^{\ j}}{\partial x}$ to the directional derivate $\frac{dP_i^{\ j}}{dx}$ along the strip boundaries is necessary because the interpolation functions are based on the strip boundary values giving

$$\frac{\partial P_i^{\ j}}{\partial x} = \frac{dP_i^{\ j}}{dx} - \frac{d\varepsilon_j(x)}{dx}\ \frac{\partial P_i^{\ j}}{\partial y} \tag{3-95}$$

Elimination of $\frac{\partial P_i^{\ j}}{\partial y}$ can be effected through the use of an other interpolation function, similar to equation (3-89), based on P_i itself.

$$\frac{\partial P_i}{\partial y} = \sum_{\ell=0}^{n} q_{i\ell}\,(y)\,P_i^{\ell} \qquad (3\text{-}96)$$

Upon substitution of the transforms eqution (3-94) becomes

$$\sum_{j=0}^{n} a_{kj}\,\{\frac{dP_i^{\,j}}{dx} - \frac{d\varepsilon_j(x)}{dx}\sum_{\ell=0}^{n} q_{i\ell}\,(\varepsilon_j)P_i^{\,\ell}\,\}$$

$$+\,Q_i\,(\varepsilon_k) - Q(\varepsilon_o) = \sum_{j=0}^{n} a_{kj}\,S_i^{\,j} \qquad (3\text{-}97)$$

The result is a set of nonlinear ordinary differential equations analogous to the set of section 3.2.1. An essential difference between the set of basic equations (3-62), (3-63) and (3-80) through (3-83) and equations (3-88) should be noted here, which makes it impossible to follow the method described by Zandbergen to the end. As a result of the interaction forces between the separate phase equations the equivalent of equations (3-88) for the present set contain some composite terms of the form

$$(1-\alpha)\,\frac{\partial p}{\partial r}\;,\quad (1-\alpha)\,\frac{\partial p}{\partial z}\quad .$$

The system in general notation becomes

$$\frac{\partial P_i}{\partial z} + T_i\,\frac{\partial F_i}{\partial z} + \frac{\partial Q_i}{\partial r} + R_i\,\frac{\partial Y_i}{\partial r} = S_i \qquad (3\text{-}98)$$

where the problem-oriented cylindrical z,r coordinates are introduced to replace the previous, more general, x,y coordinates. Integration of equations (3-98) over the intervals indicated by equation (3-92) would entail very cumbersome interpolation formulae. If a polynomial were chosen a division of the flow field into n strips would require it to be of the n-th order.

In order to avoid these problems it was suggested by VRIESEMA [62] to integrate over two strips at a time using second order polynomials as interpolation functions. The equivalent of equations (3-92) now becomes

$$\int_{\varepsilon_{k-1}}^{\varepsilon_{k+1}} \frac{\partial P_i}{\partial z}\,dr + \int_{\varepsilon_{k-1}}^{\varepsilon_{k+1}} \{\,T_i\,\frac{\partial F_i}{\partial z}\,\}\,dr\;+$$

$$+\int_{\varepsilon_{k-1}}^{\varepsilon_{k+1}} \frac{\partial Q_i}{\partial r}\,dr + \int_{\varepsilon_{k-1}}^{\varepsilon_{k+1}} \{\,R_i\,\frac{\partial Y_i}{\partial r}\,\}\,dr = \int_{\varepsilon_{k-1}}^{\varepsilon_{k+1}} S_i\,dr \qquad (3\text{-}99)$$

Using a second order Lagrange polynomial the interpolation function $g_k(r)$ reads

$$g_k\,(r) = \prod_{\substack{m=k-1\\ m\neq k}}^{m=k+1} \frac{r-r_m}{r_k-r_m} \qquad (3\text{-}100)$$

Where g_k is assumed to be independent of i. The same type of function can be used to approximate P_i as well as $\frac{\partial P_i}{\partial z}$. Thus if

$$P_i = \sum_{k-1}^{k+1} g_{i\ell} \, P_i^{\ell} \tag{3-101}$$

then equation (3-96) can be written as

$$\frac{\partial P_i}{\partial r} = \frac{\partial}{\partial r} \left[\sum_{k-1}^{k+1} g_{i\ell} \, P_i^{\ell} \right] = \sum_{k-1}^{k+1} q_{i\ell} \, P_i^{\ell} \tag{3-102}$$

A further simplification is to restrict the method to equidistant strips making it possible to write

$$\frac{d\varepsilon_j(r)}{dr} = j \, \frac{dh(z)}{dz} \tag{3-103}$$

where h denotes the strip width.
In analogy with equation (3-95) the first composite term of equation (3-98) becomes

$$T_i^j \, \frac{\partial F_i^j}{\partial z} = T_i^j \left\{ \frac{dF_i^j}{dz} - j \, \frac{dh(z)}{dz} \, \frac{\partial F_i^j}{\partial r} \right\} \tag{3-104}$$

Whereas $\frac{\partial Q_i}{\partial r}$ is suitable for direct integration in r-direction the second composite term is not and has to be approximated.

$$R_i \, \frac{\partial Y_i}{\partial r} = \sum_{k-1}^{k+1} g_{i\ell} \left\{ R_i^{\ell} \, \frac{\partial Y_i^{\ell}}{\partial r} \right\} \tag{3-105}$$

Integration of the equations (3-99) subsequently produces

$$\sum_{k-1}^{k+1} a_j \, \frac{dP_i^j}{dz} - \sum_{k-1}^{k+1} b_j \, j \frac{dh(z)}{dz} \sum_{k-1}^{k+1} q_{\ell} \, P_i^{\ell} + \sum_{k-1}^{k+1} a_j \, T_i^j \, \frac{dF_i^j}{dz} -$$

$$- \sum_{k-1}^{k+1} b_j \, j \frac{dh(z)}{dz} \, T_i^j \sum_{k-1}^{k+1} q_{\ell} F_i^{\ell} + Q_{k+1} - Q_{k-1} +$$

$$+ \sum_{k-1}^{k+1} a_j \, R_i^j \sum_{k-1}^{k+1} q_{\ell} \, Y_i^{\ell} = \sum_{k-1}^{k+1} a_j \, S_i^j \tag{3-106}$$

Whereas a_j is the second order integration formula, called Simpson's rule, b_j, following Euler's rule, is of the first order.
The reason is that the derivative of the parabolic interpolation function is linear and hence integration by Euler's rule gives the exact answer.

The general forms of $\sum_{k-1}^{k+1} a_j \, f_j$ and $\sum_{k-1}^{k+1} b_j \, f_j$ are respectively

$$\frac{h}{3}\,(f_{k-1} + 4f_k + f_{k+1}) \quad \text{and} \quad \frac{h}{2}\,(f_{k-1} + f_{k+1}) \tag{3-107}$$

Furthermore the derivative $\left[\sum_{k-1}^{k+1} q_\ell\, f_\ell\right]_m$ is

$$\begin{aligned}
f'_{k-1} &= \frac{1}{h}\,(-\frac{3}{2}\,f_{k-1} + 2f_k - \tfrac{1}{2}f_{k+1}) \\
f'_k &= \frac{1}{h}\,(-\frac{1}{2}\,f_{k-1} + \frac{1}{2}\,f_{k+1}) \\
f'_{k+1} &= \frac{1}{h}\,(\frac{1}{2}\,f_{k-1} - 2f_k + \frac{3}{2}\,f_{k+1})
\end{aligned} \tag{3-108}$$

Substitution of a_j, b_j and q_j and dropping the i-index, produces

$$\begin{aligned}
&\frac{h}{3}\,\frac{dP_{k-1}}{dz} + 4\,\frac{h}{3}\,\frac{dP_k}{dz} + \frac{h}{3}\,\frac{dP_{k+1}}{dz} - (k-1)\,\frac{dh}{dz}\,\{ -\frac{3}{2}\,P_{k-1} + 2P_k - \frac{1}{2}\,P_{k+1} \} - \\
&- (k+1)\,\frac{dh}{dz}\,\{ \frac{1}{2}\,P_{k-1} - 2P_k + \frac{3}{2}\,P_{k+1} \} + \\
&+ \frac{h}{3}\,T_{k-1}\,\frac{dF_{k-1}}{dz} + 4\,\frac{h}{3}\,T_k\,\frac{dF_k}{dz} + \frac{h}{3}\,T_{k+1}\,\frac{dF_{k+1}}{dz} - \\
&- (k-1)\,\frac{dh}{dz}\,T_{k-1}\,\{ -\frac{3}{2}\,F_{k-1} + 2F_k - \frac{1}{2}\,F_{k+1} \} - \\
&- (k+1)\,\frac{dh}{dz}\,T_{k+1}\,\{ \frac{1}{2}\,F_{k-1} - 2F_k + \frac{3}{2}\,F_{k+1} \} + \\
&+ \frac{1}{3}\,R_{k-1}\,\{ -\frac{3}{2}\,Y_{k-1} + 2Y_k - \frac{1}{2}\,Y_{k+1} \} + \frac{4}{3}\,R_k\,\{ -\frac{1}{2}\,Y_{k-1} + \frac{1}{2}\,Y_{k+1} \} + \\
&+ \frac{1}{3}\,R_k\,\{ \frac{1}{2}\,Y_{k-1} - 2Y_k + \frac{3}{2}\,Y_{k+1} \} + \\
&Q_{k+1} - Q_{k-1} = \frac{h}{3}\,S_{k-1} + \frac{4h}{3}\,S_k + \frac{h}{3}\,S_{k+1}
\end{aligned} \tag{3-109}$$

Further substitution of P_i, T_i, F_i, R_i, Y_i, Q_i and S_i is performed in Appendix 3-B resulting in six simultaneous differential equations in

$$\frac{d\alpha_i}{dz}, \quad \frac{dp_i}{dz}, \quad \frac{d\,u_{\ell z_i}}{dz}, \quad \frac{d\,u_{\ell r_i}}{dz}, \quad \frac{d\,u_{gz_i}}{dz} \quad \text{and} \quad \frac{d\,u_{gr_i}}{dz}$$

For a system of n strips, integration of the interpolation functions over the intervals of k: $\varepsilon_o - \varepsilon_1$, $\varepsilon_o - \varepsilon_2$, $\varepsilon_1 - \varepsilon_3$, ε_{k-1}, ε_{k+1}, $\varepsilon_{n-2} - \varepsilon_n$ produces 6 n equations, whereas there are 6 n + 6 unknown derivatives for n+1 strip boundaries. For the rotational symmetric flow problem ε_o is the center-line while ε_n coincides with the solid wall of the flow channel. Six additional relations to complete the set of 6 n + 6 equations are provided by the boundary conditions at the solid wall.

3.3.5.2. Integration of the set of ordinary differential equations.

The set of equations (3-109) as presented in Appendices 3-B together with the boundary condition relations form a set of algebraic equations that can be written as

$$\begin{array}{l} a_{11}x_1 + a_{12}x_2 + a_{13}x_3 \ldots\ldots a_{1(6n+6)}\,x_{(6n+6)} = b_1 \\ \vdots \\ a_{(6n+6)1}\,x \ldots\ldots\ldots\ldots\ldots\ldots\ldots\ldots\ldots a_{(6n+6)\,(6n+6)}\,x_{(6n+6)} = b_{(6n+6)} \end{array} \qquad (3\text{-}110)$$

where $x_1, x_2 \ldots\ldots x_{(6n+6)}$ are the derivatives of α, p, $u_{\ell z}$, $u_{\ell r}$, u_{gz} and u_{gr} along the strip boundaries. Solution of equations (3-110) provides the explicit expressions for these derivatives and makes the set suitable for an integration scheme according to the Runge-Kutta method, similar to the set given by equations (3-44) and (3-45).

3.3.5.3. The computer program.

A computer program, called STRIPTEASE, was written in ALGOL to perform the integration of the basic equations by the N-strip method. Apart from routines for generating and solving the matrix (3-110) and for the Runge-Kutta integration the program incorporates a section where the angular momentum flux is calculated after each Runge-Kutta integration step to find the new value for the constant C that describes the tangential flow distribution. At the start of the program Ω is calculated from the wheel flow forced on the system by the swirl vanes, using equation (3-74) with n =-1. Integration is performed according to Simpson's rule. The value of C at the exit of the vanes is found from

$$C = \frac{u_t}{r} = u_{mz}\ \mathrm{tg}\theta / r \qquad (3\text{-}111)$$

where

$$u_{mz} = \frac{(\alpha\,\rho_g\,u_{gz} + (1-\alpha)\,\rho_\ell\,u_{\ell z})}{(\alpha\,\rho_g + (1-\alpha)\,\rho_\ell)} \qquad (3\text{-}112)$$

and θ is the vane exit angle with the positive z-axis.

The new value of C after each Rung-Kutta step is subsequently calculated from equations (3-72) and (3-74), taking n equal to 1 or -1 according to the program input value.

3.4. Adaptation of one-dimensional model to the carry-under problem.

In the following section an attempt is made to establish a simplified model for the calculation of carry-under. This model will be based on a relation for downcomer slip derived from the one-dimensional momentum balance.

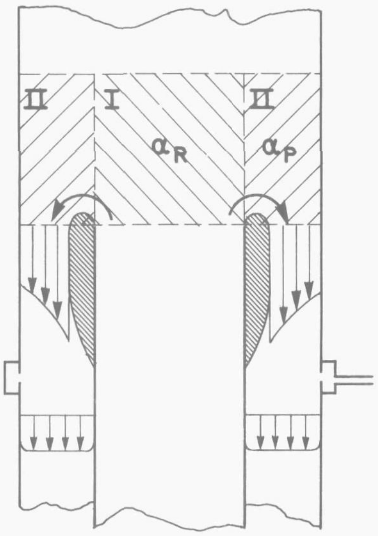

FIGURE 3-33.

Plenum for gravity separation model.

The separation is assumed to take place in two steps. The first takes place in the separation plenum above riser and downcomer. This region is divided into two regions. One cylindrical region directly above the riser with an homogeneously distributed void fraction equal to the riser void fraction and a second, annular, region above the downcomer with a void fraction $<\alpha_P>$ which is also homogeneously distributed but lower than $<\alpha_R>$.
The regions are shown in figure 3-33 and indicated as I and II.
Carry-under takes place by entraining steam from region II. Depending on the downcomer velocity steam may be entrained into the high velocity region and separate out in second instance in the low velocity region near the downcomer wall. Considering the downcomer flow as one-dimensional, dropping the <> signs, and neglecting the wall friction the momentum equation for the gas phase, equation (3-36), reduces to

$$\alpha \frac{dp}{dz} + \alpha\rho_g g + \frac{3}{4}\alpha \frac{C_D}{d}\rho_\ell(u_g-u_\ell)|u_g-u_\ell| = 0 \qquad (3\text{-}113)$$

From equation (3-43) it follows that

$$\frac{dp}{dz} = -(\alpha\rho_g + (1-\alpha)\,\rho_\ell)g \qquad (3\text{-}114)$$

Combining equations (3-113) and (3-114) to

$$\frac{3}{4}\rho_\ell \frac{C_D}{d}(u_g-u_\ell)|u_g-u_\ell| = (1-\alpha)(\rho_\ell-\rho_g)g \qquad (3\text{-}115)$$

a relation between the relative velocity (u_g-u_ℓ) and the void fraction is found. The riser data were analyzed according to equation (3-115) and $\frac{C_D}{d}$ was plotted as a function of . The result shown in figures 3-34 and 3-35 (see page 142). The data could be correlated with the relation suggested by HENCH and JOHNSTON [90] i.e. equation (3-58) giving

$$\frac{C_D}{d} = 100\ (1-\alpha)^3 \qquad (3\text{-}116)$$

for the 70 bar data and

$$\frac{C_D}{d} = 47\ (1-\alpha)^3 \qquad (3\text{-}117)$$

for 50 bar.

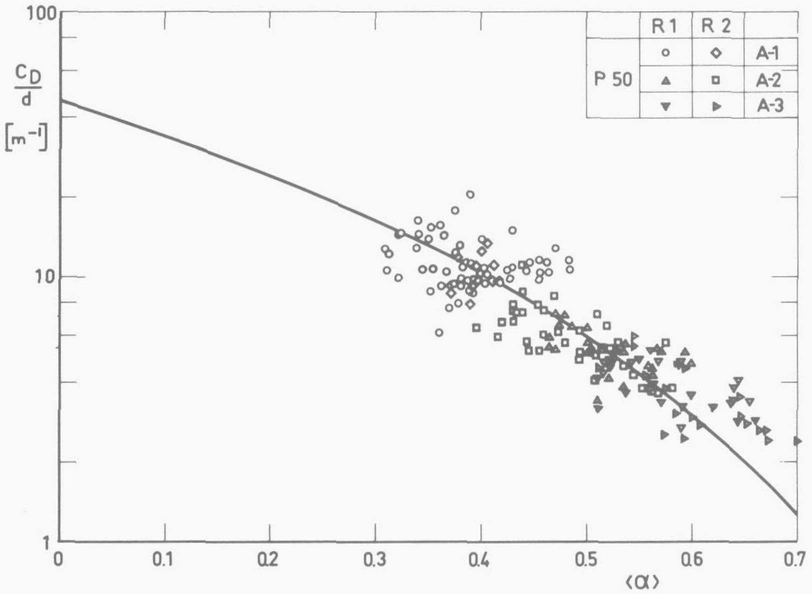

FIGURE 3-34.

C_D/d from riser data at 50 bar as a function of void fraction.

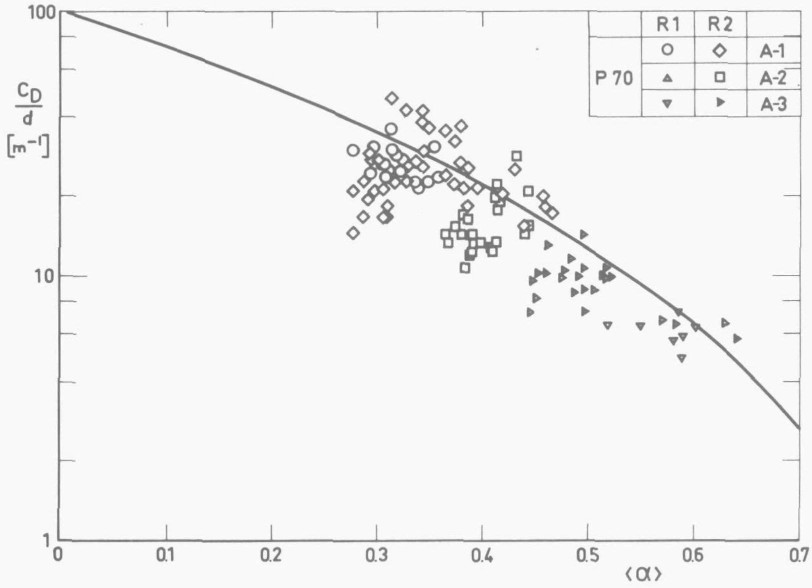

FIGURE 3-35.

C_D/d from riser data at 70 bar as a function of void fraction.

Insertion of these relations in equation (3-115) gives

$$u_g - u_\ell = \pm \frac{\sqrt{\dfrac{(\rho_\ell - \rho_g)}{\frac{3}{4}\rho_\ell \cdot K}\, g}}{1-\alpha} = \pm \frac{K_1}{1-\alpha} \qquad (3\text{-}118)$$

with K = 100 for 70 and 47 for 50 bar.
The plus sign is for upflow and the minus sign for downflow.
Division of equation (3-118) by u_ℓ gives

$$\frac{u_g}{u_\ell} = \langle s \rangle = 1 \pm \frac{K_1}{(1-\alpha)u_\ell} = 1 \pm \frac{K_1}{v_{s\ell}} \qquad (3\text{-}119)$$

The constant K_1 is now found to be 0.353 for 70 bar and 0.518 for 50 bar. The one-dimensional analysis appears to give almost exactly the same results

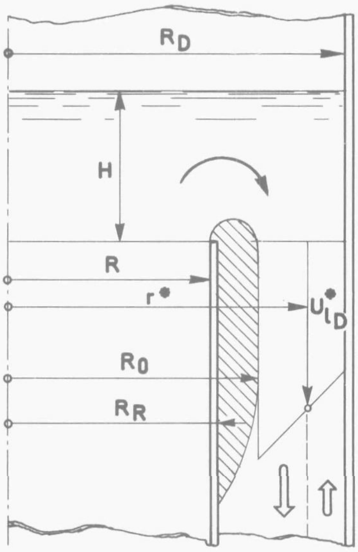

FIGURE 3-36.

Downcomer geometry and flow separation zone for gravity separation model.

as the empirical relations of equations (2-6) and (2-7). The pressure effect in K_1 is determined by the density ratio but even more by the value of K. Hench and Johnston found K = 54.9 for air-water mixtures viz. air bubbling through stagnant water. Comparing this value of K with those found for 50 and 70 bar and noting the strong increase in K between 50 and 70 bar it is probable that other effects besides pressure, such as channel diameter, influence K. The agreement between empirical and analytical slip results for the riser gives confidence that the relation might also hold for the downcomer as suggested in section 2.1.4.2.

The velocity distribution at the downcomer inlet between the flow separation zone and the downcomer wall is assumed as

$$u_{\ell D} = \frac{c}{r} \qquad (3\text{-}120)$$

The various radii are indicated in figure 3-36.
The connection between this velocity distribution and the superficial downcomer velocity is given by

$$\int_{R_0}^{R_D} (1-\alpha_p)\, u_{\ell D}\, 2\pi r\, dr = v_{s\ell D}\, \pi (R_D^{\,2} - R_R^{\,2}) \qquad (3\text{-}121)$$

By substitution of equation (3-120) and subsequent integration the distribution constant c is found as

$$c = \frac{v_{s\ell D}\, (R_D^{\,2} - R_R^{\,2})}{2(1-\alpha_p)(R_D - R_0)} \qquad (3\text{-}122)$$

Equation (3-118) gives for the relative velocity in the downcomer

$$u_{\ell D} - u_{gD} = \frac{K_1}{1-\alpha_p} \qquad (3\text{-}123)$$

and the critical liquid velocity, i.e. for $u_{gD} = 0$, becomes

$$u_{\ell D}^{\star} = \frac{K_1}{1-\alpha_p} \qquad (3\text{-}124)$$

With the use of equation (3-124) and (3-120), equation (3-122) is transformed to

$$v_{s\ell D} = \frac{2(R_D - R_0)\, K_1\, r^{\star}}{(R_D^{\,2} - R_R^{\,2})} \qquad (3\text{-}125)$$

For $r^{\star} = R_0$ equation (3-125) gives the threshold velocity for the inception of entrainment of any steam from region II. For $r^{\star} = R_D$ the same equation gives the second threshold velocity, above which no escape of the steam from the downcomer is possible anymore.

The amount of steam carried under is found from integration of the steam velocity u_{gD} over the downcomer inlet from R_0 to $r^{\star}$:

$$v_{sgD}\pi(R_D{}^2-R_R{}^2) = \int_{R_0}^{r^{\star}} \alpha_p u_{gD} \, 2\pi r \, dr \tag{3-126}$$

With $u_{gD} = u_{\ell D} - \frac{K_1}{1-\alpha_p}$ equation (3-126) becomes

$$v_{sgD} = \frac{2\pi\alpha_p}{\pi(R_D{}^2-R_R{}^2)} \left\{ \int_{R_0}^{r^{\star}} c.dr - \int_{R_0}^{r^{\star}} \frac{K}{(1-\alpha_p)} r.dr \right\} =$$

$$= \frac{2\alpha_p}{R_D{}^2-R_R{}^2} \left\{ c \, (r^{\star}-R_0) - \frac{K_1}{2(1-\alpha_p)} (r^{\star 2} - R_0{}^2) \right\} \tag{3-127}$$

Elimination of $r^{\star}$ with the aid of equation (3-125) and substitution of c from equation (3-122) gives

$$v_{sgD} = \frac{\alpha_p}{1-\alpha_p} \left\{ \frac{v_{s\ell D}{}^2 \, (R_D{}^2-R_r{}^2)}{4(R_D-R_0)^2K_1} - v_{s\ell D} \cdot \frac{R_0}{R_D-R_0} + \frac{K_1R_0{}^2}{R_D{}^2-R_R{}^2} \right\} \tag{3-128}$$

The corresponding downcomer quality is found from

$$x_D = \frac{v_{sgD} \, \rho_g}{v_{sgD} \, \rho_g + v_{s\ell D} \, \rho_\ell} \tag{3-129}$$

The quality in the downcomer below the sparger is lower as a result of the added quench water and the velocity $v_{s\ell D}$ in equation (3-129) must be replaced by

$$v_{s\ell DB} = v_{s\ell D} + \phi_{m2} \, / \, (R_D{}^2-R_R{}^2)\rho_\ell \tag{3-130}$$

The void fraction is found from equation (3-118) which, after rearranging, gives for downflow

$$\alpha_D = \frac{v_{sgD}}{v_{sgD} + v_{s\ell D} - K_1} \tag{3-131}$$

The amount of steam entrained as given by equations (3-128) is the carry-under if no steam escapes in the region $r^{\star} < r < R_D$. It therefore predicts a maximum and if the water velocity below the separation zone is too low to entrain the steam secondary separation may take place.

When the superficial downcomer velocity reaches the value $(v_{s\ell D})_{r^{\star}=R_D}$ no secondary separation becomes possible anymore.

The radius $r^{\star}$ in equation (3-127) has now to be replaced by R_D resulting in the following expression for the superficial downcomer steam velocity

$$v_{sgD} = \frac{\alpha_p}{1-\alpha_p} \left(v_{s\ell D} - K_1 \frac{R_D^2-R_0^2}{R_D^2-R_R^2}\right) \qquad (3\text{-}132)$$

The quality and void fraction in the lower downcomer region are again found from equations (3-129) and (3-131).

The void fraction α_p in region II, that forms the reservoir from which the steam is entrained, still needs to be determined. The amount of steam transported from the riser to region II above the riser is dependent on the radial transport velocity and the velocity of the bubbles rising to the surface. These velocities are somewhat arbitrary because of the rather complicated flow field. The effective rise velocity of the steam escaping from region II is assumed to be given by equation (3-118), or

$$u_{rise} = \frac{K_1}{(1-\alpha_p)} \qquad (3\text{-}133)$$

The radial velocity u_{rad}, assuming no slip in radial direction, is now defined as the ratio of the travelling distance in region II, R_D-R_R, and the residence time t_{res} in region II, where the latter value follows from

$$t_{res} = \frac{\pi(R_D^2-R_R^2)(1-\alpha_p)H}{v_{s\ell D}\ \pi(R_D^2-R_R^2)} \qquad (3\text{-}134)$$

Hence u_{rad} is found as

$$u_{rad} = \frac{R_D-R_R}{t_{res}} = v_{s\ell D} \frac{R_D-R_R}{(1-\alpha_p)H} \qquad (3\text{-}135)$$

In the model the ratio α_p/α_R is now assumed to be a function of the ratio u_{rad}/u_{rise}.

It is required that for $u_{rad} = 0$ no steam is transported to the downcomer inlet or $\alpha_p = 0$. The function that satisfies these requirements is postulated to be of the form

$$\frac{\alpha_p}{\alpha_R} = \frac{1}{1+N\dfrac{u_{rise}}{u_{rad}}} = \frac{1}{1+N\dfrac{K}{v_{s\ell D}}\dfrac{H}{R_D-R_R}} \qquad (3\text{-}136)$$

where N is a constant.

Equation (3-136) together with equation (3-128) or (3-132) constitute the model.

Two constants unknown at this stage are involved, i.e. R_0 and N. These two were found from comparison with the experiments, as shown later in chapter 4.

The fountain effect was encountered as another aspect of the carry-under behaviour. The fountain height H_F can be estimated by applying the one-dimensional momentum balance for the mixture to a free jet issuing from the riser; the momentum flux leaving the riser exit is balanced by the weight of the mixture in the jet:

$$\rho_g \alpha_R A_R u_{gR}^{\;2} + \rho_\ell (1-\alpha_R) A_R u_{\ell R}^{\;2} + \rho_\ell B \alpha_R A_R \, u_{gR}(u_{gR}-u_{\ell R}) =$$

$$(\alpha_R \rho_g + (1-\alpha_R)\rho_\ell) A_R H_F \qquad (3\text{-}137)$$

The height calculated from equation (3-137) does not apply to the submerged condition before the fountain effect occurs. But as the level control system drains the water from the separating plenum and subsequently from the downcomer the jet is no longer submerged. The value of H_F found is only an indication as the effect will begin somewhat earlier due to the buoyancy effect of the surrounding mixture.

Furthermore the jet is not one-dimensional and applying equation (3-137) may prove to be an oversimplification. Choice of a suitable value for the virtual mass coefficient obtained from appropriate experiments, might remedy this deficiency. The use of such coefficients available in literature for the flow from a small bore tube is shown in chapter 4 to give results that underpredict the experimental data.

4. COMPARISON OF CARRY-UNDER ANALYSIS WITH EXPERIMENTAL RESULTS

4.1. Empirical

Although it was decided to create no new carry-under correlation based on dimensional analysis, a comparison with the only correlation of this kind to be found in literature seems useful. This correlation, due to PETRICK [20], is based on a number of parameters

$$v_{s\ell D},\ v_{s\ell R},\ H,\ D_R,\ \eta_\ell,\ \sigma,\ \rho_g,\ \rho_\ell,\ u_{gR},\ u_{gD},\ \phi_{gR},\ \phi_{gD},\ \phi_\ell$$

From these 13 variables 10 dimensionless groups can be formed.
Petrick recombined several of the ten he primarily found reducing the set to six. Changing from the mass flow-rates ϕ_g and ϕ_ℓ to quality x_R, x_D and and flow areas A_R and A_D the arrived at the functional relation for carry-under

$$\frac{x_D}{x_R} = \left(\frac{u_{gR}}{u_{gD}},\ \frac{H}{D},\ \frac{A_D}{A_R},\ \frac{\sigma}{\eta_\ell v_{s\ell R}},\ \frac{\rho_\ell}{\rho_g}\right) \qquad (4\text{-}1)$$

However, no satisfactory correlation of all his data, i.e. air-water and steam-water, could be obtained by a plot of these dimensionless groups and Petrick tried several non-dimensionless variations of the basic groups in equation (4-1). The result is a plot of x_D/x_R and the non-dimensionless complex

$$F = \left(\frac{u_{gR}}{u_{gD}}\right)\left(\frac{\sigma^{2/3}}{G_\ell^{\,2}\eta_\ell}\right)\left(\sqrt{\frac{\rho_\ell}{\rho_\ell}}\right)\left(\sqrt{\frac{D}{H}} + \sqrt{\frac{H}{D}}\right) \qquad (4\text{-}2)$$

This plot revealed two regions that were correlated by

$$0.1 < c.F < 3 : \frac{x_D}{x_R} = -\,0.6 \log \left[c\,\frac{F}{3.7}\right] \qquad (4\text{-}3)$$

$$3 < c.F < 64 : \frac{x_D}{x_R} = -\,0.04 \log \left[c\,\frac{F}{64}\right] \qquad (4\text{-}4)$$

where the conversion constant c is to be omitted if Anglo-saxon units are used. For the MKSA-system c is 3.98.
It is clear from equation (4-2) that the final form of the complex F shows some changes with respect to the groups of equation (4-1). The velocity $v_{s\ell R}$ has been changed to the mass velocity G_ℓ. The effect of the height H of the two-phase interphase has resulted in the somewhat complicated form of $\sqrt{\frac{D}{H}} + \sqrt{\frac{H}{D}}$ to account for the competing influences of radial velocity in the separating plenum above the riser and the residence time needed for bubbles to rise to the surface.
The carry-under results x_D/x_R of the present experiments are plotted as a function of c.F in figure 4-1. The data representing "false" carry-under were excluded from the set. The selection was made on a basis of downcomer slip. The remaining data points show reasonable agreement with Petrick's correlation in the region 3 < c.F < 64. The shaded area in figure 4-1 indicates the scatter of Petrick's data.

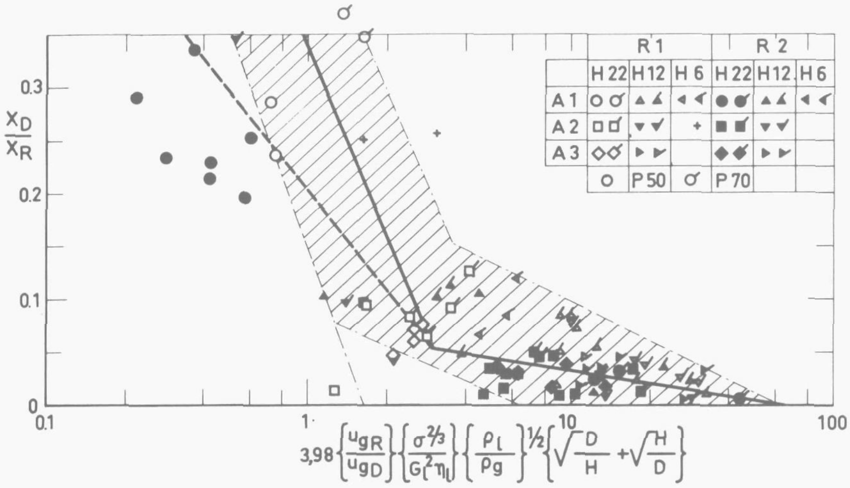

FIGURE 4-1.

Comparison of experimental carry-under data of this thesis with PETRICK's [20] correlation.

The comparison in the region 0.1 < c.F < 3 is less clear. The separation of the data points representing R1 and R2 experiments, already apparent in the other region, is more pronounced. Notwithstanding this scatter the data as a whole are overpredicted by the correlation of equation (4-3). Based on the data presented in figure 4-1 a modification of Petrick's correlation is suggested for this region:

$$0.1 < c.F < 3 \qquad \frac{x_D}{x_R} = -\,0.677 \log \left| \frac{c.F}{3.61} \right| \qquad (4\text{-}5)$$

while the correlation for the region 3 < c.F < 64 according to equation (4-4) is maintained.

Some additional remarks with respect to figure 4-1 can be made. An intriguing phenomenon is the break point in the correlation. Due to the non-dimensionless character of Petrick's correlation an indication of a change in carry-under behaviour can not be given. The implicit form makes it impossible to point to a specific influencial parameter that causes the change. It is suggested by MARSHALL [66] that a transition to the double interface condition is marked by the break point. Although this explanation is attractive it is also doubtful. The downcomer void fraction for the conditions left of the break point should, according to Marshall's own observations, be 90 to 100% which is not the case for any of Petrick's data. Moreover no mention is made of this phenomenon in Petrick's air-water data.

Another question arises with regard to the fountain effect. The riser velocities for Petrick's data in the high carry-under region are high enough to create the conditions for a fountain effect for medium high levels. But here again no quantitative answer can be given due to the lack of information regarding the level height. From the description of his experiments it is more likely that the level was not controlled but resulted from the loop operating conditions such as feedwater flow and evaporator power, and that therefore no systematic study of parameters at constant level was performed. The downcomer void fractions reported do not indicate the occurence of the fountain effect.

The more likely conclusion seems to be that the break point is in fact a gradual change in slope and marks no special effects. The higher carry-under found in Petrick's experiments might thus be a result of test loop dimensions. Furthermore the downcomer geometry is not adequately accounted for in the complex F as demonstrated by the separation of data points for R1 and R2.

4.2. Analytical.

The adapted one-dimensional carry-under model described in section 3.4. was applied to a number of the test conditions shown in figures 4-2 through 4-20.

The graphs show the threshold velocities for which $r^{\star} = R_0$ and $r^{\star} = R_D$, marking carry-under inception and the end of possible secondary separation in the downcomer respectively. These velocities are indicated by vertical lines. The downcomer quality, x_D, related to entrance conditions and conditions downstream of the sparger x_{D12}, is given as a function of the superficial downcomer velocity at the downcomer entrance ⋆). In addition the downcomer void fraction α_{D12} downstream of the sparger is shown.

Some of the void fraction curves show a minimum in the curve in the interval between the threshold velocities. This is a consequence of the flow contraction at the downcomer inlet. If the average water velocity, i.e. $v_{s\ell D}$, below this region is lower than the value of K_1, then the void fraction as calculated from equation (3-131) may be larger than 1. As the downcomer velocity increases the denominator of equation (3-131) increases not only due to the water velocity but also as a result of increased entrainment resulting in a decrease in void fraction until a minimum is reached. Beyond this minimum the superficial steam velocity increases more rapidly than the water velocity and the void fraction rises again. At downcomer velocities larger than the second threshold velocity the downcomer steam velocity is no longer a quadratic function of the water velocity (equation (3-132)) and with the diminishing increase in carry-under the downcomer void fraction passes through a maximum. This effect is amplified by the decreasing plenum void fraction α_p due to the decreasing riser quality with increasing water velocity. The very high void fractions left of the minimum found between the threshold velocities indicate a shortcoming of the model employed due to its simplicity. It is an indication that the steam bubbles can not ($\alpha_D > 1$) or only just ($1 > \alpha_D >$ minimum) be entrained and all or part of the steam initially entrained will escape again. It is more realistic therefore to approximate the real void fraction by a straight line connecting the minimum in the void fraction curve with zero at the lower threshold velocity.

This effect becomes stronger at low riser qualities. The void fraction α_p in the plenum is low and only small amounts of steam are entrained. At downcomer velocities about equal to K_1 the denominator of equation (3-131) is close to zero at carry-under inception. However, for high plenum void fractions the downcomer steam velocity v_{sgD} rises rapidly decreasing the downcomer void fraction.

The constants in the model, i.e. R_0 and N, were varied to compare the calculated values with the experiments. From inspection of the results the value of N was chosen as 0.0176.

The width of the flow separation zone and thus the value of R_0 was chosen according to

$$\frac{R_0 - R_R}{R_D - R_R} = \frac{1}{5} \qquad (4\text{-}6)$$

Examination of the results for the P70 experiments given in figures 4-2 through 4-12 (see following pages ⋆⋆) reveals an underprediction of the experimental data for R1 and overprediction for R2. The difference for R1 is also due to the false carry-under measured at the lower downcomer velocities.

⋆) *The numerals 12 in x_{D12} and α_{D12} are in accordance with the notation used for the pressure differential cell measuring the lower downcomer void fraction in the experiments.*

⋆⋆) *Experimental x_D values are indicated by Δ, and α_{D12} by ●.*

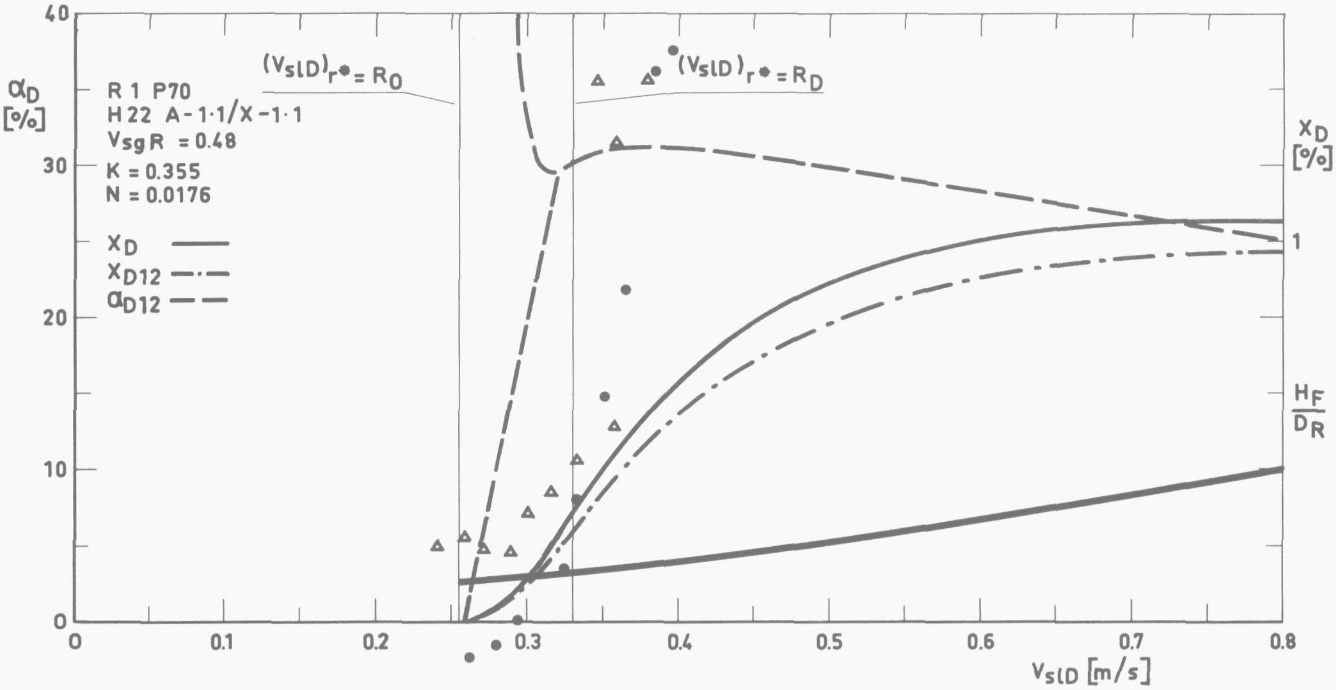

FIGURE 4-2.

Comparison of carry-under model with experiment.

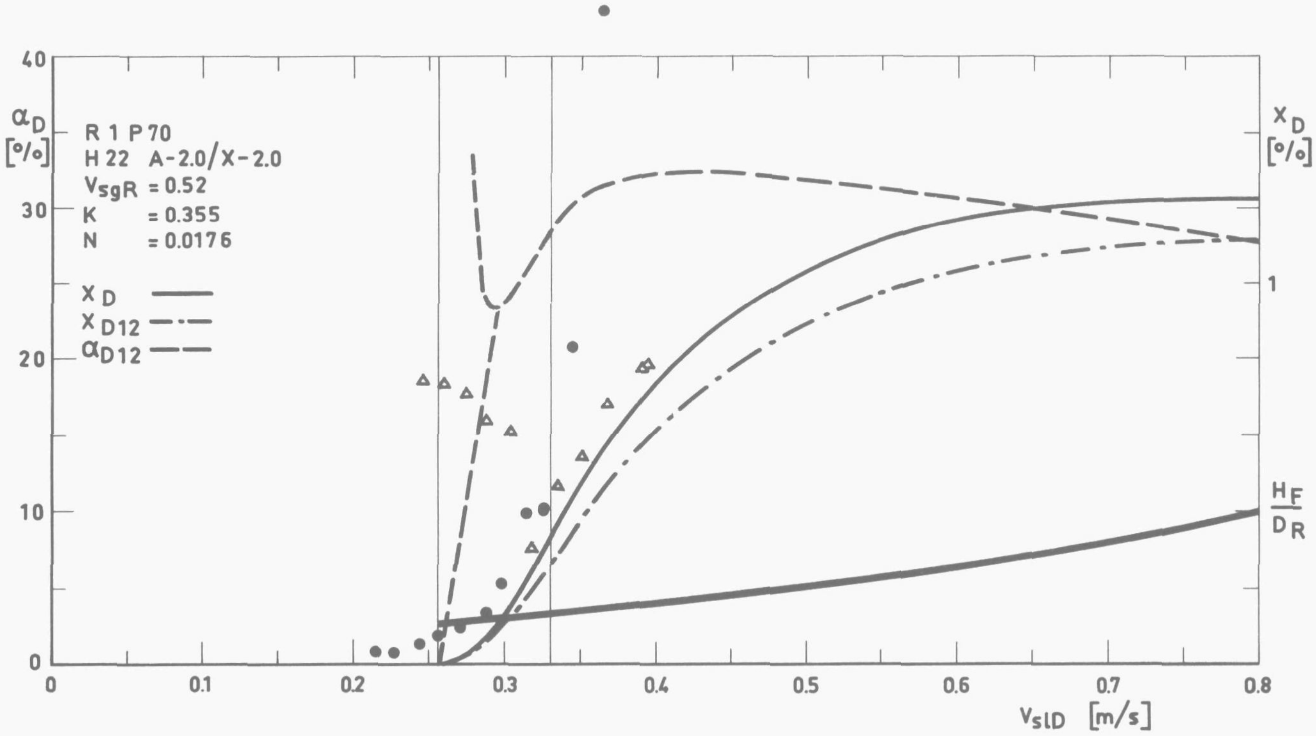

FIGURE 4-3.

Comparison of carry-under model with experiment.

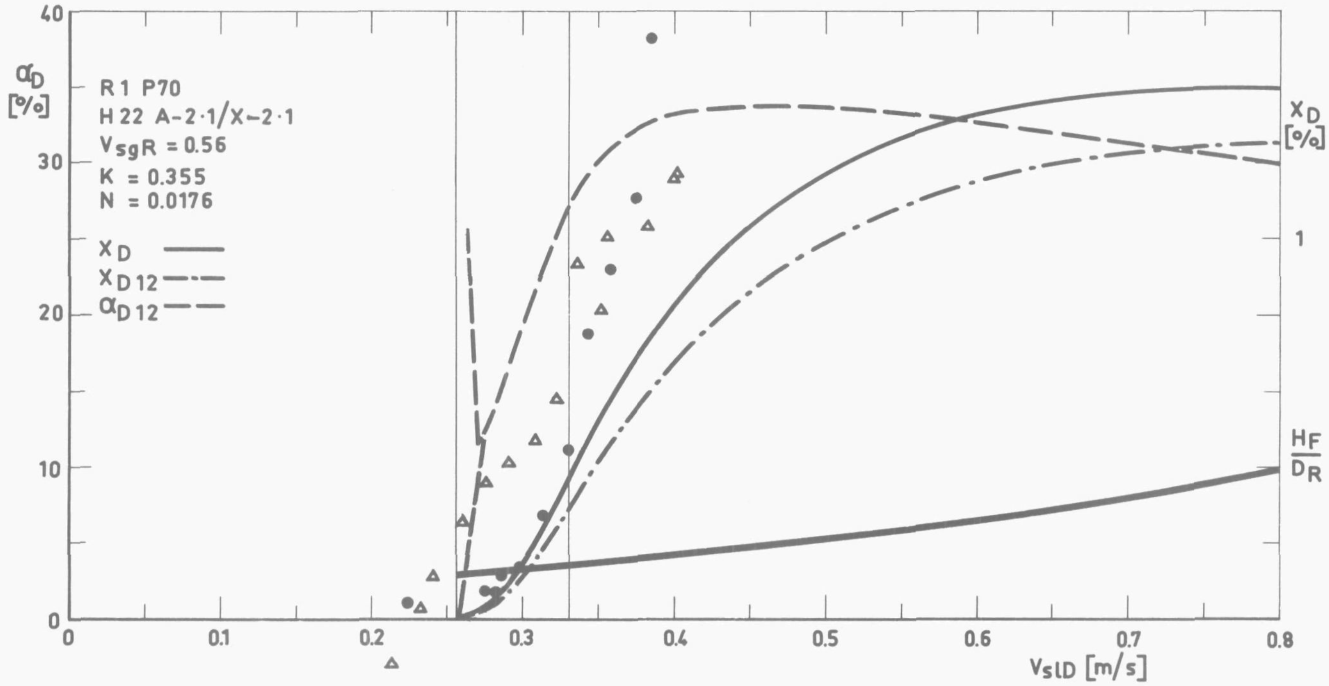

FIGURE 4-4.

Comparison of carry-under model with experiment.

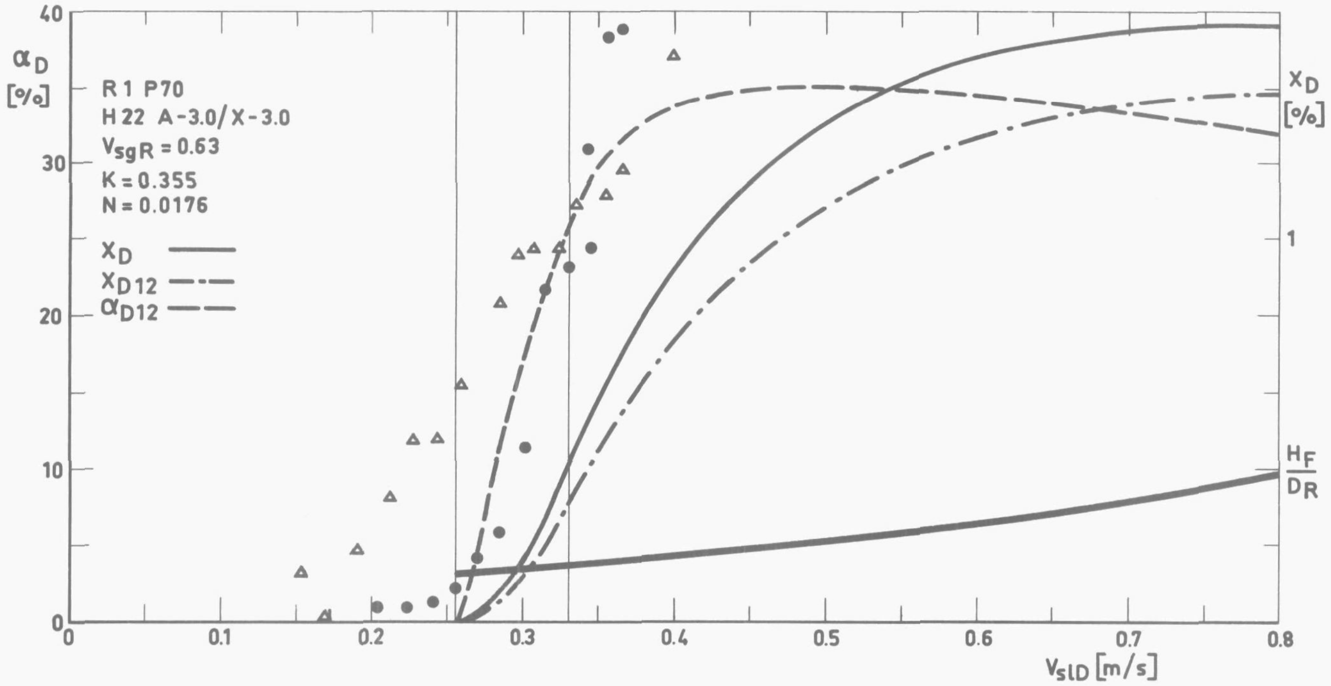

FIGURE 4-5.

Comparison of carry-under model with experiment.

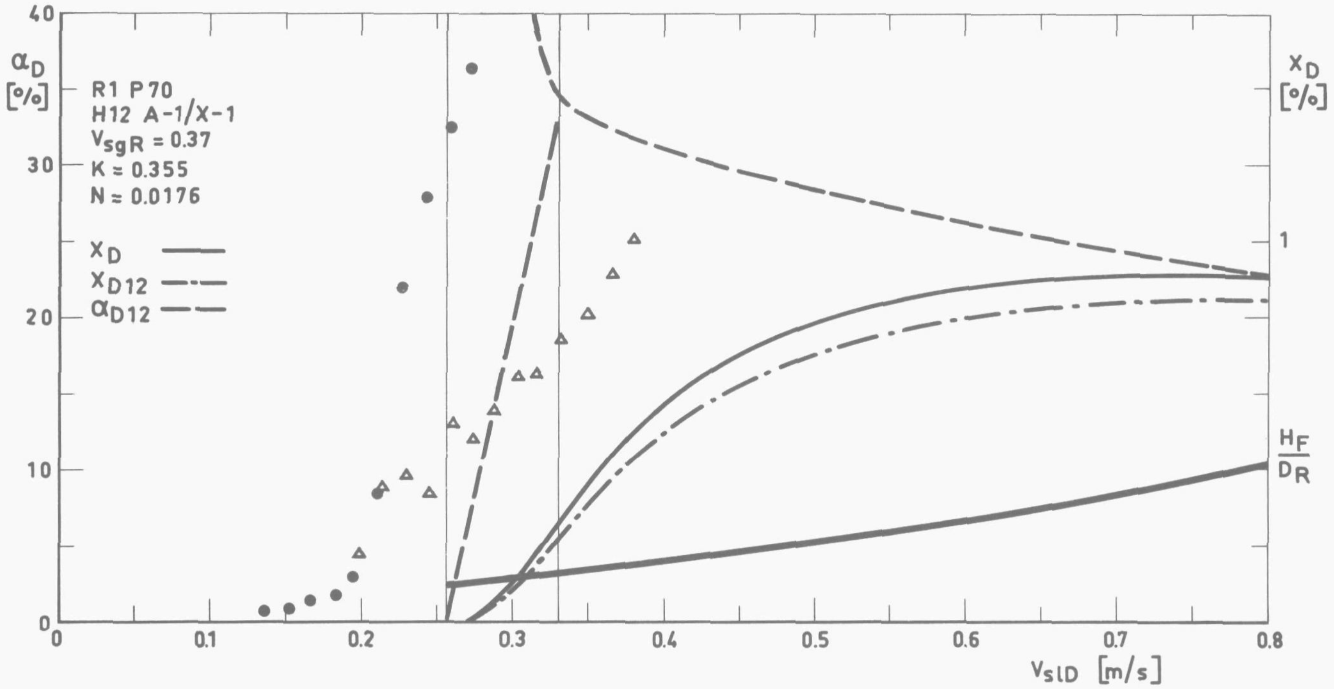

FIGURE 4-6.

Comparison of carry-under model with experiment.

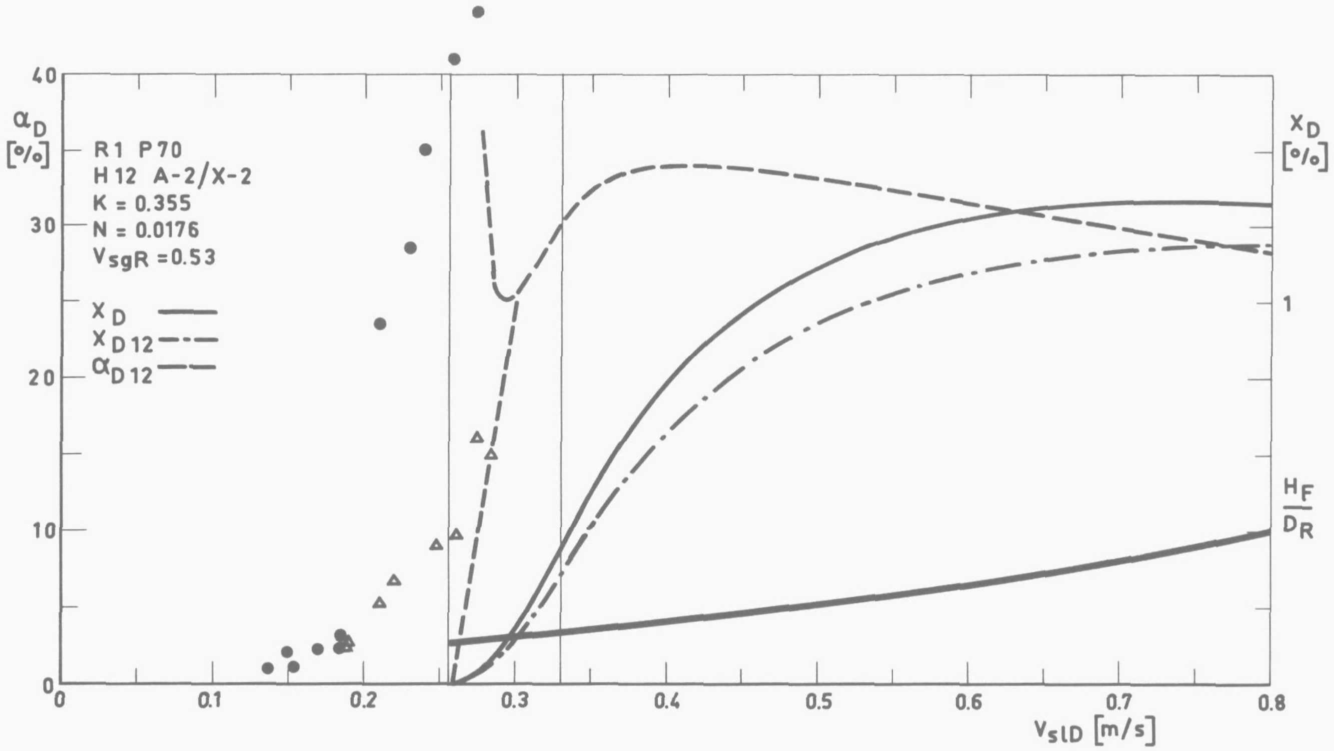

FIGURE 4-7.

Comparison of carry-under model with experiment.

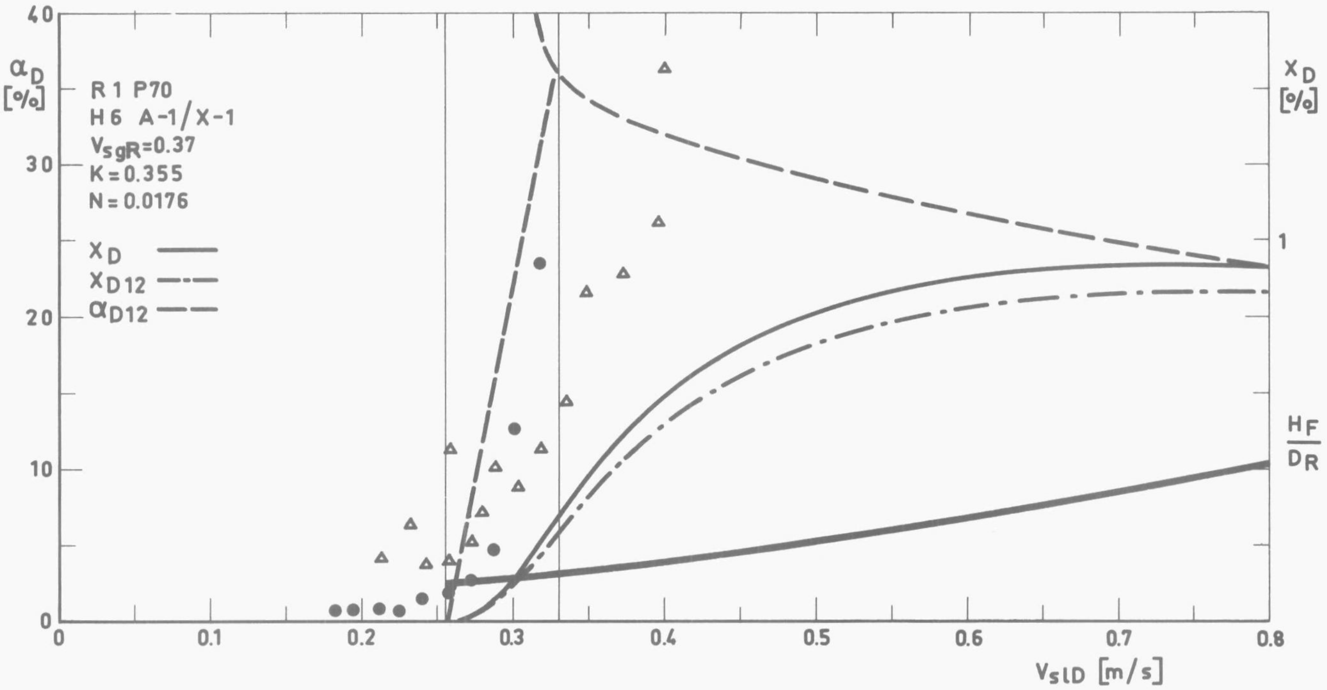

FIGURE 4-8.

Comparison of carry-under model with experiment.

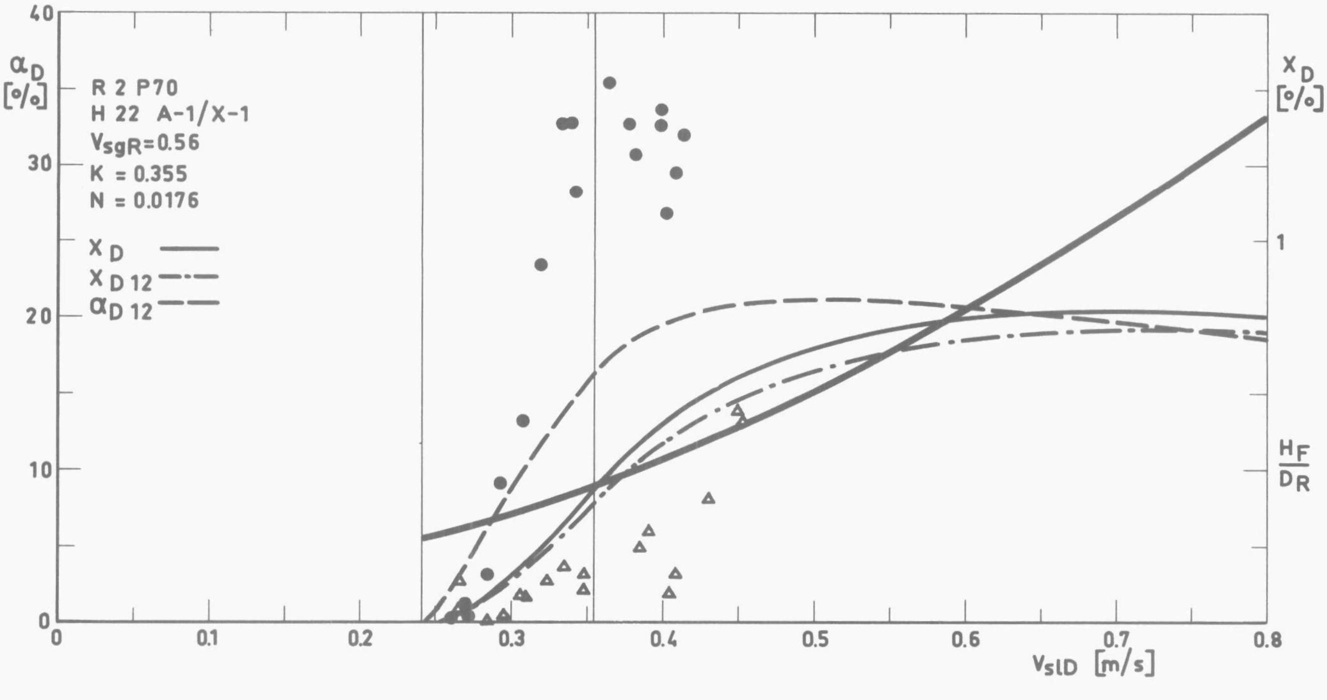

FIGURE 4-9.

Comparison of carry-under model with experiment.

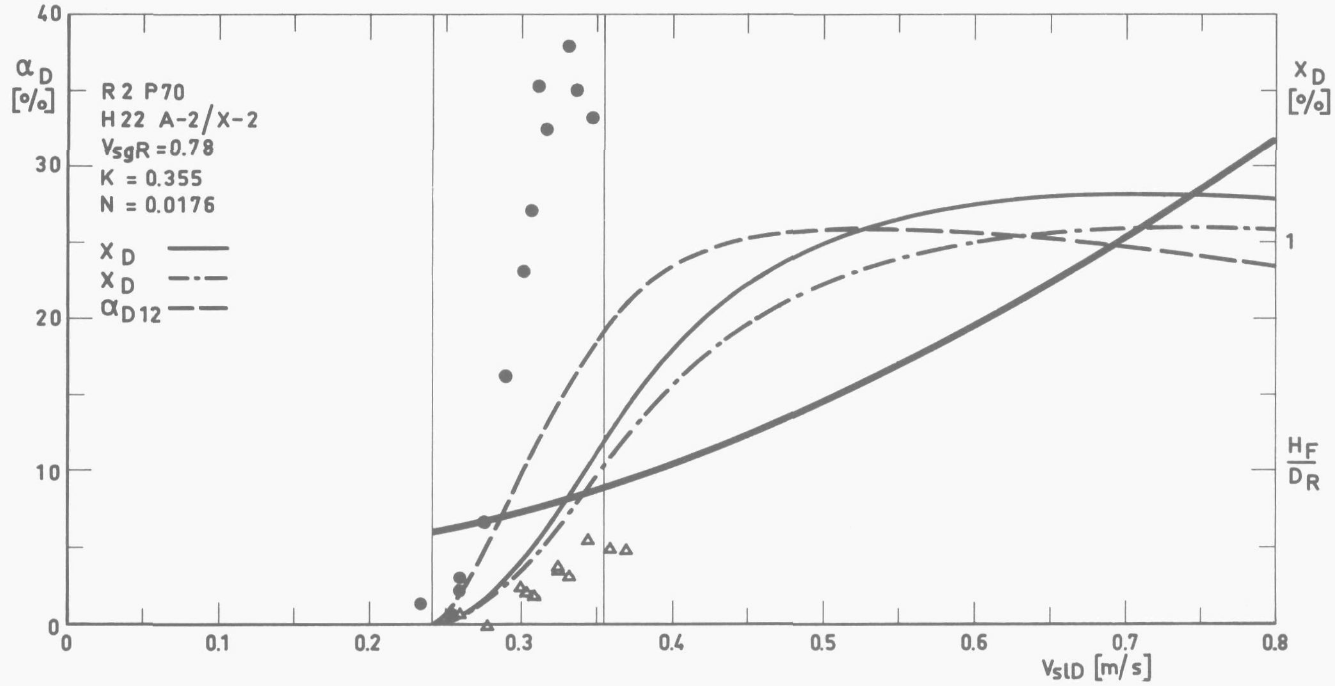

FIGURE 4-10.

Comparison of carry-under model with experiment.

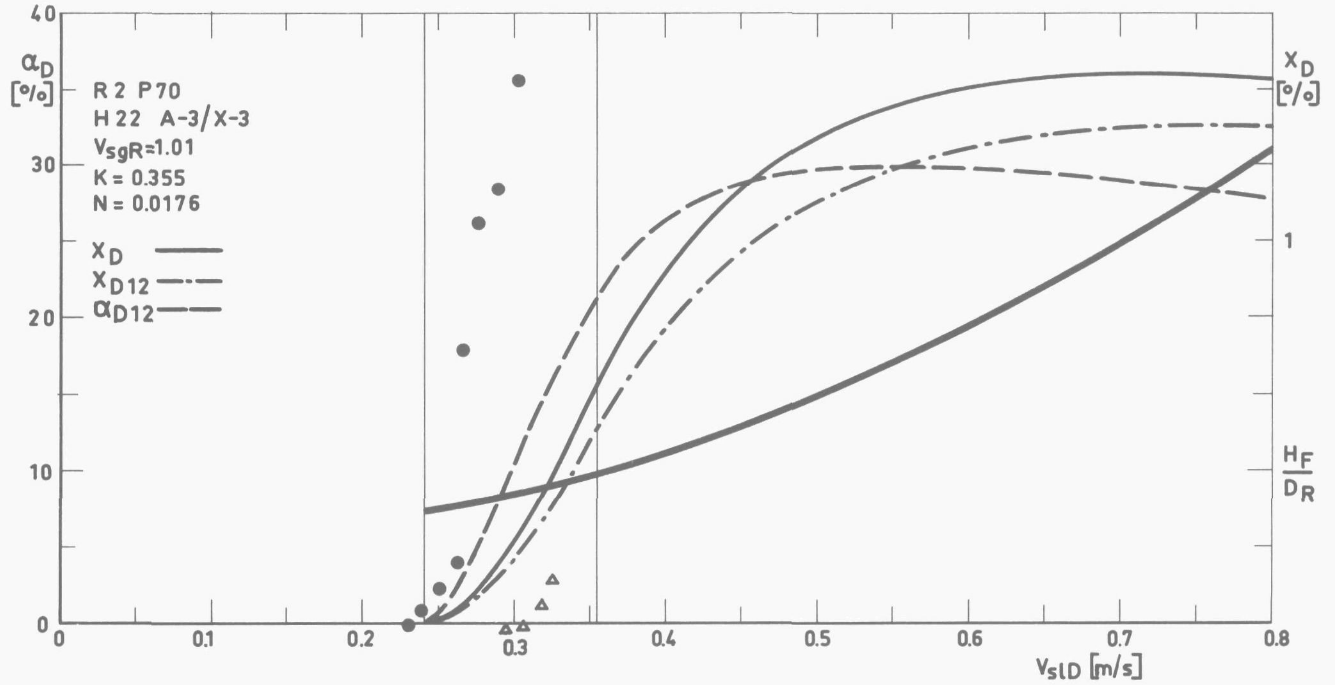

FIGURE 4-11.

Comparison of carry-under model with experiment.

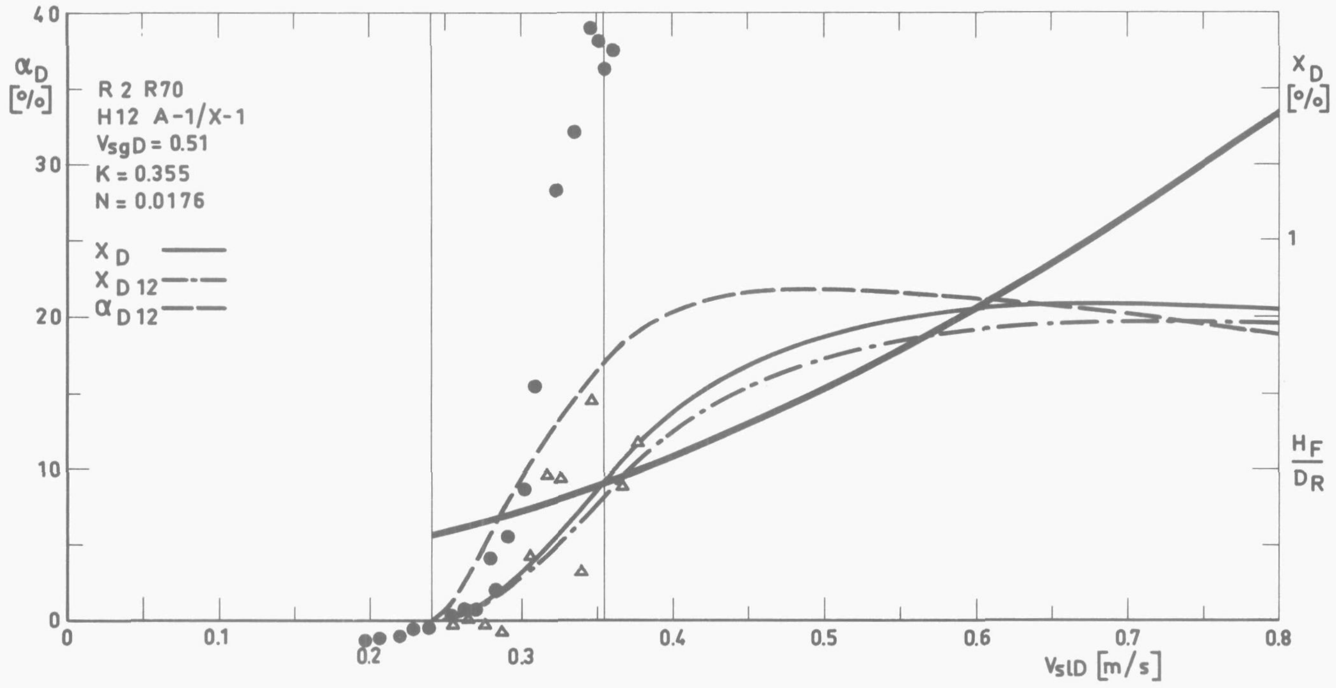

FIGURE 4-12.

Comparison of carry-under model with experiment.

Furthermore the maximum in the downcomer void fraction with increasing $v_{s\ell D}$, which is predicted by the model, is only corroborated by the experiments for R2. The continuous increase in downcomer void fraction for the R1 experiments must, in the light of this comparison, probably be attributed to a fountain effect, a phenomenon inherent to small scale experiments and possibly vanishing for large systems.

The effect of riser quality on carry-under in the model is that of a gradual increase in downcomer quality. The minimum found in these and PETRICK's [20] experiments is not explained. It may be a result of the fountain effect and "false" carry-under in the present investigation.

Petrick's experiments, where the carry-under voids are quenched outside the test vessel, would exclude "false" carry-under, but this experiments on a smaller scale would tend to suffer more from the fountain effect.

The relative carry-under x_D/x_R as formulated by Petrick remains almost constant for the model. This is shown in table 4-1 where the predicted carry-under is given for the same conditions as in figure 2-23 i.e. R1P70H22 x-1.1, x-2, x-2.1, x-3.

TABLE 4-1

run	x_D	x_D/x_R	v_{sgD}/v_{sgR}
x-1.1	0.0064	0.1211	0.1159
x-2	0.0074	0.1212	0.1149
x-2.1	0.0084	0.1215	0.1141
x-3	0.0094	0.1218	0.1137

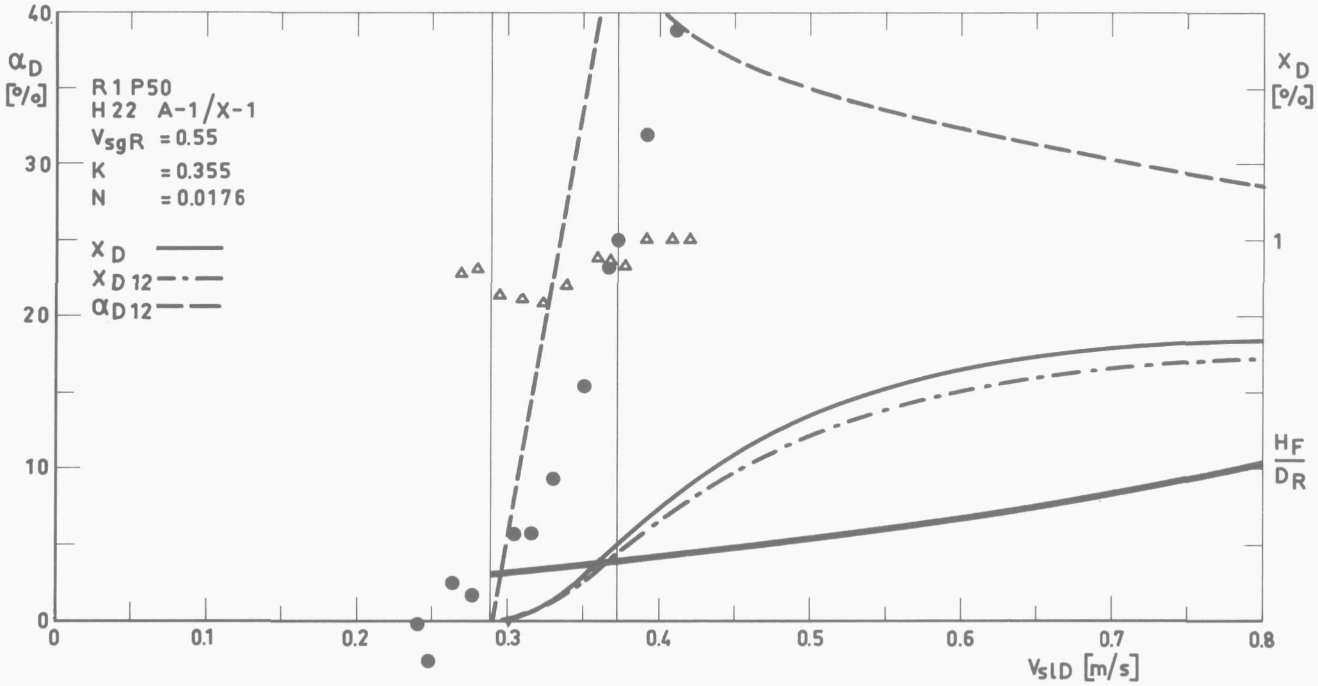

FIGURE 4-13.

Comparison of carry-under model with experiment.

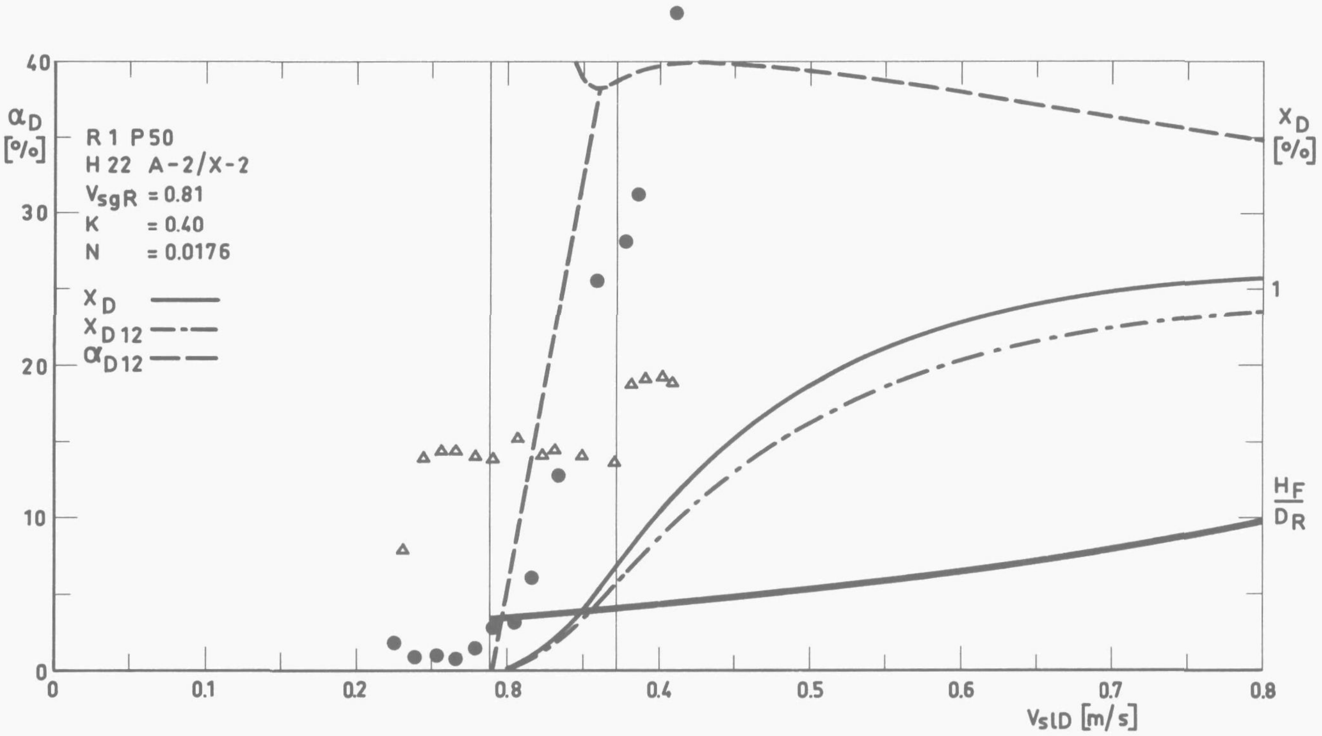

FIGURE 4-14.

Comparison of carry-under model with experiment.

A very small increase in the relative carry-under is shown. On the other hand the carry-under defined by VOLLRADT [46], i.e. (v_{sgD}/v_{sgR}) shows a slight decrease as seen in the last column of table 4-1. His experimental air-water data also show a decreasing carry-under with increasing riser air flow but on a much larger scale.

The influence of level on carry-under in the model is but very small in the range from H22 to H6. This shown in figures 4-6 and 4-8 as well as 4-9 and 4-12. There is a tendency for the lower levels to give better agreement with the model.

Except for the H12 runs the carry-under initiation is predicted fairly good by the model.

The constant K_1 in the slip relation of equation (3-119), which constitutes the basis for the carry-under model, was shown to be 0.355 for the riser experiments. This value is also used in the prediction of the P70 carry-under data and gives an acceptable comparison. Use of a K_1-value of 0.52 for the P50 runs gave substantial deviation from the test results, especially with regard to the point of carry-under initiation, which was overpredicted. It was necessary therefore to decrease the value of K_1 from 0.52 to 0.40 to obtain reasonable agreement. Whereas upflow void measurements at 70 bar could be used to determine a slip relation for both up- and downflow, this turned out to be impossible for 50 bar. The difference in hydraulic diameter of the riser and downcomer seems to be the most probable cause, which effect is then more pronounced for 50 than 70 bar.

These effects at the same time demonstrate the flexibility of a simple model when fitting experimental data and give warning that the values of constants used have only limited applicability: they are restricted to the range of variables under consideration.

On the whole the comparison of the model with the 50 bar experiments shown in figures 4-13 through 4-20 (see following pages) shows the same trends as found for 70 bar.

Also given in the aforementioned figures is the projection height of a free jet issuing from the riser as calculated by equation (3-137) and plotted as H_F/D_R. (Thick drawn line in figures 4-2 through 4-20).

The hypothetical free jet condition is somewhat similar to that in the experiments of ROSE and GRIFFITH [30] described in section 3.1.2.3. and the values for B given there may be used in equation (3-137). Experimental results shown in figure 3-7 can be approximated for this purpose by

$$B = e^{(1.89-9.27\alpha)} \tag{4-7}$$

The height H_F of the free jet was calculated for the conditions of the last test before the fountain effect occured in the experiments. The results are given in table 4-2.

TABLE 4-2

	R2P70		R2P50	
	H12	H6	H12	H6
A1		0.045		0.064
A2		0.068	0.090	0.051
A3	0.116	0.035	0.069	0.040
	R1P70	R1P50		
	H6	H12	H6	
A1			0.022	
A2		0.033	0.020	
A3	0.027	0.040		

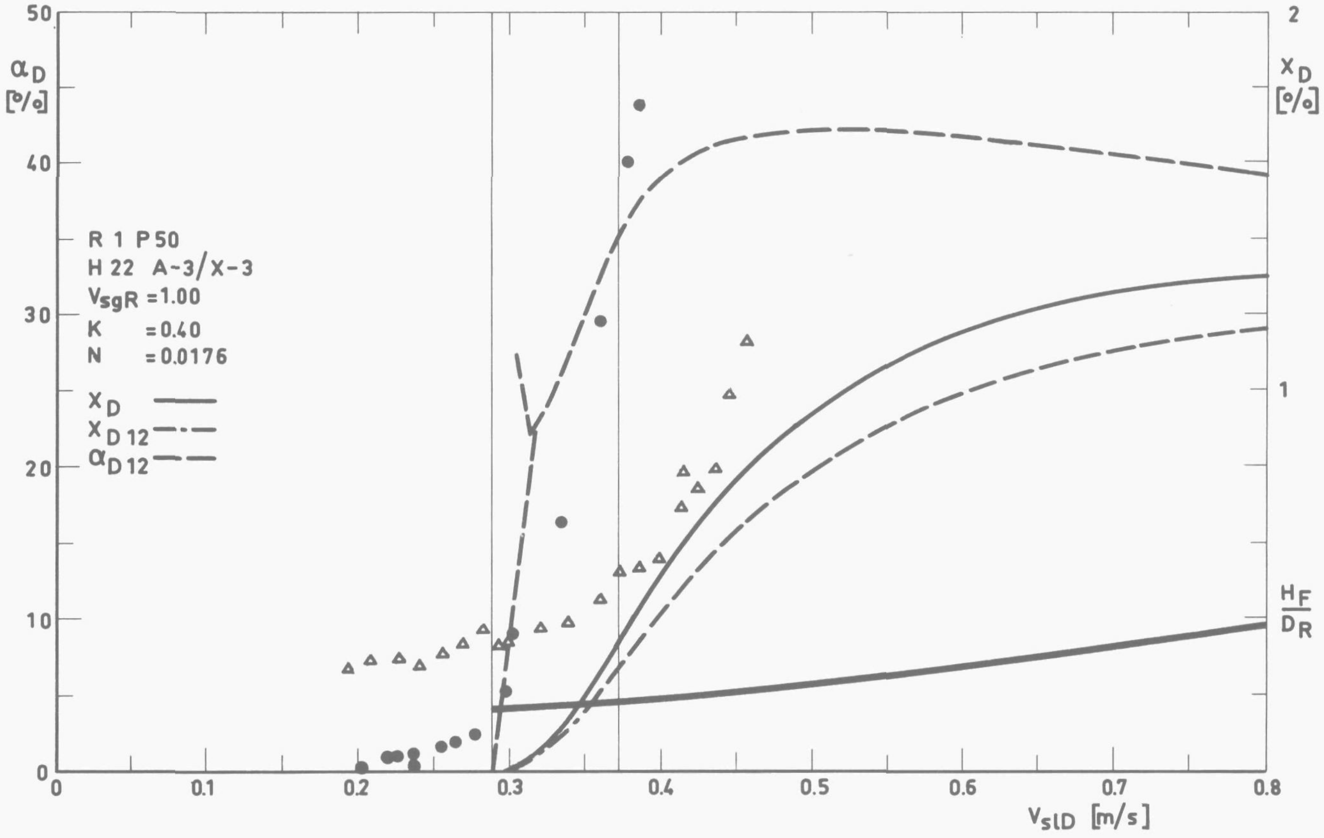

FIGURE 4-15.

Comparison of carry-under model with experiment.

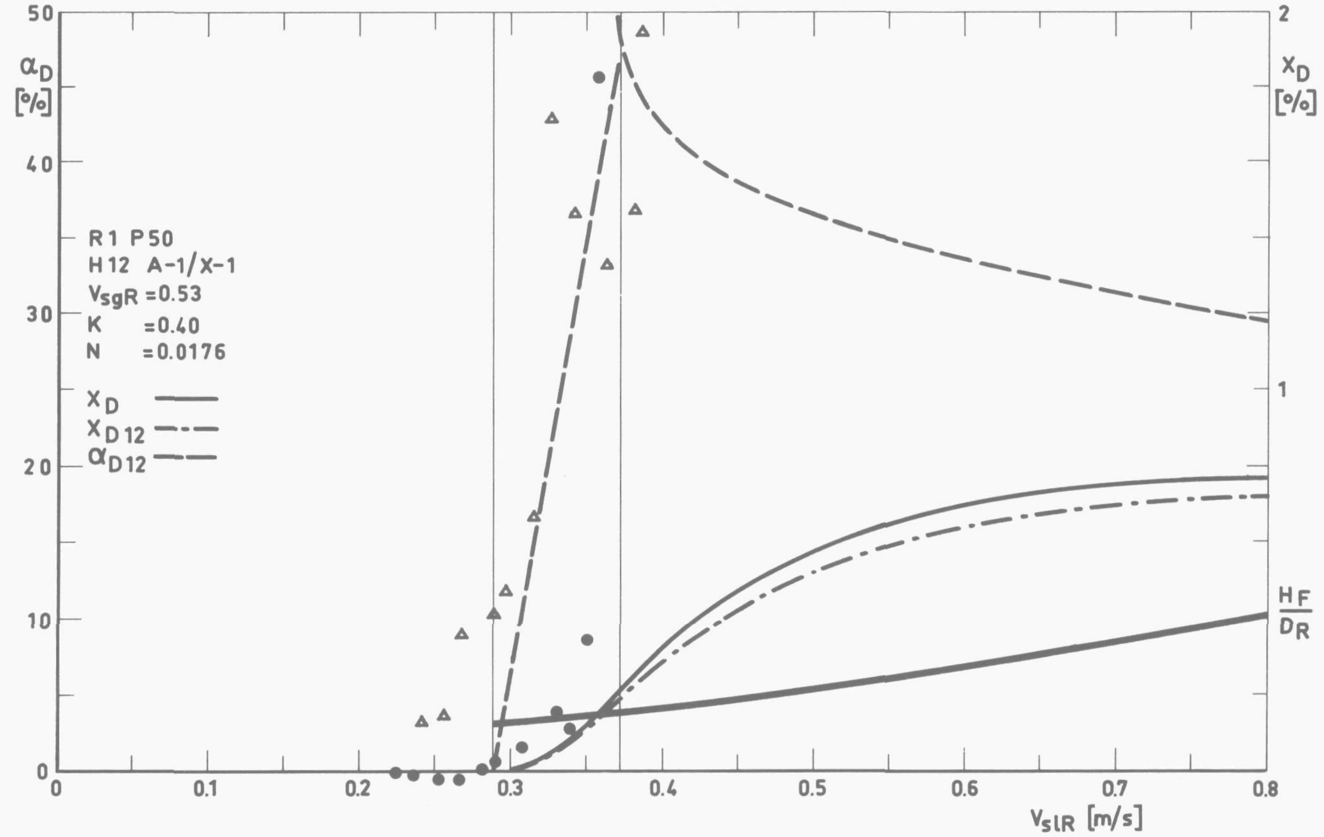

FIGURE 4-16.

Comparison of carry-under model with experiment.

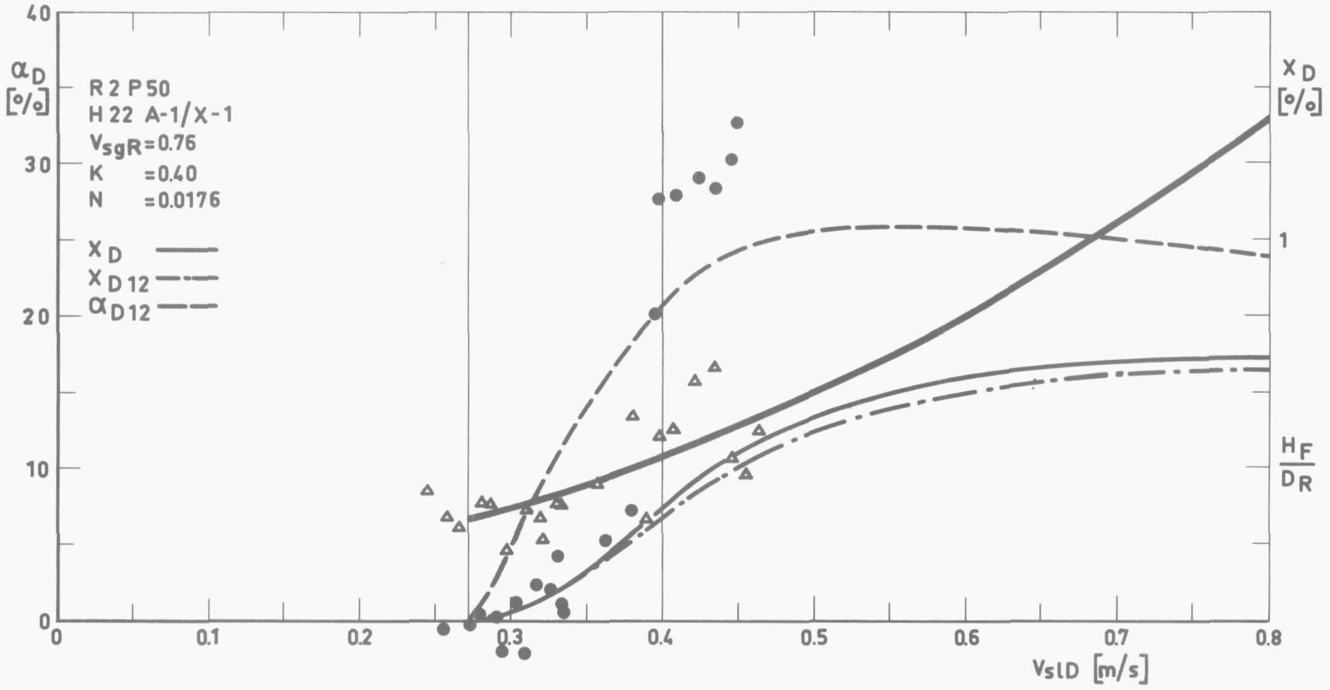

FIGURE 4-17.

Comparison of carry-under model with experiment.

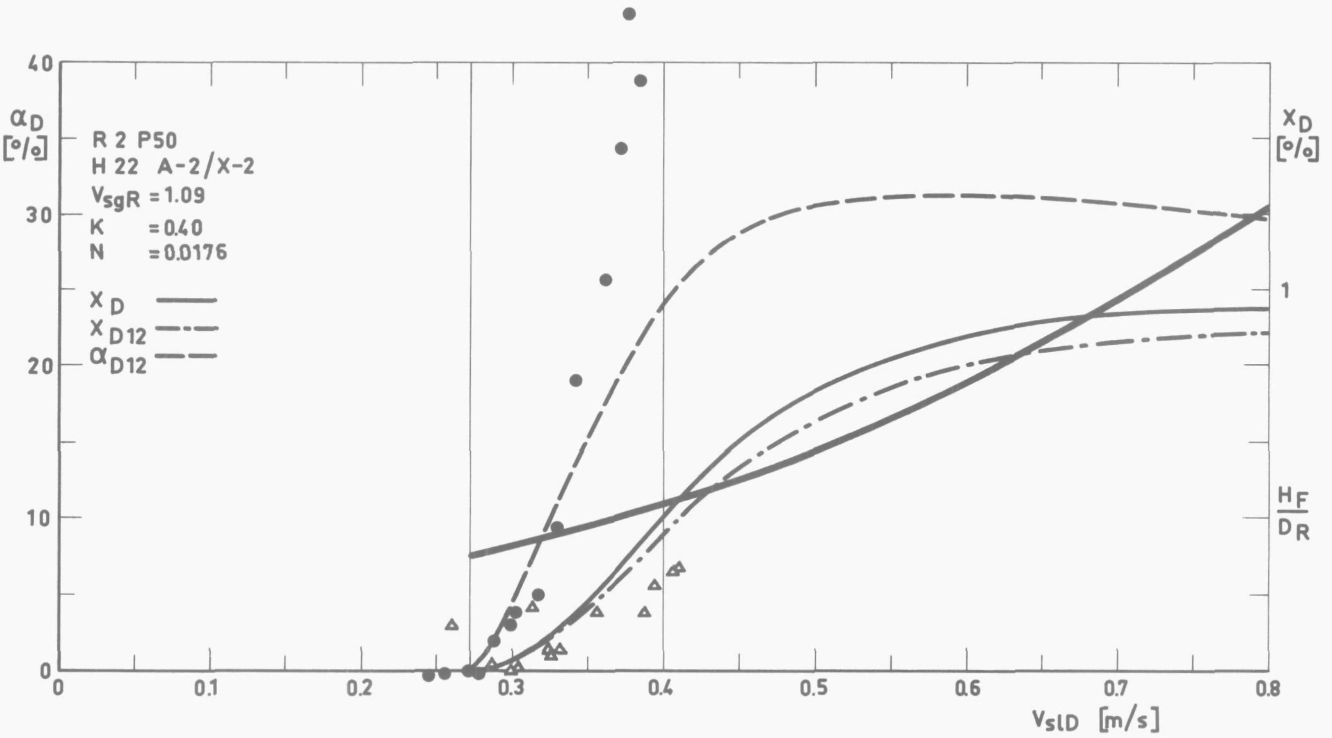

FIGURE 4-18.

Comparison of carry-under model with experiment.

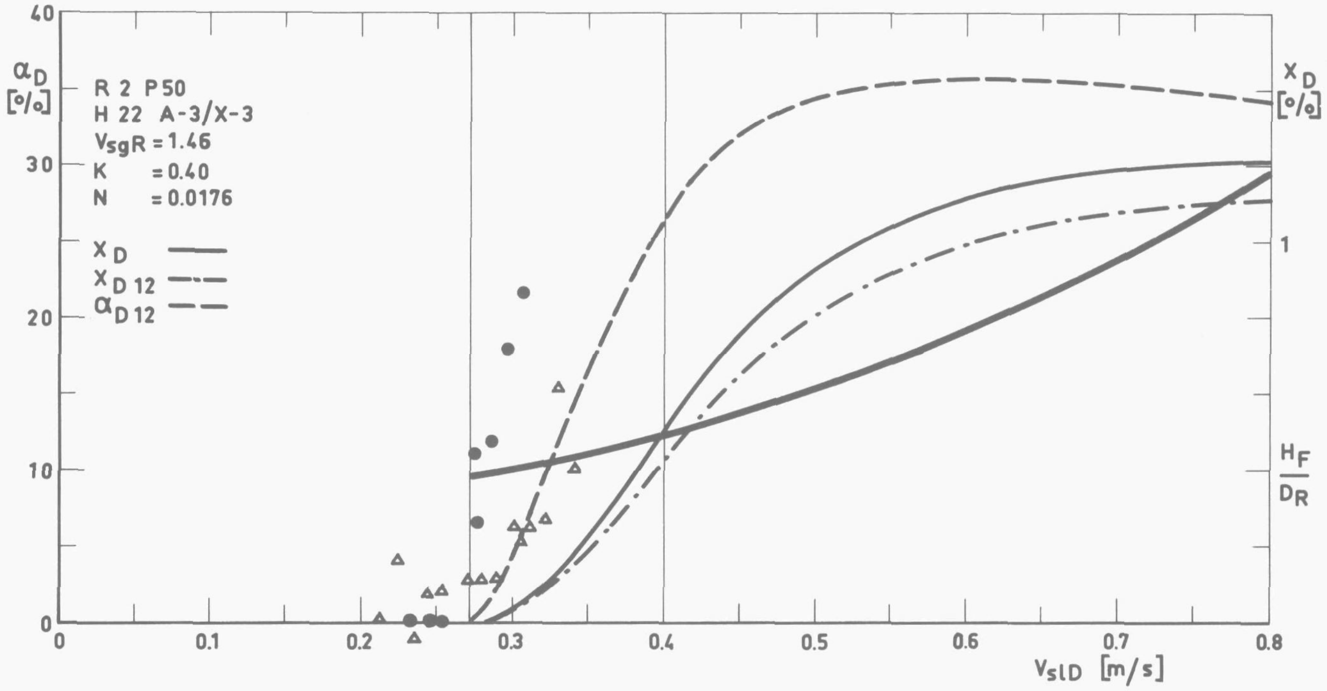

FIGURE 4-19.

Comparison of carry-under model with experiment.

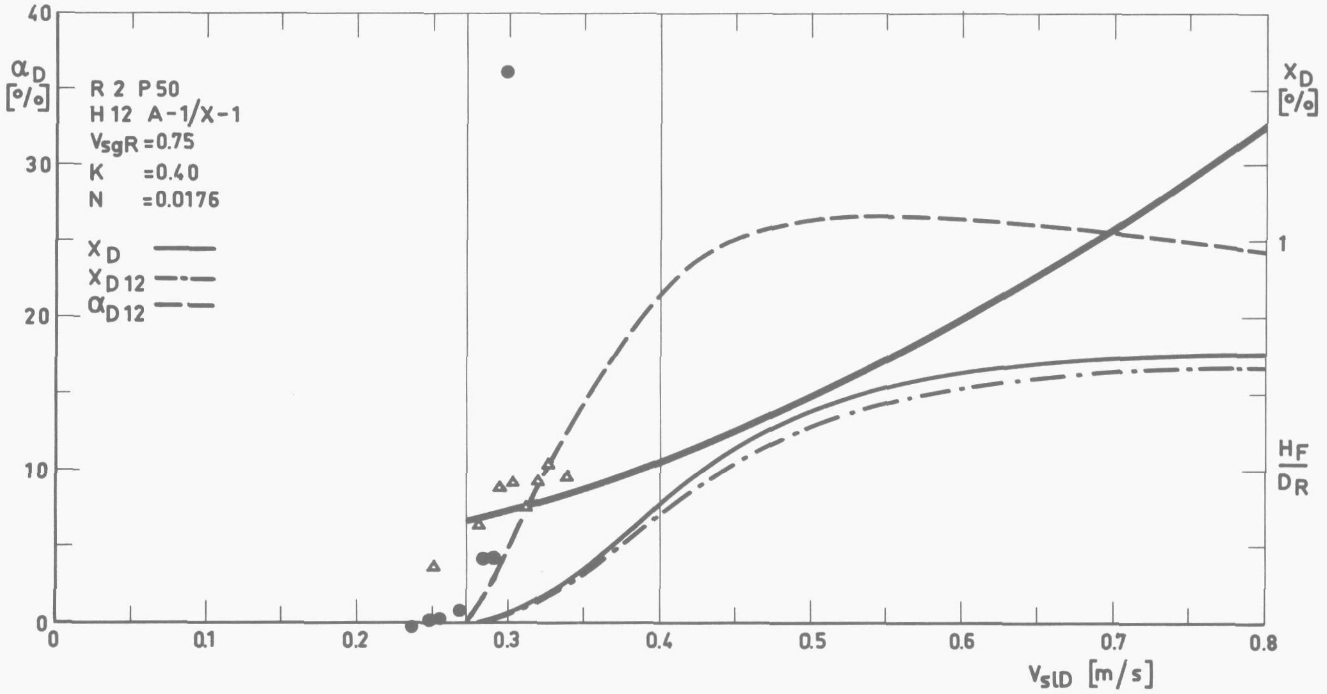

FIGURE 4-20.

Comparison of carry-under model with experiment.

The agreement of predicted projection heights of the free jet with experiment is much better for the R2 experiments. The relatively large surface oscillations of the two-phase interface must be taken into account when considering the heights given in table 4-2. Furthermore the use of equation (4-29) is questionable. It incorporates effects of the velocity profile of the outflowing mixture and errors in void measurement pertaining to Rose and Griffith's work with a 0.025 m diameter tube. These effects may be different in the present experiment. The contribution of the virtual mass to the projection height varies between 38% for R2P50H6A1 to 14% for R1P70H6A3. It is clear from table 4-2 that the projection height and thus the occurence of the fountain effect during a test run is not very accurate and does not give conservative estimates. The use of equation (3-137) and (4-7) is limited and only suitable to give an order of magnitude.

In addition to the comparison with the test results of the present small scale experiments the model was used to predict the carry-under in the Dodewaard reactor. A series of carry-under measurements [100] were performed in this reactor in 1969. For two conditions, 100% and 83% nominal power, the predicted carry-under curves are given in figures 4-21 and 4-22 (see page 162), where the data points indicate the downcomer quality measured in the reactor. The steam carried under during the tests is the difference in the amount of steam produced in the reactor core derived from measured values of reactor power and water flowrates and the measured amount of steam leaving the reactor vessel.

The predicted downcomer quality deviates from the measured values by 3.3 and 0% for 100 and 83% nominal power respectively. The agreement is exceptionally good. Considering the errors involved in the measurement of the reactor power, recirculation flow rate and subcooling of the water at reactor inlet and the limited number of compared cases, the agreement is to be seen as an indication of the applicability of the model to full size systems, but not as a direct measure of its accuracy.

To conclude this section a prediction of carry-under behaviour in a large steam generator for a PWR is given. The 481 MW_{th} steamgenerator of the Stade station [101], which is at present still under construction, was chosen for this purpose.

The circulation ratio, m, and thus the downcomer velocity is unknown but calculations for such steamgenerators [29] have shown m to be in the vicinity of 6. The Stade steamgenerators will be equipped with mechanical primary separators. The riser diameter for the hypothetical case gravity separation is employed is taken equal to the diameter of the shroud, i.e. a straight riser. The prediction for full power at 51 bar is shown in figure 4-23 (see page 163). For m = 6 a downcomer inlet quality of 1.28% is found, which in comparison with the Dodewaard values is quite acceptable. Although a warning was given against use of constants outside the range of the investigation the prediction given here is thought to give conservative results and presentation seems useful.

Should the feed water be at saturation temperature then the steam would be entrained into the lower downcomer region and the resulting void fraction is given in the figure. The riser is of constant cross section but the vessel diameter of the lower section is much smaller than that of the steamdome. The correspondingly high velocities are responsible for the low downcomer void fraction.

To quench all the voids with subcooled feedwater its temperature follows from the heat needed for condensation. With a steam production of 250.5 kg/s the amount comes to

$$Q_q = x_D \times 250.5 \times m \times r = 0.0128 \times 250.5 \times 6 \times 1633.6 = 31500 \text{ kW}$$

or $31500 / 250.5 = 125.8$ kW/kg.

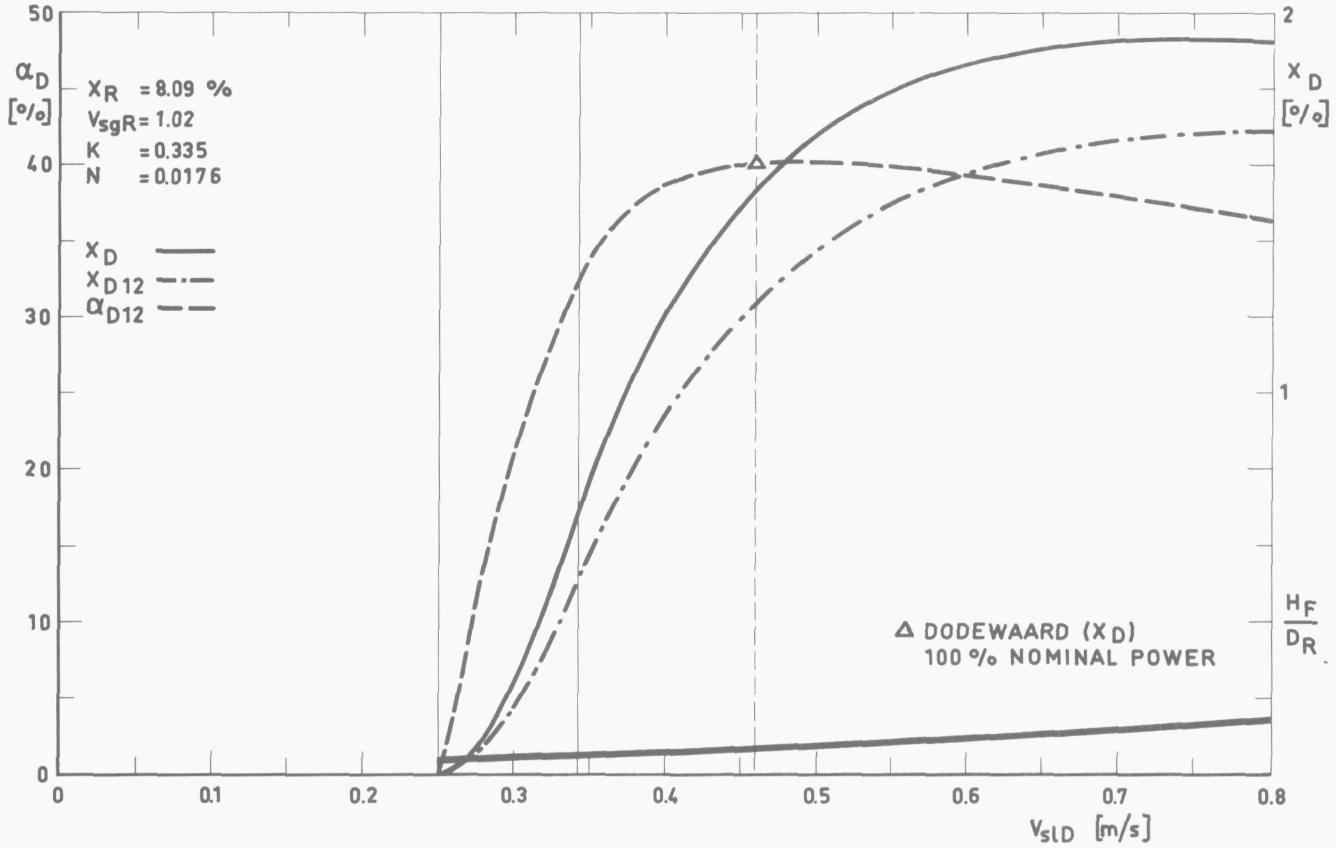

FIGURE 4-21.

Comparison of carry-under model with the measured downcomer quality in the Dodewaard reactor at 100% power.

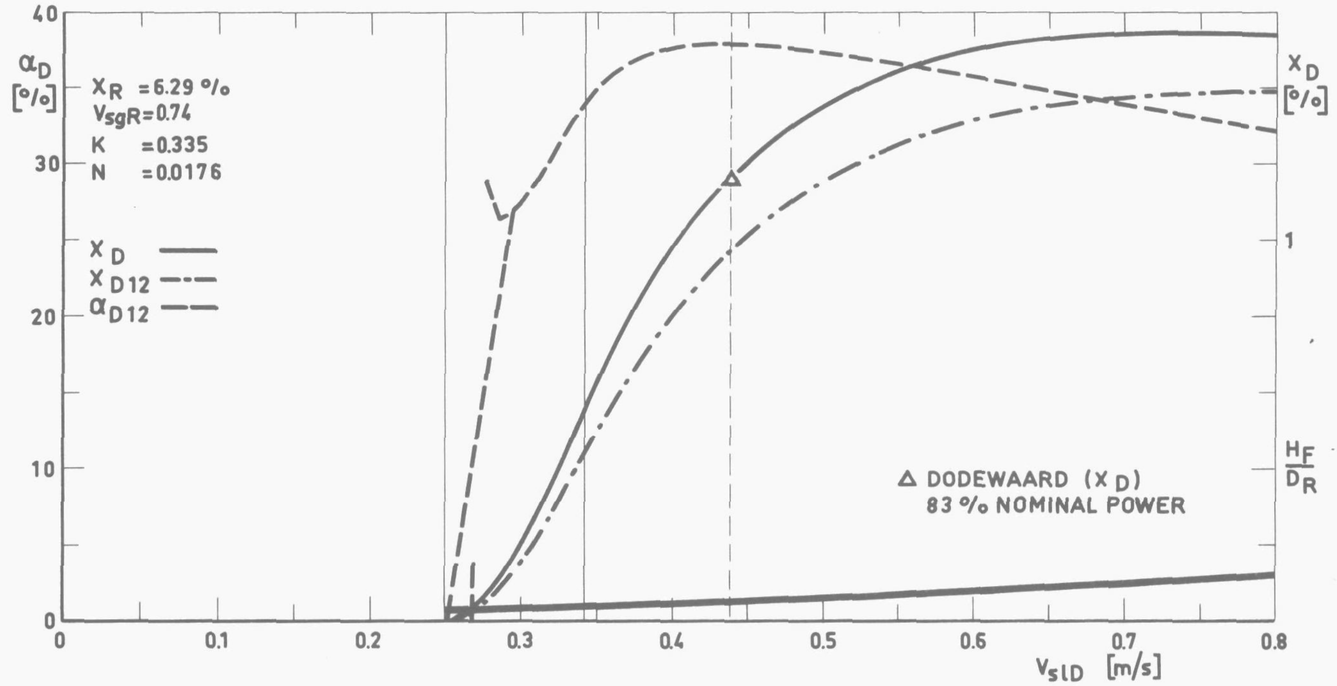

FIGURE 4-22.

Comparison of carry-under model with the measured downcomer quality in the Dodewaard reactor at 83% power.

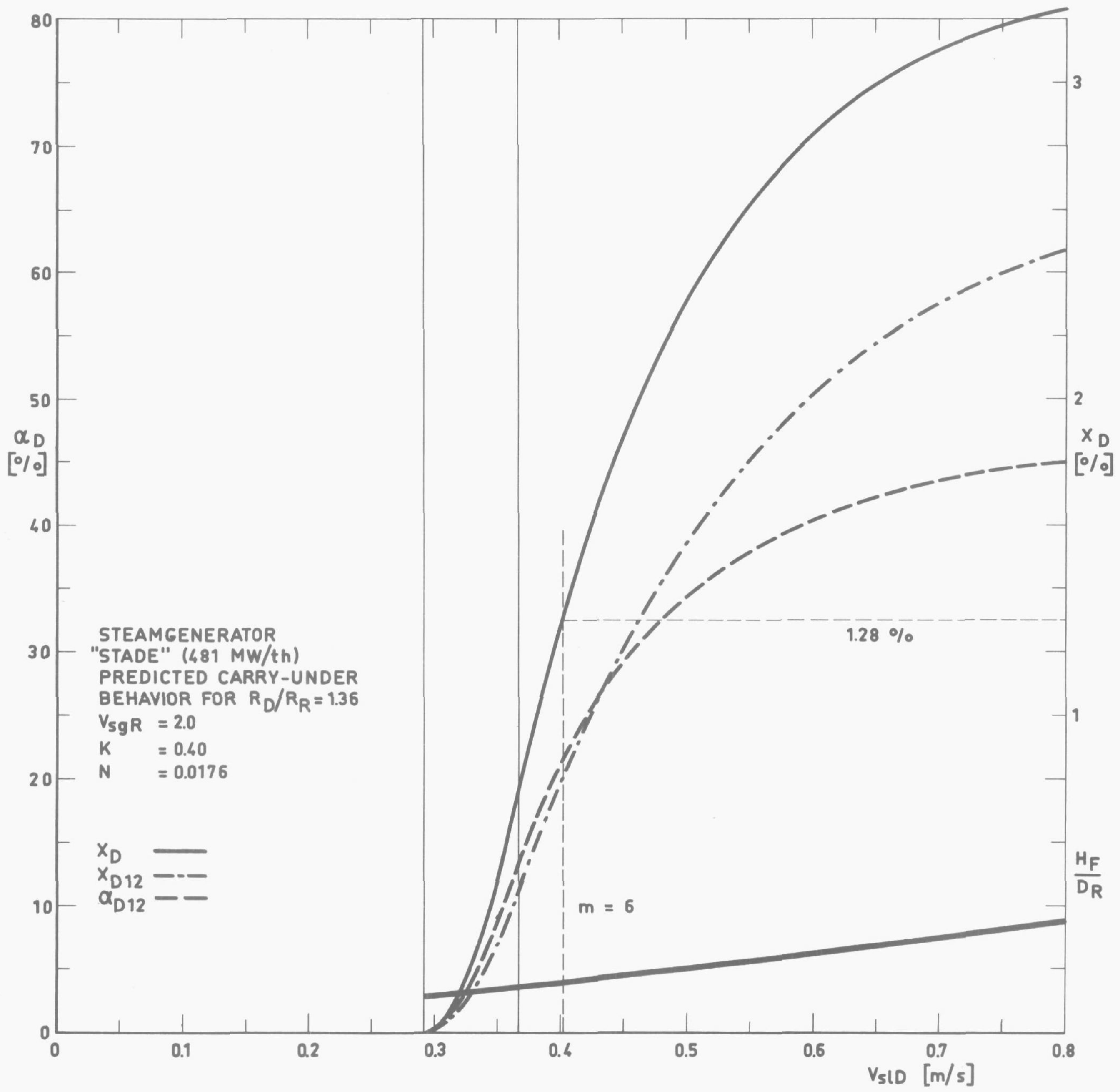

FIGURE 4-23.

Prediction of carry-under in the Stade steam generators employing gravity separation for 100% power.

From the steam tables the maximum feedwater temperature to quench all voids is found to be 239.2°C (a subcooling of 24.1°C). Where the feedwater temperature will in fact be 205°C [101] this condition is amply fulfilled. With regard to the projection height given in the figure at M = 6, i.e. $H_F/D_R \times D_R = 0.16 \times 2.48 = 0.396$ m, there still seems to be some margin between this value and the 1.5 m mixture height above the riser used in the model.

5. UNSTABLE BEHAVIOR OF TWO-DIMENSIONAL MODEL EQUATIONS: DISCUSSION OF POSSIBLE CAUSES AND REMEDIES.

It was announced in section 3.3.1. that no stable solution of the set of equations could be obtained. To illustrate the instability encountered the results for a test case are presented.
The starting conditions are homogeneously distributed void fraction (30%), axial liquid and gas velocities (2 m/s), a core pressure of 1 bar and zero radial liquid and gas velocities. The program was run for an 8-strip approximation and solid body rotation with an initial tangential velocity at the tube wall of 2 m/s.

The instability manifested itself most strongly in the radial gas velocity. The radial distribution of this velocity is shown in figure 5-1 for several steps of the Runge-Kutta integration. The unstable behavior of the radial velocity is reflected in the axial gas velocity as illustrated in figure 5-2. The corresponding void and pressure profiles are shown in figures 5-3 and 5-4.

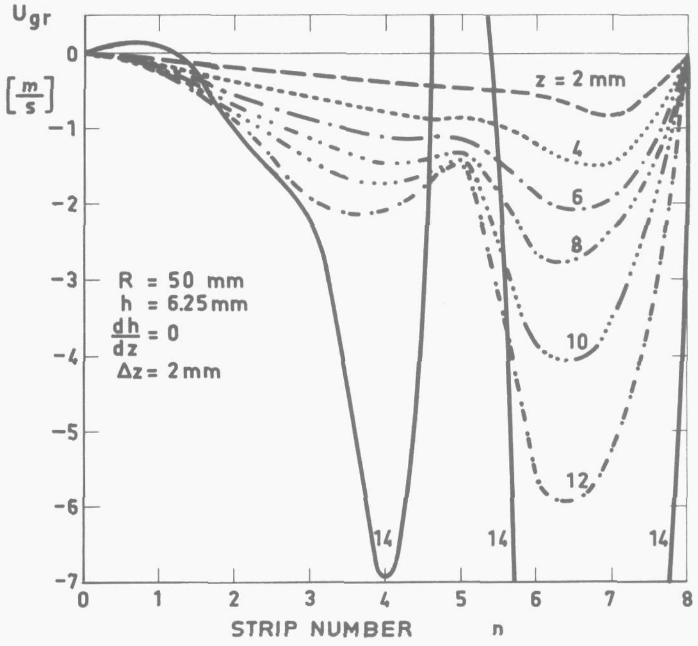

FIGURE 5-1.

Unstable radial gas velocity component from 8-strip solution.

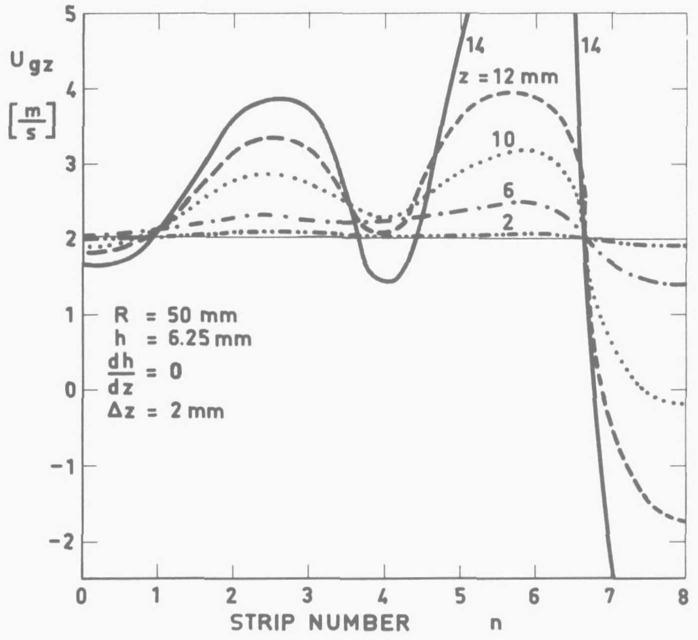

FIGURE 5-2.

Unstable axial gas velocity component from 8-strip solution.

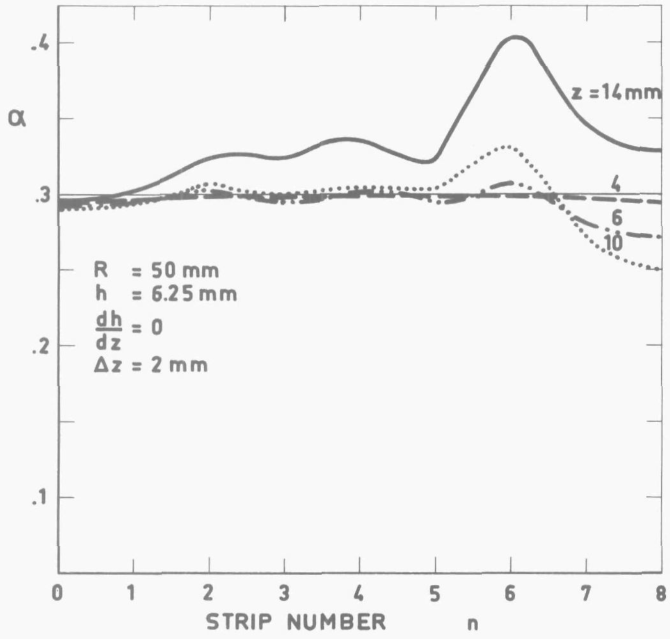

FIGURE 5-3.

Unstable void fraction from 8-strip solution.

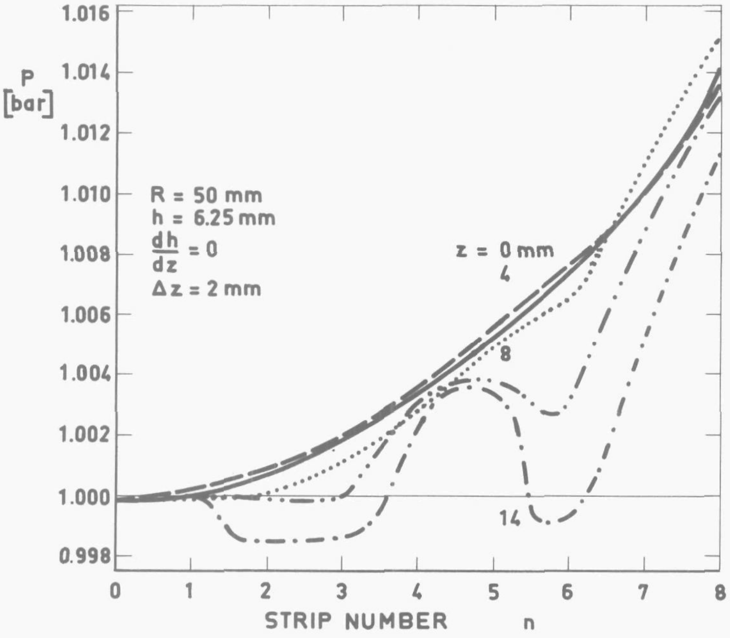

FIGURE 5-4.

Unstable pressure from 8-strip solution.

Comparing the u_{gr} and p curves for z = 14 mm, the last step before the computer routine broke off, agreement in trend is still found. Where the pressure distribution shows a positive gradient the radial gas velocity is negative and vice versa. Where the radial velocity is zero a zero gradient is found in the pressure curve. The exact location of the extremes in the curves cannot be given as only the strip boundary values are calculated. The question arises as to what is the cause of the instable behaviour and which numerical or physical inaccuracy sets if off.

From the results shown it seems that the disturbance is generated at the solid wall, making the boundary conditions suspect. However, the radial pressure gradient is also largest at the wall giving rise to the highest radial velocities in that region. To exclude this effect the program was run for the same conditions but with zero tangential velocity. All radial distributions should be homogeneous and stay that way. The radial distribution at z = 10 mm after 5 integration steps in z-direction is shown in table 5-1.

TABLE 5-1.

strip boundary number	radial gas velocity (z = 10 mm)
0	+.000000000000000
1	-.000000000000007
2	-.000000000000005
3	-.000000000000005
4	-.000000000000006
5	-.000000000000005
6	-.000000000000009
7	-.000000000000010
8	-.000000000000000

Although the instability is much weaker the same effect seems to appear. However, at z = 80 mm the numerical disturbance given in table 5-2 has

TABLE 5-2.

strip boundary number	radial liquid velocity (z = 80 mm)	radial gas velocity (z = 80 mm)
0	+.000000000	+.000000000000000
1	-.000000000	-.000000002373904
2	+.000000000	+.000000001237568
3	+.000000000	+.000000001518643
4	-.000000001	-.000000004008414
5	+.000000000	+.000000002574906
6	+.000000000	+.000000001602967
7	-.000000000	-.000000002532732
8	+.000000000	+.000000000000000

spread, giving a more or less symmetric distribution over the radius in both gas and liquid radial velocities. Although the distribution seems to stabilize its magnitude keeps increasing as shown for z = 100 in table 5-3.

TABLE 5-3

strip boundary number	radial liquid velocity (z = 100 mm)	radial gas velocity (z = 100 mm)
0	+.000000000	+.000000000000000
1	-.000000107	-.000000547029346
2	+.000000012	+.000000594215 41
3	+.000000101	+.000000514957468
4	-.000000125	-.000000638159745
5	+.000000028	+.000000141975216
6	+.000000072	+.000000365977886
7	-.000000053	-.000000269489305
8	+.000000000	+.000000000000000

The results of the non-rotating case indicate that instability is not caused by the boundary conditions. As a further check on the reliability of the other results of the program the axial gas and liquid velocities and void fraction were compared with the results of the one-dimensional program VAPOM for the same initial conditions. Figure 5-5 shows the good agreement between the two programs for this case.

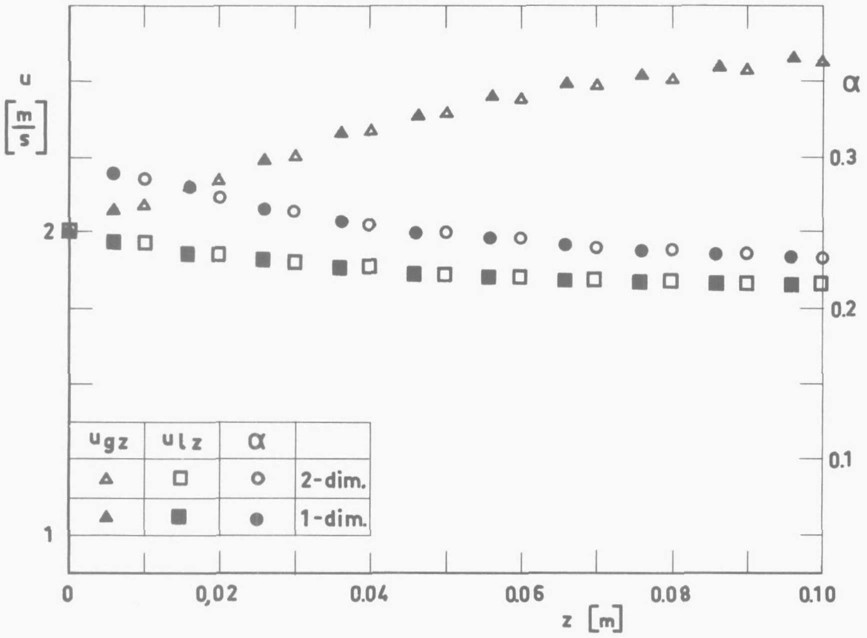

FIGURE 5-5.

Comparison of axial gas and liquid velocity component and void fraction distribution calculated with VAPOM and an 8-strip solution by STRIPTEASE.

Two posibilities remain open as possible causes for the unstable behavior. First of all the original method outlined in section 3.3.5.1. was violated where the equations deviated from true divergence equations.

Consequently two terms of the basic equations, i.e. $(1-\alpha)\frac{\partial p}{\partial r}$ in equation (3-80) and $(1-\alpha)\frac{\partial p}{\partial z}$ in equation (3-81), had to be approximated, where the error in

$$\int_{k-1}^{k+1} (1-\alpha)\frac{\partial p}{\partial r}$$

is the most serious. The test cases given above point in this direction; the worst instabilities occur where the pressure gradient is steepest and where the errors involved in the parabolic approximation can be expected to be largest.

On the other hand it is also possible that the solution of the differential equations in the form of an initial value problem is in itself unstable and that the problem should be treated as a boundary value problem.

It is hard to tell at this stage whether the deviation from the true divergence equation or this inherent instability is the cause of the failure to obtain a solution.

If the last could be proven to be the cause it might be possible to modify the procedure described in section 3.3.5. by changing the Runge-Kutta integration of the set of ordinary differential equations by a finite-difference scheme. This would reduce the set of 6n + 6 differential equations to a set of m (6n + 6) nonlinear algebraic equations, where m is the number of elements taken in z-direction. It is clear that the convergence of this large set is not guaranteed, and calls for additional research for suitable methods. Linearisation of the set in order to arrive at equations, for which many proven methods are available, is one of the possible courses. The question remains however whether in evading the possible divergence in the solution of nonlinear equations additional inaccuracies are introduced by the linearisation, jeopardizing the solution even more.

6. CONCLUSIONS

The three objectives of this study that were formulated at the beginning of the thesis have been partly attained.

An experimental study of gravity separation was designed and a test program executed using a small scale model of a riser and downcomer typical for Boiling Water Reactors operated with water and steam under reactor conditions. The experimental results permit to explain the trend of the carry-under behaviour in general, although some of the qualitative results must be attributed to the particular characteristics of the small scale of the model. The simple physical model of the gravity separation process that could be derived from these experiments was used in combination with the results of the one-dimensional mathematical analysis of two-phase flow, which was part of the third of the objectives mentioned above, to arrive at a quantitative model for the prediction of carry-under. A comparison with the experimental data shows fair agreement. Extrapolation of the experimental results through the use of this model to a larger scale seems allowed as illustrated by comparison with the results of a full size system.

The second objective concerns the experimental study of an axial upcomer type cyclone with a converging-diverging vortex tube. The testing was carried out using a clear plastic model and air-water mixtures which permitted detailed measurement of local void fractions whithin the cyclone as well as visual observation of the flow patterns. Although the efficiency and pressure drop measurements showed the two cyclone versions not to be successful in meeting the equivalent reactor specifications the experiments pointed out the trouble area's and are a basis for further investigations. Inadequate separation is due to reentrainment at the cyclone outlets and not to insufficient separation in the vortex tube.

The derivation of a two-dimensional model to describe the separation process was the third objective. The analysis of the two-phase phenomena that are fundamental to this process leads to an one-dimensional model based on conservation of mass and momentum in preparation of the eventual two-dimensional model. This first model was successfully used to quantitatively determine the interaction forces between the phases using auxiliary experiments with accelerating air-water mixtures. The drag force and virtual mass force can be expressed as a function of the void fraction.

A method of solution based on the N-strip method applied to the two-dimensional mass and momentum balance equations leads to numerical instability of the computer program: the two-dimensional problem cannot be treated as an initial value problem. It seems possible to modify the method to treat the equations as a boundary value problem.

ACKNOWLEDGEMENTS

The author wishes to express his thanks to all those who took an active part in the work, which was executed in the Laboratory for Power Engineering of the Delft University of Technology. The many hours invested in the building, the operation and maintenance of the loops as well as the collecting of the test data are gratefully acknowledged.

Thanks also go to the students, who in the course of their studies participated in the experiments.

Special thanks are due to Mrs. G.J. Hendriks who was responsible for the typing of the manuscript.

Mr. F.A.M. van der Linden executed all the drawings and graphs. His painstaking as well as artistic contribution to this thesis is highly appreciated.

The author is very grateful for the many discussions and valuable suggestions from the members of the laboratory staff. Special mention should be made of the keen interest and time given by Mr. R. Wisman, who took a very active part in the investigation.

Last but not least thanks go to Mr. A. Korving, who was responsible for a large part of the design of the test loops specially regarding instrumentation and electronics. The author is very much indebted to him for the dedication he showed in the many aspects of his work for the project ranging from instrument calibration to operation of the TR-4 computer for data reduction.

REFERENCES

1. Levy, S. Invited lecture, Symposium on two-phase flow, Exeter, (1965).

2. Lockhart, R.W. and Martinelli, R.C. Proposed correlation of data for isothermal two-phase, two-component flow in pipes. Meeting of A.I.Ch.E., Sept. 28 - Oct. 1, (1947), Buffalo.

3. Bankoff, S.G. A variable density single fluid model for two-phase flow with particular reference to steam-water flow. Journ. Heat Transf., vol. 82, no. 4, p.265, (1960).

4. Duckler, A.E. e.a. Frictional pressure drop in two-phase flow: a comparison of existing correlations. A.I.Ch.E. Journal, January (1964), pp. 38-51.

5. Hadamard, J. Comp. Rend., vol. 154, p. 109, (1911).

6. Rybcynski, W. Bull. Acad. Sci. Cracovie. A, p.40, (1911).

7. Levich, W.G. Physicochem. Hydrodyn., pp. 396-402, Prentice Hall, (1962).

8. Haberman, W.L. and Morton, R.K. An experimental study of bubbles moving in liquids, Trans. A.S.C.E., vol. 121, pp. 227-252, (1956).

9. Aybers, N.M. and Tapucu, A The motion of gas bubbles rising through stagnant liquid. Wärme- und Stoffübertragung Bd.2, pp. 118-128,(1969).

10. Rosenberg, B. David Taylor Model Basin report, no. 727, (1950).

11. Davies, R.M. and Taylor, G.I. The mechanics of large bubbles rising through extended liquids and through liquids in tubes. Proc. Royal Soc. Lon., vol. 200, series A, p. 375, (1950).

12. Rietema, K. and Rypkema, J.J.M. De stofoverdracht in een bellenkolom en haar relatie tot de stofoverdracht aan enkele bellen. De Ingenieur, pp. Ch.15-Ch.28, April (1966).

13. Garner, F.H. Diffusion mechanism in the mixing of fluids. Trans.I.Ch.E., vol. 28, pp. 88-96, (1950).

14. Eck, B. Technische Strömungslehre (1961).

15. Datta, R.C., Napier, D.H. and Newitt, M. The properties and behavior of gas bubbles formed at a circular orifice. Trans.I.Ch.E., vol. 28, pp. 15-26, (1950).

16. Soo, S.L. Fluid dynamics of multiphase systems. Univ. of Illinois, Blaisdell Co., (1968).

17. Verschoor, H. Some aspects of the motion of a swarm of gas bubbles rising through a vertical liquid column. Trans.I.Ch.E., vol. 28, pp. 52-57, (1950).

18. Marrucci, G. e.a. Experiments of bubble coalescence under controlled conditions. Paper III-4, Colloque Euromech., no. 7, (1969).

19. Howarth, W.J. Measurement of coalescence frequency in an agitated tank. A.I.Ch.E. Journal, vol. 13, no. 5, pp. 1007-1013, (1967).

20. Petrick, M. A study of vapor carry-under and associated problems. ANL-6581, (1962).

21. Baker, J.L.L. and Chao, B.T. An experimental investigation of air bubble motion in a turbulent water stream. A.I.Ch.E. Journal, vol. 11, no. 2, pp. 268-273, (1965).

22. Mertes, T.S. and Rhodes, H.B. Liquid-particle behavior. Chem.Eng.Progr., vol. 51, no. 9, pp. 429-432 and no. 11, pp. 517-522, (1955).

23. Marrucci, G. Rising velocity of a swarm of spherical bubbles. I.E.C. Fundamentals, vol. 4, no. 2, pp. 224-225, (1965).

24. Hughes, R.R. and Gilliland, E.R. The mechanism of drops. Chem.Eng.Progr., vol. 48, no. 10, p. 497-504 (1952).

25. Lamb, H. Hydrodynamics. Dover publications, New York, (1945).

26. Hinze, J.O. Stromingsleer: voortgezette cursus (lecture notes on advanced fluid dynamics). Delft University of Technology, (1965).

27. Pattle, R.E. Factors in the production of small bubbles, part II. Trans.I.Ch.E. vol. 28, pp. 33-57, (1950).

28. Muir, J.F. and Eichhorn, R. Compressible flow of an air-water mixture through a vertical, two-dimensional converging diverging nozzle. Proceedings 1963. Heat Transfer and Fluid Mechanics Institute 183, (1963).

29. Beran, F.G. Toepassing van een thermo-hydraulisch rekenprogramma op stoomgeneratoren van 475 en 28,5 MW. Report KR-197 Lab. for Power Engineering, Delft University of Technology (1969).

30. Rose, S.C. and Griffith, P. Flow properties of bubbly mixtures. ASME paper no. 65-HT-58.

31. Prins, C.A. Momentum flow in two-phase flow. Journ. of Heat Transf., vol. 91, no. 3, pp. 454-455 (1969).

32. Baehr, H.D. Mollier-i,x-Diagramme für Feuchte Luft. Springer Verlag, Berlin (1961).

33. Schmidt, E. VDI-Wasserdampftafeln. Springer Verlag, Berlin (1963).

34. Hinze, J.O. The virtual added mass of a discrete particle in an unsteady flow field. I.U.T.A.M. Symposium on flow of fluid-solid mixtures, Cambridge, March (1969).

35. Armand, A.A. The flow mechanism of a two-phase mixture in a vertical tube. AEC-tr-4490 (1961).

36. Malnes, D. Slipratio's and friction factors in the bubble flow regime in vertical tubes. Kjeller Report KR-110 (1966).

37. Craverolo, L. e.a. A device for measurement of shear stress on the wall of a conduit, its application in two-phase flow shear stress data in two-phase adiabatic vertical flow. CISE, EURAEC 930, (1964).

38. Korstanje, H.P. Het ontwerp van een apparaat, waarmee van een twee-fasen stroming de schuifspanning aan de wand te meten is. Report SWST-(= KR-107) Lab. for Power Eng., Delft University of Technology (1966).

39. Regeln für die Durchflussmessung mit genormten Düsen, Blenden und Venturidüsen. DIN (1952).

40. Niese, R.W. Het meten van de wandschuifspanning bij twee-fasen stroming. SWST-20, Lab. for Power Eng., Delft University of Technology (1968).

41. Levy, S. Steam slip-theoretical prediction from momentum model. Journ. of Heat Transf., vol. 82, no. 2, pp. 113-114 (1950).

42. VDI-Wärme-atlas, Berechnungsblätter für den Wärmeüvergang, VDI-Verlag, Düsseldorf (1963).

43. Martinelli, R.C. and Nelson, D.B. Prediction of pressure drop during forced circulation boiling of water. Trans. ASME, vol. 70, pp. 695-702 (1948).

44. Tong, S.L. Boiling heat transfer and two-phase flow. J. Wiley and Sons, Inc., New York (1965).

45. Marchaterre, J.F. and Hoglund, B.M. Correlation for two-phase flow. Nucleonics, p. 142 (1962).

46. Vollradt, J. Untersuchungen zur Phasentrennung mit Wasser/Luftgenuschen. Ph.D.Thesis, Stuttgart (1968).

47. Moen, R.H. a.o. Advances in boiling water reactor steam separation systems. ASME-paper 69-WA/NE-5 (1969).

48. Untersuchungen an Zyklonen zur Dampfabscheidung in Siedewasserreaktoren. Abschlussbericht, Teil I, Jan. 1966 bis Sept. 1968, EURAEC-2127 (= EUR-4020), (1969).

49. Steam separation technology under the Euratom program, Primary separation of steam from water by natural separation. Topical report-part I, ACNP-65002 (1965).

50. Vollradt, J. Dampfabscheidung bei Siedewasser- und Siedeüberhitzerreaktoren, Tech. überwachung vol. 9, no. 2, pp. 46-50 (1968).

51. Moen, R.H. Radial Vane steam separator development, Final report - Phase II. GEAP-5655 (= EURAEC 2060), (1968).

52. Cochran, J.T. e.a. Axial flow vapor-liquid separator. U.S. Patent 3, 216, 182 (1965).

53. Cochran, J.T. Axial flow vapour-liquid separator. British patent 1, 157, 877 (1966).

54. Lockhart, R.W. Feasibility of boiling water reactor nuclear steam supply systems with capacities up to 10.000 MWt. GECR-5155 (1967).

55. Untersuchungen an Zyklonen zur Dampfabscheidung in Siedewasserreaktoren. Abschlussbericht. Teil II. Okt. 1968 bis Dez. 1969. EURAEC-2144 (= EUR-4033), (1970).

56. Browns Ferry Nuclear Station, T.V.A., Design and Analysis Report, NP-16251.

57. Ter Linden, A.J. Untersuchungen an Zyklonabscheidern. Tonindustrie-Zeitung, vol. 77, no. 3/4, pp. 49-55 (1953).

58. Kelsall, D.F. Trans. Inst. Chem. Eng., vol. 30, pp. 87 (1952).

59. Rietema, K. and Verner, C.O. Cyclones in industry. Elsevier, Amsterdam, (1961).

60. Bradley, D. The hydrocyclone. Pergamon Press (1965).

61. Zandbergen, P.J. and Baurdoux, H.F. An application of the N-strip method of integral relations for analyzing the flow around a circular cone. Journ. of Eng. Math., vol. 3, no. 3, pp. 189-207 (1969).

62. Vriesema, B. Private communications. (1970).

63. Goemans, T. Description of the NEPTUNUS pressurizer test facility. NEP-Alg-E-11, Lab. for Power Eng., Delft University of Technology. (1969).

64. Thomas, J. Axiale scheiders. TOMAAT II. Interim rapport 3, SWST-13, Lab. for Power Engineering, Delft University of Technology. (1968).

65. Snik, J.G.J.M. van Axiale scheiders. TOMAAT II. Interim rapport 2, SWST-15, Lab. for Power Engineering, Delft University of Technology. (1967).

66. Marshall, R.C. Carry-under in gravity separation of air-water mixtures. ASME-paper-64-WA/HT-38 (1964).

67. Skaug, J.A. Summary report on carry-under investigation. Institute for Atomenergi, rapport RT-31 (1967).

68. Development of steam separation devices. Final report. CEND-136, Sept. (1961).

69. Olsen, H.O. Theoretical and experimental impedance voidmeters. Kjeller report KR-110.

70. Neal, L.G. Local parameters in co-current mercury-nitrogen flow. ANL-6625.

71. Spigt, C.L. On the hydraulic characteristics of a boiling channel with natural circulation. Ph.D.Thesis. T.H. Eindhoven, (1966).

72. Korving, A. Semi-automatisch lezen van grafieken en verwerking tot ponsband. KR-Memo-70-13.

73. Schrock, V.E. Radiation attenutation techniques in two-phase flow measurements. Two-phase flow instrumentation, 11th, ASME/AICHE, Heat transfer Conference, Aug. 1969, Minneapolis, U.S.A.

74. Nassos, G.P. Development of an electrical resistivity probe for void fraction measurements in air-water flow. ANL-6738.

75. Delhaye, J.M. Measurement of the local void fraction in two-phase air water flow with a hot-film anemometer. CEA-R-3465, (1968).

76. Schraub, F.A. ISO kinetic probe and other two-phase sampling devices: a survey, 11th ASME/AICHE, Heat Transfer Conference, Aug. 1969, Minneapolis, U.S.A.

77. Dijkman, B. Methoden tot beproeving- en beproeving van venturi scheiders. Report SWST-26. Lab. for Power Engineering, Delft University of Technology. (1970).

78. Wisman, R. Metingen aan damp- en drukverdeling van een versneld tweefasenmengsel.
Report SWST-23. Lab. for Power Engineering, Delft University of Technology. (1969).

79. Bohnet, M. Trennen zweier Flüssigkeiten in Hydrozyklon.
Chemie-Ing.-Techn., vol. 41, no. 5+6, pp. 381-387 (1969).

80. Rossum, J.J. van Separation of emulsions in a cyclone.
De Ingenieur, no. 40, Sept. (1953).

81. Ebbenhorst Tengbergen, H.J. van and Rietema, K. Efficiency of phase separations.
Cyclones in industry.
Elsevier, Amsterdam. (1961).

82. Burley, E.L. Performance of internal steam separation system in boiling water reactor.
ASME-paper 69-WA/NE-24 (1969).

83. Wisman, R. Meet- en berekeningsmethoden ter bepaling van gasvolumefractie profielen van een stromend stoomwatermengsel.
Report SWST-19, Lab. for Power Engineering, Delft University of Technology. (1968).

84. Yih, C.S., Gascogne, M.E. and Debler, W.R. Hydraulic jump in a rotating fluid.
The physics of fluids, vol. 7, no. 5, pp. 638-642 (1964).

85. Yih, C.S. Dynamics of non homogeneous fluids.
The McMillan Co. N.Y.

86. Binnie, A.M. Experiments on the swirling flow of water in a vertical pipe and a bend.
Proc. Royal Soc. (London), vol. A270, pp. 452-466 (1962).

87. Kedl, R.J. MSRE progress report ORNL-4344, p. 74 (1969).

88. Chow, V.T. Open channel flow, Section 24 in: V.L. Streeter, Handbook of fluid dynamics, McGraw Hill Book Co., N.Y. (1961).

89. Korstanje, H.P. The pressure recovery of a one-component twophase flow in a two-dimensional diffuser.
ANL-7504 (1969).

90. Hench, J.E. and Johnston, J.P. Two-dimensional diffuser performance with subsonic two-phase, air-water flow.
APED-5477 (1968).

91. Krogt, C.A.J. van der Voortgezette metingen aan damp- en drukverdeling van een twee-fasen mengsel bij hogere drukverschillen.
Report SWST-24, Lab. for Power Engineering, Delft University of Technology. (1970).

92. Olsen, H.O. — Theoretical and experimental investigation of impedance void meters. Kjeller report KR-118 (1967).

93. Petrick, M. and Kudirka, A.A. — On the relationship between the phase distributions and relative velocities in two-phase flow. Proc. Int. Conf. on Heat Transf., pp. 184-192, Chicago (1966).

94. Pieterse, G.L. and Wijk, N.E. van — Carry-under metingen. Report SWST-22. Lab. for Power Engineering, Delft University of Technology. (1969).

95. Goemans, T. — Computer oriented equations for the thermodynamic properties of steam and water. Part III. The IFC-formulation for industrial use. NEPTUNUS Pressurizer Project, report NEP-T-E-17, Lab. for Power Engineering, Delft University of Technology. (1967).

96. Kazin, I.V. — Investigation of true steam content in a circuit with natural circulation of water. Teploenergetica, vol. 10, no. 6, pp 25-29 (1963), (AEC-tr-6402).

97. Neal, L.G. — An analysis of slip in gas-liquid flow applicable to the bubble and slug flow regimes. European Atomic Energy Society Symp., Oct. 1963, Studsvik.

98. McAdams, W.H. — Heat transmission. McGraw Hill, N.Y.

99. Yeh, G.C.K. and Zuber, N. — On the problem of liquid entrainment. ANL-6244 (1960).

100. Kuyk, R.M. van — Private communication (1971).

101. Frewer, H. and Keller, W. — Das 600-MW-Kernkraftwerk Stade mit Siemens Druckwasserreaktor, Atomwirtschaft, pp. 568-573, Dez. (1967).

102. Steam separation technology under the Euratom program, Primary and secondary separation of steam from water by mechanical means. Topical report-part II, ACNP-65003 (1965).

SAMENVATTING

De scheiding van stoom en water in nucleaire ketels (de kokend water reactor en de stoomgenerator van de druk water reactor) vormt een met de eenheidsgrootte toenemend technisch en economisch probleem, waarin compacte bouw, een hoog rendement en een laag drukverlies een rol spelen.
Van de twee aspecten van onvoldoende scheiding, het met de stoom meevoeren van ketelwater naar de turbine en het meesleuren van stoom met het recirculerende water, is het laatste - de z.g. "carry-under" - gekozen als onderwerp van de onderhavige studie. Hiertoe zijn zijn de gebruikelijke splitsing in primaire en secundaire scheiding (voor mengsels met een kwaliteit van respectievelijk 4 tot 20% en 80 tot 95%), zwaartekrachtscheiding en mechanische scheiding in axiale cyclonen als vormen van primaire scheiding onderzocht.
Het onderzoek omvat een experimenteel en een analytisch deel.
Voor experimenten met zwaartekrachtscheiding onder reactorcondities met stoom en water is een opstelling gebouwd, welke een stijgpijp (onderzocht zijn twee diameters: 0,126 en 0,125 m) en een annulaire valpijp omvat, gebruikmakend van geforceerde circulatie en stoomvorming buiten de opstelling zelf in een ketel. Als belangrijkste experimentele gegevens zijn de kwaliteit en de dampvolumefractie in het valkanaal gemeten voor stijgpijpkwaliteiten in het gebied van 4 tot 20% bij superficiële watersnelheden in de valpijp tot 0,5 m/s. Deze resultaten zijn grafisch weergegeven voor drie stoommassastromen in en drie niveau's boven de stijgpijp bij 50 en 70 bar.
Een tweede orienterend experiment omvat de meting van scheidingsrendement en drukval in twee axiale stijgcyclonen met een convergerend-divergerend scheiderhuis in een atmosferische lucht-water-opstelling, waardoor het eveneens mogelijk is met behulp van de γ-absorptiemethode de radiale verdeling van de gasvolumefractie op verschillende hoogten in het scheiderhuis te meten. De metingen zijn meer ingericht ten behoeve van het onderzoek naar fundamentele stromingsproblemen in dit type scheider, dat gekozen is om zijn compacte vorm, dan om direct op industriële schaal bruikbare gegevens te verschaffen. Dit blijkt ook uit de gepresenteerde resultaten van metingen welke voor superficiële axiale waterinlaatsnelheden van 2; 2,5 en 3 m/s zijn uitgevoerd met volumetrische mengselkwaliteiten tot 30% voor twee geometrieën met een inlaatdiameter van het scheiderhuis van 0,1 m en welke onvoldoende zijn op grond van reactorspecificaties.
Het analytische deel van de studie heeft tot doel een twee-dimensionaal wiskundig model op te stellen voor de beschrijving van het gedrag van het twee-fasenmengsel in het scheiderhuis. Een overzicht wordt gegeven van de interactiekrachten tussen beide fasen welke een rol spelen bij hun relatieve beweging, zoals hydraulische weerstands- en virtuele massakrachten en de fysische verschijnselen welke eraan ten grondslag liggen.
De modelopbouw geschiedt in twee stadia. Eerst wordt een één-dimensionale versie afgeleid op basis van behoudswetten voor massa en impuls, welke gebruikt wordt voor een kwantitatieve bepaling van de daarin opgenomen interactiekrachten. De daartoe benodigde hulpexperimenten worden beschreven, waarbij lucht-water-mengsels door een kanaal met conusvormige vernauwing stromen. Met behulp van γ-absorptie wordt de radiale gasvolumefractie in 9 kanaaldoorsneden gemeten, waaruit het axiale verloop van de gemiddelde waarden volgt. Vergelijking van dit verloop en dat van de gemeten druk met door het model voorspelde waarden resulteert met behulp van "trial" and "error" in de gezochte waarden voor de interactiekrachten als functie van de gasvolumefractie bij superficiële watersnelheden van 1; 2 en 3 m/s, superficiële luchtsnelheden van 0,5 tot 3 m/s en twee vernauwingen in kanaaldiameter: van 0,1 op 0,07 en 0,1 op 0,05 m. Tevens wordt de twee-fasen-wandwrijving in een kanaal van 0,1 m gemeten. Een methode voor de directe meting van de wandschuifspanning wordt gebruikt, waarbij de kracht

op een los van de rest van het kanaal opgehangen sectie gemeten wordt. Karakteristieke eigenschappen van dit testcircuit laten geen metingen toe buiten het gebied van superficiële water- en luchtsnelheden van respectievelijk 0,8 tot 2,2 en 0 tot 0,88 m/s. Meetresultaten binnen dit gebied worden vergeleken met berekende waarden volgens Martinelli en Levy, waarbij de laatste de beste correlatie voor de gepresenteerde meetwaarden blijkt te geven.
De volgende stap is de uitbreiding van de behoudswetten voor massa en impuls voor het twee-dimensionale geval van rotatie-symmetrische stroming, gebruikmakend van de gevonden relaties voor de interactiekrachten. Een oplossingsmethode voor het stelsel van niet-lineaire partiële differentiaalvergelijkingen wordt ontwikkeld, welke gebaseerd is op de z.g. N-strip-methode. De gevolgde weg blijkt echter tot numerieke instabiliteiten te leiden. Mogelijke oorzaken worden besproken alsmede een vermoedelijke uitweg uit de impasse. Ten behoeve van het carry-under probleem wordt een vereenvoudigd model op basis van het een-dimensionale model gegeven dat steunt op de experimentele resultaten van het onderzoek naar zwaartekrachtscheiding. Een vergelijking van de door dit model voorspelde kwaliteit en dampvolumefractie in de valpijp met de experimentele waarden wordt gegeven. In het gebied waar de carry-under begint geeft het model goede resultaten. Bij hogere circulatiesnelheden treden afwijkingen op welke samenhangen met de kleine schaal van het experiment.
Tot slot wordt een vergelijking met in de Dodewaard-reactor gemeten carry-under gegeven alsmede een voorspelling van de carry-under welke zou optreden in de stoomgeneratoren van de centrale Stade wanneer daar zwaartekrachtscheiding zou worden toegepast.

APPENDIX 2-A. INSTRUMENT LISTING

Instrum. number		measured quantity	Instrument			
punched tape	control panel		type	make	range	calibration
	D1	intermediate steam outlet pressure	manometer	Econosto	0-6 ato	deadweight tester
D2		pressure steam dome	straingage manometer, strainmeter	C.E.L. (RV22), Peekel	0-70 ato	deadweight tester
D3	D3	differential pressure venturitube F4	electronic d.p. cell	Foxboro (613 DM)	0-1000 mm H_2O	(high pressure) U-tube (water)
D4	D4	differential pressure venturitube F1	electronic d.p. cell	Foxboro (613 DM)	0-1000 mm H_2O	(high pressure) U-tube (water)
	D5	steam pressure at F1	straingage manometer, strainmeter	C.E.L. (RV 22), Peekel	0-105 ato	deadweight tester
D6	D6	differential pressure riser	electronic d.p. cell, amplifier	Hottinger Baldwin (PD1), Hottinger Baldwin (KWS/3-5)	0-1000 mm H_2O	Manufacturer, U-tube (water)
D8	D8	differential pressure venturi tube F2,F3	electronic d.p. cell	Foxboro (613 DM)	0-1000 mm H_2O	(high pressure) U-tube (water)
	D9	steam pressure boiler	manometer	Econosto	0-160 ato	deadweight tester

	D10	pressure steamdome	manometer	Econosto	0-100 ato	deadweight tester
D11	D11	differential pressure downcomer	electronic d.p. cell, amplifier	Hottinger Baldwin (PD1), Hottinger Baldwin (KWS/3-5)	0-1000 mm H_2O	Manufacturer U-tube (water)
D12	D12	differential pressure downcomer	electronic d.p. cell, amplifier	Hottinger Baldwin (PD1), Hottinger Baldwin (KWS/3-5)	0-1000 mm H_2O	Manufacturer, U-tube (water)
F1		steam flowrate to vessel	venturitube (DIN-Normdüse)	Bopp & Reuther	0.05-0.564 kg/s	Manufacturer
F2		circulation flow rate	venturitube (DIN-Normdüse)	Bopp & Reuther	0.4-4.235 kg/s	Manufacturer
F3		circulation flow rate	venturitube (DIN-Normdüse)	Bopp & Reuther	1.4-13.458 kg/s	Manufacturer
F4		carry-under quench water flow rate	venturitube (DIN-Normdüse)	Bopp & Reuther	0.05-0.571 kg/s	Manufacturer
F5		steam flowrate from vessel	orifice plate (DIN-Normblende)	Schaeffer en Budenberg	0.05-0.556 kg/s	-
N1,2	N1,2	two-phase level above riser	electrical capacitance gage, silometer	own, Endress & Hauser SM-70	0-1000 mm, 0-100%	see Appendix 2-B, in situ
	N3 N4 N7	water level annular cavity	electrical resistance electrode, niveautester	Endress & Hauser (11960-St-V4A), Endress&Hauser(w4)	on/off signal	

	N8,9	waterlevel annular cavity	electrical capacitance electrode, silometer	own, Endress & Hauser SM-7	0-1000 mm 0-100%	in situ
	N10	two-phase level above riser (top N1,2)	electrical resistance electrode niveautester	own, Endress & Hauser (w4)	on/off signal	
	N11	two-phase level above riser (bottom N1,2)				
T1 T2 T3 T4 T5 T6 T7 T8 T9 T10 T11 T12		mixture or water temp. downcomer				
T13	T14	mixture temp. riser	chromel-alumel			in situ
T15,16		circulation water temp. at vessel outlet				
T17		idem at vessel inlet				
T18		steam temp. at vessel inlet				
T20		idem at F3				

T21		water temp. c.u. quench at cooler inlet	mineral insulated thermocouple with stainless steel sheath 1.6 mm dia			
T22		cooling water temp. idem at cooler outlet				none
T23		water temp. c.u. quench at cooler outlet				in situ
T24		cooling water temp. idem at cooler inlet				none
	T25	water temp. c.u. quench in sparger				in situ
T26		steam temp. steamdome				
	T27	vessel flange outside temp. section 2				none
	T28	vessel bottom cover inside temp.				none
T29		steam temp. at F1				in situ
T30	T31	water temp. c.u. quench in sparger				
	T32	circulation water temp. at pump inlet				
	T33	steam temp. steamdome				

	T34	steam temp. at F1	chromel-alumel mineral insulated thermocouple with stainless steel sheath 1.6 mm dia			in situ
T39, 40		water or mixture temp. downcomer				
	T41	vessel bottom cover outside temp.				none

APPENDIX 2-B. CAPACITANCE LEVEL GAGE CALIBRATION EXPERIMENT.

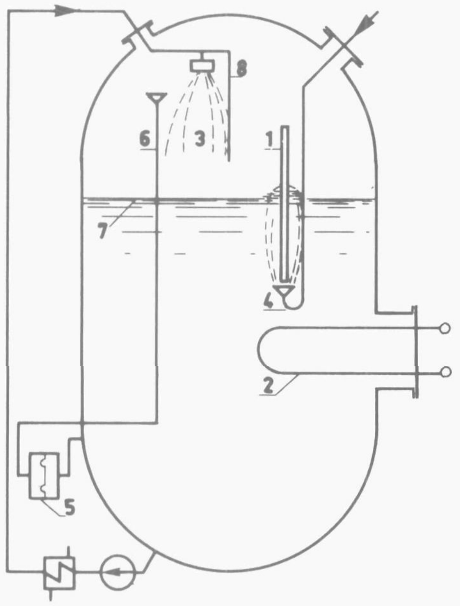

FIGURE 2-B-1.

Arrangement for capacitance level gage calibration experiment.

An experiment was carried out to investigate the influence of the steam content of a two-phase mixture on the capacitance level gage readings under test conditions of 70 bar saturation pressure.

The level gage (1), described in section 2.1.2.2.2., was mounted in a pressure vessel ★) as shown in the diagram of figure 2-B-1. The pressure in the vessel was kept constant by controlled heater elements (2) and a spray cooling system (3). Steam from the laboratory utility boiler could be blown into the vessel by means of a submerged sparger (4) creating a swarm of rising steam bubbles under the level gage. The water level in the vessel was also measured with a Barton differential pressure cell (5). The cell gives the difference in head between a constantly filled open standpipe (6) inside the vessel and the water level (7) in the vessel. The vessel connections for the Barton cell were located away from the steam bubbler to register the true liquid level. A shield (8) was provided to prevent the spray water from entering the capacitance gage and distorting the reading. The two level gage signals were recorded during the test. First the vessel level was lowered to the low level mark of the capacitance gage. Then steam was admitted to the vessel, and as the pressure commenced to rise, the spray cooling system intervened condensing the steam in the steamdome. The level, which slowly increased as a result of the condensed steam, was then measured. The amount of steam admitted was calculated from the level rise over a period of time; the velocity of the rising bubbles was derived from this value by assuming the cross section of the swarm equal to the surface area of the sparger (20.8 cm^2).

The results are plotted in figure 2-B-2.

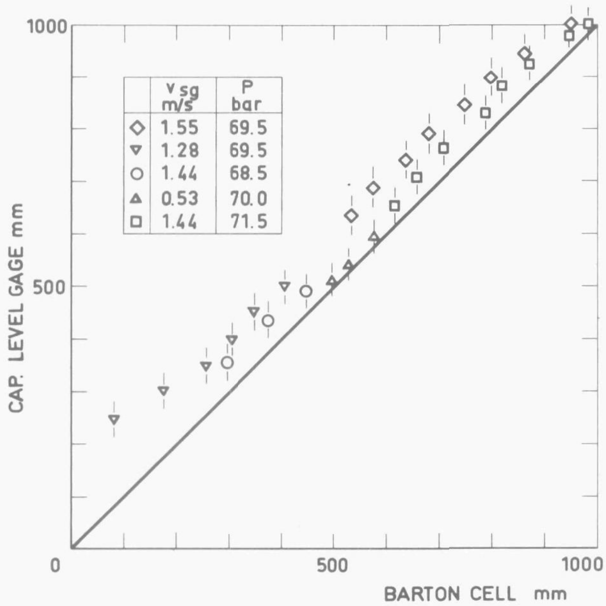

FIGURE 2-B-2.

Comparison of levels measured with capacitance gage and pressure differential cell.

★) *The pressure vessel is the pressurizer of the NEPTUNUS project, a study of PWR pressurizer dynamics carried out in the same laboratory* [63].

Data points for various steam flow rates are given; the vertical lines indicate the noise, on the recorded capacitance signal due to the surface oscillations. Would the voids have had a significant effect on the gage capacitance the indicated level would have been lower than that read form the Barton cell. The opposite effect was found however. The increasingly positive deviation of the capacitance measured level with increasing steam content of the swarm can be attributed to the mound on the surface created by the bubble stream as it broke the surface.

At low level this mound was more pronounced then at higher levels. Although this phenomenon may obscure other effects it is safe to conclude that the capacitance level gage was essentially insensitive to the steam content over the range tested, which was a fair coverage of the carry-under test conditions.

APPENDIX 2-C. CALCULATION OF Q_R AND Q_D.

1. Q_R.

The heat transferred from the riser to the downcomer is given by

$$Q_R = k_R \, \pi \, . \, D_{Ro} \, . \, L_R \, (\theta_{sat} - \theta_D) \tag{2-C-1}$$

with D_{Ro} - outside riser diameter

L_R - length of riser wall corresponding with the control volume

θ_{sat} - saturation temperature

θ_D - average downcomer temperature: T10 for the short and (T10 + T12 + T13) / 3 for the long control volume

$$k_R = \frac{1}{\frac{1}{a_i}\frac{D_{Ro}}{D_{Ri}} + \frac{D_{Ro}}{2\lambda_{ss}} \ln \frac{D_{Ro}}{D_{Ri}} + \frac{1}{a_o}} \tag{2-C-2}$$

where a_i and a_o are found from the DITTUS-BOELTER [98] correlation for forced convection

$$a_i = \frac{\lambda_\ell}{D_{Ri}} \times 0.023 \, Re^{0.8} \, Pr^{0.4} \tag{2-C-3}$$

$$a_o = \frac{\lambda_\ell}{D_{Di} - D_{Ro}} \times 0.023 \, Re^{0.8} \, Pr^{0.4} \tag{2-C-4}$$

with λ_ℓ - thermal conductivity of water

λ_{ss} - thermal conductivity of stainless steel

D_{Ri} - inside riser diameter

D_{Di} - inside downcomer diameter.

Although the Dittus-Boelter correlation is intended for single phase flow it is used here for two-phase heat transfer with essentially no change of phase. The effect of increased heat transfer is accounted for by taking the true average water velocity for the calculation of Re instead of the superficial velocity.
The combined physical properties at the right-hand side of equations (2-C-3) and (2-C-4) were approximated by a simple temperature function.

$$\lambda_\ell \left(\frac{\rho_\ell}{\eta_\ell}\right)^{0.8} \left(\frac{c_\ell \eta_\ell}{\lambda_\ell}\right)^{0.4} = (\theta + 503.0514) \, / \, 875.355 \tag{2-C-5}$$

with η_ℓ - dynamic viscosity of the water

c_ℓ - heat capacity of the water

Using this approximation Q_R is found in KW.

2. $\underline{Q_D:}$

The heat transferred from the downcomer to the cavity is given by

$$Q_D = \frac{1}{\frac{1}{k_D} + \frac{1}{a_C}} \pi \, D_{Do} \cdot L_D \, (\theta_D - \bar{\theta}_C) \qquad (2\text{-}C\text{-}6)$$

with D_{Do} - outside downcomer diameter
L_D - length of downcomer wall corresponding with the control volume
$\bar{\theta}_C$ - average temperature in the cavity

where

$$k_D = \frac{1}{\frac{D_{Do}}{D_{Di}} \frac{1}{a_o} + \frac{D_{Do}}{2\lambda_{ss}} \ln \frac{D_{Do}}{D_{Di}}} \qquad (2\text{-}C\text{-}7)$$

and the heat transfer coefficient on the cavity side is based on a natural convection correlation [42] for vertical flat walls

$$a_C = 0.129 \frac{\lambda_\ell}{L_D} (\mathrm{Gr\ Pr})^{1/3} \qquad (2\text{-}C\text{-}8)$$

Equation (2-C-8) is valid for turbulent flow i.e. if $\mathrm{Gr\ Pr} > 10^8$ where

$$\mathrm{Gr\ Pr} = 9.81 \frac{\rho_\ell^{\,2} \, c_\ell \, \beta}{\eta_\ell \, \lambda_\ell} \Delta\theta \, L_D^{\,3} \qquad (2\text{-}C\text{-}9)$$

with β - coefficient of thermal expansion
$\Delta\theta$ - temperature difference between the water in the cavity and the outside downcomer wall.

For a cavity temperature of 280°C at 70 bar Gr.Pr is

$$\mathrm{Gr.Pr} = \frac{9.81 \times 750^2 \times 5.35 \times 10^3 \times 2.7 \times 10^{-3} \times 3.32^3}{0.58 \times 10^{-4}} \Delta\theta = 5 \times 10^{12} \, \Delta\theta$$

This shows that condition (2-C-8) is amply satisfied.

The temperature difference $\Delta\theta = \theta_{Do} - \bar{\theta}_C$ is not known a priori and equation (2-C-6) has to be solved by an iterative method. In the data reduction program $\Delta\theta$ is calculated for an assumed heat flux Q_D to start with; the iteration on Q_D is stopped when the newly calculated Q_D differs no more than .05 kW from the last.

The combination given in equation (2-C-9) is approximated by

$$\frac{\lambda_\ell}{L_D} \left(\rho_\ell^{\,2} \, c_\ell \, \frac{\beta}{\eta_\ell \, \lambda_\ell} \Delta\theta \, L_D^{\,3}\right)^{1/3} = (\bar{\theta}_C + 121.99) \, / \, 132.5 \qquad (2\text{-}C\text{-}10)$$

Again Q_D is found in kW.

APPENDIX 2-D. CALCULATION OF $\bar{\theta}_C$ AND Q_S.

1. Correlation for the temperature $\bar{\theta}_C$ in the annular cavity.

The heat absorbed by the carry-under quench water upon passing through the cavity can be expressed by

$$\phi_{m\ell 2}\ \Delta h_{\ell 2} = k\ (\bar{\theta}_C - \theta_{19}) \qquad (2\text{-}D\text{-}1)$$

where k is a heat transfer coefficient corresponding to this particular form of heat exchanger and valid for the given geometry only. The geometry of the double walled corrugated steel hoses is very complicated. Moreover the heat passes through two walls, and a more or less stagnant layer of water implying a total of four film coefficients and two conduction resistances.

Exact computation of the complicated expression for k is impossible and empirical determination of all the constants involved from experiments is hardly feasable. Assuming the main modes of heat transfer to be forced convection inside the steel hose and free convection outside and between the two hoses, the expression for k was approximated by

$$\frac{1}{k} = \frac{k_1}{\theta^+ \phi_{m\ell 2}} + \frac{k_2}{(\bar{\theta}_C - \theta_{19})^{.33}} \qquad (2\text{-}D\text{-}2)$$

where $\theta^+ = \dfrac{\theta_{19} + 273.2}{647.4}$

to include effects of quench water temperature, flowrate and temperature difference over the double hose wall.

The constants k_1 and k_2 had to be found by trial and error from the XNEP-experiments. Notwithstanding the rather crude form of equation (2-D-2) to describe the complicated heat transfer mechanism k_1 and k_2 appeared to be the same for both 50 and 70 bar.

With $k_1 = 0.22$ and $k_2 = 4.6$ $\Delta h_{\ell 2}$ must be expressed in kW/kg.

The average cavity temperature $\bar{\theta}_C$ is the average of the measurements at 8 locations. An error pilot for $(\bar{\theta}_C - \theta_{19})$ is given for both pressures in figures 2-D-1 and 2-D-2 (see page 190) representing the measured and calculated results for the XNEP-measurements.

2. Correlation for Q_S.

Part of the heat represented by $\phi_{m\ell 2}\ \Delta h_{\ell 2}$ is coming from the annular cavity and part - Q_S - from the downcomer. The temperature differences for these sections are approximately $(\bar{\theta}_C - \theta_{19})$ and $(\theta_{sat} - (\theta_{25} + \theta_{30} + \theta_{31})\ /\ 3)$ respectively.

Designating $\bar{\theta}_C - \theta_{19}$ by $\Delta\theta_C$ and $(\theta_{sat} - (\theta_{25} + \theta_{30} + \theta_{31})\ /\ 3)$ by $\Delta\theta_S$

$Q_S\ /\ \phi_{m\ell 2}\ \Delta h_{\ell 2}$ was plotted as a function of $\Delta\theta_S\ /\ (\Delta\theta_C + \Delta\theta_S)$ for 70 and 50 bar. A linear correlation was found with different constants for both pressures:

$$\frac{Q_S}{\phi_{m\ell 2}\ \Delta h_{\ell 2}} = 1.41\ \frac{\Delta\theta_S}{\Delta\theta_C + \Delta\theta_S} - 0.165 \quad \text{for 70 bar} \qquad (2\text{-}D\text{-}3)$$

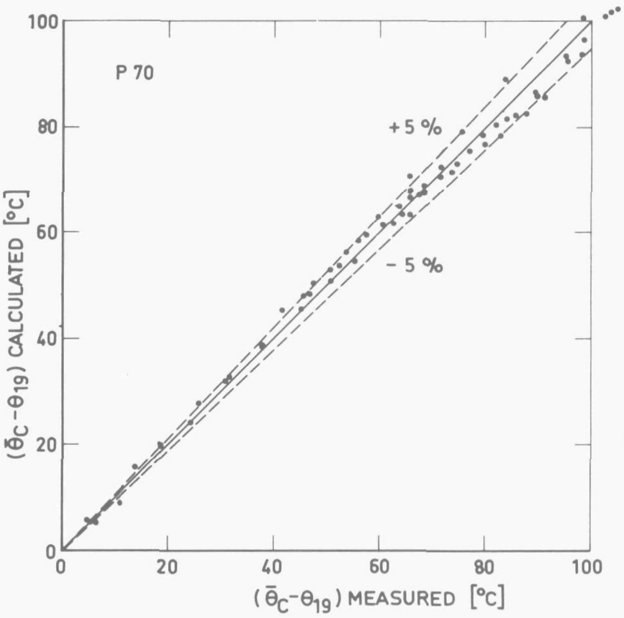

FIGURE 2-D-1.
Error plot of $(\bar{\theta}_C - \theta_{19})$ *for*
70 bar XNEP-experiments

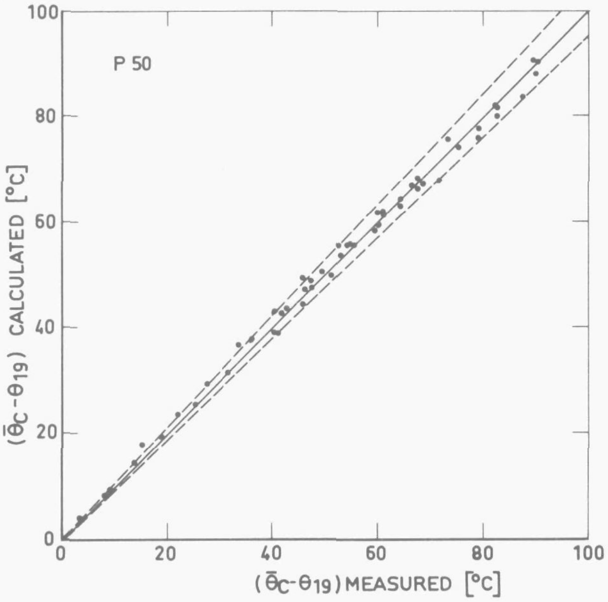

FIGURE 2-D-2.
Error plot of $(\bar{\theta}_C - \theta_{19})$ *for*
50 bar XNEP-experiments.

and

$$\frac{Q_S}{\phi_{m\ell 2}\ \Delta h_{\ell 2}} = 1.71\ \frac{\Delta\theta_S}{\Delta\theta_C + \Delta\theta_S} - 0.196 \quad \text{for 50 bar} \qquad (2\text{-D-}4)$$

An error plot for both measured and calculated values of Q_S in kW is given in figures 2-D-3 and 2-D-4.
As mentioned in section 2.1.3.1.2. most of the real X-measurements were performed without the use of T25, T30 and T31 and had to be based on θ_{25} only. The XNEP-experiments showed a systematic difference between one of the three and the average temperature. For T25 this is shown in figure 2-D-5, where the difference $\theta_{25} - \theta_{19}$ is plotted as a function of the difference between the average temperature $(\theta_{25} + \theta_{30} + \theta_{31}) / 3$ and θ_{19}, designated as $\Delta\theta_{25}$ and $\Delta < \theta_{25} >$ respectively.
The results could be fitted by

$$\Delta < \theta_{25} > = 0.717\ \Delta\theta_{25} + 0.00176\ (\Delta\theta_{25})^2 \qquad (2\text{-D-}5)$$

No difference between 50 and 70 bar results was found.

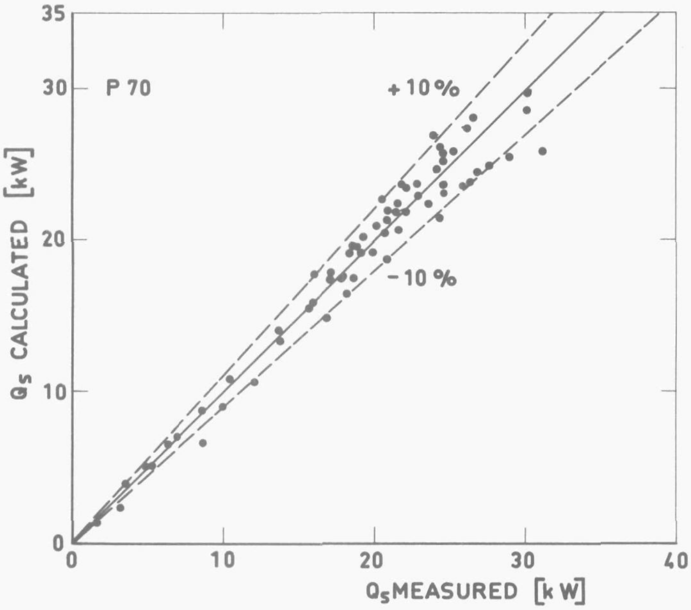

FIGURE 2-D-3.

Error plot of Q_S for 70 bar XNEP-experiments.

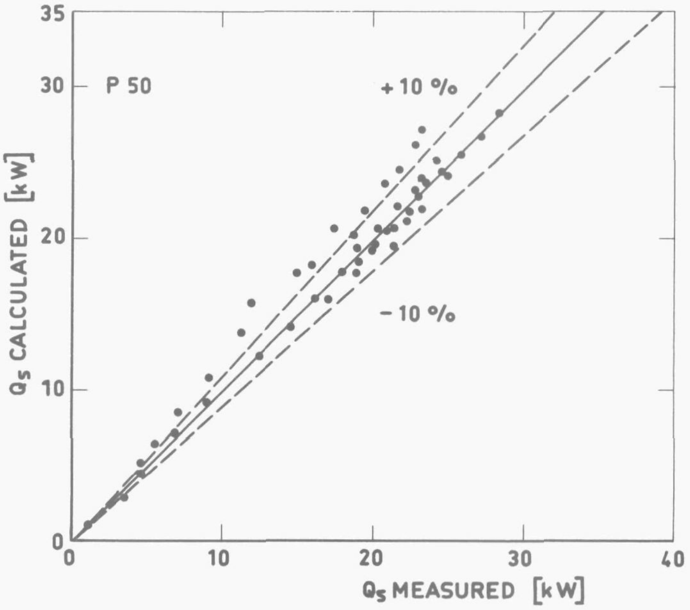

FIGURE 2-D-4.

Error plot of Q_S for 50 bar XNEP-experiments.

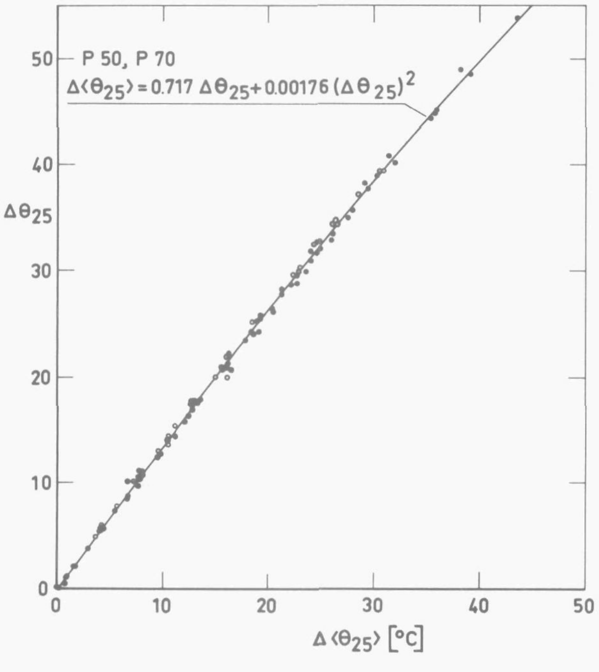

FIGURE 2-D-5.

Relation between $\Delta\theta_{25}$ and $\Delta < \theta_{25} >$ from XNEP-experiments.

APPENDIX 2-E. INSTRUMENT LISTING.

Instr. number	Measured quantity	Instrument			
		type	make	range	calibration
D1	Air pressure at F1, F2	manometer	Schaeffer & Budenberg	0-3 ato	
D2	Differential pressure F1	U-tube manometer with nonius scale, Fluid: Merriam 3000 kg/m^3	Van Essen	0-1000 mm	
D3	Pressure in calming section	U-tube, Fluid: Mercury	Van Essen	0-2000 mm	
D4	Differential pressure test separator	U-tube manometer Fluids: Merriam 3000 kg/m^3 Merriam 1750 kg/m^3	Van Essen	0-1000 mm	
D5					
D6					
D7					
D8					
D9					
D10					
D11					
D12					
D13	Pressure carry-under measuring bell	manometer			
D14	Atmospheric pressure	Mercuri barometer	R. Fuess Berlin-Steglitz (2087)		
F1	Water flowrate	Venturi tube (DIN-Normventuri-düse)	own	3-30 kg/s	
F2	Air flowrate	Rotameter	Fisher & Porter (1-35 G10/80)	1.5-22 Nℓ/s	Manufacturer
F3	Air flowrate	Rotameter	Fisher & Porter (¾-27 G10/80)	0.5-7 Nℓ/s	Manufacturer
F4	Carry-under air Flowrate	Air bell, chronometer			-
F5	Carry-over water Flowrate	Collecting tank, chronometer			- -

Instr. number	Measured quantity	Instrument			
		type	make	range	calibration
T1	Water temperature	Mercury thermometer	AA Precision	- 10, + 50°C	
T2	Air temperature at F2, F3	Mercury thermometer	AA Precision	- 10, + 50°C	
V1	Air volume fraction	Cs^{137}-scource, lead holder and collimator	own	0.1 Curie	in situ
V2		Na I-scintillation cristal and photomultipliertube, lead collimator	Quarts & Silice, Dupont, own		
V3		Spectrum stabilizer	Baird Atomic (T-321)		
V4		Highvoltage power supply, amplifier pulse height analizer	Baird Atomic (T-701)		
V5		Countrate meter	Frieseke & Höpfner (FHK 1/57 B)		
V6		x-y recorder	Hewlett & Packard (2 FAM)	38 × 25 cm	

APPENDIX 2-F. CALCULATION OF FROUDE NUMBERS IN THE VORTEX TUBE.

$$Fr = \frac{u_z}{\left[\frac{u_t^{\,2}}{r}(R-r_c)\right]^{\frac{1}{2}}} \tag{2-F-1}$$

Assuming a void fraction equal to β_1 at level 1 right at the vane exit and complete separation at level 2:

$$u_{z2}2\pi(R_2^{\,2} - r_{c2}^{\,2}) = u_{z1}(1-\beta_1)2\pi(R_1^{\,2} - r_{c1}^{\,2}) \tag{2-F-2}$$

See figure 2-F-1 for notation of radii.

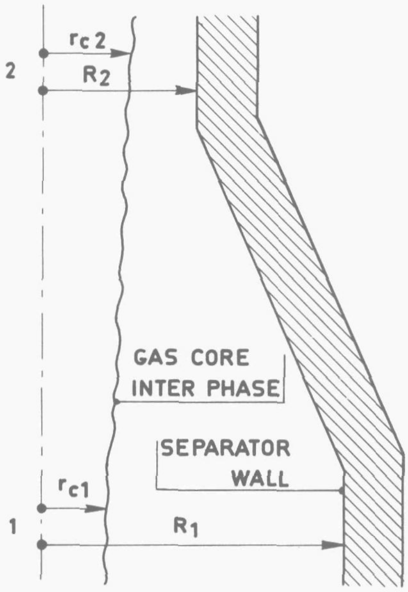

FIGURE 2-F-1.

Notation of radii in the converging section of the separator for the calculation of Froude numbers.

For solid body rotation

$$u_t = C\,.\,r \rightarrow u_{tw} = u_z tg\theta_w = CR$$

and

$$C_1 = u_{z1} tg\theta_w \,/\, R_1 \tag{2-F-3}$$

The tangential velocity at level 2 is found from conservation of angular momentum

$$\int_{r_{c1}}^{R_1} \rho_1 u_{z1} u_{t1} r 2\pi r dr = \int_{r_{c2}}^{R_z} \rho_2 u_{z2} u_{t2} r 2\pi r dr \tag{2-F-4}$$

or with

$$\rho_1 u_{z1} = \frac{\phi_{m1}}{\pi(R_1^{\,2} - r_{c1}^{\,2})} \quad \text{and} \quad \rho_2 u_{z2} = \frac{\phi_{m2}}{\pi(R_2^{\,2} - r_{c2}^{\,2})}$$

$$\frac{\pi}{2}\,\phi_{m1} C_1 (R_1^{\,2} + r_{c1}^{\,2}) = \frac{\pi}{2}\,\phi_{m2} C_2 (R_2^{\,2} + r_{c2}^{\,2}) \tag{2-F-5}$$

Where the density of water is so much higher than for air

$$\phi_{m1} \cong \phi_{m2} \tag{2-F-6}$$

and

$$C_2 = C_1 \left(\frac{R_1}{R_2}\right)^2 \frac{1 + \left(\frac{r_{c1}}{R_1}\right)^2}{1 + \left(\frac{r_{c2}}{R_2}\right)^2} \tag{2-F-7}$$

The tangential velocity at the wall at level 2 is now

$$u_{t2} = C_2 R_2 = \left(\frac{R_1}{R_2}\right)^2 \frac{1 + \left(\frac{r_{c1}}{R_1}\right)^2}{1 + \left(\frac{r_{c2}}{R_2}\right)^2} \cdot u_{z1} \operatorname{tg}\theta_w \frac{R_2}{R_1} \tag{2-F-8}$$

And the Froude number at the wall becomes

$$Fr_{W_2} = \frac{u_{z1} \left(\frac{R_1}{R_2}\right)^2 \frac{1-\left(\frac{r_{c1}}{R_1}\right)^2}{1-\left(\frac{r_{c2}}{R_2}\right)^2} (1-\beta_1)\cot\theta_w}{u_{z1} \left(\frac{R_1}{R_2}\right)^2 \frac{1+\left(\frac{r_{c1}}{R_1}\right)^2}{1+\left(\frac{r_{c2}}{R_2}\right)^2} \frac{R_2}{R_1} \left[\frac{(R_2-r_{c2})}{R_2}\right]^{\frac{1}{2}}} = \frac{\frac{1-\left(\frac{r_{c1}}{R_1}\right)^2}{1-\left(\frac{r_{c2}}{R_2}\right)^2} (1-\beta_1)\cot\theta_w}{\left(\frac{R_2}{R_1}\right) \frac{1+\left(\frac{r_{c1}}{R_1}\right)^2}{1+\left(\frac{r_{c2}}{R_2}\right)^2} \left[1-\left(\frac{r_{c2}}{R_2}\right)\right]^{\frac{1}{2}}} \tag{2-F-9}$$

At the core interface

$$u_{t2} = C_2 r_{c2} = \left(\frac{R_1}{R_2}\right)^2 \frac{1+\left(\frac{r_{c1}}{R_1}\right)^2}{1+\left(\frac{r_{c2}}{R_2}\right)^2} \cdot u_{z1} \operatorname{tg}\theta_w \frac{r_{c2}}{R_1} \tag{2-F-10}$$

and

$$Fr_{c2} = \frac{u_{z1} \left(\frac{R_1}{R_2}\right)^2 \frac{1-\left(\frac{r_{c1}}{R_1}\right)^2}{1-\left(\frac{r_{c2}}{R_2}\right)^2} (1 - \beta_1)\cot\theta_w}{u_{z1} \left(\frac{R_1}{R_2}\right)^2 \frac{1+\left(\frac{r_{c1}}{R_1}\right)^2}{1+\left(\frac{r_{c1}}{R_2}\right)^2} \frac{r_{c2}}{R_1} \left[\frac{R_2-r_{c2}}{r_{c2}}\right]^{\frac{1}{2}}} = \frac{\frac{1-\left(\frac{r_{c1}}{R_1}\right)^2}{1-\left(\frac{r_{c2}}{R_2}\right)^2} (1 - \beta_1) \cot\theta_w}{\frac{R_2}{R_1} \frac{1+\left(\frac{r_{c1}}{R_1}\right)^2}{1+\left(\frac{r_{c2}}{R_2}\right)^2} \left[\frac{r_{c2}}{R_2} \left(1-\frac{r_{c2}}{R_2}\right)\right]^{\frac{1}{2}}} \tag{2-F-11}$$

APPENDIX 2-G. RADIAL PRESSURE DISTRIBUTION.

$$\frac{dp}{dr} = \rho \, \frac{u_t^{\,2}}{r} \qquad (2\text{-}G\text{-}1)$$

$$\int_{r_c}^{R} dp \cong \rho \int_{r_c}^{R} \frac{u_t^{\,2}}{r} \, dr \qquad (2\text{-}G\text{-}2)$$

with $u_t = C.r$

$$\Delta p \cong \frac{\rho}{2} \, C^2 \, (R^2 - r_c^{\,2}) \qquad (2\text{-}G\text{-}3)$$

Using equation (2-F-8) and

$$u_{z1} 2\pi (R_1^{\,2} - r_{c1}^{\,2}) = \frac{v_{s\ell R}}{1-\beta} \, . \, 2\pi R_1^{\,2} \qquad (2\text{-}G\text{-}4)$$

$$\Delta p_2 \cong \frac{\rho}{2} \left[\left(\frac{R_1}{R_2}\right)^2 \frac{1+\left(\frac{r_{c1}}{R_1}\right)^2}{1+\left(\frac{r_{c2}}{R_2}\right)^2} \, \frac{v_{s\ell R}}{1-\beta_o} \, \frac{tg\theta_w}{R_1} \, \frac{1}{1-\left(\frac{r_{c1}}{R_1}\right)^2} \right]^2 (R_2^{\,2} - r_{c2}^{\,2}) \qquad (2\text{-}G\text{-}5)$$

For separator 1 the dimensions at the throat level for the test run with $v_{s\ell R} = 3$ and $\beta_o \cong 28\%$ are:

$$R_1 = 0.05, \quad R_2 = 0.035, \quad \frac{r_{c1}}{R_1} = 0.4, \quad \frac{r_{c2}}{R_2} = 0.715 \qquad (2\text{-}G\text{-}6)$$

Thus:

$$\Delta p_2 \cong \frac{1000}{2} \left[1.43^2 \, \frac{1+0.16}{1+0.51} \, \frac{3}{0.72} \, \frac{1}{0.05} \, \frac{1}{1-0.16} \right]^2 (0.035^2 - 0.025^2) \cong$$

$$\cong 0.073 \text{ bar} \qquad (2\text{-}G\text{-}7)$$

For separator 2 the dimensions at throat level for the test run with $v_{s\ell R} = 3$ and $\beta \cong 16\%$ are:

$$R_1 = 0.05, \quad R_2 = 0.025, \quad \frac{r_{c1}}{R_1} = 0.3, \quad \frac{r_{c2}}{R_2} = 0.5 \qquad (2\text{-}G\text{-}8)$$

$$\Delta p_2 \cong \frac{1000}{2} \left[2^2 \, \frac{1+0.09}{1+0.25} \, \frac{3}{0.84} \, \frac{1}{0.05} \, \frac{1}{1-0.09} \right]^2 (0.025^2 - 0.0125^2) \cong$$

$$\cong 0.175 \text{ bar} \qquad (2\text{-}G\text{-}9)$$

APPENDIX 3-A. CHANGE OF PHASE AND ASSOCIATED MOMENTUM EXCHANGE DUE TO CHANGE IN PRESSURE.

Consider a mixture of air, saturated with water vapor, and water of quality x, then

$$x = \frac{\phi_g}{\phi_g + \phi_\ell} = \frac{(1+\zeta)\,\phi_{gd}}{(1+\zeta)\,\phi_{gd}+\phi_\ell} \simeq (1+\zeta)\frac{\phi_{gd}}{\phi_{gd} + \phi_\ell} = (1+\zeta)\,x_{gd} \qquad (3\text{-}A\text{-}1)$$

where ζ is the relative humidity of the air defined as the amount of water vapor devided by the amount of dry air in a given volume of wet air. BAEHR [32] gives for the relative humidity of saturated wet air

$$\zeta = 0.6220\,\frac{p_{sat}}{p - p_{sat}} \qquad (3\text{-}A\text{-}2)$$

The change in mixture quality for an air water mixture of 1.5 bar after an isothermal reduction in pressure of 0.5 bar can be calculated from equations (3-A-1) and (3-A-2) and the use of the steam tables [33] to determine p_{sat}. At 20°C the change in quality is $\Delta x = 0.005\,x_{gd}$ and at 40°C it becomes $\Delta x = 0.018\,x_{gd}$.

The quality change for a steam-water mixture can also be calculated with the aid of the steam tables [33]. The enthalpy balance for a pressure change from state 1 to state 2

$$x_1 h_{g_1} + (1-x_1)h_{\ell_1} = x_2 h_{g_2} + (1-x_2)h_{\ell_2} \qquad (3\text{-}A\text{-}3)$$

simplifies to

$$x_2 = x_1\,\frac{r_1}{r_2} + \frac{(h_{\ell_1} - h_{\ell_2})}{r_2} \qquad (3\text{-}A\text{-}4)$$

For the pressure reduction from 71 to 70 bar equation (3-41) becomes

$$x_{70} = 0.994\,x_{71} + 3.45 \times 10^{-3} \qquad (3\text{-}A\text{-}5)$$

Contrary to the air-water example the procentual change in quality is dependent on the quality. For $x_{71} = 0.05$, $\Delta x = 0.063\,x_{71}$ while $\Delta x = 0.017\,x_{71}$ for $x_{71} = 0.15$.

With the use of the definition of the steam quality, given by equation (3-28) and the momentum balance equations for the gas and the liquid, equations (3-36) and (3-39) respectively the momentum flux for both phases is

$$G^2 \left\{ \frac{x^2}{\alpha\rho_g} \right\} \qquad (3\text{-}A\text{-}6)$$

and

$$G^2 \left\{ \frac{(1-x)^2}{(1-\alpha)\rho_\ell} \right\} \qquad (3\text{-}A\text{-}7)$$

The momentum flux associated with the evaporated or condensed mass is represented by

$$G^2 \left\{ \frac{\Delta x(1-x)}{(1-\alpha)\rho_\ell} \right\} \qquad (3\text{-}A\text{-}8)$$

and

$$G^2 \left\{ \frac{\Delta x . x}{\alpha . \rho_g} \right\} \qquad (3\text{-}A\text{-}9)$$

For the qualities given above the momentum flux values according to equations (3-A-6), (3-A-7), (3-A-8) and (3-A-9) are given as percentages of the liquid momentum flux of equation (3-A-7). The values of α required to evaluate these equations were taken from the correlation of MARCHATERRE and HOGLUND [45]. The reason this correlation was chosen is that it is also valid for larger diameter tubes and based on experiments at high pressures. The result is

Momentum flux due to		x = 0.05		x = 0.15	
		70 → 71	71 → 70	70 → 71	71 → 70
liquid	%	100	100	100	100
gas	%	9.5	9.5	49.5	49.5
change of phase	%	0.32	0.33	0.28	0.30

Although for steam-water mixtures Δx may reach appreciable percentages of the mixture quality the momentum transfer associated with it is negligable compared to the momentum flux of the liquid.
Moreover the pressure drop of 1 bar may be regarded as conservative.

APPENDIX 3-B. ADAPTION OF MASS AND MOMENTUM EQUATIONS TO N-STRIP METHOD.

Equation (3-62).

$$P_k = \alpha_k\,\rho_{g_k}\,u_{gz_k}$$

$$T_k = F_k = R_k = Y_k = 0$$

$$Q_k = \alpha_k\rho_{g_k}\,u_{gr_k}$$

$$S_k = -\frac{\alpha_k\rho_{g_k}u_{gr_k}}{r_k} \quad \text{and} \quad \frac{\partial\rho_g}{\partial z} = \frac{\partial\rho_g}{\partial p}\frac{\partial p}{\partial z} = \frac{1}{RT}\frac{\partial p}{\partial z}$$

$$\frac{dP_k}{dz} = \alpha_k\rho_{g_k}\frac{du_{gz_k}}{dz} + \alpha_k\frac{u_{gz_k}}{RT}\frac{d}{dz}p_k + \rho_{g_k}u_{gz_k}\frac{d}{dz}\alpha_k$$

$$\frac{h}{3}\alpha_{k-1}\rho_{g_{k-1}}\frac{d}{dz}u_{gz_{k-1}} + \frac{h}{3}\alpha_{k-1}\frac{u_{gz_{k-1}}}{RT}\frac{d}{dz}p_{k-1} + \frac{h}{3}\rho_{g_{k-1}}u_{gz_{k-1}}\frac{d}{dz}\alpha_{k-1} +$$

$$\frac{4}{3}h\alpha_k\rho_{g_k}\frac{d}{dz}u_{gz_k} + \frac{4}{3}h\alpha_k\frac{u_{gz_k}}{RT}\frac{d}{dz}p_k + \frac{4}{3}h\rho_{g_k}u_{gz_k}\frac{d}{dz}\alpha_k +$$

$$\frac{h}{3}\alpha_{k+1}\rho_{g_{k+1}}\frac{d}{dz}u_{gz_{k+1}} + \frac{h}{3}\alpha_{k+1}\frac{u_{gz_{k+1}}}{RT}\frac{d}{dz}p_{k+1} + \frac{h}{3}\rho_{g_{k+1}}u_{gz_{k+1}}\frac{d}{dz}\alpha_{k+1} =$$

$$\left.\begin{aligned}
&+\alpha_{k-1}\rho_{g_{k-1}}u_{gr_{k-1}} - \alpha_{k+1}\rho_{g_{k+1}}u_{gr_{k+1}}\\
&+(k-1)\frac{dh}{dz}\left(-\frac{3}{2}\alpha_{k-1}\rho_{g_{k-1}}u_{gz_{k-1}} + 2\alpha_k\rho_{g_k}u_{gz_k} - \frac{1}{2}\alpha_{k+1}\rho_{g_{k+1}}u_{gz_{k+1}}\right)\\
&+(k+1)\frac{dh}{dz}\left(\frac{1}{2}\alpha_{k-1}\rho_{g_{k-1}}u_{gz_{k-1}} - 2\alpha_k\rho_{g_k}u_{gz_k} + \frac{3}{2}\alpha_{k+1}\rho_{g_{k+1}}u_{gz_{k+1}}\right)
\end{aligned}\right\} Q_1'$$

$$\left. -\frac{1}{3}\frac{\alpha_{k-1}\rho_{g_{k-1}}u_{gr_{k-1}}}{(k-1)} - \frac{4}{3}\frac{\alpha_k\rho_{g_k}u_{gr_k}}{k} - \frac{1}{3}\frac{\alpha_{k+1}\rho_{g_{k+1}}u_{gr_{k+1}}}{k+1}\right\} Q_2'$$

Equation (3-63).

$$P_k = (1-\alpha_k)\,\rho_\ell u_{\ell z_k}$$

$$T_k = F_k = R_k = Y_k = 0$$

$$Q_k = (1-\alpha_k)\, \rho_\ell u_{\ell r_k}$$

$$\frac{dP_k}{dz} = (1-\alpha_k)\, \rho_\ell \frac{d}{dz} u_{\ell z_k} - \rho_\ell u_{\ell z_k} \frac{d}{dz} \alpha_k .$$

$$\begin{aligned}
&\frac{h}{3} (1-\alpha_{k-1})\, \rho_\ell \frac{d}{dz} u_{\ell z_{k-1}} - \frac{h}{3} \rho_\ell u_{\ell z_{k-1}} \frac{d}{dz} \alpha_{k-1} \\
&+ \frac{4}{3} h\, (1-\alpha_k)\, \rho_\ell \frac{d}{dz} u_{\ell z_k} - \frac{4h}{3} \rho_\ell u_{\ell z_k} \frac{d}{dz} \alpha_k \\
&+ \frac{h}{3} (1-\alpha_{k+1})\, \rho_\ell \frac{d}{dz} u_{\ell z_{k+1}} - \frac{h}{3} \rho_\ell u_{\ell z_{k+1}} \frac{d}{dz} \alpha_{k+1} = \\
&\left.\begin{aligned}
&+ (1-\alpha_{k-1})\, \rho_\ell u_{\ell r_{k-1}} - (1-\alpha_{k+1})\, \rho_\ell u_{\ell r_{k+1}} \\
&+ (k-1) \frac{dh}{dz} \left(- \frac{3}{2} (1-\alpha_{k-1}) \rho_\ell u_{\ell z_{k-1}} + 2(1-\alpha_k) \rho_\ell u_{\ell z_k} - \frac{1}{2} (1-\alpha_{k+1}) \rho_\ell u_{\ell z_{k+1}} \right) \\
&+ (k+1) \frac{dh}{dz} \left(+ \frac{1}{2} (1-\alpha_{k-1}) \rho_\ell u_{\ell z_{k-1}} - 2(1-\alpha_k) \rho_\ell u_{\ell z_k} + \frac{3}{2} (1-\alpha_{k+1}) \rho_\ell u_{\ell z_{k+1}} \right)
\end{aligned}\right\} Q_3' \\
&\left.- \frac{1}{3} \frac{(1-\alpha_{k-1}) \rho_\ell u_{\ell r_{k-1}}}{k-1} - \frac{4}{3} \frac{(1-\alpha_k) \rho_\ell u_{\ell r_k}}{k} - \frac{1}{3} \frac{(1-\alpha_{k+1}) \rho_\ell u_{\ell r_{k+1}}}{k+1} \right\} Q_4'
\end{aligned}$$

Equation (3-80).

$$P_k = (1-\alpha_k) \rho_\ell u_{\ell r_k} u_{\ell z_k} \qquad R_r = \frac{3}{4} \frac{C_D}{d} \alpha_k \rho_\ell (u_{gr_k} - u_{\ell r_k}) | u_{gr_k} - u_{\ell r_k} |$$

$$T_k = F_k = 0$$

$$R_k = (1-\alpha_k)$$

$$Y = p_k$$

$$Q_k = (1-\alpha_k) \rho_\ell u_{\ell r_k}{}^2$$

$$S_k = (1-\alpha_k) \rho_\ell f_{r_k} + R_{r_k} - \frac{(1-\alpha_k) \rho_\ell u_{\ell r_k}{}^2}{r}$$

$$\frac{dP_k}{dz} = (1-\alpha_k)\rho_\ell u_{\ell r_k} \frac{d}{dz} u_{\ell z_k} + (1-\alpha_k)\rho_\ell u_{\ell z_k} \frac{d}{dz} u_{\ell r_k} - \rho_\ell u_{\ell r_k} u_{\ell z_k} \frac{d}{dz} \alpha_k .$$

$$\frac{h}{3}(1-\alpha_{k-1})\rho_\ell u_{\ell r_{k-1}} \frac{d}{dz} u_{\ell z_{k-1}} + \frac{h}{3}(1-\alpha_{k-1})\rho_\ell u_{\ell z_{k-1}} \frac{d}{dz} u_{\ell r_{k-1}} - \frac{h}{3}\rho_\ell u_{\ell r_{k-1}} u_{\ell z_{k-1}} \frac{d}{dz} \alpha_{k-1}$$

$$+ \frac{4}{3} h(1-\alpha_k)\rho_\ell u_{\ell r_k} \frac{d}{dz} u_{\ell z_k} + \frac{4h}{3} (1-\alpha_k)\rho_\ell u_{\ell z_k} \frac{d}{dz} u_{\ell r_k} - \frac{4h}{3} \rho_\ell u_{\ell r_k} u_{\ell z_k} \frac{d}{dz} \alpha_k$$

$$+ \frac{h}{3} (1-\alpha_{k+1})\rho_\ell u_{\ell r_{k+1}} \frac{d}{dz} u_{\ell z_{k+1}} + \frac{h}{3} (1-\alpha_{k+1})\rho_\ell u_{\ell z_{k+1}} \frac{d}{dz} u_{\ell r_{k+1}} -$$

$$- \frac{h}{3} \rho_\ell u_{\ell r_{k+1}} u_{\ell z_{k+1}} \frac{d}{dz} \alpha_{k+1} =$$

$$\left.\begin{aligned}
&+ \frac{dh}{dz} \left(\frac{k+1}{2} - \frac{3(k-1)}{2}\right) (1-\alpha_{k-1})\rho_\ell u_{\ell z_{k-1}} u_{\ell r_{k-1}} \\
&- 4 \frac{dh}{dz} (1-\alpha_k)\rho_\ell u_{\ell z_k} u_{\ell r_k} \\
&+ \frac{dh}{dz} \left(\frac{3}{2}(k+1) - \frac{k-1}{2}\right) (1-\alpha_{k+1})\rho_\ell u_{\ell z_{k+1}} u_{\ell r_{k+1}}
\end{aligned}\right\} Q_5'$$

$$\left.+ (1-\alpha_{k-1})\rho_\ell u_{\ell r_{k-1}}^{\;2} - (1-\alpha_{k+1})\rho_\ell u_{\ell r_{k+1}}^{\;2}\right\} Q_6'$$

$$\left.\begin{aligned}
&- \frac{1}{3} (1-\alpha_{k-1})\left(-\frac{3}{2} p_{k-1} + 2p_k - \frac{1}{2} p_{k+1}\right) - \frac{4}{3} (1-\alpha_k)\left(-\frac{1}{2} p_{k-1} + \frac{1}{2} p_{k+1}\right) - \\
&\qquad - \frac{1}{3} (1-\alpha_{k+1})\left(\frac{1}{2} p_{k-1} - 2p_k + \frac{3}{2} p_{k+1}\right)
\end{aligned}\right\} Q_{15}'$$

$$\left.+ \frac{h}{3} (1-\alpha_{k-1})\rho_\ell f_{r_{k-1}} + \frac{4}{3} (1-\alpha_k)\rho_\ell f_{r_k} + \frac{h}{3} (1-\alpha_{k+1})\rho_\ell f_{r_{k+1}}\right\} Q_{17}'$$

$$\left.+ \frac{h}{3} R_{r_{k-1}} + \frac{4h}{3} R_{r_k} + \frac{h}{3} R_{r_{k+1}}\right\} Q_9'$$

$$\left.- \frac{1}{3} \frac{(1-\alpha_{k-1})\rho_\ell u_{\ell r_{k-1}}^{\;2}}{k-1} - \frac{4}{3} \frac{(1-\alpha_k)\rho_\ell u_{\ell r_k}^{\;2}}{k} - \frac{1}{3} \frac{(1-\alpha_{k+1})\rho_\ell u_{\ell r_{k+1}}^{\;2}}{k+1}\right\} Q_8'$$

Equation (3-81).

$$P_k = (1-\alpha_k)\rho_\ell u_{\ell z_k}{}^2 \qquad R_{z_k} = \frac{3}{4}\,\frac{C_D}{d}\,\alpha_k\rho_\ell(u_{gz_k}-u_{\ell z_k})\,|u_{gz_k}-u_{\ell z_k}|$$

$$T_k = (1-\alpha_k)$$

$$F_k = p_k$$

$$R_k = Y_k = 0$$

$$Q_k = (1-\alpha_k)\rho_\ell u_{\ell r_k} u_{\ell z_k}$$

$$S_k = -(1-\alpha_k)\rho_\ell f_z + R_{z_k} - \frac{(1-\alpha_k)\rho_\ell u_{\ell r_k} u_{\ell z_k}}{r_k}$$

$$\frac{dP_k}{dz} = 2(1-\alpha_k)\rho_\ell u_{\ell z_k}\,\frac{d}{dz}\,u_{\ell z_k} - \rho_\ell u_{\ell z_k}{}^2\,\frac{d}{dz}\,\alpha_k .$$

$$\begin{aligned}
&\frac{2}{3}\,h\,(1-\alpha_{k-1})\rho_\ell u_{\ell z_{k-1}}\,\frac{d}{dz}\,u_{\ell z_{k-1}} - \frac{h}{3}\,\rho_\ell u_{\ell z_{k-1}}{}^2\,\frac{d}{dz}\,\alpha_{k-1} + \frac{h}{3}\,(1-\alpha_{k-1})\,\frac{d}{dz}\,p_{k-1} + \\
&\frac{8h}{3}\,(1-\alpha_k)\rho_\ell u_{\ell z_k}\,\frac{d}{dz}\,u_{\ell z_k} - \frac{4h}{3}\,\rho_\ell u_{\ell z_k}{}^2\,\frac{d}{dz}\,\alpha_k + \frac{4h}{3}\,(1-\alpha_k)\,\frac{d}{dz}\,p_k + \\
&\frac{2}{3}\,h\,(1-\alpha_{k+1})\rho_\ell u_{\ell z_{k+1}}\,\frac{d}{dz}\,u_{\ell z_{k+1}} - \frac{h}{3}\,\rho_\ell u_{\ell z_{k+1}}{}^2\,\frac{d}{dz}\,\alpha_{k+1} + \frac{h}{3}\,(1-\alpha_{k+1})\,\frac{d}{dz}\,p_{k+1} =
\end{aligned}$$

$$\left.\begin{aligned}
&+\frac{dh}{dz}\left(\frac{k+1}{2} - \frac{3(k-1)}{2}\right)\,(1-\alpha_{k-1})\rho_\ell u_{\ell z_{k-1}}{}^2 \\
&+ 4\,\frac{dh}{dz}\,(1-\alpha_k)\rho_\ell u_{\ell z_k}{}^2 \\
&+\frac{dh}{dz}\left(\frac{3}{2}\,(k+1) - \frac{1}{2}\,(k-1)\right)\,(1-\alpha_{k+1})\rho_\ell u_{\ell z_{k+1}}{}^2
\end{aligned}\right\} Q_{10}'$$

$$\left.\begin{aligned}
&+\frac{k-1}{3}\,\frac{dh}{dz}\,(1-\alpha_{k-1})\left(-\frac{3}{2}\,p_{k-1}+2p_k-\frac{1}{2}p_{k+1}\right) + \frac{4}{3}\,k\,\frac{dh}{dz}\,(1-\alpha_k)\left(-\frac{1}{2}p_{k-1}+\frac{1}{2}p_{k+1}\right) + \\
&\qquad\qquad + \frac{k+1}{3}\,\frac{dh}{dz}\,(1-\alpha_{k+1})\left(\frac{1}{2}p_{k-1}-2p_k+\frac{3}{2}\,p_{k+1}\right)
\end{aligned}\right\} Q_{20}'$$

$$\left.+ (1-\alpha_{k-1})\,\rho_\ell u_{\ell r_{k-1}} u_{\ell z_{k-1}} - (1-\alpha_{k+1})\rho_\ell u_{\ell r_{k+1}} u_{\ell z_{k+1}}\right\} Q_{11}'$$

$$\left.-\frac{h}{3}\,(1-\alpha_{k-1})\rho_\ell f_z - \frac{4}{3}\,h(1-\alpha_k)\rho_\ell f_z - \frac{h}{3}\,(1-\alpha_{k+1})\rho_\ell f_z\right\} Q_{12}'$$

$$+ \frac{h}{3} R_{z_{k-1}} + \frac{4h}{3} R_{z_k} + \frac{h}{8} R_{z_{k+1}} \qquad Q_{22}'$$

$$- \frac{1}{3} \frac{(1-\alpha_{k-1})\rho_\ell u_{\ell r_{k-1}} u_{\ell z_{k-1}}}{k-1} - \frac{4}{3} \frac{(1-\alpha_k)\rho_\ell u_{\ell r_k} u_{\ell z_k}}{k} - \frac{1}{3} \frac{(1-\alpha_{k+1})\rho_\ell u_{\ell r_{k+1}} u_{\ell z_{k+1}}}{k+1} \qquad Q_{13}'$$

Equation (3-82).

$$P_k = \alpha_k \rho_{g_k} u_{gr_k} u_{gz_k} + (1-\alpha_k)\rho_\ell u_{\ell r_k} u_{\ell z_k} + B_k \alpha_k \rho_\ell u_{gz_k} u_{gr_k} - B_k \alpha_k \rho_{\ell_k} u_{gz_k} u_{\ell r_k}$$

$$T_k = F_k = R_k = Y_k = 0$$

$$Q_k = \alpha_k \rho_{g_k} u_{gr_k}{}^2 + (1-\alpha_k)\rho_\ell u_{\ell r_k}{}^2 + B_k \alpha_k \rho_\ell u_{gr_k} (u_{gr_k} - u_{\ell r_k}) + p_k$$

$$S_k = (\alpha_k \rho_{g_k} + (1-\alpha_k)\rho_\ell) f_{r_k} - \frac{\alpha_k \rho_{g_k} u_{gr_k}{}^2 + (1-\alpha_k)\rho_\ell u_{\ell r_k}{}^2}{r_k} - \frac{B_k \alpha_k \rho_\ell u_{gr_k} (u_{gr_k} - u_{\ell r_k})}{r_k}$$

$$\frac{dB_k}{dz} = \beta_k \frac{d\alpha_k}{dz} .$$

$$\frac{d}{dz} P_k = \alpha_k \rho_{g_k} u_{gr_k} \frac{d}{dz} u_{gz_k} + \alpha_k \rho_{g_k} u_{gz_k} \frac{d}{dz} u_{gr_k} + \frac{\alpha_k u_{gr_k} u_{gz_k}}{RT} \frac{d}{dz} p_k + $$

$$+ \rho_{g_k} u_{gr_k} u_{gz_k} \frac{d}{dz} \alpha_k$$

$$+ (1-\alpha_k)\rho_\ell u_{\ell r_k} \frac{d}{dz} u_{\ell z_k} + (1-\alpha_k)\rho_\ell u_{\ell z_k} \frac{d}{dz} u_{\ell r_k} - \rho_\ell u_{\ell r_k} u_{\ell z_k} \frac{d}{dz} \alpha_k$$

$$+ B_k \alpha_k \rho_\ell u_{gz_k} \frac{d}{dz} u_{gr_k} + B_k \alpha_k \rho_\ell u_{gr_k} \frac{d}{dz} u_{gz_k} + B_k \rho_\ell u_{gz_k} u_{gr_k} \frac{d}{dz} \alpha_k +$$

$$+ \beta_k \alpha_k \rho_\ell u_{gz_k} u_{gr_k} \frac{d}{dz} \alpha_k$$

$$- B_k \alpha_k \rho_\ell u_{gz_k} \frac{d}{dz} u_{\ell r_k} - B_k \alpha_k \rho_\ell u_{\ell r_k} \frac{d}{dz} u_{gz_k} - B_k \rho_\ell u_{gz_k} u_{\ell r_k} \frac{d}{dz} \alpha_k -$$

$$- \beta_k \alpha_k \rho_\ell u_{gz_k} u_{\ell r_k} \frac{d}{dz} \alpha_k$$

$$= \{ \alpha_k \rho_{g_k} u_{gr_k} + B_k \alpha_k \rho_\ell (u_{gr_k} - u_{\ell r_k}) \} \frac{d}{dz} u_{gz_k}$$

$$+ \{ \alpha_k \rho_{g_k} u_{gz_k} + B_k \alpha_k \rho_\ell u_{gz_k} \} \frac{d}{dz} u_{gr_k}$$

$$+ (1-\alpha_k) \rho_\ell u_{\ell r_k} \frac{d}{dz} u_{\ell z_k}$$

$$+ \{ (1-\alpha_k) \rho_\ell u_{\ell z_k} - B_k \alpha_k \rho_\ell u_{gz_k} \} \frac{d}{dz} u_{\ell r_k}$$

$$+ \frac{\alpha_k u_{gr_k} u_{gz_k}}{RT} \frac{d}{dz} p_k$$

$$+ \{ \rho_g u_{gr_k} u_{gz_k} - \rho_\ell u_{\ell r_k} u_{\ell z_k} + (B_k + \alpha_k \beta_k) \rho_\ell u_{gz_k} (u_{gr_k} - u_{\ell r_k}) \} \frac{d}{dz} \alpha_k .$$

$$\frac{h}{3} \{ \rho_{g_{k-1}} u_{gr_{k-1}} u_{gz_{k-1}} - \rho_\ell u_{\ell r_{k-1}} u_{\ell z_{k-1}} + (B_{k-1} + \alpha_{k-1} \beta_{k-1}) \rho_\ell u_{gz_{k-1}}$$

$$(u_{gr_{k-1}} - u_{\ell r_{k-1}}) \frac{d}{dz} \alpha_{k-1}$$

$$+ \frac{4h}{3} \{ \rho_{g_k} u_{gr_k} u_{gz_k} - \rho_\ell u_{\ell r_k} u_{\ell z_k} + (B_k + \alpha_k \beta_k) \rho_\ell u_{gz_k} (u_{gr_k} - u_{\ell r_k}) \frac{d}{dz} \alpha_k$$

$$+ \frac{h}{3} \{ \rho_{g_{k+1}} u_{gr_{k+1}} u_{gz_{k+1}} - \rho_\ell u_{\ell r_{k+1}} u_{\ell z_{k+1}} + (B_{k+1} + \alpha_{k+1} \beta_{k+1}) \rho_\ell u_{gz_{k+1}}$$

$$(u_{gr_{k+1}} - u_{\ell r_{k+1}}) \frac{d}{dz} \alpha_{k+1}$$

$$+ \frac{h}{3} \frac{\alpha_{k-1} u_{gr_{k-1}} u_{gz_{k-1}}}{RT} \frac{d}{dz} p_{k-1} + \frac{4h}{3} \frac{\alpha_k u_{gr_k} u_{gz_k}}{RT} \frac{d}{dz} p_k + \frac{h}{3} \frac{\alpha_{k+1} u_{gr_{k+1}} u_{gz_{k+1}}}{RT} \frac{d}{dz} p_k$$

$$+ \frac{h}{3} (1-\alpha_{k-1}) \rho_\ell u_{\ell r_{k-1}} \frac{d}{dz} u_{\ell z_{k-1}} + \frac{4h}{3} (1-\alpha_k) \rho_\ell u_{\ell r_k} \frac{d}{dz} u_{\ell z_k} +$$

$$+ \frac{h}{3} (1-\alpha_{k+1}) \rho_\ell u_{\ell r_{k+1}} \frac{d}{dz} u_{\ell z_{k+1}}$$

$$+ \frac{h}{3} \{ (1-\alpha_{k-1})\rho_\ell u_{\ell z_{k-1}} - B_{k-1}\alpha_{k-1}\rho_\ell u_{gz_{k-1}} \} \frac{d}{dz} u_{\ell r_{k-1}}$$

$$+ \frac{4h}{3} \{ (1-\alpha_k)\rho_\ell u_{\ell z_k} - B_k\alpha_k\rho_\ell u_{gz_k} \} \frac{d}{dz} u_{\ell r_k}$$

$$+ \frac{h}{3} \{ (1-\alpha_{k+1})\rho_\ell u_{\ell z_{k+1}} - B_{k+1}\alpha_{k+1}\rho_\ell u_{gz_{k+1}} \} \frac{d}{dz} u_{\ell r_{k+1}}$$

$$+ \frac{h}{3} \{ \alpha_{k-1}\rho_{g_{k-1}} u_{gr_{k-1}} + B_{k-1}\alpha_{k-1}\rho_\ell (u_{gr_{k-1}} - u_{\ell r_{k-1}}) \} \frac{d}{dz} u_{gz_{k-1}}$$

$$+ \frac{4h}{3} \{ \alpha_k\rho_{g_k} u_{gr_k} + B_k\alpha_k\rho_\ell (u_{gr_k} - u_{\ell r_k}) \} \frac{d}{dz} u_{gz_k}$$

$$+ \frac{h}{3} \{ \alpha_{k+1}\rho_{g_{k+1}} u_{gr_{k+1}} + B_{k+1}\alpha_{k+1}\rho_\ell (u_{gr_{k+1}} - u_{\ell r_{k+1}}) \} \frac{d}{dz} u_{gz_{k+1}}$$

$$+ \frac{h}{3} \{ \alpha_{k-1}\rho_{g_{k-1}} u_{gz_{k-1}} + B_{k-1}\alpha_{k-1}\rho_\ell u_{gz_{k-1}} \} \frac{d}{dz} u_{gr_{k-1}}$$

$$+ \frac{4h}{3} \{ \alpha_k\rho_{g_k} u_{gz_k} + B_k\alpha_k\rho_\ell u_{gz_k} \} \frac{d}{dz} u_{gr_k}$$

$$+ \frac{h}{3} \{ \alpha_{k+1}\rho_{g_{k+1}} u_{gz_{k+1}} + B_{k+1}\alpha_{k+1}\rho_\ell u_{gz_{k+1}} \} \frac{d}{dz} u_{gr_{k+1}} =$$

$$\left.\begin{aligned}
&= \frac{dh}{dz} (\frac{k+1}{2} - \frac{3}{2}(k-1)) \{ \alpha_{k-1}\rho_{g_{k-1}} u_{gr_{k-1}} u_{gz_{k-1}} + B_{k-1}\alpha_{k-1}\rho_\ell u_{gz_{k-1}} \\
&\qquad\qquad (u_{gr_{k-1}} - u_{\ell r_{k-1}}) \} \\
&- 4 \frac{dh}{dz} \{ \alpha_k\rho_{g_k} u_{gr_k} u_{gz_k} + B_k\alpha_k\rho_\ell u_{gz_{k-1}} (u_{gr_{k-1}} - u_{\ell r_{k-1}}) \} \\
&+ \frac{dh}{dz} (\frac{3}{2}(k+1) - \frac{1}{2}(k-1)) \{ \alpha_{k+1}\rho_{g_{k+1}} u_{gr_{k+1}} u_{gz_{k+1}} + \\
&\qquad\qquad + B_{k+1}\alpha_{k+1}\rho_\ell u_{gz_{k+1}} (u_{gr_{k+1}} - u_{\ell r_{k+1}}) \}
\end{aligned}\right\} Q_{14}'$$

$$+ Q_5' \quad \star)$$

$$\left.\begin{aligned}
&+ \alpha_{k-1}\rho_{g_{k-1}} u_{gr_{k-1}}^{\ 2} + B_{k-1}\alpha_{k-1}\rho_\ell u_{gr_{k-1}} (u_{gr_{k-1}} - u_{\ell r_{k-1}}) + p_{k-1} \\
&- \alpha_{k+1}\rho_{g_{k+1}} u_{gr_{k+1}}^{\ 2} - B_{k+1}\alpha_{k+1}\rho_\ell u_{gr_{k+1}} (u_{gr_{k+1}} - u_{\ell r_{k+1}}) - p_{k+1}
\end{aligned}\right\} Q_{16}'$$

$$+ Q_6'$$

★) *for* Q_5' *etc. see identical terms in preceding equations.*

$$\left.+ \frac{h}{3}\alpha_{k-1}\rho_{g_{k-1}} f_{r_{k-1}} + \frac{4h}{3}\alpha_k\rho_{g_k} f_{r_k} + \frac{h}{3}\alpha_{k+1}\rho_{g_{k+1}} f_{r_{k+1}}\right\} Q_{17}'$$

$$+ Q_7'$$

$$\left.\begin{aligned}
&- \frac{1}{3}\,\frac{\alpha_{k-1}\rho_{g_{k-1}} u_{gr_{k-1}}{}^2 + B_{k-1}\alpha_{k-1}\rho_\ell u_{gr_{k-1}}(u_{gr_{k-1}} - u_{\ell r_{k-1}})}{k-1}\\
&- \frac{4}{3}\,\frac{\alpha_k\rho_{g_j} u_{gr_k}{}^2 + B_k\alpha_k\rho_\ell u_{gr_k}(u_{gr_k} - u_{\ell r_k})}{k}\\
&- \frac{1}{3}\,\frac{\alpha_{k+1}\rho_{g_{k+1}} u_{gr_{k+1}}{}^2 + B_{k+1}\alpha_{k+1}\rho_\ell u_{gr_{k+1}}(u_{gr_{k+1}} - u_{\ell r_{k+1}})}{k+1}
\end{aligned}\right\} Q_{18}'$$

$$+ Q_8'$$

Equation (3-83).

$$P_k = \alpha_k\rho_{g_k} u_{gz_k}{}^2 + (1-\alpha_k)\rho_\ell u_{\ell z_k}{}^2 + B_k\alpha_k\rho_\ell u_{gz_k}{}^2 - B_k\alpha_k\rho_\ell u_{gz_k} u_{\ell z_k} + p_k$$

$$T_k = F_k = R_k = Y_k = 0$$

$$Q_k = \alpha_k\rho_{g_k} u_{gr_k} u_{gz_k} + (1-\alpha_k)\rho_\ell u_{\ell r_k} u_{\ell z_k} + B_k\alpha_k\rho_\ell u_{gr_k}(u_{gz_k} - u_{\ell z_k})$$

$$S_k = -(\alpha_k\rho_{g_k} + (1-)\rho_\ell) f_z - \frac{\alpha_k\rho_{g_k} u_{gr_k} u_{gz_k} + (1-\alpha_k) u_{\ell r_k} u_{\ell z_k} + B_k\alpha_k\rho_\ell u_{gr_k}(u_{gz_k} - u_{\ell z_k})}{r_k}$$

$$\frac{d}{dz} P_k = 2\alpha_k\rho_{g_k} u_{gz_k}\frac{d}{dz} u_{gz_k} + \frac{\alpha_k u_{gz_k}{}^2}{RT}\frac{d}{dz} p_k + \rho_{g_k} u_{gz_k}{}^2\frac{d}{dz}\alpha_k + \frac{d}{dz} p_k$$

$$+ 2\,(1-\alpha_k)\rho_\ell u_{\ell z_k}\frac{d}{dz} u_{\ell z_k} - \rho_\ell u_{\ell z_k}{}^2\frac{d}{dz}\alpha_k$$

$$+ 2B_k\alpha_k\rho_\ell u_{gz_k}\frac{d}{dz} u_{gz_k} + B_k\rho_\ell u_{gz_k}{}^2\frac{d}{dz}\alpha_k + \beta_k\alpha_k\rho_\ell u_{gz_k}{}^2\frac{d}{dz}\alpha_k$$

$$- B_k \alpha_k \rho_\ell u_{gz_k} \frac{d}{dz} u_{\ell z_k} - B_k \alpha_k \rho_\ell u_{\ell z_k} \frac{d}{dz} u_{gz_k} - B_k \rho_\ell u_{gz_k} u_{\ell z_k} \frac{d}{dz} \alpha_k -$$

$$- \beta_k \alpha_k \rho_\ell u_{gz_k} u_{\ell z_k} \frac{d}{dz} \alpha_k$$

$$= \{ \rho_{g_k} u_{gz_k}{}^2 - \rho_\ell u_{\ell z_k}{}^2 + (B_k + \alpha_k \beta_k) \rho_\ell u_{gz_k} (u_{gz_k} - u_{\ell z_k}) \} \frac{d}{dz} \alpha_k$$

$$+ \{ \frac{\alpha_k u_{gz_k}{}^2}{RT} + 1 \} \frac{d}{dz} p_k$$

$$+ \{ 2(1-\alpha_k) \rho_\ell u_{\ell z_k} - B_k \alpha_k \rho_\ell u_{gz_k} \} \frac{d}{dz} u_{\ell z_k}$$

$$+ \{ 2\alpha_k \rho_{g_k} u_{gz_k} + B_k \alpha_k \rho_\ell (2u_{gz_k} - u_{\ell z_k}) \} \frac{d}{dz} u_{gz_k} .$$

$$\frac{h}{3} \{ \rho_{g_{k-1}} u_{gz_{k-1}}{}^2 - \rho_\ell u_{\ell z_{k-1}}{}^2 + (B_{k-1} + \alpha_{k-1} \beta_{k-1}) \rho_\ell u_{gz_{k-1}} (u_{gz_{k-1}} - u_{\ell z_{k-1}}) \} \frac{d}{dz} \alpha_{k-1}$$

$$+ \frac{4h}{3} \{ \rho_{g_k} u_{gz_k}{}^2 - \rho_\ell u_{\ell z_k}{}^2 + (B_k + \alpha_k \beta_k) \rho_\ell u_{gz_k} (u_{gz_k} - u_{\ell z_k}) \} \frac{d}{dz} \alpha_k$$

$$+ \frac{h}{3} \{ \rho_{g_{k+1}} u_{gz_{k+1}}{}^2 - \rho_\ell u_{\ell z_{k+1}}{}^2 + (B_{k+1} + \alpha_{k+1} \beta_{k+1}) \rho_\ell u_{gz_{k+1}} (u_{gz_{k+1}} - u_{\ell z_{k+1}}) \} \frac{d}{dz} \alpha_{k+1}$$

$$+ \frac{h}{3} \{ \frac{\alpha_{k-1} u_{gz_{k-1}}{}^2}{RT} + 1 \} \frac{d}{dz} p_{k-1}$$

$$+ \frac{4h}{3} \{ \frac{\alpha_k u_{gz_k}{}^2}{RT} + 1 \} \frac{d}{dz} p_k$$

$$+ \frac{h}{3} \{ \frac{\alpha_{k+1} u_{gz_{k+1}}{}^2}{RT} + 1 \} \frac{d}{dz} p_{k+1}$$

$$+ \frac{h}{3} \{ 2(1-\alpha_{k-1}) \rho_\ell u_{\ell z_{k-1}} - B_{k-1} \alpha_{k-1} \rho_\ell u_{gz_{k-1}} \} \frac{d}{dz} u_{\ell z_{k-1}}$$

$$+ \frac{4h}{3} \{ 2(1-\alpha_k) \rho_\ell u_{\ell z_k} - B_k \alpha_k \rho_\ell u_{gz_k} \} \frac{d}{dz} u_{\ell z_k}$$

$$+ \frac{h}{3} \{ 2(1-\alpha_{k+1}) \rho_\ell u_{\ell z_{k+1}} - B_{k+1} \alpha_{k+1} \rho_\ell u_{gz_{k+1}} \} \frac{d}{dz} u_{\ell z_{k+1}}$$

$$+ \frac{h}{3} \{ 2\alpha_{k-1} \rho_{g_{k-1}} u_{gz_{k-1}} + B_{k-1} \alpha_{k-1} \rho_\ell (2u_{gz_{k-1}} - u_{\ell z_{k-1}}) \} \frac{d}{dz} u_{gz_{k-1}}$$

$$+ \frac{4h}{3} \{ 2\alpha_k \rho_{g_k} u_{gz_k} + B_k \alpha_k \rho_\ell (2u_{gz_k} - u_{\ell z_k}) \} \frac{d}{dz} u_{gz_k}$$

$$+ \frac{h}{3} \{ 2\alpha_{k+1} \rho_{g_{k+1}} u_{gz_{k+1}} + B_{k+1} \alpha_{k+1} \rho_\ell (2\, u_{gz_{k+1}} - u_{\ell z_{k+1}}) \} \frac{d}{dz} u_{gz_{k+1}}$$

$$\left.\begin{aligned}
&= \frac{dh}{dz} \left(\frac{k+1}{2} - \frac{3}{2}(k-1)\right) \{ \alpha_{k-1} \rho_{g_{k-1}} u_{gz_{k-1}}{}^2 + \\
&\qquad\qquad + B_{k-1} \alpha_{k-1} \rho_\ell u_{gz_{k-1}} (u_{gz_{k-1}} - u_{\ell z_{k-1}}) + p_{k-1} \} \\
&4 \frac{dh}{dz} \{ \alpha_k \rho_{g_k} u_{gz_k}{}^2 + B_k \alpha_k \rho_\ell u_{gz_k} (u_{gz_k} - u_{\ell z_k}) + p_k \} \\
&+ \frac{dh}{dz} \left(\frac{3}{2}(k+1) - \frac{k-1}{2}\right) \{ \alpha_{k+1} \rho_{g_{k+1}} u_{gz_{k+1}} + \\
&\qquad\qquad + B_{k+1} \alpha_{k+1} \rho_\ell u_{gz_{k+1}} (u_{gz_{k+1}} - u_{\ell z_{k+1}}) + p_{k+1} \}
\end{aligned}\right\} Q_{19}'$$

$$+ Q_{10}'$$

$$\left.\begin{aligned}
&+ \alpha_{k-1} \rho_{g_{k-1}} u_{gr_{k-1}} u_{gz_{k-1}} + B_{k-1} \alpha_{k-1} \rho_\ell u_{gr_{k-1}} (u_{gz_{k-1}} - u_{\ell z_{k-1}}) \\
&- \alpha_{k+1} \rho_{g_{k+1}} u_{gr_{k+1}} u_{gz_{k+1}} - B_{k+1} \alpha_{k+1} \rho_\ell u_{gr_{k+1}} (u_{gz_{k+1}} - u_{\ell z_{k+1}})
\end{aligned}\right\} Q_{21}'$$

$$+ Q_{11}'$$

$$\left. - \frac{h}{3} \alpha_{k-1} \rho_{g_{k-1}} f_z - \frac{4h}{3} \alpha_k \rho_{g_k} f_z - \frac{h}{3} \alpha_{k+1} \rho_{g_{k+1}} f_z \right\} Q_{23}'$$

$$+ Q_{12}'$$

$$\left.\begin{aligned}
&- \frac{1}{3} \frac{\alpha_{k-1} \rho_{g_{k-1}} u_{gr_{k-1}} u_{gz_{k-1}} + B_{k-1} \alpha_{k-1} \rho_\ell u_{gr_{k-1}} (u_{gz_{k-1}} - u_{\ell z_{k-1}})}{k-1} \\
&- \frac{4}{3} \frac{\alpha_k \rho_{g_k} u_{gr_k} u_{gz_k} + B_k \alpha_k \rho_\ell u_{gr_k} (u_{gz_k} - u_{\ell z_k})}{k} \\
&- \frac{1}{3} \frac{\alpha_{k+1} \rho_{g_{k+1}} u_{gr_{k+1}} u_{gz_{k+1}} + B_{k+1} \alpha_{k+1} \rho_\ell u_{gr_{k+1}} (u_{gz_{k+1}} - u_{\ell z_{k+1}})}{k+1}
\end{aligned}\right\} Q_{24}'$$

$$+ Q_{13}'$$

STELLINGEN

1. De door A.S.M.E., A.S.T.M., B.S. en T.ü.V., aanbevolen sondes voor het trekken van stoommonsters bij garantiemetingen betreffende het vochtgehalte van - fossiel of nucleair opgewekte - stoom zijn ongeschikt voor dit doel.

2. In een PWR-stoomgenerator is géén mechanische primaire scheider beter dan een slechte.

3. Het verdient aanbeveling de omvang en uitbreidingen van de wetenschappelijke staf van de afdelingen Werktuigbouwkunde en Algemene Wetenschappen op elkaar af te stemmen.

4. De Nederlandse architect mist in zijn opleiding enige colleges biologie, waarin hem geleerd wordt dat de bewoners van zijn hoogbouwcreaties naast volwassenen voor een aanzienlijk percentage uit kinderen bestaan.

5. Een ongenuanceerde doorvoering van de inspraakgedachte in bestuurlijke organisaties leidt tot de willekeur van het amateurisme.

6. Petrick's bewering dat in zijn slipcorrelatie voor neergaande twee-fasen stroming het effect van de systeemdruk is begrepen, is in strijd met de werkelijkheid.
   (M. Petrick. A study of vapor carry-under and associated problems.
   ANL-6581).

7. Bij de overgrote meerderheid van de Nederlandse bedrijven ondervindt een sollicitant geen nadeel van een universitaire promotie.

8. De toename der theoretische kennis van metallurgische en technologische aspecten van de fabricage van zeer zware laaggelegeerde ferrietische drukvaten voor de petro-chemische industrie heeft niet geleid tot de aanvaarding van geavanceerde ontwerpen door de verbruikers.

9. Het centraal geregelde salaris- en bevorderingsbeleid bij de Technische Hogeschool te Delft is in tegenspraak met de, op zich wenselijke, zelfstandige positie van de laboratorium-bedrijfsingenieur en werkt remmend op de optimale en sociaal verantwoorde uitoefening van zijn functie.

10. Het aantal gedetailleerde, bij voorkeur op formaat A0 gemaakte, constructiewerktekeningen dat de werktuigbouwkundige student tot op heden tijdens zijn Delftse studie dient te maken, staat in schrille tegenstelling tot de eisen die later aan zijn capaciteiten van ingenieur-constructeur worden gesteld.

11. Zonder bijkomende hulpmiddelen is het menselijk oog het meest onbetrouwbare meetinstrument in de twee-fasen stroming.

12. De Minister van Onderwijs toont als werkgever onrustbarend weinig interesse in de tastbare resultaten van de in het wetenschappelijk onderzoek van zijn gepromoveerde werknemers geïnvesteerde gelden.